Integrating New Techniques to Accelerate the Discovery of Hydrogen-Bonded Organic Frameworks

Peng Cui

Department of Chemistry and Materials Innovation Factory,
University of Liverpool

Thesis submitted in accordance with the requirements of the University of Liverpool for the degree of Doctor of Philosophy

June 2021

Supervisor: Prof. Andrew I. Cooper

Abstract

Organic molecules tend to crystallise as densely packed nonporous structures to maximise the intermolecular interactions. However, sometimes molecular crystals can crystallise to form porous structures with channels. Finding crystals with pores that are stable remains a significant challenge and is often a time-consuming process. The primary aim of this thesis was to accelerate the design, discovery, and characterisation of porous hydrogen-bonded organic frameworks (HOFs) by integrating high throughput (HT) screening, crystal structure prediction (CSP), and three-dimensional electron diffractions (3-D ED) into their discovery.

Firstly, a HT crystallisation workflow was developed and combined with CSP calculations to search for porous predicted crystal structures of two well-studied molecules, trimesic acid (**TMA**) and adamantane-1,3,5,7-tetracarboxylic acid (**ADTA**). Using the HT crystallisation workflow, a new porous polymorph of **TMA**, δ-**TMA**, which remained 'hidden' for half a century, and three new solvent-stabilised diamondoid frameworks of **ADTA** were found experimentally after being predicted by CSP calculations. Then, the crystallisation of five molecular analogues of **TMA**, that had comparable 3-fold symmetry and three molecules that each contained four carboxylic acids were explored.

The results presented in chapters 2 and 3 indicated that 2-D HOFs with weak interlayer interactions are metastable, which led to the HOFs densifying during crystal activation or with time. In chapter 4, 5',5""-(anthracene-9,10-diyl) bis (([1,1'3',1"-terphenyl]-4,4"-dicarboxylic acid)) (**ABTPA)**, which has four carboxylic acid groups and also contains an out-of-plane π-conjugated anthracene core molecule was investigated. **ABTPA** formed a 2-D HOF structure, which then transformed during a solvent exchange procedure. The activated crystals were characterised by 3-D ED and had robust dynamic porosity (SA_{BET} = 1183 m^2 g^{-1}). CSP was used to understand the underlying energetics behind the structural transformation.

Acknowledgements

Firstly, I would give my great thanks to Prof. Andrew Cooper FRS for giving me the opportunity to undertake my PhD in the Cooper group. Over the past four years, Andy has given me a lot of help and guidance in my project, papers, and thesis. Without his help, this thesis would not have been possible.

I would also like to thank my research coordinator, Dr Marc Little, who has helped me throughout my PhD. He has shown great patience and passed on his professional knowledge. He has always tried his best to help me with my project, solve the problems in my experiments, and encouraged me to move ahead with my project. He has been on my side every day and I am grateful for his help.

In addition, I would like to thank my great collaborators. Prof. Graeme Day, Dr. Peter Spackman, and Dr. David McMahon at the University of Southampton for a lot of excellent work on crystal structure prediction. I would also like to thank my collaborators, Dr Ken Inge and Eric Svensson Grape at Stockholm University for carrying out electron diffraction analysis during my project. I really appreciate all the work both groups have contributed to my PhD and publications.

It has been a real pleasure to work with all the group members in the Cooper group, especially thanks to Dr. Ben Alston, for helping me with the high throughput Chemspeed platform, and Rob Clowes, for giving me a lot of training on the sorption instruments and helping to interpret isotherms. Also, I would like to thank Ming, Xiaofeng, Linjiang, Guohong, Yang, Chris, Yue, Seb, Zhongfu, Hui, Ai, Lunjie, and Qiang who have given me a lot of help in my life and experiments.

Lastly, I would like to take this opportunity to thank my family for supporting me throughout my PhD. Thanks to my parents, sister, especially, my wife, Shuping, who has encouraged me every day during my PhD.

List of publications

1. Mining predicted crystal structure landscapes with high throughput crystallisation: old molecules, new insights, *Chem. Sci.*, **2019**, 10, 9988-9997. DOI: 10.1039/C9SC02832C

Peng Cui, David P. McMahon, Peter R. Spackman, Ben M. Alston, Marc A. Little, Graeme M. Day and Andrew I. Cooper.

2. An expandable hydrogen-Bonded organic framework characterised by three-dimensional electron diffraction, *J. Am. Chem. Soc.*, **2020**, 142, 12743-12750. DOI: 10.1021/jacs.0c04885

Peng Cui, Erik Svensson Grape, Peter R. Spackman, Yue Wu, Rob Clowes, Graeme M. Day, A. Ken Inge, Marc A. Little, and Andrew I. Cooper.

3. Inducing social self-sorting in organic cages to tune the shape of the internal cavity, *Angew. Chem. Int. Ed.*, **2020**, 59, 2-11. DOI: 10.1002/anie.202007571

Valentina Abet, Filip T Szczypínski, Marc A Little, Valentina Santolini, Christopher D Jones, Robert Evans, Craig Wilson, Xiaofeng Wu, Michael F Thorne, Michael J Bennison, **Peng Cui**, Andrew I Cooper, Kim E Jelfs, Anna Grace Slater

4. 3D cage COFs: A dynamic three-dimensional covalent organic framework with high-connectivity organic cage nodes, *J. Am. Chem. Soc.*, **2020**, 142, 16842-16848. DOI: 10.1021/jacs.0c07732

Qiang Zhu, Xue Wang, Rob Clowes, **Peng Cui**, Linjiang Chen, Marc A Little, Andrew I Cooper.

5. Crystallography companion agent for high-throughput materials discovery, *Nature Computational Science*, **2021**, 1, 290-297. DOI: 10.1038/s43588-021-00059-2

Phillip M Maffettone, Lars Banko, **Peng Cui**, Yury Lysogorskiy, Marc A Little, Daniel Olds, Alfred Ludwig, Andrew I Cooper.

6. Organic cage inclusion crystals exhibiting guest-enhanced multiphoton harvesting, *Chem*, **2021**, under review.

Guo-Hong Ning, **Peng Cui**, Igor Sazanovich, James Pegg, Zhongfu Pang, Mike Towrie, Kim E Jelfs, Marc A Little, Andrew I Cooper.

List of abbreviations

POCs	Porous organic cages
MOFs	Metal organic frameworks
COFs	Covalent organic frameworks
HOFs	Hydrogen-bonded organic frameworks
BET	Brunauer-Emmett-Teller
SA_{BET}	BET surface area
HTS	High-throughput screening
HT	High-throughput
CSP	Crystal structure prediction
ESF	Energy structure function map
TGA	Thermogravimetric analysis
DSC	Differential scanning calorimetry
NMR	Nuclear magnetic resonance
SEM	Scanning electron microscopy
PXRD	Powder X-ray Diffraction
SCXRD	Single Crystal X-ray Diffraction
3-D ED	3-D Electron Diffraction
DCM	Dichloromethane
$CHCl_3$	Chloroform
MeOH	Methanol
EtOH	Ethanol
MeCN	Acetonitrile
DMF	N,N-dimethylformamide
DMA	Dimethylacetamide
DEF	N,N-diethylformamide
THF	Tetrahydrofuran
DMB	Dimethoxybenzene
DMSO	Dimethylsulfoxide

TMA	Trimesic acid
ADTA	Adamantane-1,3,5,7-tetracarboxylic acid
ABTPA	5',5""-(Anthracene-9,10-diyl)bis(([1,1'3',1"-terphenyl]-4,4"-dicarboxylic acid))
M1	3,3',3"-(Benzene-1,3,5-triyl) tripropiolic acid
M2	1,3,5-Tri(4-carboxyphenyl) benzene
M3	5"-(4'-((Oxo-l3-methyl)-l3-oxidaneyl) - [1,1'-biphenyl]-4-yl)-[1,1':4',1":3",1"':4"',1""- quinquephenyl] -4,4""- dicarboxylic acid
M4	5'-(4-Carboxy-2,3,5,6-tetrafluorophenyl) -2,2",3,3",5,5",6,6"-octafluoro-[1,1':3',1"-terphenyl]-4,4"-dicarboxylic acid
M5	4,4',4"-(1,3,3a[1],4,6,7,9-Heptaazaphenalene-2,5,8-triyl) tribenzoic acid
M6	1,2,4,5-Benzenetetracarboxylic acid
M7	Biphenyl-3,3',5,5'-tetra-carboxylic acid
M8	[1,1′:4′,1″] Terphenyl- 3,3″,5,5″-tetracarboxylic acid

Colour key

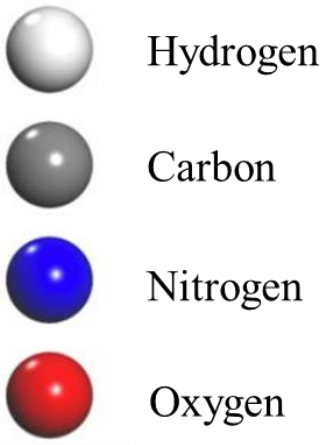

Contents

Chapter 1

Introduction

1. Supramolecular chemistry

Supramolecular chemistry is defined as 'chemistry beyond the molecule' and is the subject of association of chemical species held together by non-covalent interactions, such as electrostatics, hydrophobic forces, hydrogen bonding, coordination bonds, and van der Waals forces.[1,2] These comparatively weak and reversible forces are key to controlling how molecules self-assemble into systems and how biological systems function. Lehn (cryptand complex), Cram (host-guest complex), and Pedersen (crown ether complex) were awarded the Nobel Prize in 1987 for their development and application of molecules with highly selective structure specific interaction (Figure 1.1). They laid the foundations of one of the most active fields in chemical research which Cram has coined the term host-guest chemistry and Lehn calls it supramolecular chemistry.

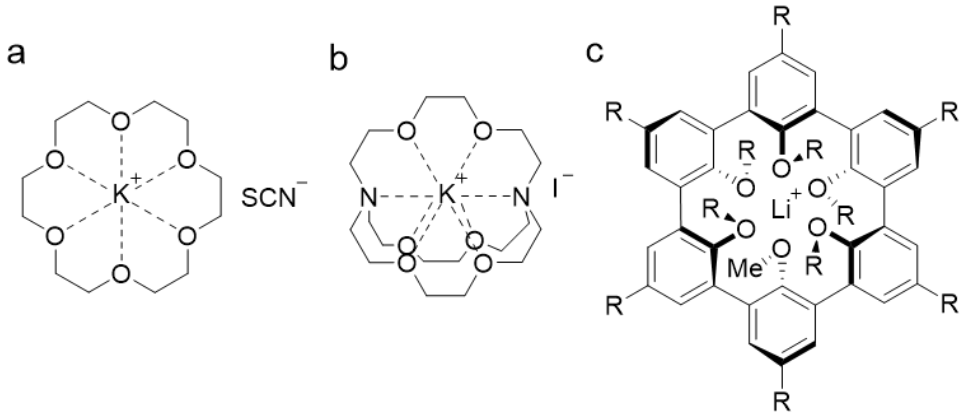

Figure 1.1 a) Crown ether complex according to Pedersen; b) cryptand complex according to Lehn; c) host-guest complex according to Cram, R=Me= -CH_3.

In the last few decades, supramolecular chemistry has become an interdisciplinary research topic that spans biology, chemistry, material science, and nanotechnology. Supramolecular systems have shown great potential in applications, such as catalysis,[3] drug delivery,[4] molecular recognition,[5] and electrochemical sensing[6]. Supramolecular chemistry crosses the boundaries between various chemical disciplines and focuses on the interrelation and interaction between molecules, thus opening new routes to develop molecular devices for the materials and biological sciences.[7–9] In contrast to

traditional polymers formed by monomer polymerisation or chain polymerisation, supramolecular systems are spontaneously formed through reversible, and often lower energy, non-covalent bonds that form between small organic molecules. The existence of non-covalent bonds makes the aggregation and degradation of supramolecular systems reversible, which enables them to be processed in solution,[10] for example, to self-repair[11] and respond to environmental stimuli[12].

A large proportion of supramolecular chemistry research focuses on developing new design rules, structure characterisation, the determination of important properties, and applications of new supramolecular systems (*e.g.*, rotanes,[13] microemulsions,[14] and cyclodextrin nanotubes[15]) and various nanometer supramolecular devices (*e.g.*, molecular motors,[16,17] elevators,[18] and sensors[19,20]).

1.1 Host-guest chemistry

Host-guest chemistry is a branch of supramolecular chemistry,[21–23] where host molecules form complexes with guest molecules or ions. The host and guest molecules in the complexes are held together by non-covalent forces, such as hydrogen bonds and van der Waals forces, and hydrophobic interactions. The host molecules tend to have cavities (or pores), such as crown ethers,[24,25] cavitands,[26] and metal-organic polyhedra[27] because guest molecules can bind in their internal (intrinsic) cavities. In the solid state, molecules can also be directed to pack inefficiently to form structures that contain external (extrinsic) voids, such as metal organic frameworks (MOFs)[28], covalent organic frameworks (COFs)[29], and hydrogen bonded organic frameworks (HOFs)[30]. Structures with extrinsic cavities act also as supramolecular hosts and the guests can range from inorganic anions,[31] and monatomic cations,[32] to more sophisticated molecules (*e.g.,* hormone,[33] pheromone[34]).

The formation of host-guest complexes does not destroy the structure and valence of the original molecules because there is not always a need for a strong chemical bond between host and guest, which requires that host and guest have a high degree of matching and adaptability in terms of spatial geometry, electric charge, hydrophilicity, and symmetry.[35] Therefore, molecular and site recognition is the basis of

supramolecular system, and recognition is the process of selective binding between a given receptor and an agent to produce some specific functions.[36]

1.2 Self-assembly

Self-assembly is a process in which the basic structural units (molecules, nanomaterials, microns, or larger scales) spontaneously form ordered structures.[37,38] In the process of self-assembly, the basic structural units spontaneously organise or aggregate into a stable structure with regular geometric appearance under the influences of non-covalent bonds. The process of self-assembly is not a simple superposition of the weak forces among a large number of atoms, ions, and molecules, but a complex synergistic effect, in which the individual components spontaneously self-sort at the same time and gather together to form a compact and ordered assembly.[39,40]

There are two types of self-assembly in nature: thermodynamic self-assembly,[41,42] in which the system takes on the most energy-stable form, such as a raindrop; and coded-self-assembly,[43,44] widely found in living organisms, in which instructions controlling the order of assembly are contained in components.

Molecular self-assembly is controlled by molecular recognition, which is driven by weak and reversible non-covalent interactions, such as hydrogen bonds. Molecular recognition ensures a high degree of order in the self-assembled systems, and the structural stability and integrity are maintained by non-covalent interactions. Molecular self-assembly can be divided into the self-assembly of infinite network structures,[45] such as nanotubes,[46] Langmuir-Blodgett film,[47] cable hydrocarbons[48], and rotating hydrocarbons[49]. In addition to molecular self-assembly, another molecular assembly method is called the templatation effect, such as the assembly at a silicon interface.[50,51]

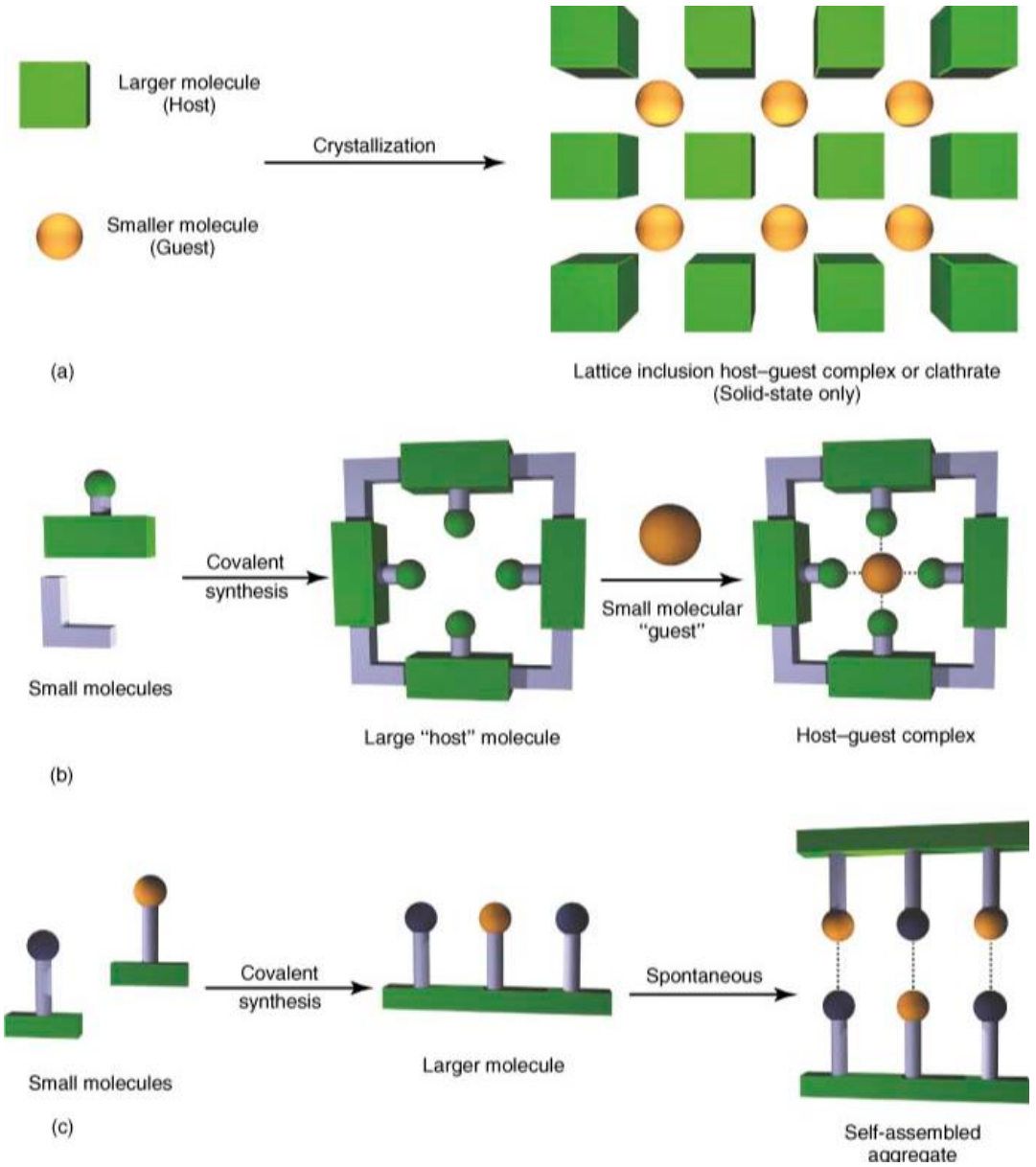

Figure 1.1. Key design approaches encountered in supramolecular chemistry. (a) Solid-state formation of host-guest lattice inclusion complex, (b) molecular host synthesis and associated host-guest complexation, and (c) self-assembly of supramolecular building blocks. Reprint from Supramolecular Chemistry, J. W. Steed and J. L. Atwood, Wiley: Chichester, 2nd Ed., 2009. Copyright 2009 Wiley.

1.3 Chemical equilibrium

Chemical equilibrium is the point in a chemical reaction at which there is no further change in the relevant ionic and molecular species. It refers to the balance of two competitive reactions ($\rightarrow$ and $\leftarrow$) in a reversible reaction. In this dynamic process,

the forward and reverse reactions proceed at the same rate (↔). At equilibrium, the two opposing reactions go on at equal rates, or velocities and there is no change in the amounts of substances involved. Supramolecular assembly is the basic structural units (molecules, nanomaterials, microns, or larger scales) spontaneously form ordered structures with weak non-covalent bonds under chemical equilibrium.

1.4 Crystal engineering

In 1962, von Hippel described the fundamentals of crystal engineering in detail under the term 'molecular engineering'.[52] Later, Desiraju defined crystal engineering as "*the understanding of intermolecular interactions in the context of crystal packing and the utilisation of such understanding in the design of new solids with desired physical and chemical properties*" in 1989.[53] Non-covalent bonding is used to organise molecules and ions in solid state, and hydrogen bonds have been widely used in organic systems. More recently, the use of halogen bonds has also proved to be beneficial in providing additional control in crystal engineering.[54]

Crystal engineering can be broken down into two main parts: synthesis and analysis. The interplay between these two parts in modern crystal engineering had been summarised by Braga and Desiraju as "*reason and imagination come into play simultaneously in the quest for new functionalised solids, while experiment and computation are of equal significance in the prediction and design of crystal structures*".[55]

Crystal engineering is a kind of synthetic chemistry in molecular crystals. It can be thought of as the design and understanding of the way of molecules that crystallise to form materials with new structures. Crystallisation is a self-assembly process, which the components encounter and recognise one another in the solution. The crystal structure that is observed experimentally is often a function of the different crystallisation conditions, and polymorphs that crystals formed from the same molecules but with different packing arrangements are common.

2. Porous organic crystalline framework materials

Porous framework materials have been widely explored in the last several decades because they have pores that can be chemically and structurally modified, which has led to potential applications in gas storage, separations, catalysis, and host-guest chemistry.[56,57] The first porous framework material, a zeolite mineral, stilbite, was discovered by Swedish mineralogist Cronstedt in 1756.[58] Afterward, significant research about the synthesis, characteriasation, and applications of zeolites has been published.[59–62] In the last three decades, researchers have developed new classes of porous solid, including metal organic frameworks (MOFs)[63,65], covalent organic frameworks (COFs)[29], porous organic cages (POCs)[64], and hydrogen bonded organic frameworks (HOFs)[65] to explore new potential applications for porous frameworks materials.

2.1 Metal organic frameworks (MOFs)

In 1999, Yaghi and co-workers reported the first permanently porous MOF (MOF-5).[63] In the structure of MOF-5, the metal ions clusters coordinate to the organic ligands to form a three-dimensional MOF structure. Subsequently, organic ligands with different functional groups and structures have been reported to coordinate to metal ion clusters using the same chemistry to form MOFs with different network topologies and porosities. The different metal ion clusters have been shown to influence the size and shape of pores because of the different coordinated directionality.

The general synthesis method of MOFs is similar to that used to synthesise zeolites, which often use hydrothermal or solvothermal techniques. Some MOFs have also been synthesised using solvent-free methods, including ball mill grinding[66], and chemical vapour deposition[67]. The selection of the metal ion cluster and organic ligand is very important because both act as the multi connection nodes in MOFs structures to control and synthesise the desired structures. Post-synthetic modification of MOFs, which includes exchanging the organic ligands and metal modes, provides a new way to get new structures and multi-functional MOFs.[68,69] The structures and

compositions of MOFs can affect their chemical properties, and different pore environments can more strongly adsorb different gases, such as CO_2[70–72], CH_4[73,74], and H_2[75–77]. MOFs have also been reported to selectively adsorb heavy metal[78], fluorocarbon refrigerant[28], and nuclear waste[79]. The pore sizes and environments in MOFs are very important for controlling gas selectively, and MOFs have been shown to selectively separate gas a range of gas mixtures, including CH_4/CO_2[80–82], C_2H_4/C_2H_6[83] and C_2H_4/C_2H_2[84]. The existence of metal ions in combination with porosity has led to MOFs being widely used as catalysts.[85–87] MOFs can also be used as sensor materials[88,89] and biomedical microrobots[90].

2.2 Covalent organic frameworks (COFs)

COFs are made from light elements, mainly C, N, B, O, and often have 2- and 3-dimensional extended structures. The first COF was also reported by Yaghi in 2005,[29] who used condensation reactions between boronic acid groups to form the 2-D COFs, COF-1, and COF-5, which had good thermal stability and permanent porosity. Two years later, four 3-D COFs were synthesised with the same condensation reaction.[91] In 2009, the first COF that was synthesised using Schiff-base condensation of amines and aldehyde was reported.[92] Because of the higher stability of imine COFs over their boroxine counterparts, imine COFs have been the focus of a larger amount of COF research in the last decade.[93,94]

Most COFs are synthesised in Pyrex tubes in organic solvents containing a catalytic amount of acid and at high temperatures for several days.[95,96] Other novel synthetic methods, such as liquid-assisted grinding[97], continuous flow synthesis[98], interfacial synthesis[99,100], 3-D printing[101], and high-throughput construction[102] have also been reported. Although COFs are crystalline materials, their structures are usually determined by constructing models and comparing their simulated powder X-ray diffraction (PXRD) patterns to the experimental PXRD data. Culturing single crystals of COF materials remains a significant challenge, and only a few single crystal COFs have been reported, including some characterised by 3-D electron diffraction (ED)[103–105] and single crystal X-ray diffraction (SCXRD)[106–108]. One reason is because the

synthetic methods do not always enable a high amount of self-sorting during synthesis, which creates the less-crystalline COF products. However, because of their light skeleton density, high thermal and chemical stability, permanent porosity, and structural tunability, COFs have been widely used in diverse applications, such as gas storage[109,110], separation[111–113], catalysis[114–116], photo reduction[117,118], and lithium batteries[119–121].

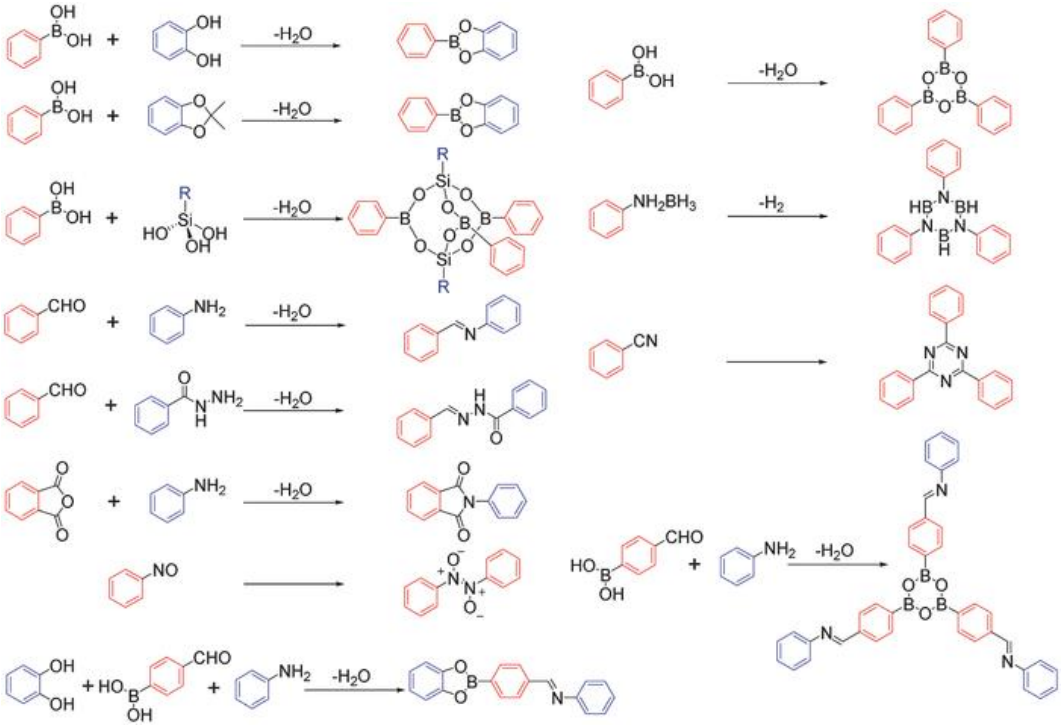

Figure 1.3. Some typical reaction types used to synthesise COFs.

2.3 Porous organic cages (POCs)

Unlike MOFs and COFs, which possess porous interconnected 2- or 3-dimensional networks, porous organic cages are discrete molecules with porous intrinsic cavities. POCs tend to close pack in the solid state to maximise attractive intermolecular interactions and minimise the relative energy of their structures. It is, therefore, rare to obtain stable structures of POCs with open channels and voids after removal of guests, such as solvent molecules, from their structures[122]. In 2009, the Cooper group reported a series of permanently porous organic cages that were synthesised by reacting a trialdehyde with three different diamine to form [4+6] imine-cage

products.[123] In the following years, more imine POCs were reported, including by the Mastalerz group who using triptycene linkers.[124–128] As well as imine cages, carbon-carbon bonded porous cages were synthesised and reported by Doonan *et al*.[129] To date, the POC with the highest surface area (3758 m^2 g^{-1}) that had a mesoporous internal pore diameter of 3.1 nm was reported by Mastalerz group in 2014 using boronate ester chemistry.[130] Despite their high porosity, the cages synthesised with reversible boronate ester chemistry are unstable to moisture and their limited solubility makes them difficult to process. By contrast, imine POCs are stable in boiling water[131] and post-synthetically modified amine POCs are stable in acid and base environment[132]. The reversible imine condensation is the most commonly used synthetic route to POC.[133–135] There are also some other reversible bond-forming reactions constructing cages.[136,137] Some new technologies, such as computational design[138,139], crystal structure prediction[140], and high throughput synthesis[141], which can help people to construct cages directionally and efficiently, were developed in last decade.

POCs have permanent porosity and their cavity size and porosity can be tuned using chemical synthesis, making them ideal candidates for exploring applications in gas pair separation, such as CO_2/CH_4[125], CO_2/N_2[142], H_2/N_2[143], D_2/H_2[144], and rare gas capture[145]. POCs are also soluble in common organic solvents and can be deposited onto gas chromatography columns for performing organic separations, such as isomer separations.[146–148] They can also be processed with polymers of intrinsic microporosity (PIMs) to form mixed matrix membranes (MMM).[149] POCs films have been deposited on quartz crystal microbalance and used to sense small molecule analytes.[150,151] More recently, POCs have been dissolved in large solvents that are size-excluded from their intrinsic cavities to form porous liquids.[152–154]

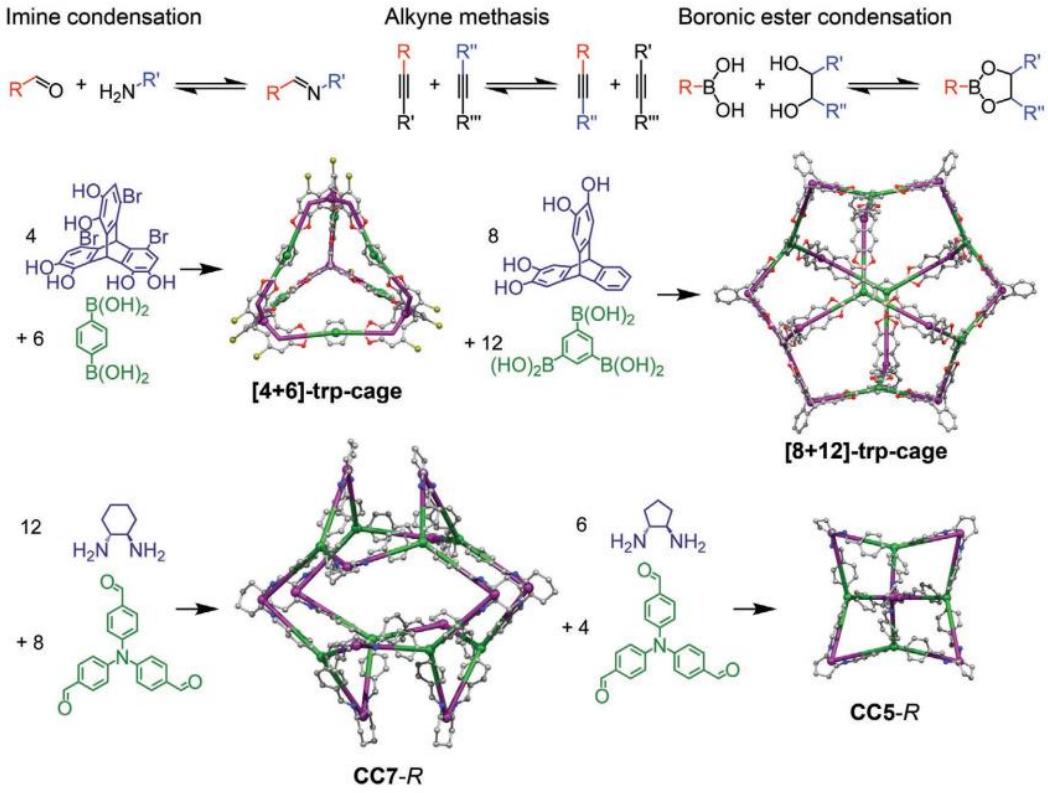

Figure 1.4. Typical reaction types used to synthesise POCs. The boronic ester cages, [4+6] type[155] and [8+12] type[130], and the imine cages, CC7[156], and CC5[140]. Reprinted from *Adv. Funct. Mater.*, 2020, 1909842[64]. Copyright 2020 WILEY-VCH.

2.4 Hydrogen bonded organic frameworks (HOFs)

Hydrogen bonded organic frameworks (HOFs) are an exciting class of networked solid that are constructed from organic moieties and stabilised by non-covalent hydrogen bonding interactions.[157,158] This area attracted scientists' interest more than two decades ago, and directional hydrogen bonding interactions play an indispensable role in stabalising their structures and constructing open frameworks with significant porosity.[159] However, in comparison to covalent and ionic bonds, the strength of hydrogen bonds can be relatively weak. A combination of other non-covalent intermolecular interactions, such as π-π interactions, are sometimes required to stabilise HOFs with permanent porosity.

Generally, HOF units comprise two indispensable parts, a scaffold (or backbone) and a hydrogen bonding interaction site. Both parts contribute to the construction of HOF networks and their stability. As for the scaffold part, rigid molecules are usually used

because these are most likely to produce more robust networks, as rigid scaffolds often inhibit the inevitable rotation of building motifs. Several hydrogen bonding interaction sites have been attached to organic scaffold via designable synthetic routes.[160,161] Usually, the size and structural symmetry of the scaffold can influence the number of hydrogen bonding interaction sites in the building motifs. Finally, the assembly of interaction sites in adjacent building motifs leads to the formation of HOFs with continuous hydrogen bonding interactions.

In 1969, Duchamp reported the first HOF structure of 1,3,5-benzenetricarboxylic acid, which featured a 2-dimensional hydrogen bonded network[65]. In the following two decades, only a few examples of HOFs were reported, but in the 1990s Wuest and co-workers reported a series of papers that were focused on the design of HOFs using an approach they referred to as *molecular tectonics*[162–165]. In 2010, the Chen group revisised one of the Wuest HOFs and found that it had permanent porosity, and the Chen group has subsequently developed HOFs for applications in gas sorption and separation[30,166–168]. The discoveries by Wuest, Chen, and others arouse the attention of chemists who were interested in developing functional HOFs materials.

There are several challenges related to the development of HOF materials with permanent porosity. HOFs usually exhibited relatively low stability due to the weak strength of hydrogen bonds.[169] Many HOFs materials are, therefore, only stabilised by the presence of guest solvent in their pores, and when the guest solvents are removed the framework can collapse. Despite much progress during the last two decades, there still only remains a limited number of HOFs materials with permanent porosity. Despite this, the design of novel HOFs still attracts great interest from scientists from all over the world. The main reasons are that HOFs possess several unique properties. Firstly, HOFs exhibit low densities because of the absence of metal elements and heavy inorganic elements, unlike MOFs, which consist of metal-based units and organic linkers by coordination interactions. Secondly, it is often feasible to grow high-quality crystals of HOFs materials, which provides an easy way to investigate their structures and is an advantage over most COF materials. Thirdly, it is often quite simple to regenerate HOFs in solutions, for example, by recrystallisation, which is

often unique to molecular crystals, including for HOFs, and unlike zeolites, MOFs, and COFs, which often need to be synthesised using fresh precursors. These advantages allow HOFs to compete as promising porous materials in various application (Table 1.1).

Table 1.1 Comparison of different porous organic crystalline materials.

	MOFs	**COFs**	**POCs**	**HOFs**
Building units	hybrid	organic	organic	organic
Connected bonds	coordination bond	covalent bond	covalent bond	hydrogen bond
Synthesis method	hydrothermal	hydrothermal, grinding	RT reaction	crystallisation
Porosity	micro/mesoporous	micro/mesoporous	micro/mesoporous	mostly microporous
Density	high	low	low	low
Crystallinity	high	modest to high	amorphous to high	high
Stability	sensitive to water/humidity	good	good	few good examples
Regeneration	weak	weak	excellent	excellent
Designable	excellent	good	excellent	good
Selling points	Structural and chemical control, various applications	Low density and wide application	Solution processing, computational prediction	Different polymorphs, various candidates, computational prediction
Summary	Established and highly active field	Less developed than MOFs, but promising	Slow development but many new applications	Less stable examples, under development

3. Hydrogen bonding

Hydrogen bonding is primarily an electrostatic force of attraction between a hydrogen atom which is covalently bound to a more electronegative atom or groups (hydrogen bond donor, nitrogen, oxygen, or fluorine) and another electronegative atom (hydrogen bond acceptor). Hydrogen bonding is one of the most important non-covalent interactions in both biological (DNA[170,171], peptides[172,173]) and chemical (host-guest architectures[174,175], supramolecular networks[176–179]) systems. A typical hydrogen bond system includes a hydrogen bond between electronegative donor and acceptor atoms ($X^{\delta-}–H^{\delta+}\cdots Y^{\delta-}$, with X and Y often being O, N, F). Normal hydrogen bonds typically range in strength from *ca.* 4-60 kJ mol^{-1}. The strong hydrogen bond would extend to 60-120 kJ mol^{-1}, but it is still lower than the coordination bonds (90-350 kJ mol^{-1}) and covalent bonds (300-600 kJ mol^{-1})[180].

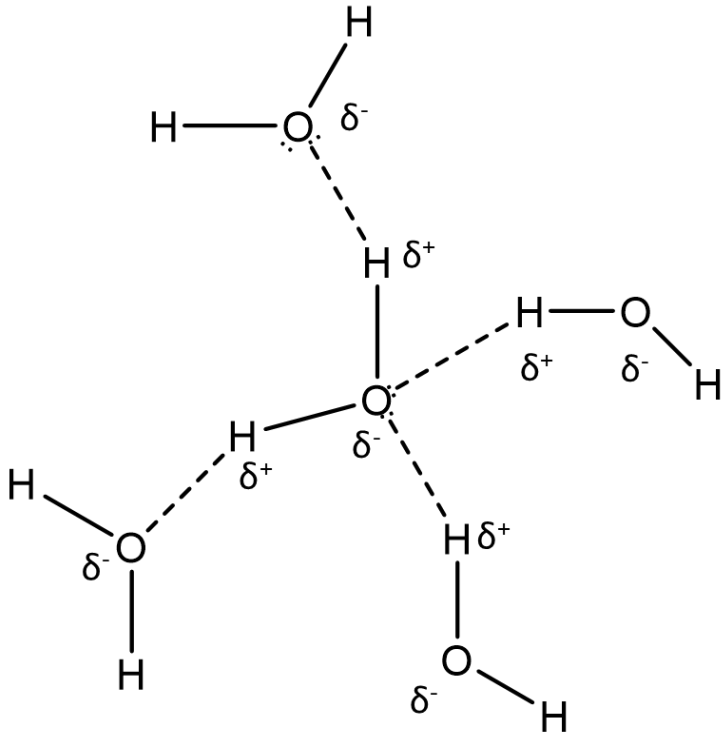

Figure 1.5 Typical hydrogen boning in water. The H-bonding was presented with dashed line. The lone pair electrons of O atoms were showed with black points around O atoms.

Table 1.2 Properties of hydrogen bonded interactions.[159]

X−H···Y	**Strong**	**Moderate**	**Weak**
Bond energy (kJ mol^{-1})	60-120	16-60	<12
Bond lengths (Å)			
H···Y	1.2-1.5	1.5-2.2	2.2-3.2
X−Y	2.2-2.5	2.5-3.2	3.2-4.0
Bond angles (°)	175-180	130-180	90-150
Examples	HF complexes	Acids/alcohols	C-H hydrogen bond

The strongest hydrogen bonds are formed between strong acids and good hydrogen bond acceptors, for example, HF_2^-, which possesses high hydrogen bond energies (120 kJ mol^{-1}) and linear geometry. Moderate hydrogen bonds are formed by neutral donor and acceptor groups, for example, the self-assembly of carboxylic acids. The angles of moderate hydrogen bonds are slightly bent. Such moderately strong hydrogen bonds are feasible to construct stable and rigid HOFs. In many HOFs systems, the highly directional and relatively strong hydrogen bonds, mainly intermolecular O/N-H···O/N interactions, have been widely used to form HOFs.[158] The mean bond length of the O-H···O interaction is 2.77 Å, which was determined from nearly 140,000 crystal structures in the Cambridge Structural Database (CSD).[181] By comparison, the mean bond length of the N-H···O interaction is 2.88 Å, which was determined from nearly 120,000 structures in the CSD. Typically, the stronger the hydrogen bond, the shorter bond length, and the better directionality (Table 1.2).

4. The organic synthons used in HOFs

It is important to choose appropriate synthons to construct molecular architectures. In 1995, the concept of synthons was proposed by Desiraju, who defined them as "*structural units within supermolecules, which can be formed and/or assembled by*

known or conceivable synthetic operations involving intermolecular interactions".[182] Hence, synthons are the spatial arrangement of intermolecular interactions. The right selection of synthons plays a vital role in the construction of HOFs. Many molecular moieties can be used for H-bonded interactions to build porous HOFs, including carboxylic acid, urea, diaminotriazine (DAT) and heterocycles, and so on.[158]

4.1 Carboxylic acid

The carboxylic acid dimer has been widely used for constructing exotic molecular HOF assemblies (Figure 1.6a).[183] The self-assembly of carboxylic acid in crystals was summarised by Leiserowitz,[184] and the commonly encountered $R_2^2(8)$ synthon involves the interaction between two hydrogen bond donors and two hydrogen bond acceptors from two -COOH groups and takes the form of a cyclic 8-membered ring.

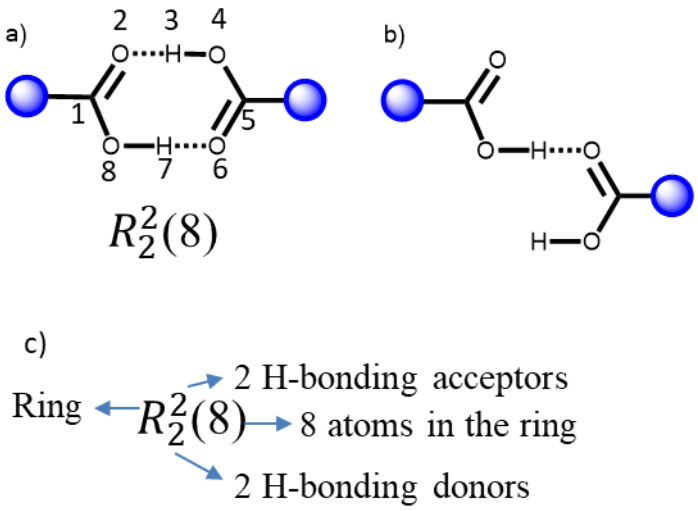

Figure 1.6 The typical hydrogen bond type formed by carboxylic acid, a) paired $R_2^2(8)$ hydrogen bond, b) single hydrogen bond, c) an explanation of $R_2^2(8)$ notation.

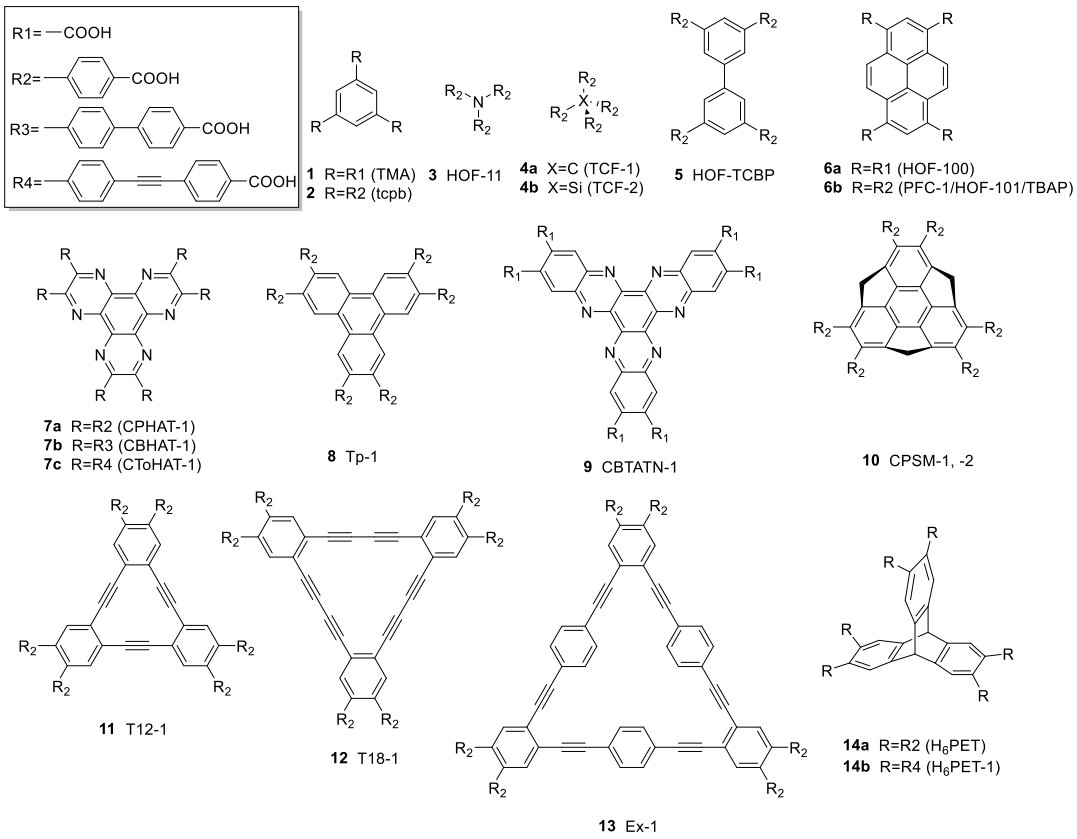

Figure 1.7. Some of the carboxylic acid molecules used as HOF building blocks.

The first HOF constructed with carboxylic acid molecule can be traced to 1969 when Marsh and Duchamp reported the α-polymorph of trimesic acid (**TMA**, Figure 1.7, **1**).[65] The α-polymorph has interpenetrated waved honeycomb sheets of **TMA** that are close-packed to form a nonporous structure. In 1987 Herbestein reported a layered honeycomb structure of **TMA** with hexagonal shaped 1-D channels that were occupied by long-aliphatic chain template solvents.[185] Afterward, more HOF structures tended to be reported with carboxyphenyl groups (Figure 1.7, **R2**). The possible reasons are: 1) the synthesis of compounds with carboxyphenyl group are much simple using coupling chemistry; 2) the introduction of carboxyphenyl group can increase the solubility and conjugation of the compounds; 3) the extended carboxyphenyl can generate larger pore HOFs to improve their porosity. An 8-fold interpenetrated HOF was constructed with compound **2** (Figure 1.7) and the Brunauer-Emmett-Teller surface area (SA_{BET}) of this HOF was as high as 1095 $m^2\ g^{-1}$, despite the structure being interpenetrated.[186,187] Compound **3** (Figure 1.7) forms an

11-fold interpenetrated structure (**HOF-11**) when crystallised from THF/hexane and the activated structure possessed the SA_{BET} 687 m^2 g^{-1}.[188] Two flexible HOFs (**TCF-1** and **TCF-2**) were reported with the tetrahedral compounds (**4a**, **4b** Figure 1.7), which showed dynamic behavior during gas sorption with CO_2 and Xe.[189] Compound **5** (Figure 1.7) was reported to form a stable HOF that has a large surface area with SA_{BET} value of 2066 m^2 g^{-1}.[190] A highly stable HOF was reported with the π-conjugated compound **6b** (Figure 1.7). Cao and co-workers firstly reported the **PFC-1**, which is photoactive and can encapsulate Doxorubicin. **PFC-1** was also used for synergetic chemo-photodynamic therapy.[191] The Farha group also presented **PFC-1**, which they referred to as **HOF-101**, and a biphenyl analogue, named **HOF-102**, which they used to fabricate a fiber composite for photochemical detoxification of a mustard gas simulant.[192] The Cooper group also explored **PFC-1**, which is referred to as **TBAP**, with crystal structure prediction. The semi-conductor properties and high water stability of **TBAP** made it an excellent metal-free organic photocatalyst for proton reduction in water.[193] Hisaki and co-workers have done a lot of great work on the carboxylic acid HOFs and have discovered HOFs with permanent porosities that were constructed by the shape-fitting and docking of twisted hexaazatriphenyilene (**HAT**) derivatives **7a**, **7b** and **7c**.[194] The same group also reported that activated **CPHAT-1a** retains single crystallinity and investigated its ability to adsorb iodine.[195] Compound **8**, **9**, **11**, **12**, **13** have been used to construct layered HOF networks and highly ordered triangular porous frameworks.[196–199] The bucky-bowl-shaped compound **10** was found to form single-layered (**CPSM-1**) and double-layered (**CPSM-2**) HOFs. However, **CPSM-2** did not have permanent porosity and instead underwent anisotropic contraction along *c*-axis under high pressure.[200] The triptycene derivatives **14a**, **14b** were used to form HOFs by Stoddart and co-workers. For **14a**, two types of different interpenetrated isomeric **PHTHOF-1** and **PHTHOF-2** with *acs*-network topologies were reported. The BET surface area values for **PHTHOF-1** and **PHTHOF-2** were 1140 and 1690 m^2 g^{-1}, respectively.[201] An extended analogue, **14b**, was found to form a more complicated porous HOF supramolecular poly-knot structure.[202]

4.2 Urea

Urea is one of the oldest synthons that has been used to form crystalline hydrogen-bonded architectures and it usually forms double hydrogen-bonded strands. In 1950, Smith reported the crystal structure of urea-hydrocarbon and thiourea-hydrocarbon complexes.[203,204] Afterward, some works about accommodation of guest molecules in channels was summarised.[205] Smith also reported in 2008 a macrocyclic urea derivative, in which stereoselective reactions could happen in its 1-D channels.[206]

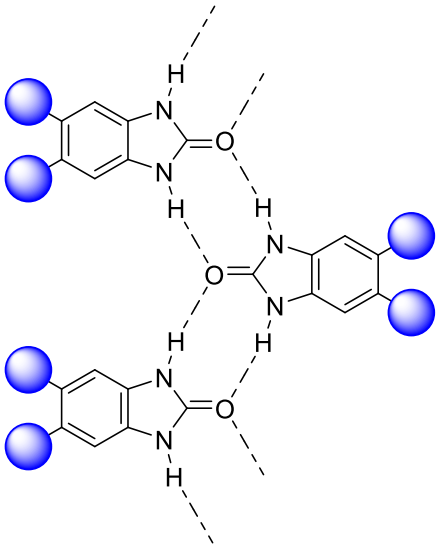

Figure 1.8 An example of the double hydrogen-bonded strands of molecules with urea motifs.

In 2012, Mastalerz crystallised **TTBI** from DMSO/acetone and found it formed a highly porous HOF (Figure 1.9) with a density of 0.755 g cm^{-3} and the BET_{SA} of activated HOF structure was 2796 m^2 g^{-1}.[207] At the time, it was the highest surface area of any porous material consisting of discrete molecules, until another polymorph, **T2-γ**, which has BET_{SA} as high as 3425 m^2 g^{-1}, was reported in 2017[208].

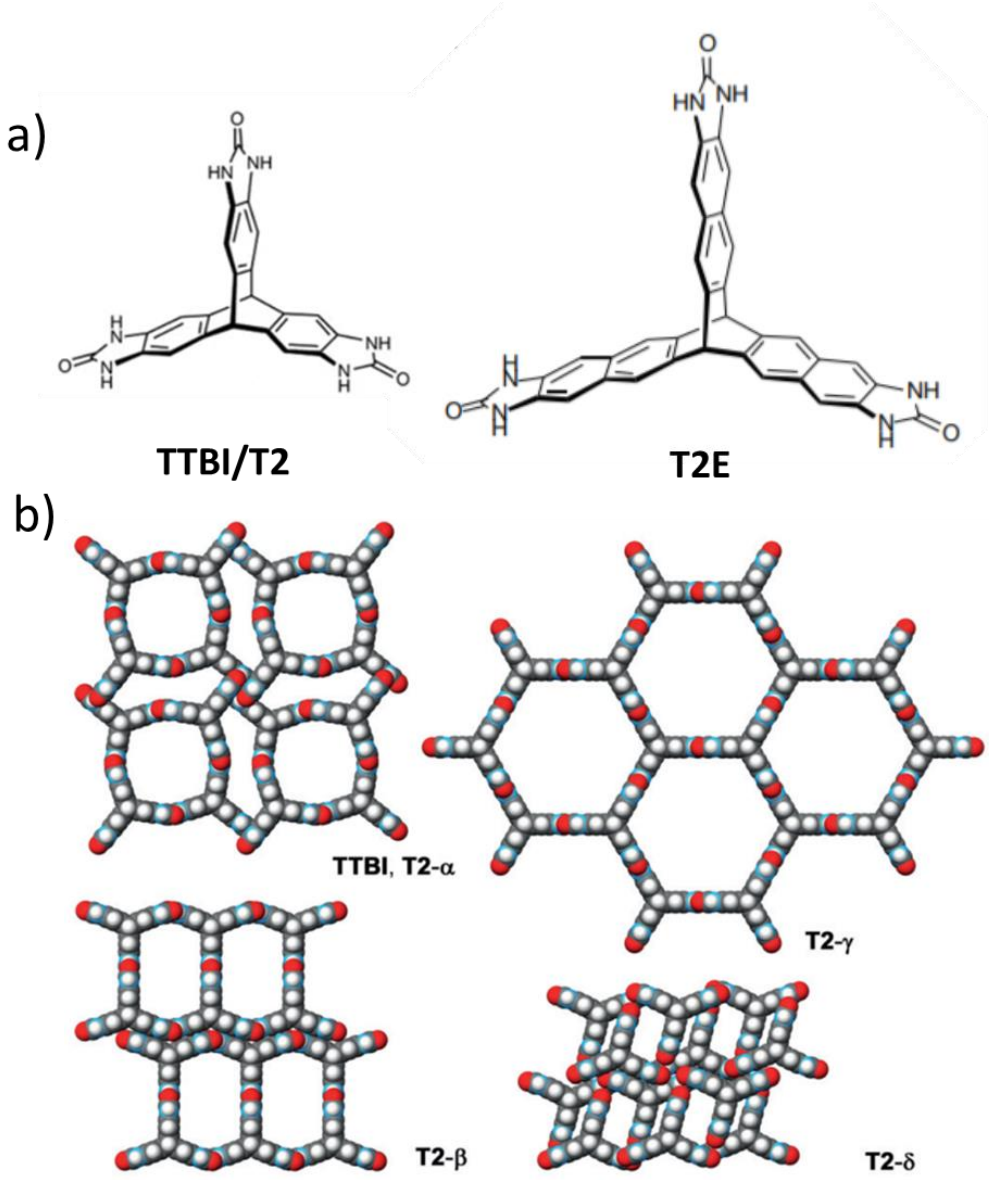

Figure 1.9 a) The structure of **TTBI**/**T2** and **T2E**. b) The different polymorphs of **TTBI**/**T2**, grey: carbon; red: oxygen; white: hydrogen. Reprinted from *Nature* 2017, **543**, 657–664[208]. Copyright 2017, with permission from Nature Research.

The Cooper and Day groups combined computational crystal structure predictions (CSP) and property predictions to generate "energy-structure-function" (ESF) maps. With their ESF maps, the possible structures and their associated properties can be described in a single plot. For the molecule, **T2**, four structures with relatively low lattice energies (**T2-α**, **T2-β**, **T2-γ** and **T2-δ**) were found in the predicted ESF map. Of these structures, **T2-γ**, with very low density, 0.412 g cm^{-3}, was found in the lab

after being crystallised from dimethylacetamide and acetone. The activated **T2-γ** has the highest BET_{SA}, 3425 m^2 g^{-1}, and could also be transformed into **T2-α** phase under certain conditions. Also, **T2-α** could transform into **T2-β** and then **T2-δ**.[208]

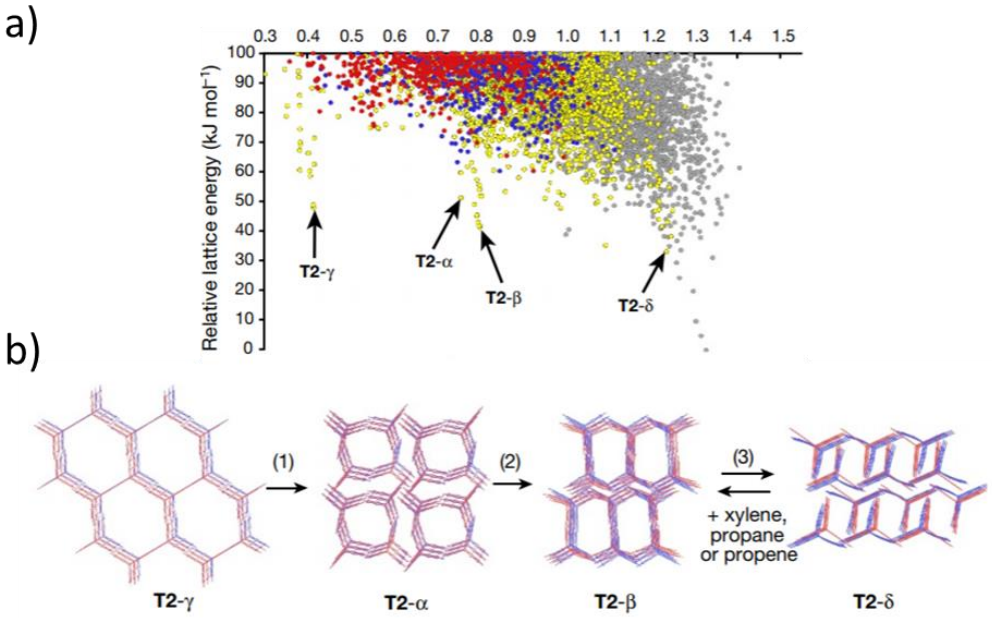

Figure 1.10 a) Crystal structure prediction (CSP) energy–density plots for **T2**, b) Overlays of predicted (red) and experimental (blue) structures for **T2-γ**, **T2-α**, **T2-β** and **T2-δ**. The transformation conditions were: (1) loss of solvent at room temperature, heating at 340 K or mechanical grinding at room temperature; (2) heating at 358–383 K; (3) direct removal of DMSO and then acetone from DMSO/acetone solvate. **T2-δ** transforms back to a solvate of **T2-β** upon exposure to xylene, propane, or propene. Reprinted from *Nature* 2017, **543**, 657–664[208]. Copyright 2017, with permission from Springer Nature.

4.3 Diaminotriazine (DAT)

Three typical hydrogen-bonded models of diaminotriazine are shown in Figure 1.11. The research of hydrogen bonding of **DAT** complexes showed that **DAT** can form 2-D and 3-D frameworks by forming different hydrogen bonded networks.[209,210]

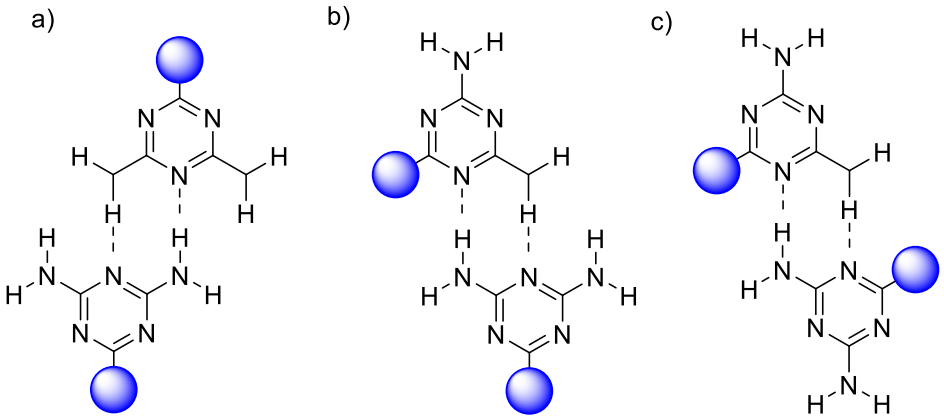

Figure 1.11. Three typical hydrogen-bonded models of **DAT** complexes.

The Wuest group reported a lot of porous HOFs by appending the **DAT** group to different organic molecules. In 1997 they reported **HOF-1**[163], which the Chen group demonstrated had permanent porosity and a BET_{SA} is 359 m^2 g^{-1}. The Chen group also found **HOF-1** can selectively adsorb C_2H_2/C_2H_4 under ambient conditions.[30] Wuest and co-workers later discovered the crystalline structures of a series of tetraphenylbenzene (compound **15**, Figure 1.12) and hexaphenylbenzene derivatives (compound **16**).[211] After characterisation of the porosity of **HOF-1**, Chen and co-workers found a series of HOFs (**HOF-2**[212], **HOF-3**[213], **HOF-4**[214], **HOF-5**[215], **HOF-6**[216], **HOF-7**[217], **HOF-9**[218]) with different crystal structures, pore sizes, and functionalities, based on the compound with **DAT** group.

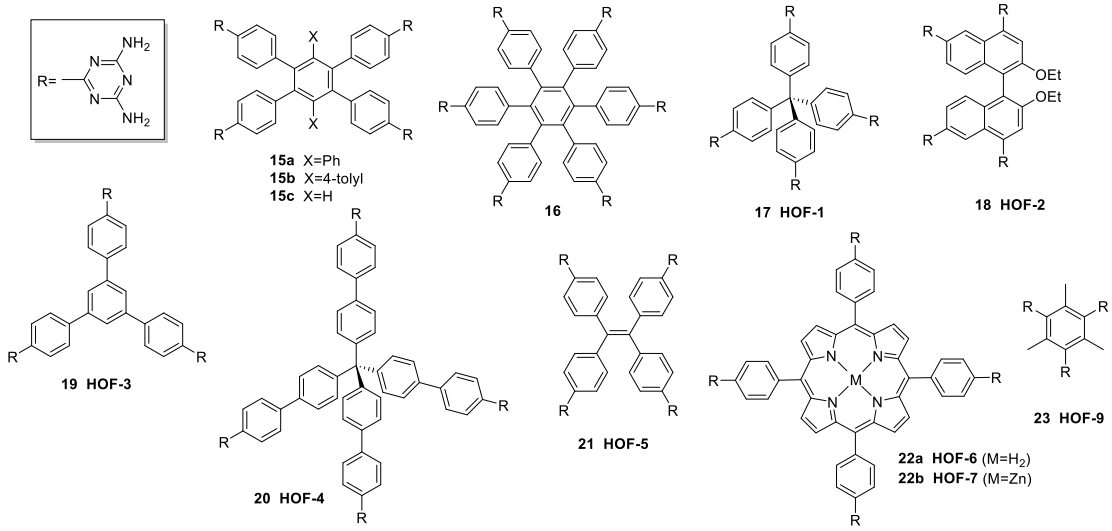

Figure 1.12. Some reported HOFs based on **DAT** group.

4.4 Heterocycles

Many heterocycles, such as pyridine, pyrazole, and imidazole, which contain electronegative atom, nitrogen, as a proton acceptor, were used to build porous HOFs (Figure 1.13).

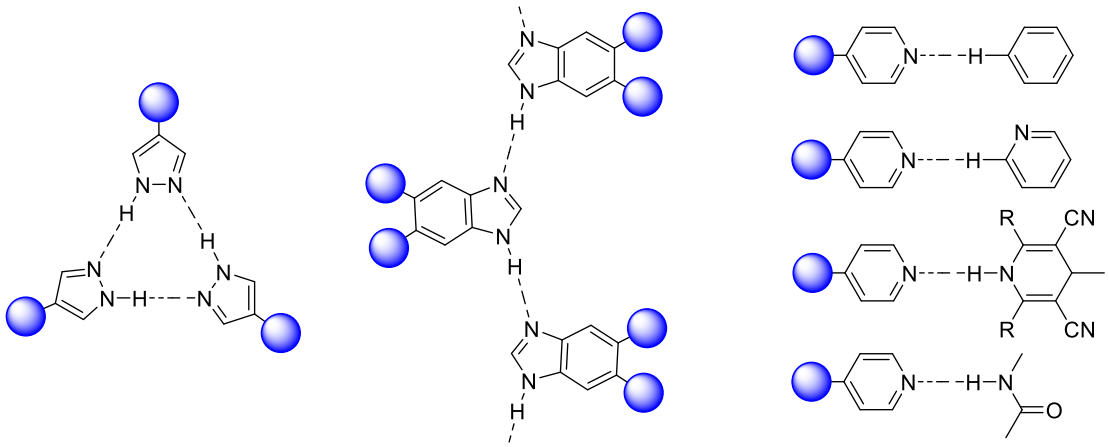

Figure 1.13. The hydrogen bonded types based on heterocycles.

A series HOFs based on tripyrazole derivatives (compound **24**, **25**, Figure 1.14) were reported by Miljanic and Wu groups.[166,219] These tripyrazole HOFs have high BET_{SA} from 903 $m^2\ g^{-1}$ to 1821 $m^2\ g^{-1}$, and the strong π-π interaction between the relatively electron-rich pyraole moieties and electron-poor fluorobenzene stabilised the structures. Compound **26** formed a porous HOF with 1-D channels (**FDM-15**), which could accommodate C_{60}.[220] The HOFs constructed with compound **27** had 1-D hexagonal pore channels.[221] **HOF-8** showed selectively adsorbed CO_2 and benzene.[167] **SOF-1** was formed with compound **28** and had a 3-D network.[222] The weak hydrogen bonds in **SOF-1** made it flexible and the structure showed different porosities to different gasses. While the more simple compound **29** was recently reported to assemble into structures with high structural complexity.[223]

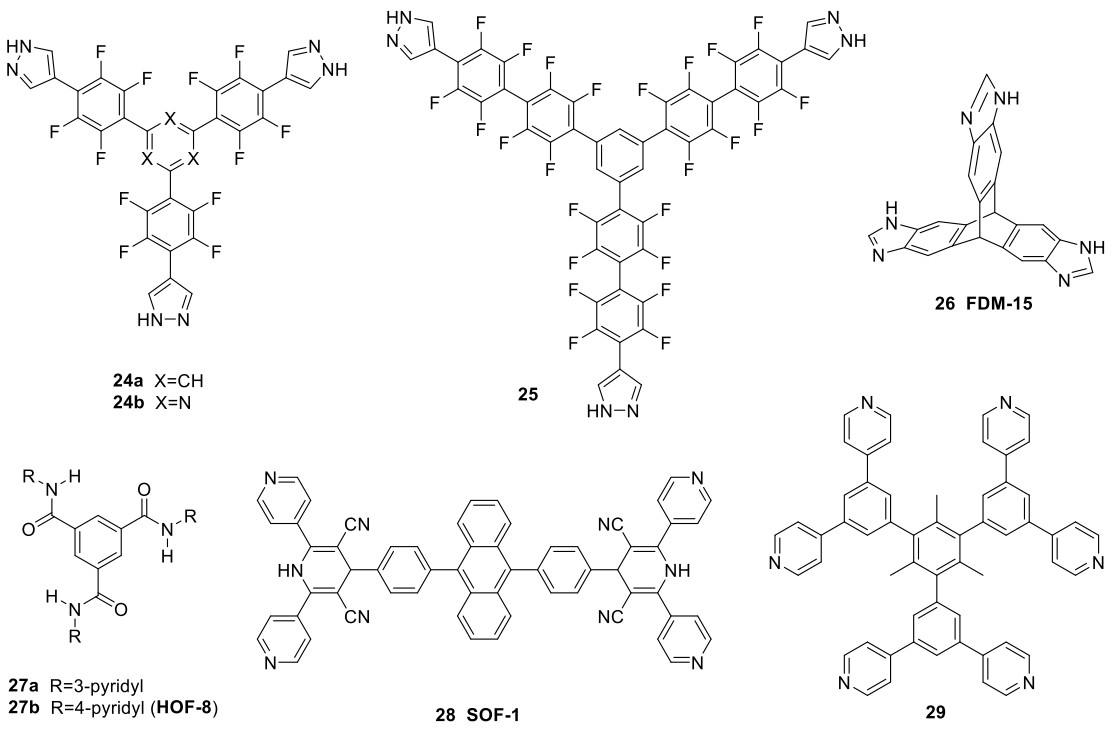

Figure 1.14. Some reported HOFs formed with heterocycles.

From the examples that drawn in section 4, the appropriate selection of building synthons is important for construction of predesigned molecular architectures. Construction of HOFs with permanent porosity requires a combination of noncovalent intermolecular interactions, such as π–π interactions, with H-bonds, because H-bonding alone is too weak to maintain low-density porous materials.

5. Permanent porosity in HOFs

For HOF materials, hydrogen bonds (4-60 kJ mol^{-1}) alone can be too weak to build a low density permanent porous structure. Also, during crystal activation, solvated porous frameworks can undergo structural transformations because their crystal structures can be metastable. This procedure often results in the loss of crystallinity and porosity. Also, microcrystals can be formed during the transformations, which can be more difficult to characterise, for example, by single-crystal X-ray diffraction. Likewise, rapid crystallisation techniques can form kinetic polymorphs (apparently stable; the structural transformation can happen spontaneously with a very slow rate)

with higher porosity than the thermodynamic polymorphs (stable, cannot transform into other polymorphs spontaneously), but quick crystallisation tends to produce microcrystals.[129] It is common for HOFs to undergo structural transformations during activation.[202,224,225] For example, **HOF-1** (Figure 1.12, compound **17**), based on tetrahedral diaminotriazine, transformed after activation. However, the activated structure of **HOF-1** could not be determined because of the loss of crystallinity after activation.[30,163] A combination of noncovalent intermolecular interactions, such as π-π interactions, with hydrogen bond, is important to construct permanent porous HOFs.[191] Increasing the number of hydrogen bond donors and acceptors can also improve the permanent porosity in HOFs.[208]

6. Crystallisation methods

Crystals are solid materials in which the constituents (atoms, ions, molecules) are packed in an ordered array to generate extended crystal lattices. The process of crystal formation is called crystallisation, and from solution, crystallisation can be thought of as a two-step process. The first step is nucleation or "birth" of new crystals[226,227], and the second step is the growth of larger crystals[228,229]. Nucleation processes can be heterogeneous and homogeneous. For heterogeneous processes, nucleation usually happened at a surface, for example, a dust particle or the wall of the container, which acts as the center and the atoms, ions or molecules arranged in ordered directions. For homogeneous nucleation, a few particles come into correct juxtaposition during the random movement. The mechanism is more likely as the degree of supersaturation or supercooling increases. Heterogeneous nucleation is a more common process. Crystal growth is a process in which pre-existing crystals become larger. There are several methods commonly used to crystallise different solids to form crystalline materials.

In this section, 5 common crystallisation methods that were used in construction of HOFs are introduced. In my project, the methods that described in section 6.2, 6.3 and 6.5 were mostly used in the crystallisation of HOFs.

6.1 Sublimation

Sublimation is a technique that is used by scientists to purify compounds and it is the transition of a substance directly from the solid state into the gas state[230,231]. Typically, the solids are placed in a sublimation tube and heated under vacuum. The compounds volatilise and then condense on the cooler surfaces of the tube as a pure compound, which can be collected from the cooling surface. The non-volatile residue of the impure compound is often left behind. If there are several components in the impure compounds, a temperature gradient can be applied to separate the different fractions.

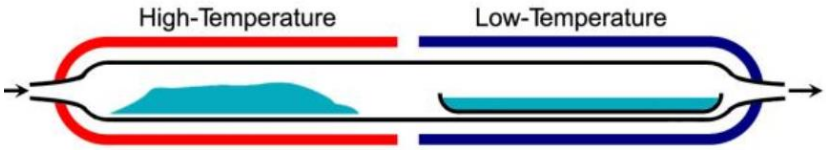

Figure 1.15 The simplified sublimation apparatus showing the position of compounds in the high-temperature part and pure phase after condersing in the low-temperature part. The arrow is the evacuation direction.

6.2 Recrystallisation

Recrystallisation is a common technique used in research labs to purify chemicals. Usually, the chemicals, which contain the pure compound and its impurities are dissolved in a small quantity of hot solvent to make a saturated solution. After the solution is cooled, the solubility of the compound drops and the desired compounds can crystallise from the solution.[232,233] The **M7** molecule that introduced in chapter 3 was recrystallised with this method.

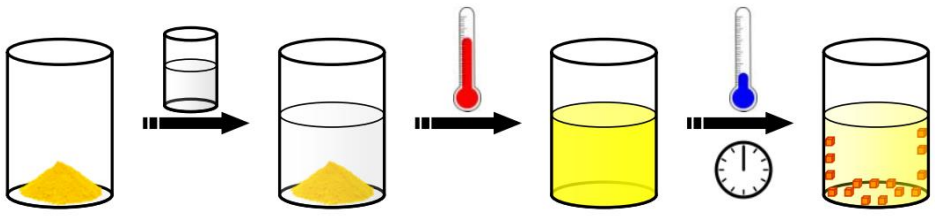

Figure 1.16. Graphical representation of recrystallisation processes. Solvent added (clear) to compound (orange) → solvent heated to give saturated compound solution (light orange) → saturated compound solution (light orange) allowed to cool over time to give crystals (orange) and a saturated solution (light orange).

Multi-solvents can also be used for recrystallisation.[234] After dissolving the compound and impurities in the first solvent, a second solvent that does not dissolve the compound in then slowly added (Figure 1.17).

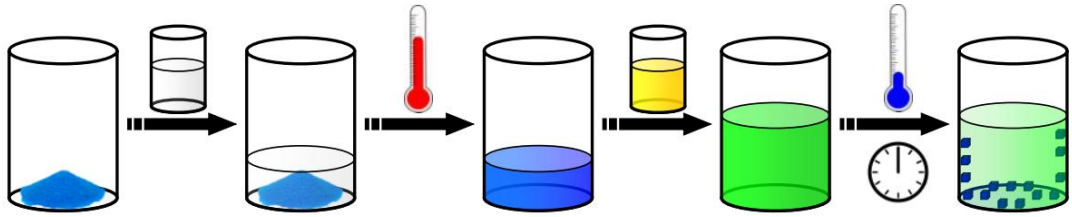

Figure 1.17 Graphical representation of the recrystallisation process. Solvent added (clear) to compound (blue) → solvent heated to give saturated compound solution (blue) → second solvent (yellow) added to the compound solution to give mixed solvent system (green) → mixed solvent system (green) allowed to cool over time to give crystals (blue) and a saturated mixed solvent system (light green).

In a multi-solvents system, evaporation can also be applied after mixing to change the proportions of solvents to influence the crystallisation procedure (Figure 1.18).[234]

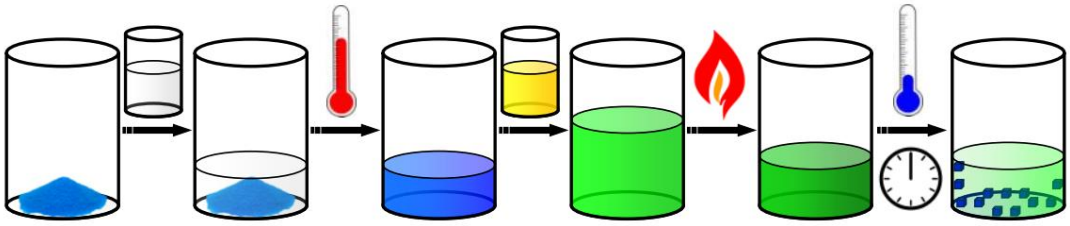

Figure 1.18 Graphical representation of multi-solvent recrystallisation processes. Solvent added (clear) to compound (blue) → solvent heated to give saturated compound solution (blue) → second solvent (yellow) added to the compound solution to give mixed solvent system (green) → volatile first solvent (clear) is removed (*e.g.* evaporation) from first mixed solvent system (green) to give a second mixed solvent system (dark-green) → mixed solvent system (green) allowed to cool over time to give crystals (blue) and a saturated mixed solvent system (light green).

Another common recrystallisation method is hot filtration, where a single solvent system is used to separate compounds from insoluble impurities.[235,236] When the

materials were dissolved in the smallest amount of hot solvent, there are still some insoluble impurities left in the solution. The solution is filtered to remove the insoluble components and the filtrate is then cooled down to induce crystallisation. One important aspect of this procedure is that the filtration apparatus must be kept hot to avoid the dissolved compounds crystallising on the filter paper and funnel during the filtration.

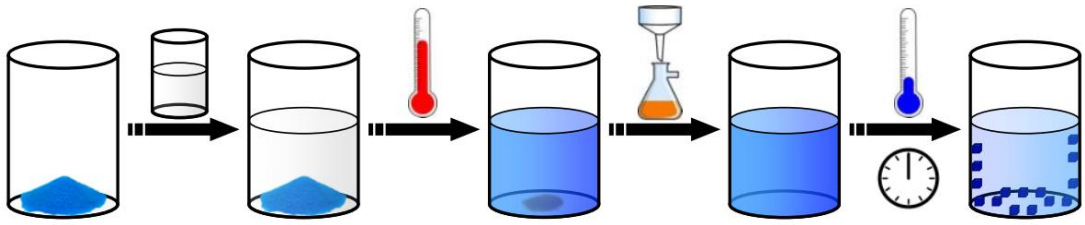

Figure 1.19 Graphical representation of hot recrystallisation process. Solvent added (clear) to an impure compound (blue) → solvent heated to give saturated compound solution (blue) + insoluble substance (grey) → saturated compound solution (blue) filtered to remove insoluble substance → saturated compound solution (blue) allowed to cool over time to give crystals (blue) and a saturated solution (light blue).

6.3 Slow vapour diffusion

In vapour diffusion crystallisations, a compound is dissolved in a good solvent which could dissolve the compound at RT (> 0.5 mg/mL) with a low boiling point (usually <100 °C) in a small vial.[208,237] The vial is then loaded into a larger vial that contains an anti-solvent that has a low boiling point or low vapour pressure and is miscible with the good solvent. This method can take a long time, but the rate of diffusion can often be crudely tuned, e.g., by partially capping the small vial or leaving it fully open. The **M7** and **M8** molecules that introduced in chapter 3 were crystallised with this method.

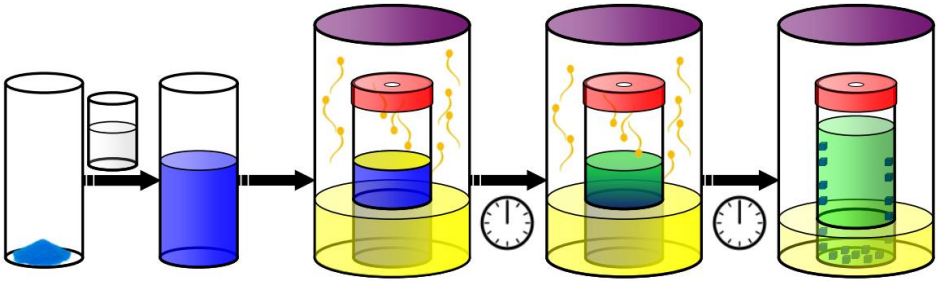

Figure 1.20 Graphical representation of slow vapour diffusion crystallisation process. A solvent is used (clear) to dissolve the compound (blue) in a small vessel to give a compound solution (blue) → the small vessel is placed in a larger vessel contain anti-solvent (yellow). The larger vessel is sealed, the small vessel is also sealed and there is a small hole in the cap. This hole allows volatile anti-solvent vapour (yellow) to slowly evaporate from the larger vessel and condense into the small vessel, to give a mixed solvent system (green-blue) → over time this gives crystals (blue) and a saturated mixed solvent system (light green).

6.4 Interface layering

The interfacial method is similar to the vapour diffusion method. The interface layering is liquid-liquid diffusion.[237,238] One liquid is the good solvent that dissolves the compound. The other liquid is anti-solvent. This anti-solvent is layered on top of the good solvent carefully. Due to the diffusion, the solvent composition is changed, and the compound is increasingly insoluble and crystallises at the interface.

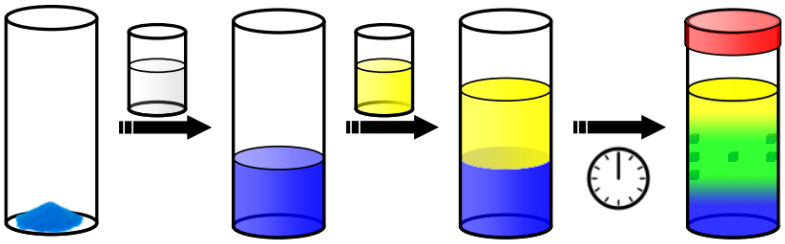

Figure 1.21 Graphical representation of interfacial layering crystallisation process. Solvent added (clear) to compound (blue) to give compound solution (blue) → the second solvent added (yellow) carefully so that the two solvents do not mix, and the vessel is sealed → the two solvents mix (diffuse) slowly over time to give crystals (blue) at the solvent interface (green).

Another related technique involved using 'H' shape tubes to crystallise compounds.[239] One tube chamber contains a good solvent and compound, while the other tube chamber contains a solvent that cannot dissolve the compound. There is a fine glass sinter in the middle of 'H' shape tube to restrict the mixing rate of the two solvents.

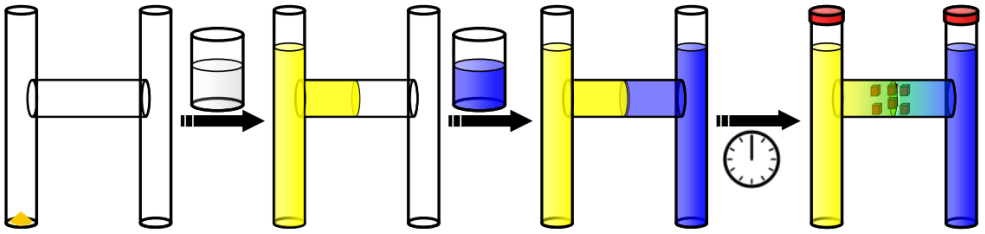

Figure 1.22 Graphical representation of crystallisation process in 'H' shaped crystallisation tubes. Solvent added (clear) to compound (yellow) to give a compound solution (yellow) in left tube chamber → the second solvent added (blue) to the other tube chamber → the two solvents mix slowly over time, the mixing is slowed by a fine sinter separating the two solvent chambers, to give crystals (yellow) at the solvent interface (green) over time.

6.5 Solvent evaporation

Solvents evaporation is also a good way to grow nice crystals or compounds.[220,240] The compound is initially dissolved in a suitable solvent that usually has a low boiling point and the solvent is allowed to slowly evaporate. Slow evaporation of the single solvent can result in a saturated solution from which crystals can form. It was mostly used in my thesis especially in chapter 2 and chapter 4.

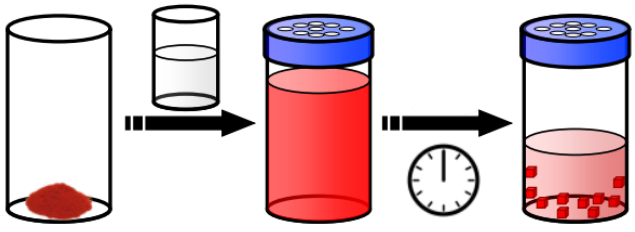

Figure 1.23 Graphical representation of slow evaporation crystallisation process. Solvent added (clear) to compound to give compound solution (red) → vessel sealed but a small hole allows solvent vapour (clear) to slowly evaporate from compound solution (red) over time to give crystals (red) and a saturated solution (light red).

If an anti-solvent, which cannot dissolve the compound, is added into the above system, a multi-solvent crystallisation system can be generated. The anti-solvent can also accelerate the crystallisation procedure.[241,242]

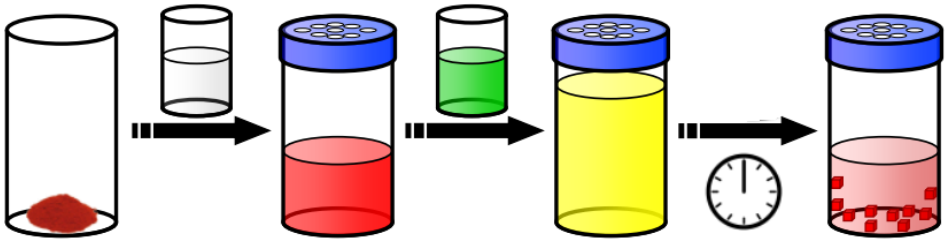

Figure 1.24 Graphical representation of mixed anti-solvent crystallisation processes. Solvent added (clear) to compound (red) to give compound solution (red) → the second solvent added (green) to the compound solution (red) to give mixed solvent system (yellow) → vessel sealed but a small hole allows solvent vapour (clear) to slowly evaporate over time to give crystals (red) and a saturated mixed solvent solution (light red).

7. X-ray crystallography

X-rays were first discovered by the German scientist Wilhelm Röntgen on November 8, 1895. Röntgen explored the generation, penetration, and propagation of X-ray in the following two years, and he was awarded a Noble prize for his discovery in 1901. The wavelength of most X-rays ranges from 0.1-10 nm, making them ideal to study interatomic distances in crystals. In 1912, the German physicist Max von Laue observed the diffraction of X-rays by crystals and proved that X-rays. In the same year, English physicist William Lawrence Bragg and Sir William Henry Bragg devoted themselves to researching X-rays and presented Bragg's Law. Laue was awarded his Noble prize in 1914 and the Braggs were awarded their Noble prizes in 1915. Their discoveries and research into the way X-ray were diffracted from crystal provided an efficient technique for many scientific fields and had a far-reaching consequence in physics and chemistry. The main reason is that X-rays can determine crystal structures as the wavelength is comparable to the size of atoms and molecules

and gives rise to measurable diffraction effects.

7.1 Bragg's Law

When X-rays bombard a crystal, intense reflections are generated at certain incidence angles. To generate diffraction peaks, the differences in the travel paths must be equal to integer multiples of the wavelength to allow the waves to interfere constructively. As Figure 1.25 shows, if the crystal lattice planar distances are d and the travel path length difference between the ray paths is AB + BC, constructive interference will happen with a combination of X-rays wavelength (λ), crystal lattice planar spacing (d), the order of diffraction (n), and angle of incidence (θ). The general relationship between X-rays wavelength (λ), crystal lattice planar spacing (d), and angle of incidence (θ) is known as Bragg's Law, expressed as $n\lambda=2d \sin \theta$.

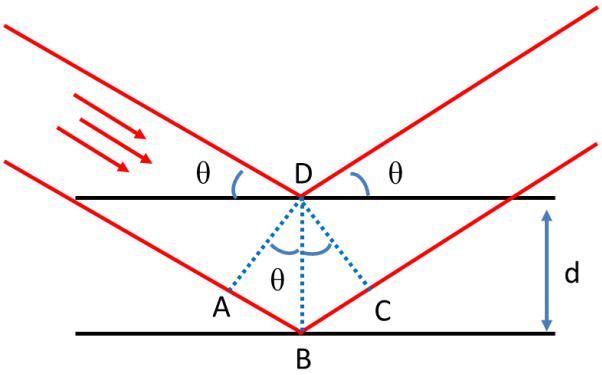

Figure 1.25. A schematic representation of Bragg's Law.

7.2 Source of X-ray

7.2.1 X-ray tube

X-ray tubes are widely used to produce a source of X-rays in most laboratories. A schematic representation of a conventional X-ray tube is shown in Figure 1.26. The tube consists of an evacuated glass (or ceramic material) tube and a metal cathode wire filament that an electrical current can pass through. In the vacuum chamber, electrons are fired at high velocity into the water-cooled anode metal block, and although most electron kinetic energy is converted into heat and is wasted, a small fraction generates the X-ray source. Beryllium windows in the X-ray tube, which are

transparent to X-rays, enable the X-ray to escape from the X-ray chamber and be directed toward a sample of interest.

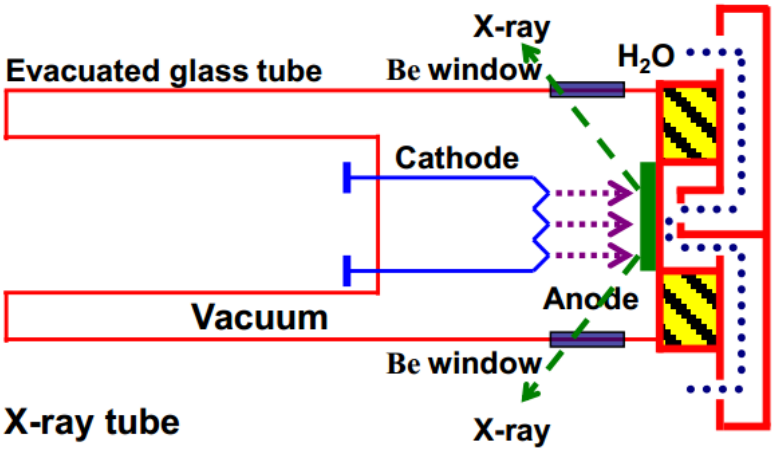

Figure 1.26. A schematic representation of a conventional X-ray tube.

7.2.2 Synchrotron radiation

Synchrotron storage rings can produce more intense X-rays and other parts of the electromagnetic spectrum than conventional X-ray tubes. Synchrotron radiation was first discovered from a General Electric synchrotron accelerator, which was built in 1946 in New York. It was announced by Frank Elder in 1947[243] that accelerating electrons at the close to the speed of light using magnets in a circular orbit produced electromagnetic radiation. However, the cyclic pathway for the electrons needs to be in the range of hundreds of meters, so such facilities are vastly expensive and are often national and international facilities. Such facilities also have lots of other scientific applications because of the other radiation wavelengths produced.

Most operational synchrotrons now have third generational sources with complex arrays of many magnets, which are located in straight sections between bending magnets that produced X-ray. The fourth generation of synchrotron sources are based on very long accelerators and undulators, such as X-ray free-electron lasers (XFELs), which are being planned and constructed. They can produce very short and rapid pulses of extremely high-intensity X-rays.

The synchrotron radiation possessed many advantages. There is broad-spectrum, so the users can select the required wavelength. The high-intensity beam allows rapid

data collection to be performed, which can shorten the experiment to several seconds and minutes, while it may take several days with an in-house facility. A small divergence and size source can be generated with the high collimated and stable photon beam. The most important use in this thesis is that the high intensities X-rays are focused on the very small crystals and determine their structures.

7.3 Single crystal X-ray diffraction (SCXRD)

Single crystal X-ray diffraction (SCXRD) is a precise method of X-ray crystallography. In an experiment, an X-ray beam strikes a single crystal and produces diffractions spots. The diffraction pattern is then measured by using a detector. During the experiment, the crystal is rotated to measure the diffraction through different faces of the crystal and the orientation of the crystal is measured during this process. The spots are called diffractions spots and correspond to X-ray being diffracted from a set of evenly spaced planes in a crystal. Quite often it is a non-destructive analytic technique and provides detailed information of crystals, such as unit cell parameters, the length, and angle of bonds, and atomic positions.

Finding a suitable single crystal is often the rate-limiting step for SCXRD analysis. An idea crystal should be sufficiently large (ideally larger than 0.01 mm in all dimensions) and pure in composition without obvious cracks or twinning. After thousands of diffraction spots are measured, corrections for instrumental factors, polarisation effects, X-ray absorption, and (potentially) crystal decomposition must be applied to the entire data set. The reflection data is then combined to produce a list of reflections in a hkl format. The hkl reflection file is finally used to solve the structure and refine the structural model.

The conversion of intensities I to $|F_o|$ (observed structure amplitudes) or F_o^2 is called data reduction. Solve a structure and obtain the atomic positions in the unit cell from hkl reflection file. The most common method for solving crystal structure (phase determination) is by direct methods, which works well for most structures.

7.4 Powder X-ray diffraction (PXRD)

When several single crystals of the same sample are packed together and irradiated with X-rays each crystal gives its own diffraction pattern and these patterns are superimposed. If there is a sufficiently large enough amount of a single crystal sample, the spots form continuous diffraction rings.

When the conditions satisfy Bragg's Law ($n\lambda=2d \sin \theta$) during interaction of X-rays with the samples, constructive interference is produced. This law relates the wavelength of electromagnetic radiation to the diffraction angle and the lattice spacing in a crystalline sample. Because of the random position of the multi-crystalline powder material, when the sample was scanned in a range of 2θ angles, all possible diffraction directions of the lattice are attained. X-ray powder diffraction is most widely used for the identification of crystalline materials where the quality of the crystalline materials is not good enough to obtain single-crystal structure. The technique is also more suitable for confirming the purity of materials and for performing *in-situ* measurements.

7.5 Disorder

While in an ideal crystal, atoms should be highly ordered with each atom in the crystal occupying a single site, in reality, atoms often vibrate around their sites. The large amplitudes of vibration are called dynamic disorder and low temperature data collections are often used to reduce the dynamic disorder. Static disorder can also be found in crystals, which is a random variation in the detailed contents of the asymmetric unit with atoms or groups of atoms occupying two or more different positions in a crystal. If the disorder is random, the average site occupancy can sometimes be determined by X-ray diffraction.

Types of commonly observed disorder in molecular crystals are methyl (CH_3) and trifluoromethyl (CF_3) group attached to the aromatic benzene ring (such as toluene and tolyl substituent), long alkyl chains and tetrahydrofuran (THF). For the methyl group, there is no single orientation, and the energy barrier of the rotation C-C bond is low. So, in some crystal structures, there can be three clear positions for hydrogen or

fluorine atoms and six other positions with lower peak heights of them. In case of high disorder and disordered atoms, the atom sites are closer than the normal bonding distance, some constraints, and restraints are used. Constraints, the rigid mathematical relationships that must be obeyed, are often used during structure refinement when certain parameters should have particular value rather than being free to be valued. Sometimes, constraints can give a good agreement between observed and calculated diffractions. Restraints are a more flexible approach and are also known as soft constraints. As non-diffraction experimental observations, restraints are combined with diffraction data which cannot change the refined parameters.

7.6 Twinning

Twinning often happens during the crystallisation procedure and can lead to the intergrowth of two separate crystals. Twinned crystals can share same some diffraction signal, which added the symmetry of structure. The twinning can be defined by different symmetry operations, 1) twin plane which was caused by the reflection across a mirror plane; 2) twin axis which was caused by the rotation axis in crystal; 3) twin centre which was caused by the inversion through a point. For example, the twinning tends to be happened when a monoclinic structure with the β angle close to 90° or the length of a and c axis is similar. During diffraction data collection of twinned crystals, two diffraction patterns, which the reflections coincide were observed. Two parameters, twin laws and twin fraction were used to determine the two-component twinned crystals. Twin laws, defined by twin planes or the direction of twin axes, were expressed by a 3x3 matrix that related to the orientations of two components. Twin fraction gives the relative amounts of the two components present in the crystal.

8. References

1. Lehn, J. M. Supramolecular chemistry: Receptors, catalysts, and carriers. *Science.* **227**, 849–856 (1985).
2. Lehn, J. -M. Supramolecular Chemistry—Scope and Perspectives Molecules, Supermolecules, and Molecular Devices (Nobel Lecture). *Angew. Chemie Int. Ed. English* **27**, 89–112 (1988).

3. Zhang, D., Martinez, A. & Dutasta, J. P. Emergence of Hemicryptophanes: From Synthesis to Applications for Recognition, Molecular Machines, and Supramolecular Catalysis. *Chem. Rev.* **117**, 4900–4942 (2017).
4. Zhou, J., Yu, G. & Huang, F. Supramolecular chemotherapy based on host-guest molecular recognition: A novel strategy in the battle against cancer with a bright future. *Chem. Soc. Rev.* **46**, 7021–7053 (2017).
5. Dong, R. *et al.* Functional supramolecular polymers for biomedical applications. *Adv. Mater.* **27**, 498–526 (2015).
6. Yan, X., Wang, F., Zheng, B. & Huang, F. Stimuli-responsive supramolecular polymeric materials. *Chem. Soc. Rev.* **41**, 6042–6065 (2012).
7. Fyfe, M. C. T. & Stoddart, J. F. Synthetic Supramolecular Chemistry. *Acc. Chem. Res.* **30**, 393–401 (1997).
8. Nguyen, S. B. T., Gin, D. L., Hupp, J. T. & Zhang, X. Supramolecular chemistry: Functional structures on the mesoscale. *Proc. Natl. Acad. Sci. U. S. A.* **98**, 11849–11850 (2001).
9. Lu, D. *et al.* The Supramolecular Chemistry of Cycloparaphenylenes and Their Analogs. *Front. Chem.* **7**, 668 (2019).
10. Lanigan, N. & Wang, X. Supramolecular chemistry of metal complexes in solution. *Chem. Commun.* **49**, 8133–8144 (2013).
11. Yang, Y. & Urban, M. W. Self-Healing of Polymers via Supramolecular Chemistry. *Adv. Mater. Interfaces* **5**, 1800384 (2018).
12. Alberti, S., Soler-Illia, G. J. A. A. & Azzaroni, O. Gated supramolecular chemistry in hybrid mesoporous silica nanoarchitectures: Controlled delivery and molecular transport in response to chemical, physical and biological stimuli. *Chem. Commun.* **51**, 6050–6075 (2015).
13. Bogdan, N. *et al.* New [4.4]cyclophanes: Molecular parallelograms, triangles, rhombuses, pentagons, and supramolecular constructions. *J. Org. Chem.* **73**, 5831–5838 (2008).
14. Spatz, J. P., Mößmer, S. & Möller, M. Mineralisation of gold nanoparticles in a block copolymer microemulsion. *Chem. - A Eur. J.* **2**, 1552–1555 (1996).
15. Park, C. *et al.* Cyclodextrin-covered organic nanotubes derived from self-assembly of dendrons and their supramolecular transformation. *Proc. Natl. Acad. Sci. U. S. A.* **103**, 1199–1203 (2006).
16. Chen, J. *et al.* Artificial muscle-like function from hierarchical supramolecular assembly of photoresponsive molecular motors. *Nat. Chem.* **10**, 132–138 (2018).
17. Zhang, Q., Qu, D. H., Tian, H. & Feringa, B. L. Bottom-Up: Can Supramolecular Tools Deliver Responsiveness from Molecular Motors to Macroscopic Materials *Matter* **3**, 355–370 (2020).
18. Badjic, J. D. *et al.* Operating molecular elevators. *J. Am. Chem. Soc.* **128**, 1489–1499 (2006).
19. Fabbrizzi, L. & Poggi, A. Sensors and switches from supramolecular chemistry. *Chem. Soc. Rev.* **24**, 197–202 (1995).
20. Sun, X. & James, T. D. Glucose Sensing in Supramolecular Chemistry. *Chem. Rev.* **115**, 8001–8037 (2015).
21. Schneider, H. J. Binding mechanisms in supramolecular complexes. *Angew. Chemie - Int. Ed.* **48**, 3924–3977 (2009).
22. Chang, C. E. & Gilson, M. K. Free energy, entropy, and induced fit in host-guest recognition: Calculations with the second-generation mining minima algorithm. *J. Am. Chem. Soc.* **126**,

13156–13164 (2004).

23. Hans-Jörg, S. Mechanisms of Molecular Recognition : Investigations of Organic Host-Guest Complexes. *Angew. Chemie Int. Ed. English* **30**, 1417–1436 (1991).
24. Foundation, S. Cyclic Polyethers and their complexes with metal salts. *J. Am. Chem. Soc.* 2495–2496 (1967).
25. Conn, M. M. & Rebek, J. Self-assembling capsules. *Chem. Rev.* **97**, 1647–1668 (1997).
26. Cram, D. J. Cavitands: Organic hosts with enforced cavities. *Science.* **219**, 1177–1183 (1983).
27. Fujita, M. Metal-directed self-assembly of two- and three-dimensional synthetic receptors. *Chem. Soc. Rev.* **27**, 417–425 (1998).
28. Zheng, J. *et al.* Pore-Engineered Metal-Organic Frameworks with Excellent Adsorption of Water and Fluorocarbon Refrigerant for Cooling Applications. *J. Am. Chem. Soc.* **139**, 10601–10604 (2017).
29. Côté, A. P. *et al.* Chemistry: Porous, crystalline, covalent organic frameworks. *Science.* **310**, 1166–1170 (2005).
30. He, Y., Xiang, S. & Chen, B. A microporous hydrogen-bonded organic framework for highly selective C 2H2/C2H4 separation at ambient temperature. *J. Am. Chem. Soc.* **133**, 14570–14573 (2011).
31. Gale, P. A. & Gunnlaugsson, T. Preface: Supramolecular chemistry of anionic species themed issue. *Chem. Soc. Rev.* **39**, 3595–3596 (2010).
32. Pluth, M. D. & Raymond, K. N. Reversible guest exchange mechanisms in supramolecular host–guest assemblies. *Chem. Soc. Rev.* **36**, 161–171 (2007).
33. El-Sheshtawy, H. S., El-Refaey, A. & El-Khouly, M. E. Supramolecular off-on-off fluorescent biosensor for total Free thyroid hormones detection based on their differential binding with cucurbit[7]uril to fluorescent perylene derivative. *J. Photochem. Photobiol. A Chem.* **382**, 111945 (2019).
34. Yannakopoulou, K., Ripmeester, J. A. & Mavridis, I. M. Release of the Prays oleae pheromone as a consequence of supramolecular structure: Study of the β-cyclodextrin-(Z)-tetradec-7-en-1-al complex by X-ray crystallography and NMR spectroscopy in the solid state and in solution. *J. Chem. Soc. Perkin Trans. 2* **2**, 1639–1644 (2002).
35. Steed, J. W., Atwood, J. L. & Gale, P. A. Definition and Emergence of Supramolecular ChemistryAdapted in part from Supramolecular Chemistry , J. W. Steed and J. L. Atwood, Wiley: Chichester, 2nd Ed., 2009. *Supramol. Chem.* (2012)
36. Lehn, J. -M. Perspectives in Supramolecular Chemistry—From Molecular Recognition towards Molecular Information Processing and Self-Organisation. *Angew. Chemie Int. Ed. English* **29**, 1304–1319 (1990).
37. Stupp, S. I. & Palmer, L. C. Supramolecular chemistry and self-assembly in organic materials design. *Chem. Mater.* **26**, 507–518 (2014).
38. Menger, F. M. Supramolecular chemistry and self-assembly. *Proc. Natl. Acad. Sci. U. S. A.* **99**, 4818–4822 (2002).
39. Mattia, E. & Otto, S. Supramolecular systems chemistry. *Nat. Nanotechnol.* **10**, 111–119 (2015).
40. Lehn, J. -M. Supramolecular chemistry — Molecular information and the design of supramolecular materials. *Makromol. Chemie. Macromol. Symp.* **69**, 1–17 (1993).

41. Shi, Z. *et al.* Thermodynamics and selectivity of two-dimensional metallo-supramolecular self-assembly resolved at molecular scale. *J. Am. Chem. Soc.* **133**, 6150–6153 (2011).
42. Sevim, S. *et al.* Self-assembled materials and supramolecular chemistry within microfluidic environments: From common thermodynamic states to non-equilibrium structures. *Chem. Soc. Rev.* **47**, 3788–3803 (2018).
43. Mc Laughlin, C. K., Hamblin, G. D. & Sleiman, H. F. Supramolecular DNA assembly. *Chem. Soc. Rev.* **40**, 5647–5656 (2011).
44. Shi, J. & Bergstrom, D. E. Assembly of Novel DNA Cycles with Rigid Tetrahedral Linkers. *Angew. Chemie (International Ed. English)* **36**, 111–113 (1997).
45. Cook, T. R., Zheng, Y. R. & Stang, P. J. Metal-organic frameworks and self-assembled supramolecular coordination complexes: Comparing and contrasting the design, synthesis, and functionality of metal-organic materials. *Chem. Rev.* **113**, 734–777 (2013).
46. Liu, Y. *et al.* Self-assembled supramolecular nanotube yarn. *Adv. Mater.* **25**, 5875–5879 (2013).
47. Huang, X. *et al.* Self-Assembled Spiral Nanoarchitecture and Supramolecular Chirality in Langmuir-Blodgett Films of an Achiral Amphiphilic Barbituric Acid. *J. Am. Chem. Soc.* **126**, 1322–1323 (2004).
48. van Nostrum, C. F., Nolte, R. J. M., Picken, S. J. & Schouten, A. J. Synthesis and Supramolecular Chemistry of Novel Liquid Crystalline Crown Ether-Substituted Phthalocyanines: Toward Molecular Wires and Molecular Ionoelectronics. *J. Am. Chem. Soc.* **117**, 9957–9965 (1995).
49. Pisula, W., Feng, X. & M̈llen, K. Tuning the columnar organisation of discotic polycyclic aromatic hydrocarbons. *Adv. Mater.* **22**, 3634–3649 (2010).
50. Bibal, B., Mongin, C. & Bassani, D. M. Template effects and supramolecular control of photoreactions in solution. *Chem. Soc. Rev.* **43**, 4179–4198 (2014).
51. Baris, B. *et al.* Robust and open tailored supramolecular networks controlled by the template effect of a silicon surface. *Angew. Chemie - Int. Ed.* **50**, 4094–4098 (2011).
52. Von Hippel, A. R. Molecular designing of materials. *Science.* **138**, 91–108 (1962).
53. G.R. Desiraju. *Crystal Engineering: The Design of Organic Solids*. (Elsevier Science;, 1989).
54. Metrangolo, P., Neukirch, H., Pilati, T. & Resnati, G. Halogen bonding based recognition processes: A world parallel to hydrogen bonding. *Acc. Chem. Res.* **38**, 386–395 (2005).
55. Braga, D., Grepioni, F. & Desiraju, G. R. Crystal engineering and organometallic architecture. *Chem. Rev.* **98**, 1375–1405 (1998).
56. Hynek, J., Chahal, M. K., Payne, D. T., Labuta, J. & Hill, J. P. Porous framework materials for singlet oxygen generation. *Coord. Chem. Rev.* **425**, 213541 (2020).
57. Dincă, M. & Long, J. R. Introduction: Porous Framework Chemistry. *Chem. Rev.* **120**, 8037–8038 (2020).
58. Cronstedt, A. F. Ron och beskriting om en obekant b ä rg ant, som kallas zeolites. *Akad, Handl* **17**, 120–130 (1756).
59. Moshoeshoe, M., Silas Nadiye-Tabbiruka, M. & Obuseng, V. A Review of the Chemistry, Structure, Properties and Applications of Zeolites. *Am. J. Mater. Sci.* **2017**, 196–221 (2017).
60. Haw, J. F. Zeolite acid strength and reaction mechanisms in catalysis. *Phys. Chem. Chem. Phys.* **4**, 5431–5441 (2002).
61. Weckhuysen, B. M. & Yu, J. Recent advances in zeolite chemistry and catalysis. *Chem. Soc.*

Rev. **44**, 7022–7024 (2015).

62. Montalvo, S. *et al.* Application of natural zeolites in anaerobic digestion processes: A review. *Appl. Clay Sci.* **58**, 125–133 (2012).
63. Li, H., Eddaoudi, M., O'Keeffe, M. & Yaghi, O. M. Design and synthesis of an exceptionally stable and highly porous metal- organic framework. *Nature* **402**, 276–279 (1999).
64. Little, M. A. & Cooper, A. I. The Chemistry of Porous Organic Molecular Materials. *Adv. Funct. Mater.* **41**, 1909842 (2020).
65. Duchamp, D. J. & Marsh, R. E. The crystal structure of trimesic acid (benzene-1,3,5-tricarboxylic acid). *Acta Crystallogr. Sect. B Struct. Crystallogr. Cryst. Chem.* **25**, 5–19 (1969).
66. Pichon, A. & James, S. L. An array-based study of reactivity under solvent-free mechanochemical conditions - Insights and trends. *CrystEngComm* **10**, 1839–1847 (2008).
67. Stassen, I. *et al.* Chemical vapour deposition of zeolitic imidazolate framework thin films. *Nat. Mater.* **15**, 304–310 (2016).
68. Burrows, A. D., Frost, C. G., Mahon, M. F. & Richardson, C. Post-synthetic modification of tagged metal-organic frameworks. *Angew. Chemie - Int. Ed.* **47**, 8482–8486 (2008).
69. Das, S., Kim, H. & Kim, O. Metathesis in single crystal: Complete and reversible exchange of metal ions constituting the frameworks of metal-organic frameworks. *J. Am. Chem. Soc.* **131**, 3814–3815 (2009).
70. McDonald, T. M. *et al.* Cooperative insertion of CO2 in diamine-appended metal-organic frameworks. *Nature* **519**, 303–308 (2015).
71. Hu, Z., Wang, Y., Shah, B. B. & Zhao, D. CO 2 Capture in Metal-Organic Framework Adsorbents: An Engineering Perspective . *Adv. Sustain. Syst.* **3**, 1800080 (2019).
72. Ding, M., Flaig, R. W., Jiang, H. L. & Yaghi, O. M. Carbon capture and conversion using metal-organic frameworks and MOF-based materials. *Chem. Soc. Rev.* **48**, 2783–2828 (2019).
73. Li, B., Wen, H. M., Zhou, W., Xu, J. Q. & Chen, B. Porous Metal-Organic Frameworks: Promising Materials for Methane Storage. *Chem* **1**, 557–580 (2016).
74. Sun, B., Kayal, S. & Chakraborty, A. Study of HKUST (Copper benzene-1,3,5-tricarboxylate, Cu-BTC MOF)-1 metal organic frameworks for CH4 adsorption: An experimental Investigation with GCMC (grand canonical Monte-carlo) simulation. *Energy* **76**, 419–427 (2014).
75. Salles, F. *et al.* Adsorption and diffusion of H2 in the MOF type systems MIL-47(V) and mil-53(cr): A combination of microcalorimetry and qens experiments with molecular simulations. *J. Phys. Chem. C* **113**, 7802–7812 (2009).
76. FitzGerald, S. A. *et al.* Quantum dynamics of adsorbed H2 in the microporous framework MOF-5 analysed using diffuse reflectance infrared spectroscopy. *Phys. Rev. B - Condens. Matter Mater. Phys.* **77**, (2008).
77. Chen, B., Ockwig, N. W., Millward, A. R., Contreras, D. S. & Yaghi, O. M. High H2 adsorption in a microporous metal-organic framework with open metal sites. *Angew. Chemie - Int. Ed.* **44**, 4745–4749 (2005).
78. Sun, D. T. *et al.* Rapid, Selective Heavy Metal Removal from Water by a Metal-Organic Framework/Polydopamine Composite. *ACS Cent. Sci.* **4**, 349–356 (2018).
79. Li, B. *et al.* Capture of organic iodides from nuclear waste by metal-organic framework-based molecular traps. *Nat. Commun.* **8**, 485 (2017).

80. Bastin, L. *et al.* A microporous metal-organic framework for separation of CO 2/N2 and CO2/CH4 by fixed-bed adsorption. *J. Phys. Chem. C* **112**, 1575–1581 (2008).
81. Venna, S. R. & Carreon, M. A. Highly permeable zeolite imidazolate framework-8 membranes for CO 2/CH4 separation. *J. Am. Chem. Soc.* **132**, 76–78 (2010).
82. Finsy, V. *et al.* Separation of CO2/CH4 mixtures with the MIL-53(Al) metal-organic framework. *Microporous Mesoporous Mater.* **120**, 221–227 (2009).
83. Liao, P. Q., Zhang, W. X., Zhang, J. P. & Chen, X. M. Efficient purification of ethene by an ethane-trapping metal-organic framework. *Nat. Commun.* **6**, 8697 (2015).
84. Fan, C. Bin *et al.* Significant Enhancement of C2H2/C2H4 Separation by a Photochromic Diarylethene Unit: A Temperature- and Light-Responsive Separation Switch. *Angew. Chemie - Int. Ed.* **56**, 7900–7906 (2017).
85. García-García, P., Müller, M. & Corma, A. MOF catalysis in relation to their homogeneous counterparts and conventional solid catalysts. *Chem. Sci.* **5**, 2979–3007 (2014).
86. Llabrés i Xamena, F. X., Abad, A., Corma, A. & Garcia, H. MOFs as catalysts: Activity, reusability and shape-selectivity of a Pd-containing MOF. *J. Catal.* **250**, 294–298 (2007).
87. Shen, K., Chen, X., Chen, J. & Li, Y. Development of MOF-Derived Carbon-Based Nanomaterials for Efficient Catalysis. *ACS Catal.* **6**, 5887–5903 (2016).
88. Chernikova, V., Yassine, O., Shekhah, O., Eddaoudi, M. & Salama, K. N. Highly sensitive and selective SO2 MOF sensor: The integration of MFM-300 MOF as a sensitive layer on a capacitive interdigitated electrode. *J. Mater. Chem. A* **6**, 5550–5554 (2018).
89. Ling, W. *et al.* Materials and Techniques for Implantable Nutrient Sensing Using Flexible Sensors Integrated with Metal–Organic Frameworks. *Adv. Mater.* **30**, 1800917 (2018).
90. Wang, X. *et al.* MOFBOTS: Metal–Organic-Framework-Based Biomedical Microrobots. *Adv. Mater.* **31**, 1901592 (2019).
91. El-Kaderi, H. M. *et al.* Designed synthesis of 3D covalent organic frameworks. *Science (80-.).* **316**, 268–272 (2007).
92. Uribe-Romo, F. J. *et al.* A crystalline imine-linked 3-D porous covalent organic framework. *J. Am. Chem. Soc.* **131**, 4570–4571 (2009).
93. Ding, S. Y. & Wang, W. Covalent organic frameworks (COFs): From design to applications. *Chem. Soc. Rev.* **42**, 548–568 (2013).
94. Zhan, X., Chen, Z. & Zhang, Q. Recent progress in two-dimensional COFs for energy-related applications. *J. Mater. Chem. A* **5**, 14463–14479 (2017).
95. Fang, Q. *et al.* Designed synthesis of large-pore crystalline polyimide covalent organic frameworks. *Nat. Commun.* **5**, 4503 (2014).
96. Segura, J. L., Mancheño, M. J. & Zamora, F. Covalent organic frameworks based on Schiff-base chemistry: Synthesis, properties and potential applications. *Chem. Soc. Rev.* **45**, 5635–5671 (2016).
97. Das, G., Balaji Shinde, D., Kandambeth, S., Biswal, B. P. & Banerjee, R. Mechanosynthesis of imine, β-ketoenamine, and hydrogen-bonded imine-linked covalent organic frameworks using liquid-assisted grinding. *Chem. Commun.* **50**, 12615–12618 (2014).
98. Peng, Y. *et al.* Room Temperature Batch and Continuous Flow Synthesis of Water-Stable Covalent Organic Frameworks (COFs). *Chem. Mater.* **28**, 5095–5101 (2016).
99. Liu, X. H. *et al.* On-surface synthesis of single-layered two-dimensional covalent organic frameworks via solid-vapour interface reactions. *J. Am. Chem. Soc.* **135**, 10470–10474 (2013).

100. Sun, B., Liu, J., Cao, A., Song, W. & Wang, D. Interfacial synthesis of ordered and stable covalent organic frameworks on amino-functionalised carbon nanotubes with enhanced electrochemical performance. *Chem. Commun.* **53**, 6303–6306 (2017).
101. Zhang, M. *et al.* Hierarchical-Coassembly-Enabled 3D-Printing of Homogeneous and Heterogeneous Covalent Organic Frameworks. *J. Am. Chem. Soc.* **141**, 5154–5158 (2019).
102. Lan, Y. *et al.* Materials genomics methods for high-throughput construction of COFs and targeted synthesis. *Nat. Commun.* **9**, 5274 (2018).
103. Zhang, Y. B. *et al.* Single-crystal structure of a covalent organic framework. *J. Am. Chem. Soc.* **135**, 16336–16339 (2013).
104. Gao, C. *et al.* Isostructural Three-Dimensional Covalent Organic Frameworks. *Angew. Chemie - Int. Ed.* **58**, 9770–9775 (2019).
105. Sun, T., Wei, L., Chen, Y., Ma, Y. & Zhang, Y. B. Atomic-Level Characterisation of Dynamics of a 3D Covalent Organic Framework by Cryo-Electron Diffraction Tomography. *J. Am. Chem. Soc.* **141**, 10962–10966 (2019).
106. Beaudoin, D., Maris, T. & Wuest, J. D. Constructing monocrystalline covalent organic networks by polymerisation. *Nat. Chem.* **5**, 830–834 (2013).
107. Ma, T. *et al.* Single-crystal x-ray diffraction structures of covalent organic frameworks. *Science.* **361**, 48–52 (2018).
108. Evans, A. M. *et al.* Seeded growth of single-crystal two-dimensional covalent organic frameworks. *Science (80-.).* **361**, 52–57 (2018).
109. Li, Z. *et al.* A 2D azine-linked covalent organic framework for gas storage applications. *Chem. Commun.* **50**, 13825–13828 (2014).
110. Jackson, K. T., Rabbani, M. G., Reich, T. E. & El-Kaderi, H. M. Synthesis of highly porous borazine-linked polymers and their application to H2, CO2, and CH4 storage. *Polym. Chem.* **2**, 2775–2777 (2011).
111. Duan, K., Wang, J., Zhang, Y. & Liu, J. Covalent organic frameworks (COFs) functionalised mixed matrix membrane for effective CO2/N2 separation. *J. Memb. Sci.* **572**, 588–595 (2019).
112. Kang, Z. *et al.* Mixed Matrix Membranes (MMMs) Comprising Exfoliated 2D Covalent Organic Frameworks (COFs) for Efficient CO2 Separation. *Chem. Mater.* **28**, 1277–1285 (2016).
113. Liu, Y., Liu, D., Yang, Q., Zhong, C. & Mi, J. Comparative study of separation performance of COFs and MOFs for CH 4/CO2/H2 mixtures. *Ind. Eng. Chem. Res.* **49**, 2902–2906 (2010).
114. Wu, Y., Xu, H., Chen, X., Gao, J. & Jiang, D. A π-electronic covalent organic framework catalyst: π-walls as catalytic beds for Diels-Alder reactions under ambient conditions. *Chem. Commun.* **51**, 10096–10098 (2015).
115. Xu, H. *et al.* Catalytic covalent organic frameworks via pore surface engineering. *Chem. Commun.* **50**, 1292–1294 (2014).
116. Yan, S. *et al.* Three-dimensional Salphen-based Covalent-Organic Frameworks as Catalytic Antioxidants. *J. Am. Chem. Soc.* **141**, 2920-2924 (2019).
117. Lin, S. *et al.* Covalent organic frameworks comprising cobalt porphyrins for catalytic CO2 reduction in water. *Science.* **349**, 1208–1213 (2015).
118. Wang, X. *et al.* Sulfone-containing covalent organic frameworks for photocatalytic hydrogen evolution from water. *Nat. Chem.* **10**, 1180–1189 (2018).
119. Bai, L., Gao, Q. & Zhao, Y. Two fully conjugated covalent organic frameworks as anode

materials for lithium ion batteries. *J. Mater. Chem. A* **4**, 14106–14110 (2016).

120. Liao, H., Ding, H., Li, B., Ai, X. & Wang, C. Covalent-organic frameworks: Potential host materials for sulfur impregnation in lithium-sulfur batteries. *J. Mater. Chem. A* **2**, 8854–8858 (2014).
121. Xu, F. *et al.* Electrochemically active, crystalline, mesoporous covalent organic frameworks on carbon nanotubes for synergistic lithium-ion battery energy storage. *Sci. Rep.* **5**, 8225 (2015).
122. Barbour, L. J. Crystal porosity and the burden of proof. *Chem. Commun.* 1163–1168 (2006).
123. Tozawa, T. *et al.* Porous organic cages. *Nat. Mater.* **8**, 973–978 (2009).
124. Mastalerz, M. One-pot synthesis of a shape-persistent endo-functionalised nano-sized adamantoid compound. *Chem. Commun.* 4756–4758 (2008).
125. Mastalerz, M., Schneider, M. W., Oppel, I. M. & Presly, O. A salicylbisimine cage compound with high surface area and selective CO2/CH4 adsorption. *Angew. Chemie - Int. Ed.* **50**, 1046–1051 (2011).
126. Schneider, M. W. *et al.* Periphery-substituted [4+6] salicylbisimine cage compounds with exceptionally high surface areas: Influence of the molecular structure on nitrogen sorption properties. *Chem. - A Eur. J.* **18**, 836–847 (2012).
127. Schneider, M. W., Hauswald, H. J. S., Stoll, R. & Mastalerz, M. A shape-persistent exo-functionalised [4 + 6] imine cage compound with a very high specific surface area. *Chem. Commun.* **48**, 9861–9863 (2012).
128. Schneider, M. W., Oppel, I. M., Griffin, A. & Mastalerz, M. Post-modification of the interior of porous shape-persistent organic cage compounds. *Angew. Chemie - Int. Ed.* **52**, 3611–3615 (2013).
129. Avellaneda, A. *et al.* Kinetically controlled porosity in a robust organic cage material. *Angew. Chemie - Int. Ed.* **52**, 3746–3749 (2013).
130. Zhang, G., Presly, O., White, F., Oppel, I. M. & Mastalerz, M. A permanent mesoporous organic cage with an exceptionally high surface area. *Angew. Chemie - Int. Ed.* **53**, 1516–1520 (2014).
131. Hasell, T., Schmidtmann, M., Stone, C. A., Smith, M. W. & Cooper, A. I. Reversible water uptake by a stable imine-based porous organic cage. *Chem. Commun.* **48**, 4689–4691 (2012).
132. Liu, M. *et al.* Acid- and base-stable porous organic cages: Shape persistence and pH stability via post-synthetic 'tying' of a flexible amine cage. *J. Am. Chem. Soc.* **136**, 7583–7586 (2014).
133. Jiang, S. *et al.* Selective gas sorption in a [2+3] 'propeller' cage crystal. *Chem. Commun.* **47**, 8919–8921 (2011).
134. Jiang, S. *et al.* Porous organic molecular solids by dynamic covalent scrambling. *Nat. Commun.* **2**, 207 (2011).
135. Jones, J. T. A. *et al.* On-off porosity switching in a molecular organic solid. *Angew. Chemie - Int. Ed.* **50**, 749–753 (2011).
136. Horng, Y. C. *et al.* Preparation of a reversible redox-controlled cage-type molecule linked by disulfide bonds. *European J. Org. Chem.* 1511–1514 (2009).
137. Dhara, A. & Beuerle, F. Reversible Assembly of a Supramolecular Cage Linked by Boron-Nitrogen Dative Bonds. *Chem. - A Eur. J.* **21**, 17391–17396 (2015).
138. Berardo, E. *et al.* Computationally-inspired discovery of an unsymmetrical porous organic cage. *Nanoscale* **10**, 22381–22388 (2018).
139. Berardo, E., Greenaway, R. L., Miklitz, M., Cooper, A. I. & Jelfs, K. E. Computational

screening for nested organic cage complexes. *Mol. Syst. Des. Eng.* **5**, 186–196 (2020).

140. Jones, J. T. A. *et al.* Modular and predictable assembly of porous organic molecular crystals. *Nature* **474**, 367–371 (2011).
141. Greenaway, R. L. *et al.* High-throughput discovery of organic cages and catenanes using computational screening fused with robotic synthesis. *Nat. Commun.* **9**, 2849 (2018).
142. Hong, S. *et al.* Porphyrin Boxes: Rationally Designed Porous Organic Cages. *Angew. Chemie - Int. Ed.* **54**, 13241–13244 (2015).
143. Jiang, S. *et al.* Molecular dynamics simulations of gas selectivity in amorphous porous molecular solids. *J. Am. Chem. Soc.* **135**, 17818–17830 (2013).
144. Liu, M. *et al.* Barely porous organic cages for hydrogen isotope separation. *Science.* **366**, 613–620 (2019).
145. Chen, L. *et al.* Separation of rare gases and chiral molecules by selective binding in porous organic cages. *Nat. Mater.* **13**, 954–960 (2014).
146. Zhang, J. H. *et al.* Homochiral Porous Organic Cage with High Selectivity for the Separation of Racemates in Gas Chromatography. *Anal. Chem.* **87**, 7817–7824 (2015).
147. Kewley, A. *et al.* Porous organic cages for gas chromatography separations. *Chem. Mater.* **27**, 3207–3210 (2015).
148. Zhang, J. H., Xie, S. M., Wang, B. J., He, P. G. & Yuan, L. M. Highly selective separation of enantiomers using a chiral porous organic cage. *J. Chromatogr. A* **1426**, 174–182 (2015).
149. Bushell, A. F. *et al.* Nanoporous organic polymer/cage composite membranes. *Angew. Chemie - Int. Ed.* **52**, 1253–1256 (2013).
150. Brutschy, M., Schneider, M. W., Mastalerz, M. & Waldvogel, S. R. Porous organic cage compounds as highly potent affinity materials for sensing by quartz crystal microbalances. *Adv. Mater.* **24**, 6049–6052 (2012).
151. Brutschy, M., Schneider, M. W., Mastalerz, M. & Waldvogel, S. R. Direct gravimetric sensing of GBL by a molecular recognition process in organic cage compounds. *Chem. Commun.* **49**, 8398–8400 (2013).
152. Giri, N. *et al.* Liquids with permanent porosity. *Nature* **527**, 216–220 (2015).
153. Giri, N. *et al.* Alkylated organic cages: From porous crystals to neat liquids. *Chem. Sci.* **3**, 2153–2157 (2012).
154. Kearsey, R. J., Alston, B. M., Briggs, M. E., Greenaway, R. L. & Cooper, A. I. Accelerated robotic discovery of type II porous liquids. *Chem. Sci.* **10**, 9454–9465 (2019).
155. Elbert, S. M. *et al.* Shape-persistent tetrahedral [4+6] boronic ester cages with different degrees of fluoride substitution. *Chem. - A Eur. J.* **24**, 11438–11443 (2018).
156. Jelfs, K. E. *et al.* Large self-assembled chiral organic cages: Synthesis, structure, and shape persistence. *Angew. Chemie - Int. Ed.* **50**, 10653–10656 (2011).
157. Karmakar, A. *et al.* Hydrogen-Bonded Organic Frameworks (HOFs): A New Class of Porous Crystalline Proton-Conducting Materials. *Angew. Chemie - Int. Ed.* **55**, 10667–10671 (2016).
158. Hisaki, I., Xin, C., Takahashi, K. & Nakamura, T. Designing Hydrogen-Bonded Organic Frameworks (HOFs) with Permanent Porosity. *Angew. Chemie - Int. Ed.* **58**, 11160–11170 (2019).
159. Han, Y. F., Yuan, Y. X. & Wang, H. B. Porous hydrogen-bonded organic frameworks. *Molecules* **22**, 266 (2017).
160. Horváth, D. V. *et al.* Polymorphism of a porous hydrogen bond-assisted ionic organic

framework. *CrystEngComm* **20**, 1779–1782 (2018).

161. Karak, S., Kumar, S., Pachfule, P. & Banerjee, R. Porosity prediction through hydrogen bonding in covalent organic frameworks. *J. Am. Chem. Soc.* **140**, 5138–5145 (2018).
162. Simard, M., Su, D. & Wuest, J. D. Use of Hydrogen Bonds to Control Molecular Aggregation. Self-Assembly of Three-Dimensional Networks with Large Chambers. *J. Am. Chem. Soc.* **113**, 4696–4698 (1991).
163. Brunet, P., Simard, M. & Wuest, J. D. Molecular tectonics. Porous hydrogen-bonded networks with unprecedented structural integrity. *J. Am. Chem. Soc.* **119**, 2737–2738 (1997).
164. Helzy, F., Maris, T. & Wuest, J. D. Engineering Hydrogen-Bonded Hexagonal Networks Built from Flexible 1,3,5-Trisubstituted Derivatives of Benzene. *J. Org. Chem.* **81**, 3076–3086 (2016).
165. Trolliet, C., Poulet, G., Tuel, A., Wuest, J. D. & Sautet, P. A theoretical study of cohesion, structural deformation, inclusion, and dynamics in porous hydrogen-bonded molecular networks. *J. Am. Chem. Soc.* **129**, 3621–3626 (2007).
166. Chen, T. H. *et al.* Thermally robust and porous noncovalent organic framework with high affinity for fluorocarbons and CFCs. *Nat. Commun.* **5**, 5131 (2014).
167. Luo, X. Z. *et al.* A microporous hydrogen-bonded organic framework: Exceptional stability and highly selective adsorption of gas and liquid. *J. Am. Chem. Soc.* **135**, 11684–11687 (2013).
168. Lü, J. *et al.* A Robust Binary Supramolecular Organic Framework (SOF) with high CO2adsorption and selectivity. *J. Am. Chem. Soc.* **136**, 12828–12831 (2014).
169. Luo, J., Wang, J. W., Zhang, J. H., Lai, S. & Zhong, D. C. Hydrogen-bonded organic frameworks: Design, structures and potential applications. *CrystEngComm* **20**, 5884–5898 (2018).
170. Hopfner, K. P. *et al.* Structural biochemistry and interaction architecture of the DNA double-strand break repair Mre11 nuclease and Rad50-ATPase. *Cell* **105**, 473–485 (2001).
171. Harding, S. E., Channell, G. & Phillips-Jones, M. K. The discovery of hydrogen bonds in DNA and a re-evaluation of the 1948 Creeth two-chain model for its structure. *Biochem. Soc. Trans.* **46**, 1171–1182 (2018).
172. Klotz, I. M. & Franzen, J. S. Hydrogen Bonds between Model Peptide Groups in Solution. *J. Am. Chem. Soc.* **84**, 3461–3466 (1962).
173. Dąbrowski, J., Nowak, W. & Ptak, A. How strong are hydrogen bonds in the peptide model? *Phys. Chem. Chem. Phys.* **22**, 1392–1399 (2020).
174. Fonari, M. S. *et al.* Hydrogen bonding assemblies in host-guest complexes with 18-crown-6. *J. Mol. Struct.* **647**, 129–140 (2003).
175. Paul, R. & Paul, S. Synergistic host-guest hydrophobic and hydrogen bonding interactions in the complexation between endo-functionalised molecular tube and strongly hydrophilic guest molecules in aqueous solution. *Phys. Chem. Chem. Phys.* **20**, 16540–16550 (2018).
176. Pandurangan, K., Kitchen, J. A., McCabe, T. & Gunnlaugsson, T. Hydrogen bonding interactions and supramolecular networks of pyridine-aryl based thiosemicarbazides and their Zn(II) complexes. *CrystEngComm* **15**, 1421–1431 (2013).
177. Mayoral, M. J., Bilbao, N. & González-Rodríguez, D. Hydrogen-Bonded Macrocyclic Supramolecular Systems in Solution and on Surfaces. *ChemistryOpen* **5**, 10–32 (2016).
178. Slater, A. G., Perdigão, L. M. A., Beton, P. H. & Champness, N. R. Surface-based supramolecular chemistry using hydrogen bonds. *Acc. Chem. Res.* **47**, 3417–3427 (2014).

179. González-Rodríguez, D. & Schenning, A. P. H. J. Hydrogen-bonded supramolecular π-functional materials. *Chem. Mater.* **23**, 310–325 (2011).
180. Jiang, J., Zhao, Y. & Yaghi, O. M. Covalent Chemistry beyond Molecules. *J. Am. Chem. Soc.* **138**, 3255–3265 (2016).
181. Lin, R. B. *et al.* Multifunctional porous hydrogen-bonded organic framework materials. *Chem. Soc. Rev.* **48**, 1362–1389 (2019).
182. Desiraju, G. R. Supramolecular Synthons in Crystal Engineering—A New Organic Synthesis. *Angew. Chemie Int. Ed. English* **34**, 2311–2327 (1995).
183. Ivasenko, O. & Perepichka, D. F. Mastering fundamentals of supramolecular design with carboxylic acids. Common lessons from X-ray crystallography and scanning tunneling microscopy. *Chem. Soc. Rev.* **40**, 191–206 (2011).
184. Leiserowitz, L. Molecular packing modes. Carboxylic acids. *Acta Crystallogr. Sect. B Struct. Crystallogr. Cryst. Chem.* **32**, 775–802 (1976).
185. Herbstein, F. H., Kapon, M. & Reisner, G. M. Catenated and non-catenated inclusion complexes of trimesic acid. *J. Incl. Phenom.* **5**, 211–214 (1987).
186. Zentner, C. A. *et al.* High surface area and Z′ in a thermally stable 8-fold polycatenated hydrogen-bonded framework. *Chem. Commun.* **51**, 11642–11645 (2015).
187. Lai, H. W. H., Wiscons, R. A., Zentner, C. A., Zeller, M. & Rowsell, J. L. C. Supramolecular Assembly of Tris(4-carboxyphenyl)arenes: Relationship between Molecular Structure and Solid-State Catenation Motifs. *Cryst. Growth Des.* **16**, 821–833 (2016).
188. Yang, W. *et al.* Highly Interpenetrated Robust Microporous Hydrogen-Bonded Organic Framework for Gas Separation. *Cryst. Growth Des.* **17**, 6132–6137 (2017).
189. Bassanetti, I. *et al.* Flexible porous molecular materials responsive to CO2, CH4 and Xe stimuli. *J. Mater. Chem. A* **6**, 14231–14239 (2018).
190. Hu, F. *et al.* An Ultrastable and Easily Regenerated Hydrogen-Bonded Organic Molecular Framework with Permanent Porosity. *Angew. Chemie - Int. Ed.* **56**, 2101–2104 (2017).
191. Yin, Q. *et al.* An Ultra-Robust and Crystalline Redeemable Hydrogen-Bonded Organic Framework for Synergistic Chemo-Photodynamic Therapy. *Angew. Chemie - Int. Ed.* **57**, 7691–7696 (2018).
192. Ma, K. *et al.* Ultrastable Mesoporous Hydrogen-Bonded Organic Framework-Based Fiber Composites toward Mustard Gas Detoxification. *Cell Reports Phys. Sci.* **1**, 100024 (2020).
193. Aitchison, C. M. *et al.* Photocatalytic proton reduction by a computationally identified, molecular hydrogen-bonded framework. *J. Mater. Chem. A*, 8, 7158-7170 (2020).
194. Hisaki, I. *et al.* Docking Strategy To Construct Thermostable, Single-Crystalline, Hydrogen-Bonded Organic Framework with High Surface Area. *Angew. Chemie* **130**, 12832–12837 (2018).
195. Hisaki, I. *et al.* Hexaazatriphenylene-Based Hydrogen-Bonded Organic Framework with Permanent Porosity and Single-Crystallinity. *Chem. - A Eur. J.* **23**, 11611–11619 (2017).
196. Hisaki, I., Ikenaka, N., Tohnai, N. & Miyata, M. Polymorphs of layered assemblies of hydrogen-bonded hexagonal networks caused by conformational frustration. *Chem Commun.*, **52** 300–303 (2016).
197. Hisaki, I. *et al.* A Series of Layered Assemblies of Hydrogen-Bonded, Hexagonal Networks of C3-Symmetric π-Conjugated Molecules: A Potential Motif of Porous Organic Materials. *J. Am. Chem. Soc.*, **138**, 6617–6628 (2016).

198. Hisaki, I., Nakagawa, S., Sato, H. & Tohnai, N. Alignment of paired molecules of C60 within a hexagonal platform networked through hydrogen-bonds. *Chem. Commun.* **52**, 9781–9784 (2016).
199. Hisaki, I. *et al.* Acid Responsive Hydrogen-Bonded Organic Frameworks. *J. Am. Chem. Soc.* **141**, 2111–2121 (2019).
200. Hisaki, I., Toda, H., Sato, H., Tohnai, N. & Sakurai, H. A Hydrogen-Bonded Hexagonal Buckybowl Framework. *Angew. Chemie - Int. Ed.* **56**, 15294–15298 (2017).
201. Li, P. *et al.* Interpenetration Isomerism in Triptycene-Based Hydrogen-Bonded Organic Frameworks. *Angew. Chemie - Int. Ed.* **58**, 1664–1669 (2019).
202. Li, P. *et al.* Assembly of a Porous Supramolecular Polyknot from Rigid Trigonal Prismatic Building Blocks. *J. Am. Chem. Soc.* **141**, 12998–13002 (2019).
203. Smith, A. E. The crystal structure of urea-hydrocarbon and thiourea-hydrocarbon complexes [9]. *J. Chem. Phys.* **18**, 150–151 (1950).
204. Smith, A. E. The crystal structure of the urea–hydrocarbon complexes. *Acta Crystallogr.* **5**, 224–235 (1952).
205. Harris, K. D. M. Meldola Lecture: understanding the properties of urea and thiourea inclusion compounds. *Chem. Soc. Rev.* **26**, 279 (1997).
206. Yang, J. *et al.* Origins of selectivity for the [2+2] cycloaddition of α,β- unsaturated ketones within a porous self-assembled organic framework. *J. Am. Chem. Soc.* **130**, 612–621 (2008).
207. Mastalerz, M. & Oppel, I. M. Rational construction of an extrinsic porous molecular crystal with an extraordinary high specific surface area. *Angew. Chemie - Int. Ed.* **51**, 5252–5255 (2012).
208. Pulido, A. *et al.* Functional materials discovery using energy-structure-function maps. *Nature* **543**, 657–664 (2017).
209. Zerkowski, J. A., MacDonald, J. C. & Whitesides, G. M. Investigations into the Robustness of Secondary and Tertiary Architecture of Hydrogen-Bonded Crystalline Tapes. *Chem. Mater.* **6**, 1250–1257 (1994).
210. Beijer, F. H. *et al.* Hydrogen-bonded complexes of diaminopyridines and diaminotriazines: Opposite effect of acylation on complex stabilities. *J. Org. Chem.* **61**, 6371–6380 (1996).
211. Maly, K. E., Gagnon, E., Maris, T. & Wuest, J. D. Engineering hydrogen-bonded molecular crystals built from derivatives of hexaphenylbenzene and related compounds. *J. Am. Chem. Soc.* **129**, 4306–4322 (2007).
212. Li, P. *et al.* A homochiral microporous hydrogen-bonded organic framework for highly enantioselective separation of secondary alcohols. *J. Am. Chem. Soc.* **136**, 547–549 (2014).
213. Li, P. *et al.* A rod-packing microporous hydrogen-bonded organic framework for highly selective separation of C2H2/CO2at room temperature. *Angew. Chemie - Int. Ed.* **54**, 574–577 (2015).
214. Li, P. *et al.* A microporous six-fold interpenetrated hydrogen-bonded organic framework for highly selective separation of C2H4/C2H6. *Chem. Commun.* **50**, 13081–13084 (2014).
215. Wang, H. *et al.* A Flexible Microporous Hydrogen-Bonded Organic Framework for Gas Sorption and Separation. *J. Am. Chem. Soc.* **137**, 9963–9970 (2015).
216. Yang, W. *et al.* Microporous Diaminotriazine-Decorated Porphyrin-Based Hydrogen-Bonded Organic Framework: Permanent Porosity and Proton Conduction. *Cryst. Growth Des.* **16**, 5831–5835 (2016).

217. Yang, W. *et al.* A microporous porphyrin-based hydrogen-bonded organic framework for gas separation. *Cryst. Growth Des.* **15**, 2000–2004 (2015).
218. Wang, H. *et al.* A microporous hydrogen-bonded organic framework with amine sites for selective recognition of small molecules. *J. Mater. Chem. A* **5**, 8292–8296 (2017).
219. Hashim, M. I. *et al.* Dissecting Porosity in Molecular Crystals: Influence of Geometry, Hydrogen Bonding, and [π···π] Stacking on the Solid-State Packing of Fluorinated Aromatics. *J. Am. Chem. Soc.* **140**, 6014–6026 (2018).
220. Yan, W. *et al.* A triptycene-based porous hydrogen-bonded organic framework for guest incorporation with tailored fitting. *Chem. Commun.* **53**, 3677–3680 (2017).
221. Palmans, A. R. A., Vekemans, J. A. J. M., Kooijman, H., Spek, A. L. & Meijer, E. W. Hydrogen-bonded porous solid derived from trimesic amide. *Chem. Commun.* 2247–2248 (1997).
222. Yang, W. *et al.* Exceptional thermal stability in a supramolecular organic framework: Porosity and gas storage. *J. Am. Chem. Soc.* **132**, 14457–14469 (2010).
223. Yamagishi, H. *et al.* Self-assembly of lattices with high structural complexity from a geometrically simple molecule. *Science.* **361**, 1242–1246 (2018).
224. Li, P. *et al.* Interpenetration Isomerism in Triptycene-Based Hydrogen-Bonded Organic Frameworks. *Angew. Chemie - Int. Ed.* **58**, 1664–1669 (2019).
225. Hisaki, I. *et al.* A Series of Layered Assemblies of Hydrogen-Bonded, Hexagonal Networks of C3-Symmetric π-Conjugated Molecules: A Potential Motif of Porous Organic Materials. *J. Am. Chem. Soc.* **138**, 6617–6628 (2016).
226. Vekilov, P. G. Nucleation. *Cryst. Growth Des.* **10**, 5007–5019 (2010).
227. Lutsko, J. F. How crystals form: A theory of nucleation pathways. *Sci. Adv.* **5**, (2019).
228. Myerson, A. S. & Ginde, R. Crystals, crystal growth, and nucleation. *Handb. Ind. Cryst.* 33–65 (2002).
229. De Yoreo, J. J. Principles of Crystal Nucleation and Growth. *Rev. Mineral. Geochemistry* **54**, 57–93 (2003).
230. Acree, W. & Chickos, J. S. Phase Transition Enthalpy Measurements of Organic and Organometallic Compounds. Sublimation, Vapourisation and Fusion Enthalpies From 1880 to 2015. Part 1. C1-C10. *J. Phys. Chem. Ref. Data* **45**, (2016).
231. Chickosa, J. S. & Acree, W. E. Enthalpies of sublimation of organic and organometallic compounds. 1910-2001. *J. Phys. Chem. Ref. Data* **31**, 537–698 (2002).
232. Yu, T. *et al.* The HOF structures of nitrotetraphenylethene derivatives provide new insights into the nature of AIE and a way to design mechanoluminescent materials. *Chem. Sci.* **8**, 1163–1168 (2017).
233. Hu, F. *et al.* An Ultrastable and Easily Regenerated Hydrogen-Bonded Organic Molecular Framework with Permanent Porosity. *Angew. Chemie - Int. Ed.* **56**, 2101–2104 (2017).
234. Jozwiakowski, M. J., Nguyen, N. A. T., Sisco, J. M. & Spancake, C. W. Solubility behavior of lamivudine crystal forms in recrystallisation solvents. *J. Pharm. Sci.* **85**, 193–199 (1996).
235. Dhakshinamoorthy, A., Alvaro, M. & Garcia, H. Aerobic oxidation of thiols to disulfides using iron metal-organic frameworks as solid redox catalysts. *Chem. Commun.* **46**, 6476–6478 (2010).
236. Case, P. A., Wheeler, M. C. & Desisto, W. J. Effect of residence time and hot gas filtration on the physical and chemical properties of pyrolysis oil. *Energy and Fuels* **28**, 3964–3969 (2014).

237. Aitchison, C. M. *et al.* Photocatalytic proton reduction by a computationally identified, molecular hydrogen-bonded framework. *J. Mater. Chem. A* **8**, 7158–7170 (2020).
238. Wang, Y. *et al.* Cyclopentane Hydrate Crystal Growth Behavior at the Three-Phase Interface with the Presence of Fine-Grained Sediments. *Energy and Fuels* **35**, 1433–1441 (2021).
239. Barta, Č., Žemlička, J. & René, V. Growth of CaCO3 and CaSO4 · 2H2O crystals in gels. *J. Cryst. Growth* **10**, 158–162 (1971).
240. Suresh, S. The Growth and the Optical, Mechanical, Dielectric and Photoconductivity Properties of a New Nonlinear Optical Crystal—L-Phenylalanine-4-nitrophenol NLO Single Crystal. *J. Cryst. Process Technol.* **03**, 87–91 (2013).
241. Münch, A. S., Katzsch, F., Weber, E. & Mertens, F. O. R. L. Synthesis, spectroscopic characterisation and structural investigation of a new symmetrically trisubstituted benzene derivative: 3,3′, 3′′-(Benzene-1,3,5-triyl)tripropiolic acid. *J. Mol. Struct.* **1043**, 103–108 (2013).
242. Zentner, C. A. *et al.* High surface area and Z′ in a thermally stable 8-fold polycatenated hydrogen-bonded framework. *Chem. Commun.* **51**, 11642–11645 (2015).
243. Elder, F. R., Gurewitsch, A. M., Langmuir, R. V. & Pollock, H. C. Radiation from electrons in a synchrotron [8]. *Phys. Rev.* **71**, 829–830 (1947).

Chapter 2
Mining Predicted Crystal Structure Landscapes with High Throughput Crystallisation: Old Molecules, New Insights

The work reported herein is published in Chemical Science, Cui *et al.* 2019, 10, 9988-9997.[1]

Contributions to this chapter

Peng Cui scaled up crystallisations and led the experimental work. Dr. David P. McMahon, Dr. Peter R. Spackman, Prof. Andy I. Cooper, and Prof. Graeme M. Day performed crystal structure prediction (CSP) calculations. Peng Cui developed the high-throughput crystallisation workflow. Peng Cui and Dr. Marc A. Little interpreted X-ray diffraction data. Dr. Peter R. Spackman implemented software to perform hydrogen-bonded network analysis.

1. Abstract

n this chapter, two molecules that have been widely studied by the crystal engineering community, trimesic acid (**TMA**, Figure 2.1a) and adamantane-1,3,5,7-tetracarboxylic acid (**ADTA**, Figure 2.1b), were chosen as candidates to explore if crystal structure prediction (CSP) calculations could uncover new, experimentally accessible, crystal forms. By screening a large array of crystallisation conditions experimentally, it was found that **TMA** forms several continuous 2-D networks via $R_2^2(8)$ hydrogen bond interactions (Figure 2.1c), while 3-D hydrogen-bonded frameworks that featured different amounts of interpenetration were constructed with **ADTA** (Figure 2.1d). The discovery of the experimental crystal structures was accelerated by using a high-throughput crystallisation screening protocol, which was developed to screen binary solvent crystallisation conditions and search for new polymorphs identified in local minima of their CSP energy landscapes. A new porous polymorph of **TMA** (**δ-TMA**) which has a guest-free hexagonal pore structure and several guest-stabilised structures of **ADTA** was found.

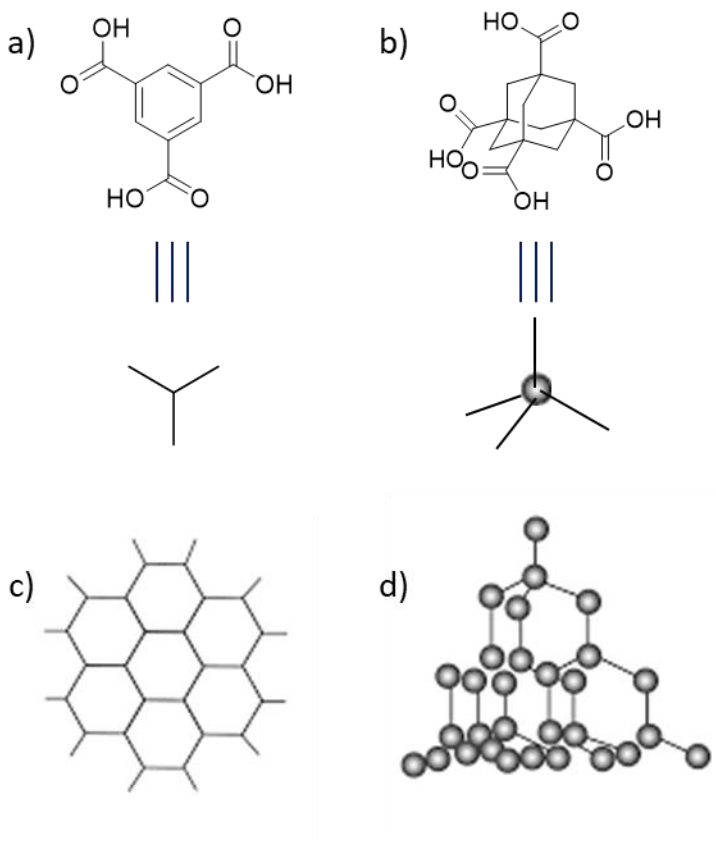

Figure 2.1 Chemical structures of **TMA** (a) and **ADTA** (b); c) the diagram of 2-D hydrogen-bonded structure constructed with **TMA**, d) the diagram of 3-D hydrogen-bonded structure constructed by **ADTA**.

2. Introduction

2.1 High-throughput screening

High throughput screening (HTS) methods have been widely developed by the pharmaceutical industry for small molecule synthesis and drug discovery.[2,3] One reason is that HTS methods allow researchers to carry out hundreds or thousands of experimentations in parallel. Usually, robots play important role in the development of HTS methods. A conceptual advantage of HTS is that more assays can be executed by research, and potential 'hits' can be determined using an indication about material performance, which can guide the selection of 'hits' to follow-up. Compared with traditional batch screening methods, HTS methods can possess a lot of advantages, such as the array format can be significantly larger (*e.g.*, 96-well plates are commonly

available, as are even larger plate formats); typically, smaller assay volumes are required (*e.g.*, down to μL and μg quantities); and the addition of the assay components can be screened in a far more diverse way. Throughput and reduced assay volumes have been increased significantly by new HTS technologies (*e.g.*, the development of automated synthesis and characterisation platforms). Some of key advances include new fluorescence methods, detection platforms, and liquid-handling technologies. Screening tens or even hundreds of thousands of samples per day in miniaturised assay volumes will soon become routine. Furthermore, new technologies are now being applied to information-rich cell-based assays, and this is beginning to remove one of the key bottlenecks downstream from primary screening.[4] In 1986, HTS had its origin in natural products screening, which using 96-well plates and assay volumes of 50-100 μL to substitute fermentation broths with dimethyl sulfoxide (DMSO) solutions of synthetic compounds. Along with technological improvements, computational screening also became practical for generating compound libraries, further increasing the rate of drug discovery.[5,6] Also, large arrays of hypothesis-driven, rationally designed experiments are powerful tools for solving complex chemical problems. HTS showed power and versatility when presented with the challenge of finding conditions for an unprecedented tandem Heck-Suzuki cyclisation on unprotected 2-haloaryl acrylamides.[7]

More recently, the Cooper Group at Liverpool has used HTS in cage synthesis[8] and porous liquids discovery[9]. The traditional synthesis of imine cages usually takes ~5 days for the reaction to go to completion, which can be a time-consuming process if multiple cages are synthesised via batch methods.[10] HTS allows the researcher to execute a larger number of small scale reactions at the same time. Hence, while the traditional route may take months or years to find and synthesise a new library of organic cages, the same could be achieved in few weeks using a HTS method.

2.2 Crystal structure prediction (CSP)

Predicting organic crystal structures is important in the academic and industrial

sectors, particularly for pharmaceuticals where polymorphism can lead to the formation of drug products with different properties.[11,12] However, it remains difficult to predict how a candidate molecule will crystallise in the lab, which makes it challenging to design crystal structures from scratch. One reason for this is because it is often the summation of relatively weak and non-directional intermolecular interactions that determine how a molecule crystallises in the lab. Typically, this results in the lattice and free energy differences between polymorphs being only a few kJ/mol or very rarely exceeding 10 kJ/mol.[13] Crystal structure prediction (CSP)[14–17] was developed to guide the discovery of molecular crystals and understand how intermolecular interactions direct crystallisation. More recently, CSP has been used to predict porous host crystal structures[18,19]. CSP methods often locate many possible structures within a small energy range (typically between 10–100 kJ/mol). However, small energy differences in lattice energies are challenging to predict reliably without expensive computational effort. Since 2007, significant progress has been made in the CSP of small organic molecules, with several different methods proving effective.[20,21] In a recent study, calculated energy-structure-function maps[18,22] were used to pre-screen the probable function of molecules *in silico* before experiments; in this case, for porosity, methane storage capacity, and guest molecule selectivity. This led to the discovery of hydrogen-bonded organic frameworks (HOFs) based on rigid triptycene benzimidazalones with unprecedentedly low bulk densities (0.41 g cm^{-3}) and apparent Brunauer-Emmett-Teller surface area (SA_{BET}) as high as 3230 m^2 g^{-1}.[18] The experimental porous crystal structures were found to correspond to low density, stable regions, or 'spikes' on the energy-density representation of the predicted crystal energy landscape. Such features might be used to predict the formation of other porous HOFs in the future.

*2.3 The history and known structures of **TMA** and **ADTA***

In 1969, Duchamp *et al.* reported the 'α-polymorph' of **TMA** (Figure 2.1a, 2.2a)[23], which comprises triply interlocked pleated hexagonal networks of **TMA** molecules and is a four-fold interpenetrated structure. Herbstein reported the first non-catenated

hexagonal networks of **TMA** seventeen years later (Figure 2.2c).[24] In Herbstein's structure, the hexagonal packing of **TMA** was stabilised in an offset arrangement, and disordered alkane guests occupied its large pores. Herbstein also discovered that **TMA** can be crystallised from the vapour phase, to produce the γ-polymorph by condensation on a cold surface (Figure 2.2b).[25] The γ-polymorph was recently shown to adsorb acetic acid reversibly after activation.[26] Zaworotko reported a 2:1 **TMA**:acetic acid solvate, which features triply inclined interpenetration between truncated 1D and hexagonal 2D nets (Figure 2.2f).[27]

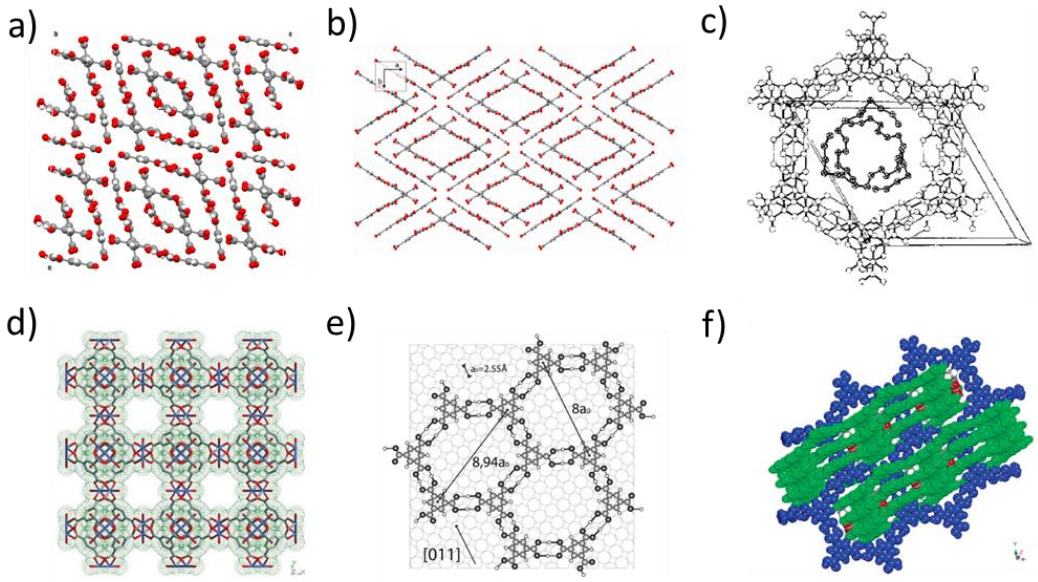

Figure 2.2 Typical frameworks based on **TMA**. a) α-**TMA**; b) γ-**TMA**. Reprinted from *Cryst. Growth Des.*, 2018, 18, 6621–6626. Copyright from 2018 American Chemical Society. c) non-catenated hexagonally arranged networks of **TMA**. Reprinted from *J. Incl. Phen.*, 1987, **5**, 211-214. Copyright 1987 Springer. d) **HKUST-1**; reprinted from *Science*, 1999, **5405**, 1148-1150. Copyright from 1999, American Association for the Advancement of Science; e) 2-D ordering of **TMA** on metal surface. Reprinted from *J. Phys. Chem. B*, 2002, **106**, 6907–6912. Copyright from 2002, The Royal Society of Chemistry; f) acetic acid solvate of **TMA** with triple inclined interpenetration. Reprinted from *Cryst. Growth Des.*, 2006, 6, 2429–2431. Copyright from 2006 American Chemical Society.

In addition to these structures, many solvates of **TMA** have been reported, including

structures that were crystallised in DMF[28], DMSO[29], water[30], methanol[31], butanol, hexanol, and heptanol (Table 2.1).[32] The 2-D ordering of **TMA** on metal surfaces has also been investigated (Figure 2.2c),[33] and **TMA** is an archetypal ligand for MOF synthesis (*e.g.*, **HKUST-1**, Figure 2.2d).[34] As such, **TMA** has been widely studied by the crystal engineering community for decades. The continued fascination with this molecule results from the complexity of its solid form landscape and the large number of competing structures that can be produced.

A second archetypal hydrogen bonding molecule is **ADTA** (Figure 2.1b), which was first reported by Ermer to form a 5-fold interpenetrated diamondoid hydrogen-bonded net in 1988 (Figure 2.3b).[35]

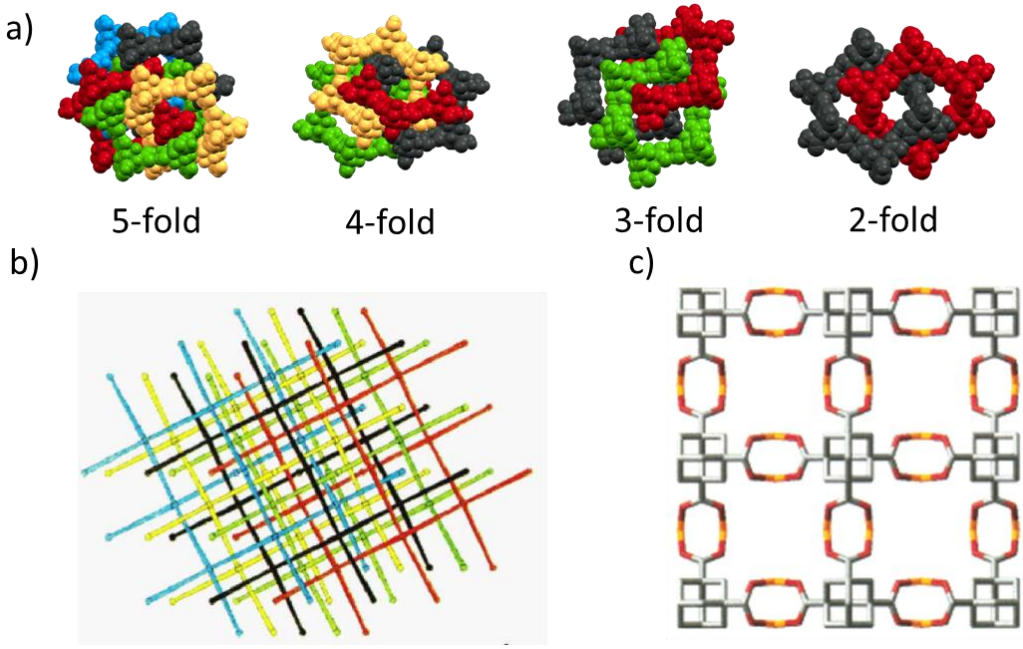

Figure 2.3 a) **ADTA** structures shown to features different amounts of interpenetration, from 5-fold to 2-fold with the unique diamondoid nets coloured in black, red, green, yellow, and blue; b) graphical representation of the 5-fold interpenetrated form of **ADTA** reported by Emmer viewed along the crystallographic *c* axis; Reprinted from *J. Am. Chem. Soc.*, 1988, 110, 3747–3754. Copyright from 1988 American Chemical Society c) dehydrated MOF-11 formed from Cu ions and **ADTA,** shown using line representation. Cu: orange; O: red; C: gray. Hydrogen atoms are omitted for clarity. Reprinted from *J. Am. Chem. Soc.*, 2000, 122, 11559–11560. Copyright from 2000 American Chemical Society.

Table 2.1 Previously reported **TMA** and **ADTA** crystal structures.[23-25, 28-32, 35, 39-43]

Name	Solvent	Space Group	*a* (Å)	*b* (Å)	*c* (Å)	*α* (°)	*β* (°)	*γ* (°)	*V* (Å^3)	Reference
1115589		*C*2/*c*	26.52	16.42	26.55		91.53		11557.7	[23]
1137091	acetone	*C*2/*c*	26.54	16.48	26.60		92.65		11625.4	[25]
204677	DMF	$P2_1/c$	16.65	14.41	7.23		90.72		1735.59	[28]
696617	DMSO	$P2_1/m$	8.74	6.84	10.71		96.19		636.59	[29]
856377	DMSO	*Pnma*	18.91	21.09	5.28				2104.97	[39]
274617	$2H_2O$	$Pna2_1$	21	13.34	3.69				1032.91	[30]
1275695	$0.83(H_2O)$	*P*1	16.64	18.55	9.51	95.81	91.06	94.35	2911.26	[40]
112933	MeOH_H_2O	$P\bar{1}$	3..70	8.97	18.04	77.76	86.86	88.04	580.77	[41]
670472	heptanol	$P\bar{1}$	8.25	8.47	11.98	94.37	104.87	110.39	745.69	[32]
670473	butanol	$P\bar{1}$	9.05	9.06	9.29	63.16	88.49	83.96	675.90	[32]
670474	hexanol	$P\bar{1}$	8.28	8.62	12.00	104.20	93.13	110.89	765.37	[32]
1272474	dioxane	$P\bar{1}$	9.53	9.54	8.03	89.68	95.01	92.03	726.37	[42]
233070	MeOH	$P\bar{1}$	7.88	8.96	8.96	111.93	96.72	110.57	526.24	[31]
233071	2MeOH	$P\bar{1}$	3.75	9.58	17.73	91.21	91.88	94	635.21	[31]
1841046	HAc	*I*222	24.223	15.332	16.531				6139.4	[26]
2**TMA**_pyrene_2ethanol		*C*2/*c*	28.13	16.55	14.73		95.13		6827	[43]
2**TMA**_n-tetradecane		$P3_1$ or $P3_2$	16.5	16.5	10.07					[24]
2**TMA**_isooctane		*C*2/*c*	28.60	16.60	6.93		102.55			[24]
2**TMA**_CRO_2H2O		$P\bar{1}$	7.50	8.02	14.71	77.05	79.48	84.41	846.69	[44]
2**TMA**_HEL		*C*2/*c*	23.07	16.18	9.15		92.83		3411.1	[45]
1165614 (**ADTA**)		$I4_1$/a	7.510			22.266			1255.8	[35]

The 5-fold structure was found to have a density of 1.65 g cm^{-3}, while the hypothetical density of the non-interpenetrated diamondoid net is calculated to be just 0.336 g cm^{-3}, *i.e.*, one-fifth of 5-fold form. To modulate the interpenetration, Ermer

later functionalised the adamantane core with dioxo or dimethylidene groups to sterically direct the formation of 3-fold and 2-fold interpenetrated networks, respectively[36]. Like **TMA**, **ADTA** was also an archetypal ligand for MOF synthesis. The interaction of **ADTA** and Zn or Cu constructed three-dimensional coordinated frameworks (Figure 2.3c).[37,38]

2.4 Development of HT Crystallisation Workflow

A HT workflow was developed to screen crystallisation conditions for candidate molecules where CSP calculations had revealed that porous, low-density structures, existed in relatively low energy regions on their predicted landscapes. For the experimental workflow, the solubilities of the candidate molecules were screened to determine which solvents dissolved the candidates and those that had poor or no solubility (referred to hereafter as 'bad' or 'anti' solvents). A Chemspeed liquid handling platform was then used to transfer stock solutions of the candidate and form binary solvent mixtures that were used to screen crystallisation conditions (see Section 2.2.2). After several days, the crystals that crystallised from binary solvent mixtures were transferred into high throughput PXRD plate for X-ray analysis. By comparing the experimental PXRD patterns with published structures, and the simulated patterns of the target structures in the CSP dataset, the samples with different or similar patterns were chosen for screening by SCXRD. Since the candidates were all crystallised from solvents, the solvated structures were also thermally activated as part of the HT workflow. *n*-Pentane was usually used in solvent exchange procedure and then the crystals were evacuated at RT with dynamic vacuum to obtain the active structure. PXRD was again used to check for changes to their patterns after activation. To investigate the stability and properties of the structures, sorption tests were performed, in addition to further solid-state analysis (*e.g.*, DSC, TGA). Finally, the experimental structures were compared with the predicted crystal structures to prove the accuracy of the crystal structure prediction method.

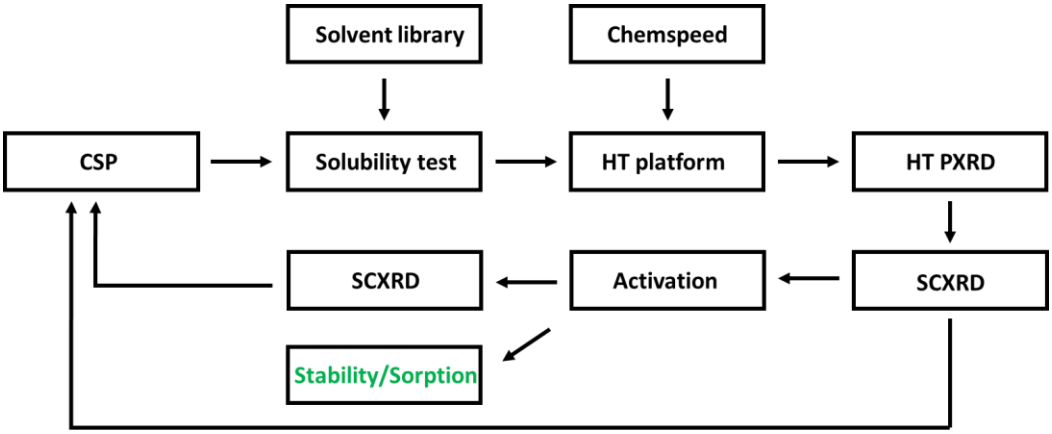

Scheme 2.1 The HT crystallisation workflow that was developed in this chapter.

3 Results and Discussion

*3.1 Crystal structure prediction (CSP) of **TMA***

The hydrogen-bonding carboxylic acid groups in **TMA** are flexible and can have different geometries. The lowest energy conformer, **TMA1**, has 3-fold rotational symmetry, while the **TMA2** conformer (generated by flipping the orientation of the carboxylic acid group) is 1.003 kJ/mol higher in intramolecular energy. The two conformers were used in the CSP calculations.

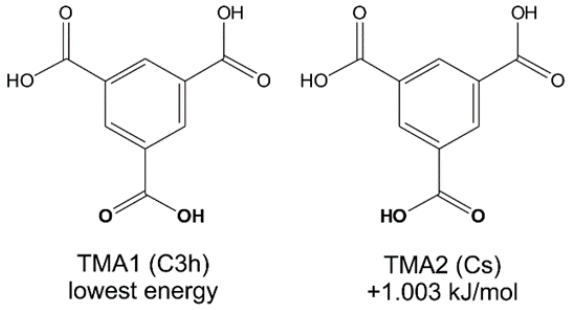

Figure 2.4 Two-dimensional schematics for the **TMA1** and **TMA2** conformers, showing the change in hydrogen position on a single carboxylic acid group.

Due to increased computational expense, searching for new crystal packings has typically been limited to those crystal structures that have only 1 or 2 molecules in the asymmetric unit (Z`= 1 and 2). Hence, the landscape of predicted structures does not

contain the known Z`= 6 α-**TMA**[23], nor the Z`= 3 γ-**TMA** structures[24]. For comparison to the CSP dataset, the energies of α- and γ-**TMA** were calculated using ordered approximations of their high-Z disordered structures (Figure 2.5a). Their energies are within 7.7 (α) and 8.2 (γ) kJ/mol of the CSP global minimum, which is within the usual energetic range of polymorphism[46], and lie on the low energy edge of the energy-density distribution plot, where observed crystal structures are often found. Furthermore, hexagonal networks of hydrogen bonding across the crystal structure landscape were also found.

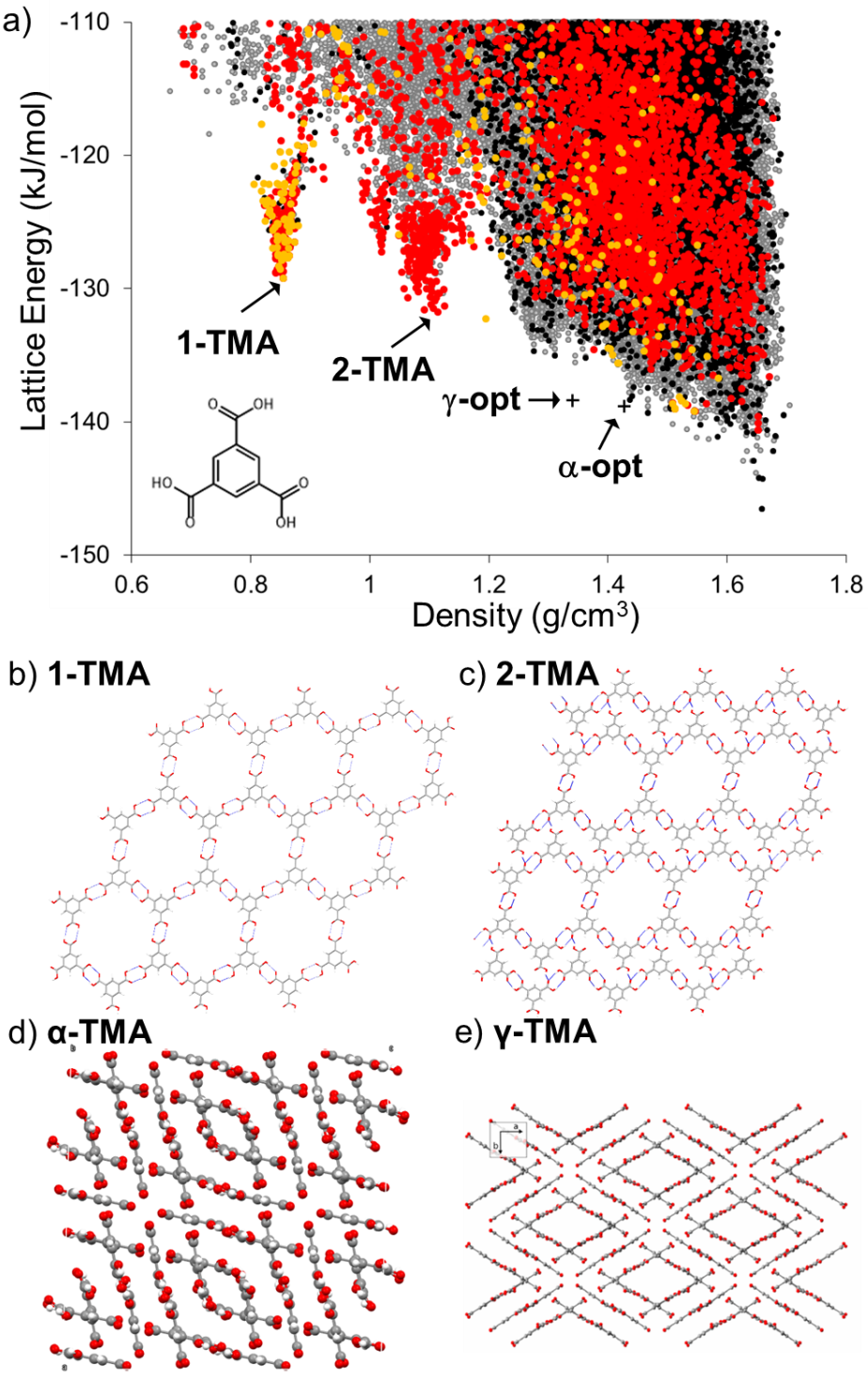

Figure 2.5 a) CSP energy landscape for **TMA** (Z`=1 black, Z`=2 grey). The structures containing hexagonal hydrogen-bonded sheets were coloured orange (Z`=1) and red (Z`=2). The known α and γ polymorphs are indicated by crosses; b) the structure of **1-TMA** with 0.855 g/cm^3 density at low energy-density spike; c) the spike minimum energy structure, **2-TMA**, at 1.11 g/cm^3; d) the structure of α-**TMA**; e) the structure of γ-**TMA**.

The CSP results show the usual overall trend with higher lattice energies predicted for structures with lower crystal density. However, two clear low energy 'spikes' of unusually stable, low-density structures were found in the density regions around ~ 0.8 and 1.1 g/cm^3, and resided significantly below the densities of the known α (ρ = 1.44 g/cm^3) and γ (ρ = 1.34 g/cm^3) forms. The minimum of the lower density spike, whose structure, **1-TMA**, is shown in Figure 2.5b, has a density of 0.85 g/cm^3 and an energy 17.3 kJ/mol above the global minimum predicted structure, while the minimum of the higher density spike, **2-TMA**, shown in Figure 2.5c, is 14.8 kJ/mol above the global minimum. These 'spike' features are reminiscent of the low-energy, low-density 'spikes' corresponding to isolable porous structures on the crystal structure landscape of triptycene trisbenzimidazolone[18]. The shape of the energy-density distribution suggests that these sets of crystal structures occupy deep, low energy regions of the lattice energy surface separated from the region of densely packed structures by a large energy barrier. Moreover, the predicted lattice energies for **1-TMA** and **2-TMA** are both within 20 kJ/mol of the predicted global minimum structure. By comparison, the porous polymorphs of triptycene trisbenzimidazolone were predicted to be 49.6 kJ/mol above the global minimum and could be stabilised by crystallisation solvent[18]. Accordingly, the predicted **TMA** structures signified with **1-TMA** and **2-TMA** in Figure 2.5a might be accessible by experiment.

3.2 High-throughput crystallisation screening

3.2.1 Solubility test

A total of 38 organic solvents were used to generate a solvent library as part of the HT crystallisation workflow (Table 2.2). Initially, the solubility of **TMA** in the organic solvent from the library was determined using the general protocol: 1 mL of organic solvent was added to a sample vial containing **TMA** (~ 5 mg). The vial was then agitated at room temperature and if the **TMA** fully dissolved, more **TMA** was added in ~ 1 mg portions. If the organic solvents can dissolve ≥ 15 mg/mL of **TMA**, at RT, and had boiling points below 120 °C, they were chosen as good solvents for the HT-crystallisation screen and used to make stock solutions of **TMA**. For **TMA**, eight

good organic solvents were found. The order of increased **TMA** solubility in these solvents was determined to be: THF > methanol > ethanol > 1,4-dioxane > tetrahydropyran > 1-propanol, 2-propanol, and 1-butanol. The eight good solvents were used to prepare 15 mg/mL stock solutions of **TMA** for the HT crystallisation screen. All of the solvents that did not dissolve **TMA** at a concentration ≥ 15 mg/mL, were used as anti-solvents (bad solvent) for the HT crystallisation experiment.

Table 2.2. Solvents used during the HT crystallisation screening. The solvents are numbered 1-38 and these numbers are used throughout Chapter 2.

1. methanol	2. THF	3. ethanol	4. 2-propanol
5. tetrahydropyran	6. 1-propanol	7. 1,4-dioxane	8. 1-butanol
9. diethyl ether	10. *n*-pentane	11. DCM	12. acetone
13. methyl acetate	14. chloroform	15. diisopropyl ether	16. *n*-hexane
17. 1,3-dioxolane	18. ethyl acetate	19. trifluoroethanol	20. hexafluorobenzene
21. cyclohexane	22. acetonitrile	23. p-difluorobenzene	24. n-heptane
25. toluene	26. tetrachloroethylene	27. *o*-xylene	28. *m*-xylene
29. *p*-xylene	30. triethylorthoformate	31. cyclohexanone	32. mesitylene
33. *n*-butylbenzene	34. 1,2-dimethoxybenzene	35. 1,3-dimethoxybenzene	36. diphenyl ether
37. isooctane	38. tetradecane		

3.2.2 HT crystallisation experiment with Chemspeed platform

For the HT crystallisation screen, stock solutions of **TMA** (1.5 g, 7 mmol) in the organic solvents (100 mL) were prepared in the eight good solvents at RT. For each crystallisation, a 1 mL portion of the **TMA** stock solution was transferred into 36 different sample vials, loaded in racks on the Chemspeed platform at room temperature. 1 mL portions of the 36 other solvents (1-36) listed in Table 2.2 were then added into one of these vials to form 1:1 (*v*:*v*) binary solvent mixtures. The process was repeated with the seven other 'good solvent' stock solutions. After mixing, the solvents were allowed to evaporate at room temperature over several days

or weeks, resulting in crystallisation of **TMA**.

A Chemspeed SWING POWDERDOSE robotic platform equipped with both solid and liquid dispensing tools (Figure 2.6) was used in HT crystallisation procedure. Liquid handling was carried out via a four-needle overhead dispensing tool powered by 4 syringe pumps (syringe volumes: 1, 10 or 25 ml). After each dispense, the syringe was washed with ethanol for the next dispensing. HT crystallisations were carried out in standard 8 ml glass vials, held in removable racks (80 vials in a 16 x 5 array). The dispensing was carried at RT in a closed hood system.

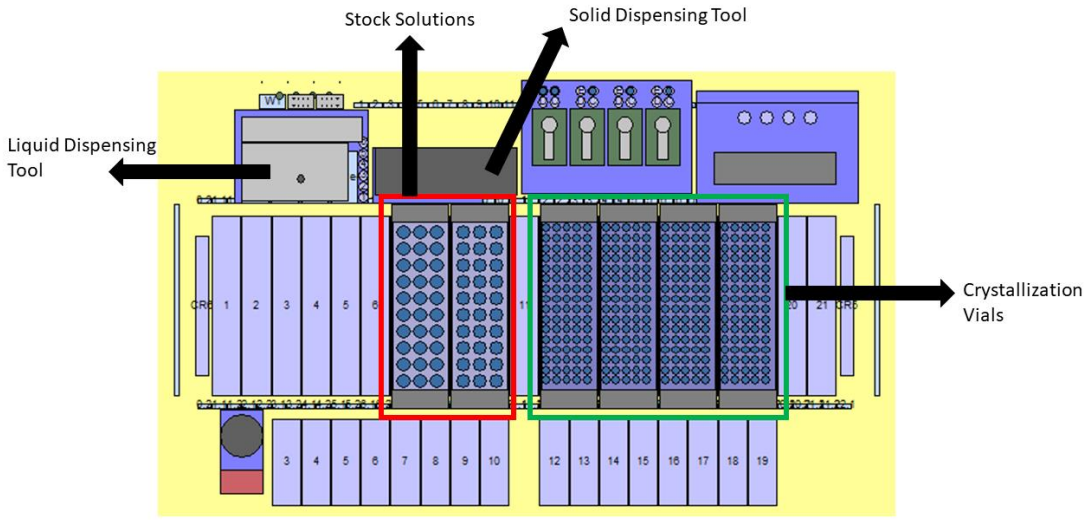

Figure 2.6 Chemspeed SWING POWDERDOSE robotic platform setup for HT crystallisation experiment.

3.2.3 Sample labelling scheme

For the HT crystallisation screens, we used the following sample labeling scheme: **TMA**_[good solvent number]-[anti-solvent number]. Hence, if the 'good solvent' was methanol (#1), and the anti-solvent was 1,3-dimethoxylbenzene (#35), the following sample code was used: **TMA**_1-35.

*3.3 HT screening results of **TMA***

After allowing all of the volatile 'good solvent' to evaporate, the crystalline solids were then isolated by filtration and transferred into a HT PXRD or transferred directly into a HT PXRD plate if all of the bad solvents had not evaporated. No further sample

preparation was undertaken before further sample analysis. Approximately 10 mg of **TMA** was used during the HT PXRD measurement. The experimental PXRD patterns were screened alongside the simulated PXRD pattern of the predicted low-density polymorph, **1-TMA**, and the simulated PXRD patterns for the **TMA** structures reported in the Cambridge Crystallographic Data Centre (CCDC) and the literature (Table 1.1). Samples were initially screened based on observed peak position, rather than peak intensity, as the powdered samples had not been carefully prepared (*e.g.*, by grinding to remove large particles and improve averaging if the crystals had plate-shaped morphologies). Here, the PXRD patterns of the different samples were compared to the simulated PXRD pattern of the predicted low-density polymorph, **1-TMA**, as well as the simulated PXRD patterns of the known **TMA** structures. When obvious differences were observed, especially in the first two peaks, attempts were made to determine the structures obtained from these crystallisation conditions using SCXRD.

*3.3.1 PXRD patterns of screened **TMA***

PXRD patterns for 288 powdered samples were recorded at room temperature. The PXRD patterns were compared with all the simulated patterns from published structures and predicted porous hexagonal structure **1-TMA** (Figure 2.5b). When structures of samples whose PXRD patterns were different from published structures attempts were made to determine their structures by SCXRD. After performing the PXRD comparison, 6 samples (**TMA**_2-33 (THF/*n*-butylbenzene), **TMA**_3-31 (ethanol/cyclohexanone), **TMA**_3-36 (ethanol/diphenyl ether), **TMA**_7-35 (dioxane/1,3-dimethoxybenzene), **TMA**_8-32 (butanol/mesitylene) and **TMA**_8-35 (butanol/1,3-dimethoxybenzene)) were found to possess similarities between the simulated PXRD pattern of predicted low-density polymorph, **1-TMA**, in the low-angle 2θ range (< 10°, Figure 2.7b).

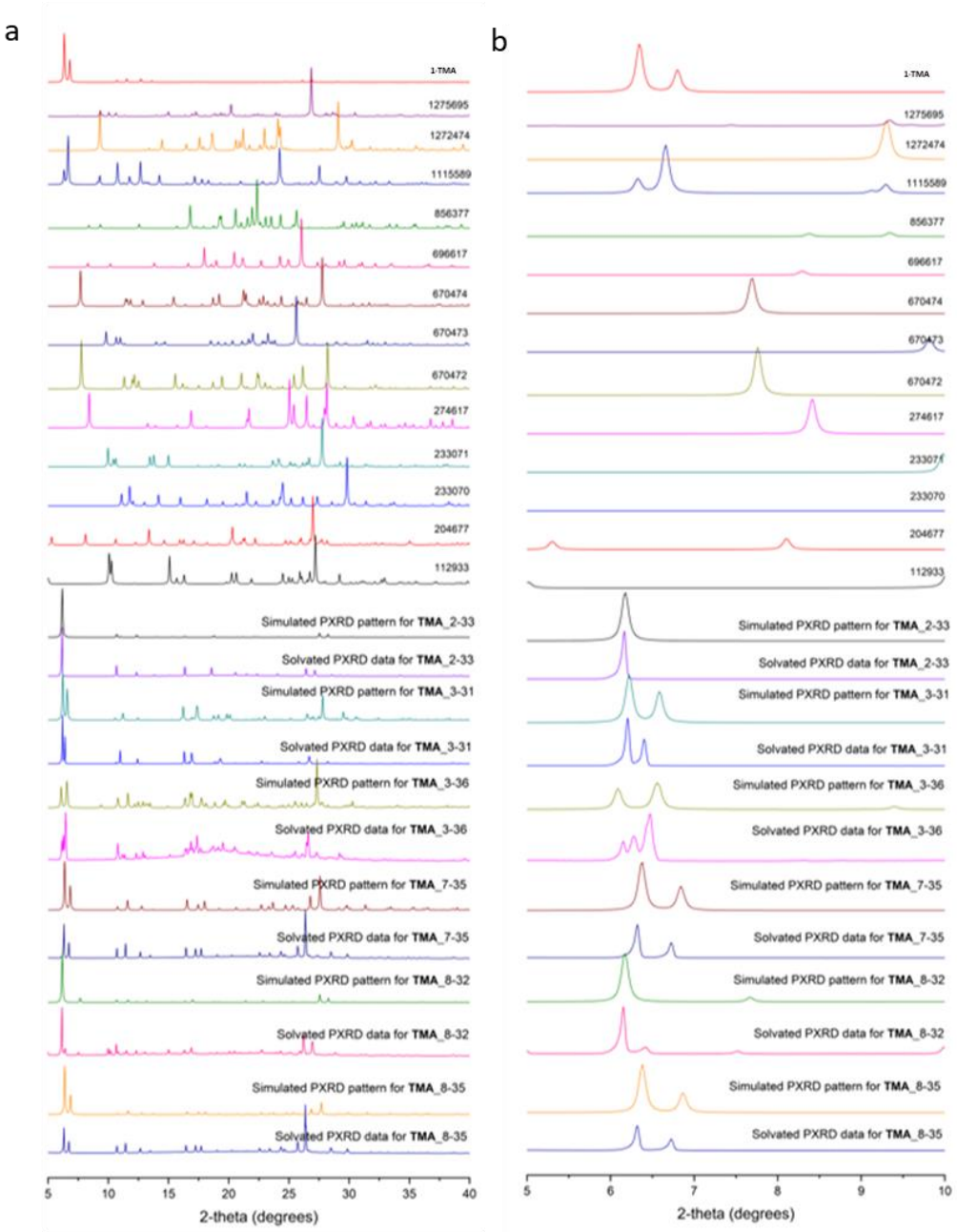

Figure 2.7. a) PXRD patterns of the simulated predicted low-density polymorph, **1-TMA** (top, red) and simulated PXRD patterns of the previously reported **TMA** structures shown in Table 1, and the solvated data for the experimental hits from the HT crystallisation screen; b) PXRD patterns from 5° to 10° 2-theta degrees for clarity.

The structures of these 6 samples were determined by SCXRD (section 3.3.2). The need for HT methods is clear: only 6/280 (~2%) of the experimental conditions trialed gave a crystalline form with a PXRD pattern that appeared similar to that of the

predicted structure, **1-TMA**. The vast majority of crystallisation conditions led to either direct crystallisation to the known α-polymorph or produced an unstable, transient phase that transformed into the α-polymorph upon loading onto the PXRD plate. This explains why **1-TMA** has remained hidden for 50 years.[23] Then the structures of these six samples were determined with SCXRD.

*3.3.2 Single crystal structures of screened **TMA***

TMA_2-33

TMA_2-33 crystallised from THF and *n*-butylbenzene solution in the trigonal space group $P3_121$. The asymmetric unit for this phase comprises one complete **TMA** and disordered solvent molecules that could not be accurately modelled as THF or *n*-butylbenzene. The disordered solvent was tentatively modelled as water (Figure 2.8a). In the $P3_121$ structure, one **TMA** molecule formed three $R_2^2(8)$ hydrogen bonding motifs between the three neighboring **TMA** molecules which constructed a continuous honeycomb-like network (Figure 2.8b). The offset **TMA** molecules formed an 'A-B-C' packing model (Figure 2.8b) and the distance between the adjacent **TMA** layers was 3.4 Å (Figure 2.8c).

Crystal data for **TMA**_2-33 (100 K): Formula $C_9H_6O_6 \cdot 2H_2O$; M = 246.17, colourless block shape crystals; $a = b$ =16.5141(6) Å, c = 9.7096(4) Å; V = 2293.20(19) Å^3; ρ = 1.070 g/cm^3; Z = 6; μ(Mo-Kα) = 0.097 mm^{-1}; F (000) = 768.0; crystal size = 0.134 × 0.063 × 0.039 mm; T = 100 (2) K. 24980 reflections measured (5.07 < 2θ < 52.74 °), 3095 unique (R_{int} = 0.0516), 2533 ($I > 2\sigma(I)$); R_1 = 0.0638 for observed and R_1 = 0.0740 for all reflections; wR_2 = 0.2217 for all reflections; max/min difference electron density = 0.405 and -0.272 e·Å^{-3}; data/restraints/parameters = 3095/6/174; GOF = 1.062; CCDC No. 1915315. For the displacement ellipsoid plot from the crystal structure, see Figure 2.8.

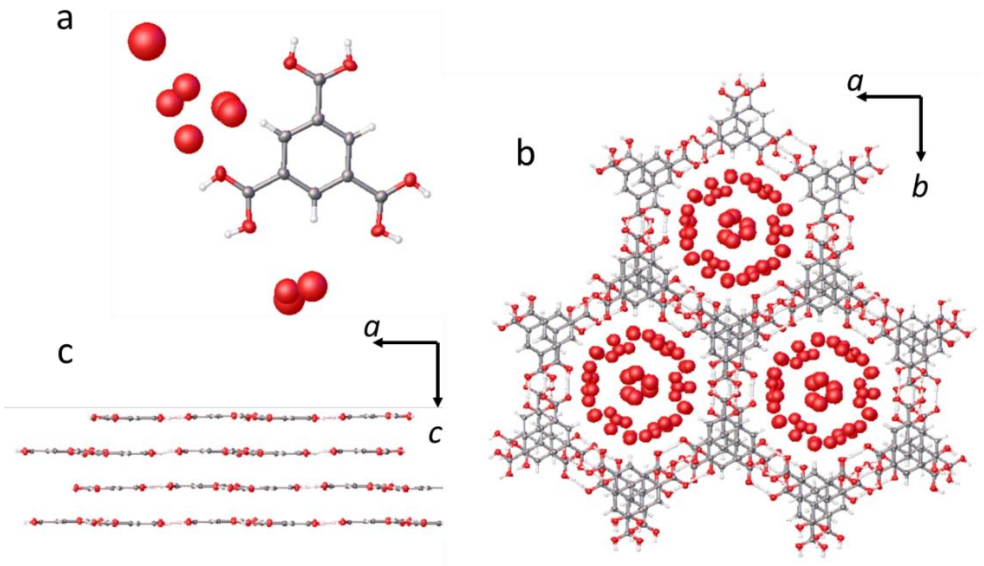

Figure 2.8. a) Displacement ellipsoid plot from the single crystal structure of **TMA**_2-33. The hydrogen atoms on the carboxylic acid group were modelled with 50% occupancy. Each disordered oxygen atom was modelled with 25 % occupancy, ellipsoids are displayed at 50% probability. Atom labels are omitted for clarity. Grey: carbon; red: oxygen; white: hydrogen. b) Crystal packing of **TMA**_2-33 viewed along [001]. c) Crystal packing of **TMA**_2-33 viewed along [010] with omitted disordered oxygen atoms for clarity. Red: oxygen; grey: carbon; white: hydrogen.

TMA_3-31

TMA_3-31 crystallised from ethanol and cyclohexanone solution in the monoclinic space group *C*2/*c*. The asymmetric unit for this phase comprises one complete **TMA** and a disordered solvent molecule that was modelled as cyclohexanone, $C_6H_{10}O$ (Figure 2.9a). In this structure, one **TMA** molecule formed three $R_2^2(8)$ hydrogen bonding motifs between the three neighboring **TMA** molecules which constructed a continuous honeycomb-like network. There are four cyclohexanone molecules occupied in the pore viewed along the *c* axis (Figure 2.9b). The offset **TMA** molecules formed an 'A-B' packing model (Figure 2.9b) and the distance of the adjacent **TMA** layers was 3.2 Å (Figure 2.9c).

Crystal data for **TMA**_3-31 (100 K): Formula $C_9H_6O_6 \cdot C_6H_{10}O$; M = 308.28, monoclinic *C*2/*c*, colourless block shape crystals; a =27.254(3) Å, b = 16.7260(16) Å, c

= 6.7365(6) Å, β = 100.207(3) °; V = 3022.3(5) Å^3; ρ = 1.355 g/cm^3; Z = 8; μ(Mo-Kα) = 0.109 mm^{-1}; F (000) = 1296.0; crystal size = 0.085 × 0.058 × 0.047 mm; T = 100 (2) K. 16923 reflections measured (2.87 < 2θ < 52.90 °), 3117 unique (R_{int} = 0.0463), 2261 (I > 2σ(I)); R_1 = 0.0731 for observed and R_1 = 0.0943 for all reflections; wR_2 = 0.2492 for all reflections; max/min difference electron density = 0.767 and -0.485 e·Å^{-3}; data/restraints/parameters = 3117/116/257; GOF = 1.065; CCDC No. 1915304. For the displacement ellipsoid plot from the crystal structure, see Figure 2.9.

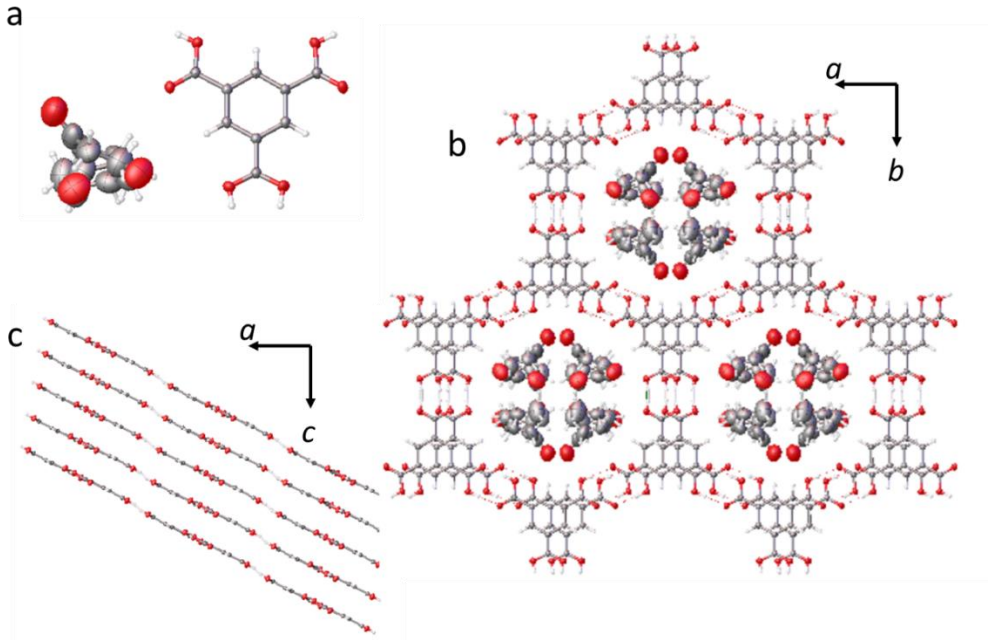

Figure 2.9. a) Displacement ellipsoid plot from the single crystal structure of **TMA**_3-31. The hydrogen atoms on the carboxylic acid group were modelled with 50% occupancy. Ellipsoids are displayed at 50% probability. Atom labels were omitted for clarity. Grey: carbon; red: oxygen; white: hydrogen. b) Crystal packing of **TMA**_3-31 viewed along [001]. c) Crystal packing of **TMA**_3-31 viewed along [010] omitted disordered oxygen atoms for clarity. Red: oxygen; grey: carbon; white: hydrogen.

TMA_3-36

TMA_3-36 crystallised from ethanol and diphenyl ether solution in the triclinic space group $P\bar{1}$. The asymmetric unit for the $P\bar{1}$ phase comprises three complete **TMA** and two ordered solvent molecules, which were modelled as diphenyl ether, $C_{12}H_{10}O$

(Figure 2.10a). In this structure, one **TMA** molecule formed three $R_2^2(8)$ hydrogen bonding motifs between the three neighboring **TMA** molecules which constructed a continuous honeycomb-like network (Figure 2.10b). The offset **TMA** molecules formed an 'A-B' packing model (Figure 2.10b) and the distance of the adjacent **TMA** layers was 3.3 Å (Figure 2.10c).

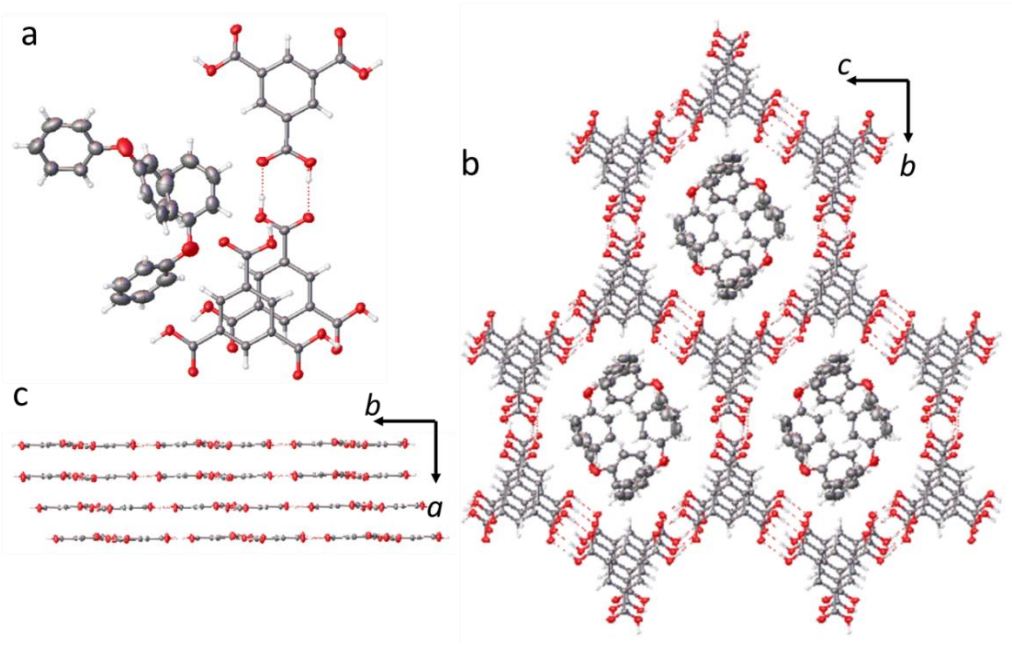

Figure 2.10. a) Displacement ellipsoid plot from the single crystal structure of **TMA**_3-36. Ellipsoids are displayed at 50% probability. Atom labels were omitted for clarity. Grey: carbon; red: oxygen; white: hydrogen. b) Crystal packing of **TMA**_3-36 viewed along [100]. c) Crystal packing of **TMA**_3-36 viewed along [001] omitted ordered diphenyl ether for clarity. Red: oxygen; grey: carbon; white: hydrogen.

Crystal data for **TMA**_3-36 (200 K): Formula $3(C_9H_6O_6)\cdot 2\ (C_{12}H_{10}O)$; M = 970.81, triclinic $P\bar{1}$, colourless block shape crystals; a =10.50240(6) Å, b = 15.88590(7) Å, c = 16.60930(7) Å, α = 113.7260(4) °, β = 98.4480(4) °, γ = 106.8020(4) °; V = 2316.46(2) Å^3; ρ = 1.392 g/cm^3; Z = 2; μ(0.6889 Å) = 0.100 mm^{-1}; F (000) = 1008.0; crystal size = 0.078 × 0.028 × 0.024 mm; T = 200 (2) K. 36998 reflections measured ($2.72 < 2\theta < 56.30$ °), 12320 unique (R_{int} = 0.0281), 8999 ($I > 2\sigma(I)$); R_1 = 0.0429 for observed and R_1 = 0.0559 for all reflections; wR_2 = 0.1429 for all reflections; max/min difference

electron density = 0.306 and -0.380 e·Å^{-3}; data/restraints/parameters = 12320/196/700; GOF = 1.100; CCDC No. 1915309. For the displacement ellipsoid plot from the crystal structure, see Figure 2.10.

TMA_8-35

TMA_8-35 crystallised from 1-butanol and 1,3-dimethoxybenzene solution in the monoclinic space group *C*2/*m*. The asymmetric unit for the *C*2/*m* phase comprises one complete **TMA** and disordered solvent molecules were tentatively modelled as water (Figure 2.11a). In this structure, one **TMA** molecule formed three $R_2^2(8)$ hydrogen bonding motifs to the three neighboring **TMA** molecules to form a continuous honeycomb-like 2-D network (Figure 2.11b). The **TMA** molecules were packed in an 'A-A' stacking mode (Figure 2.11b) and the distance between the adjacent **TMA** layers was 3.6 Å (Figure 2.11c).

Crystal data for **TMA**_8-35 (100 K): Formula $C_9H_6O_6 \cdot 5.4\ H_2O$; M = 296.14, monoclinic *C*2/*m*, colourless hexagonal shape crystals; a =25.768(4) Å, b = 16.425(2) Å, c = 3.6006(5) Å, β = 93.333(4)°; V = 1521.3(4) Å^3; ρ = 1.340 g/cm^3; Z = 4; μ(Mo-Kα) = 0.125 mm^{-1}; F (000) = 647.0; crystal size = 0.021 × 0.011 × 0.01 mm; T = 100 (2) K. 8267 reflections measured (4.96 < 2θ < 52.90 °), 1618 unique (R_{int} = 0.0521), 1293 (I > 2σ(I)); R_1 = 0.0887 for observed and R_1 = 0.1014 for all reflections; wR_2 = 0.2458 for all reflections; max/min difference electron density = 0.588 and -0.433 e·Å^{-3}; data/restraints/parameters = 1618/0/115; GOF = 1.785; CCDC No. 1915314. For the displacement ellipsoid plot from the crystal structure, see Figure 2.11.

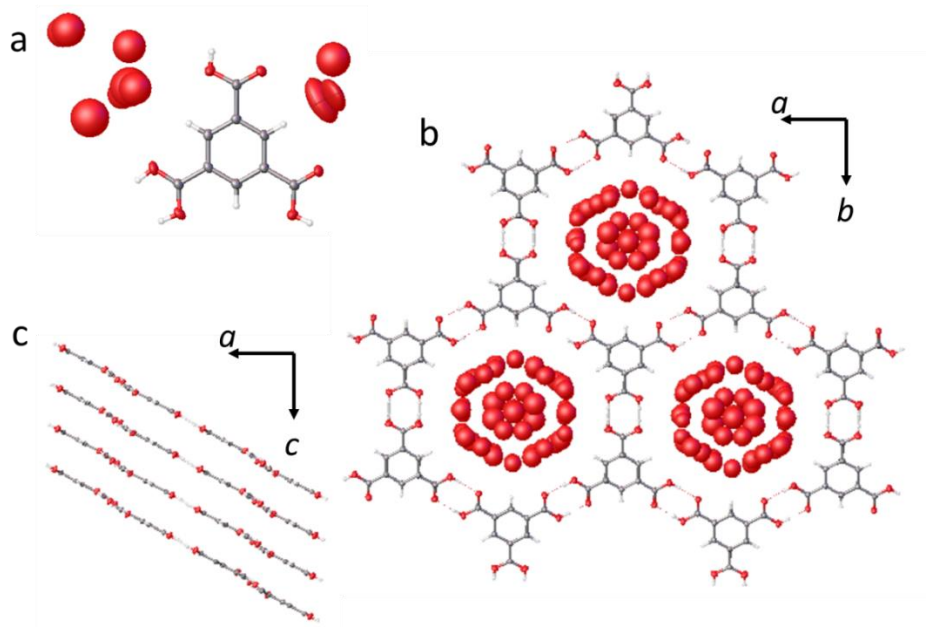

Figure 2.11. a) Displacement ellipsoid plot from the single crystal structure of **TMA**_8-35. The hydrogen atoms on the carboxylic acid groups were modelled with 50 % occupancy. Each disordered oxygen atom was tentatively modelled with 25% occupancy, ellipsoids are displayed at 50% probability. Atom labels were omitted for clarity. Grey: carbon; red: oxygen; white: hydrogen. b) Crystal packing of **TMA**_8-35 viewed along [001]. c) Crystal packing of **TMA**_8-35 viewed along [010] disordered oxygen atoms omitted for clarity. Red: oxygen; grey: carbon; white: hydrogen.

TMA_7-35

TMA_7-35 crystallised from 1,4-dioxane and 1,3-dimethoxybenzene solution in the monoclinic space group *C*2/*m*. The asymmetric unit for the second *C*2/*m* phase likewise comprises one complete **TMA** and disordered solvent molecules which were tentatively modelled as water (Figure 2.12a). The X-ray data was integrated and scaled as a two-component twin using TWINABS and the X-ray crystal structure was refined with a two-component HKLF5 reflection file and BASF refined to 0.07. In the second *C*2/*m* structure, one **TMA** molecule formed three $R_2^2(8)$ hydrogen bonding motifs to three neighboring **TMA** molecules, which again led to the formation of a continuous honeycomb-like network (Figure 2.12b). The **TMA** molecules were also packed in an

'A-A' stacking mode (Figure 2.12b) at a comparable stacking distance of 3.6 Å (Figure 2.12c).

Crystal data for **TMA**_7-35 (100 K): Formula $C_9H_6O_6 \cdot 7.5O$; M = 330.14, monoclinic *C2/m*, colourless hexagonal shape crystals; a =25.869(4) Å, b = 16.419(3) Å, c = 3.6060(6) Å, β = 93.617(4) °; V = 1528.6(4) Å^3; ρ = 1.435 g/cm^3; Z = 4; μ(Mo-Kα) = 0.143 mm^{-1}; F (000) = 672.0; crystal size = 0.017 × 0.011 × 0.009 mm; T = 100 (2) K. 1664 reflections measured (4.96 < 2θ < 54.99 °), 1533 unique (R_{int} = 0.0431), 1533 (I > 2σ(I)); R_1 = 0.0688 for observed and R_1 = 0.0727 for all reflections; wR_2 = 0.2049 for all reflections; max/min difference electron density = 0.317 and -0.415 e·Å^{-3}; data/restraints/parameters = 1664/1/137; GOF = 1.070; CCDC No. 1915308. For the displacement ellipsoid plot from the crystal structure, see Figure 2.12.

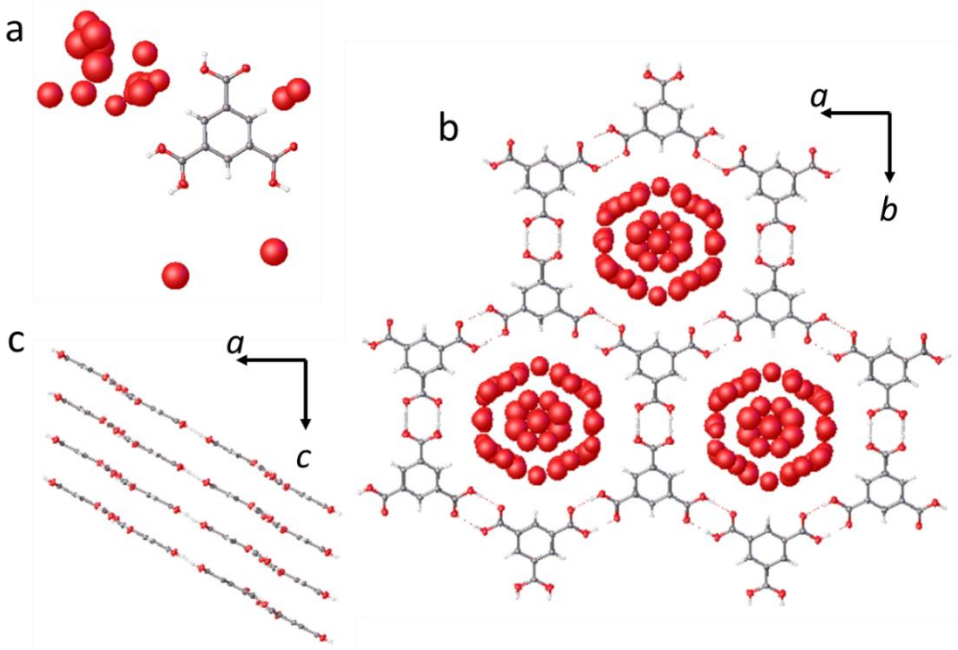

Figure 2.12. a) Displacement ellipsoid plot from the single crystal structure of **TMA**_7-35. The hydrogen atoms on the carboxylic acid group were modelled with 50% occupancy. Each disordered oxygen atom in the crystal pores was modelled with 25% occupancy, ellipsoids are displayed at 50% probability. Atom labels were omitted for clarity. Grey: carbon; red: oxygen; white: hydrogen. b) Crystal packing of **TMA**_7-35 viewed along [001]. c) Crystal packing of **TMA**_7-35 viewed along [010] omitted disordered oxygen atoms for clarity. Red: oxygen; grey: carbon; white: hydrogen.

TMA_8-32

TMA_8-32 crystallised from a 1-butanol and mesitylene solution in the trigonal space group $P3_221$. The asymmetric unit for the $P3_221$ phase comprises two complete **TMA** and disordered solvent molecules which were tentatively modelled as water, $8(H_2O)$ (Figure 2.13a). The X-ray crystal structure was refined with the TWINLAW [$\bar{1}00$ $0\bar{1}0$ 001] and BASF refined to 0.459. Despite best efforts, the X-ray data quality for the $P3_221$ structure was poor and the whole structure was refined with a rigid-bond RIGU restraint to restrain atomic displacement parameters during refinement. In the structure, one **TMA** molecule formed three $R_2^2(8)$ hydrogen bonding motifs to the three neighboring **TMA** molecules, which generated a continuous honeycomb-like network (Figure 2.13b). The offset **TMA** molecule was packed in an 'A-B' stacking mode (Figure 2.13b) and the distance between the **TMA** layers was 3.6 Å (Figure 2.13c).

Crystal data for **TMA**_8-32 (100 K): Formula $2C_9H_6O_6 \cdot 8H_2O$; M = 548.28, colourless block shape crystals; $a = b$ =16.5230(16) Å, c = 19.400(2) Å; V = 4586.9(10) Å^3; ρ = 1.191 g/cm^3; Z = 6; μ(Mo-Kα) = 0.113 mm^{-1}; F (000) = 1680; crystal size = 0.015 × 0.013 × 0.009 mm; T = 100 (2) K. 25344 reflections measured ($4.94 < 2\theta < 52.26$ °), 6239 unique (R_{int} = 0.0919), 3656 ($I > 2\sigma(I)$); R_1 = 0.0777 for observed and R_1 = 0.1344 for all reflections; wR_2 = 0.2266 for all reflections; max/min difference electron density = 0.379 and -0.312 e·Å^{-3}; data/restraints/parameters = 6239/230/363; GOF = 0.981; CCDC No. 1915313. For the displacement ellipsoid plot from the crystal structure, see Figure 2.13.

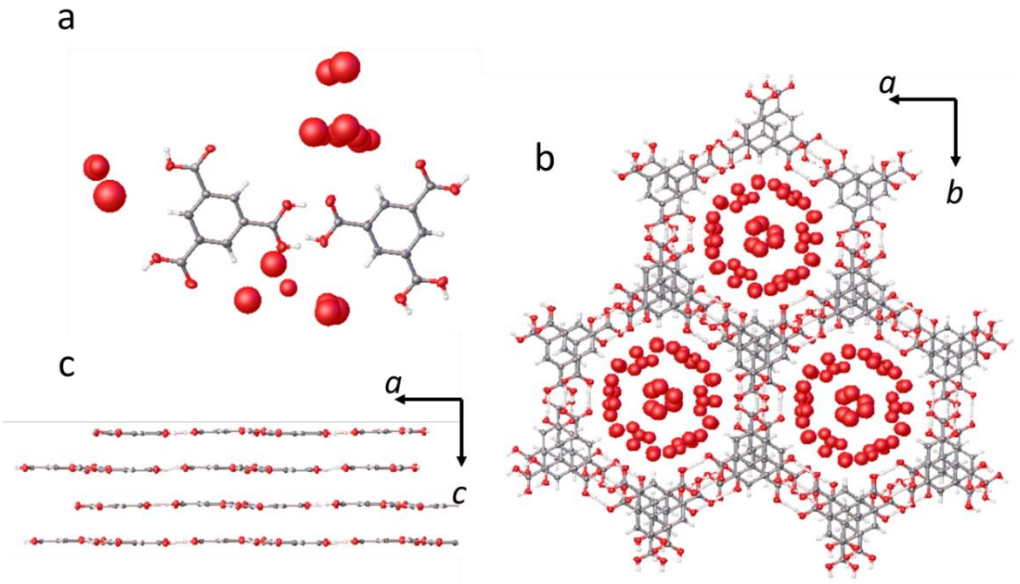

Figure 2.13. a) Displacement ellipsoid plot from the single crystal structure of **TMA**_8-32. The hydrogen atoms on the carboxylic acid group were modelled with 50% occupancy. Each disordered oxygen atom was modelled with 25% occupancy, ellipsoids are displayed at 50% probability. Atom labels were omitted for clarity. Grey: carbon; red: oxygen; white: hydrogen. b) Crystal packing of **TMA**_8-32 viewed along [001]. c) Crystal packing of **TMA**_8-32 viewed along [010] omitted disordered oxygen atoms for clarity. Red: oxygen; grey: carbon; white: hydrogen.

Two other structures in this HT screen, crystallised from 2-propanol/EtOAc and 1-propanol/EtOAc solvent mixtures (**TMA**_4-18 and **TMA**_6-18) were also identified, which feature hydrogen bonds between the **TMA** molecules and hydroxyl groups in the solvent molecules; these structures are 1:1 solvates (Figure 2.14, 2.15).

TMA_4-18

TMA_4-18 crystallised from a 2-propanol and ethyl acetate solution in the monoclinic space group *C2/c*. The asymmetric unit for **TMA**_4-18 comprises one complete **TMA** and ordered solvent molecules that were modelled as 2-propanol, C_3H_8O. In the structure, intermolecular hydrogen bond interactions between the carboxylic acid groups of **TMA** and the hydroxy group of the solvent molecules were observed. These **TMA** solvent interactions disrupted the hydrogen bonding interactions between the

carboxylic groups of adjacent **TMA** molecules. As a result, in **TMA**_4-18, only one $R_2^2(8)$ hydrogen bonding motif between two neighboring **TMA** molecules was observed (Figure 2.14c), in contrast to the extended hydrogen-bonded networks in the target **TMA** structures.

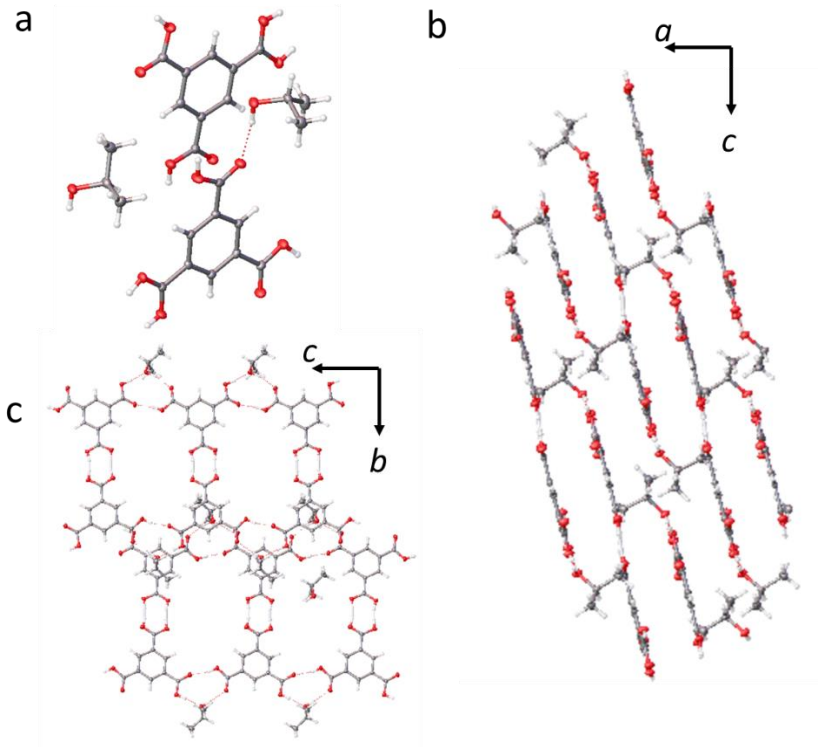

Figure 2.14. a) Displacement ellipsoid plot from the single crystal structure of **TMA**_4-18. Ellipsoids are displayed at 50% probability. Atom labels were omitted for clarity. Grey: carbon; red: oxygen; white: hydrogen. b) Crystal packing of **TMA**_4-18 viewed along the [010] direction. c) Adjacent two layers crystal packing of **TMA**_4-18 viewed along the [100] direction. Red: oxygen; grey: carbon; white: hydrogen.

Crystal data for **TMA**_4-18 (100 K): Formula $C_9H_6O_6 \cdot C_3H_8O$; M = 270.23, monoclinic $C2/c$, colourless block shape crystals; a =19.0126(17) Å, b = 9.6004(8) Å, c = 27.383(2) Å, β = 90.563(2) °; V = 4998.0(8) Å^3; ρ = 1.437 g/cm^3; Z = 8; μ(Mo-Kα) = 0.120 mm^{-1}; F (000) = 2272.0; crystal size = 0.188 × 0.101 × 0.079 mm; T = 100 (2) K. 23878 reflections measured (2.97 < 2θ < 52.89 °), 5145 unique (R_{int} = 0.0448), 4122 ($I > 2\sigma(I)$); R_1 = 0.0564 for observed and R_1 = 0.0687 for all reflections; wR_2 = 0.1624 for all reflections; max/min difference electron density = 0.651 and -0.317 e·Å^{-3};

data/restraints/parameters = 5145/3/373; GOF = 1.036; CCDC No. 1915311. For the displacement ellipsoid plot from the crystal structure, see Figure 2.14.

TMA_6-18

TMA_6-18 crystallised from a 1-propanol and ethyl acetate solution in the triclinic space group $P\bar{1}$. The asymmetric unit for **TMA**_6-18 comprises one complete **TMA** and an ordered solvent molecule that was modelled as 1-propanol, C_3H_8O. In the structure, intermolecular hydrogen bond interactions between the carboxylic acid groups of **TMA** and the hydroxy group of the solvent molecules were observed. These **TMA** solvent interactions disrupted the hydrogen bonding interactions between the carboxylic groups of adjacent **TMA** molecules. As a result, in **TMA**_6-18, only one $R_2^2(8)$ hydrogen bonding motif between two neighboring **TMA** molecules was observed (Figure 2.15c). again, in contrast to the extended hydrogen-bonded networks in the target **TMA** structures.

Crystal data for **TMA**_6-18 (100 K): Formula $C_9H_6O_6 \cdot C_3H_8O$; M = 270.23, triclinic $P\bar{1}$, colourless block shape crystals; a = 9.1671(17) Å, b = 9.4589(18) Å, c = 9.6179(17) Å, α = 93.220(5) °, β = 116.280(5) °, γ = 118.728(5) °; V = 616.2(2) Å^3; ρ = 1.457 g/cm^3; Z = 2; μ(Mo-Kα) = 0.121 mm^{-1}; F (000) = 284; crystal size = 0.15 × 0.15 × 0.09 mm; T = 100 (2) K. 8579 reflections measured (5.026 < 2θ < 62.278 °), 3929 unique (R_{int} = 0.0833), 2510 ($I > 2\sigma(I)$); R_1 = 0.0486 for observed and R_1 = 0.0759 for all reflections; wR_2 = 0.1203 for all reflections; max/min difference electron density = 0.302 and -0.330 e·Å^{-3}; data/restraints/parameters = 3929/3/189; GOF = 0.912; CCDC No. 1915310. For the displacement ellipsoid plot from the crystal structure, see Figure 2.15.

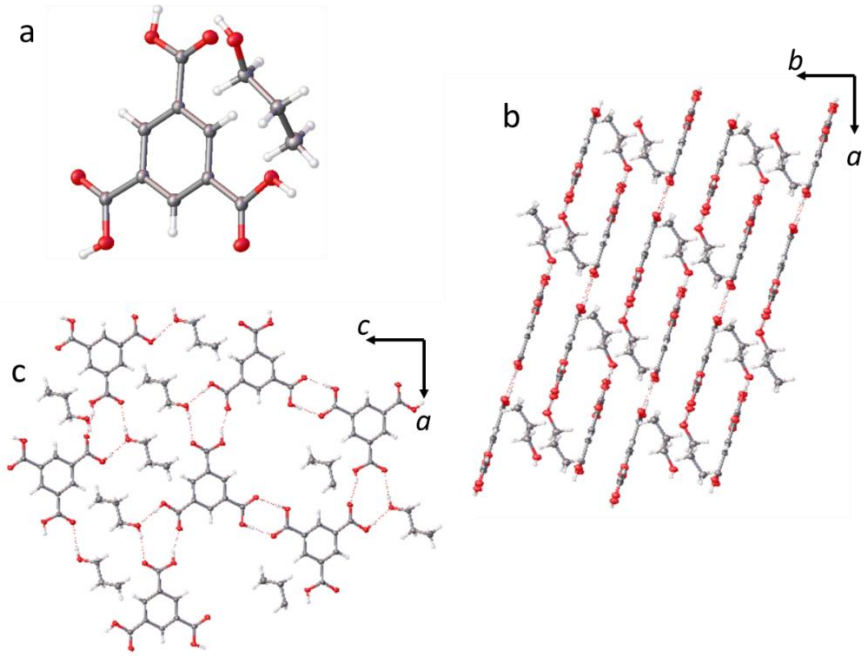

Figure 2.15. a) Displacement ellipsoid plot from the single crystal structure of **TMA**_6-18. Ellipsoids are displayed at 50 % probability. Atom labels were omitted for clarity. Grey: carbon; red: oxygen; white: hydrogen. b) Crystal packing of **TMA**_6-18 viewed along [001]. c) Layered packing of **TMA** and solvent in the crystal structure of **TMA**_6-18 viewed along [010]. Red: oxygen; grey: carbon; white: hydrogen.

For the hexagonally packed **TMA** structures, differences in the crystallographic symmetry were observed due to the stacking geometry of the hexagonal **TMA** networks. Among the solvated crystal structure, close structural matches that were based on comparable simulated and experimental PXRD patterns were found between the predicted low-density polymorph, **1-TMA** (Figure 2.5b), and the two solvates; 1,4-dioxane/1,3-dimethoxybenzene (**TMA**_7-35) and 1-butanol/1,3-dimethoxybenzene (**TMA**_8-35) (Figure 2.11, 2.12). Hence, even though solvent affected the packing of **TMA** molecules in their solvated crystal structures the crystal packing of **TMA** closely matched that found in the predicted low-density polymorph, **1-TMA**, which enabled **TMA**_7-35 and **TMA**_8-35 to be identified experimentally (Figure 2.5b).

To investigate the stability of the six hexagonally packed **TMA** structures (**TMA**_2-33, 3-31, 3-36, 7-35, 8-32, and 8-35) in the absence of the crystallisation

solvent, the solvent in the pores were exchanged with the *n*-pentane, and then the crystals were activated at room temperature after 2 hours under vacuum. PXRD analysis showed that all six of the resulting *n*-pentane solvates transformed into the same phase after activation under dynamic vacuum (Figure 2.16-2.21).

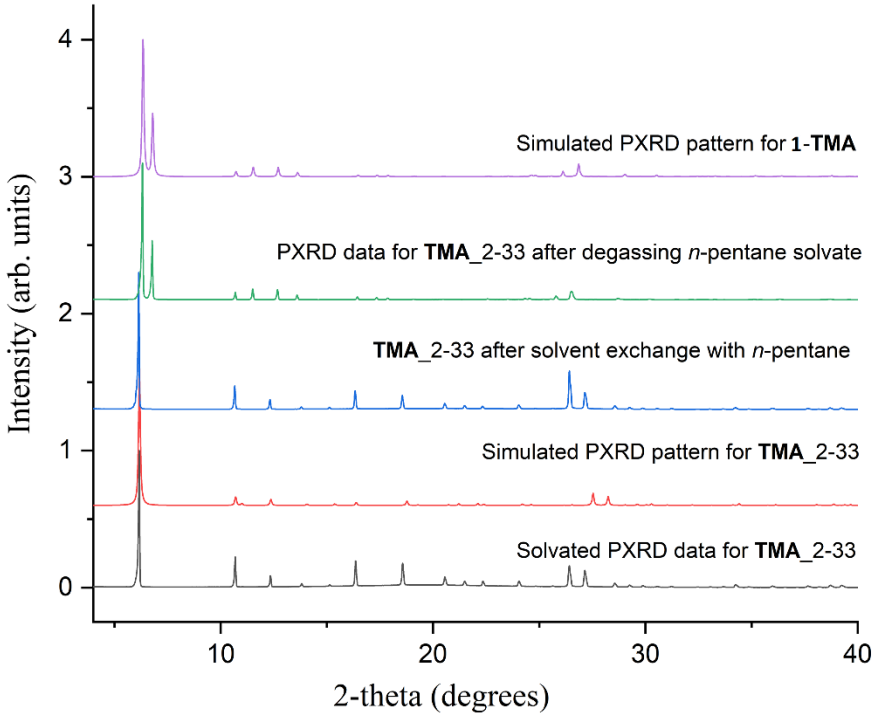

Figure 2.16. PXRD patterns of solvated PXRD data for **TMA**_2-33 (black), simulated PXRD pattern for **TMA**_2-33 (red); after exchanging with *n*-pentane (blue); after degassing the *n*-pentane exchanged sample at room temperature for 2 hrs (green); and the simulated PXRD pattern of the predicted low-density **TMA** phase, **1-TMA** (purple).

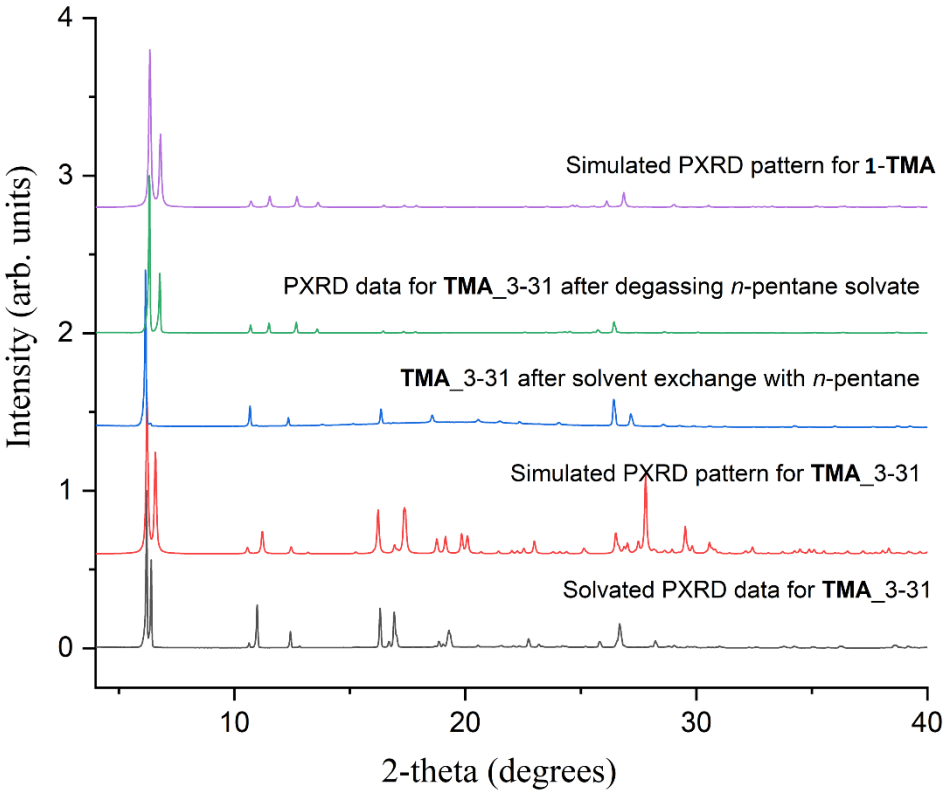

Figure 2.17. PXRD patterns of solvated PXRD data for **TMA**_3-31 (black), simulated PXRD pattern for **TMA**_3-31 (red); after exchanging with *n*-pentane (blue); after degassing the *n*-pentane exchanged sample at room temperature for 2 hrs (green); and the simulated PXRD pattern of the predicted low-density **TMA** phase, **1-TMA** (purple).

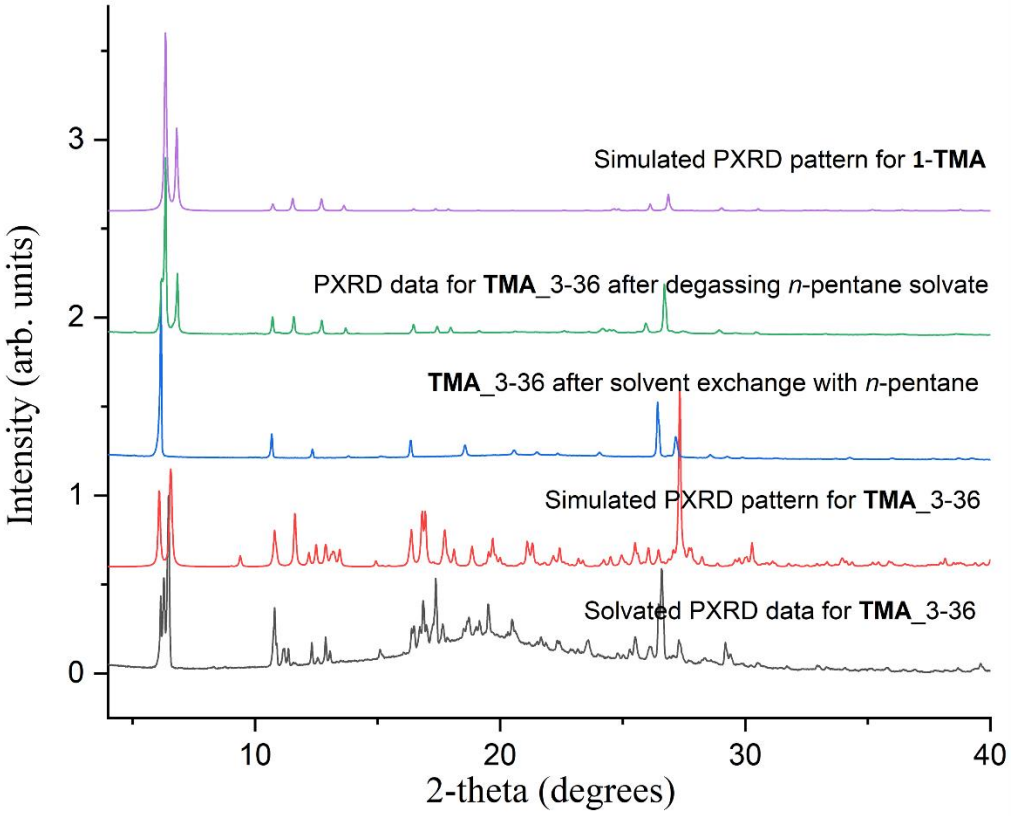

Figure 2.18. PXRD patterns of solvated PXRD data for **TMA**_3-36 (black), simulated PXRD pattern for **TMA**_3-36 (red); after exchanging with *n*-pentane (blue); after degassing the *n*-pentane exchanged sample at room temperature for 2 hrs (green); and the simulated PXRD pattern of the predicted low-density **TMA** phase, **1-TMA** (purple).

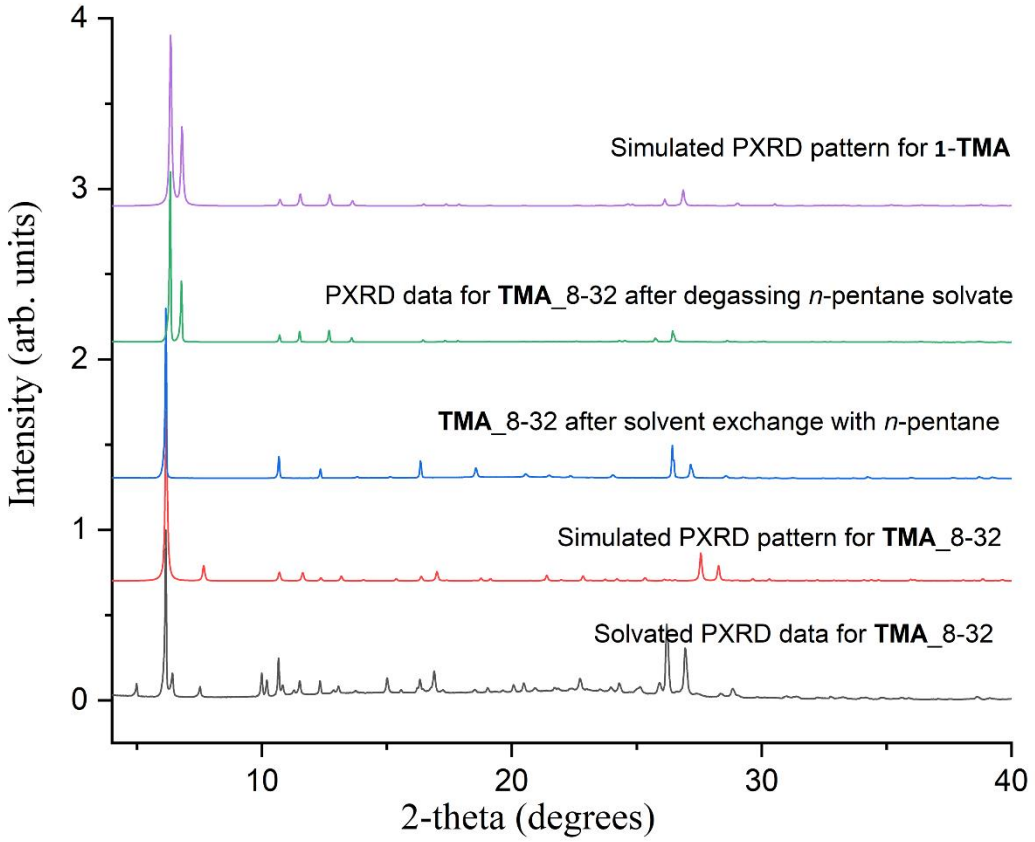

Figure 2.19. PXRD patterns of solvated PXRD data for **TMA**_8-32 (black), simulated PXRD pattern for **TMA**_8-32 (red); after exchanging with *n*-pentane (blue); after degassing the *n*-pentane exchanged sample at room temperature for 2 hrs (green); and the simulated PXRD pattern of the predicted low-density **TMA** phase, **1-TMA** (purple).

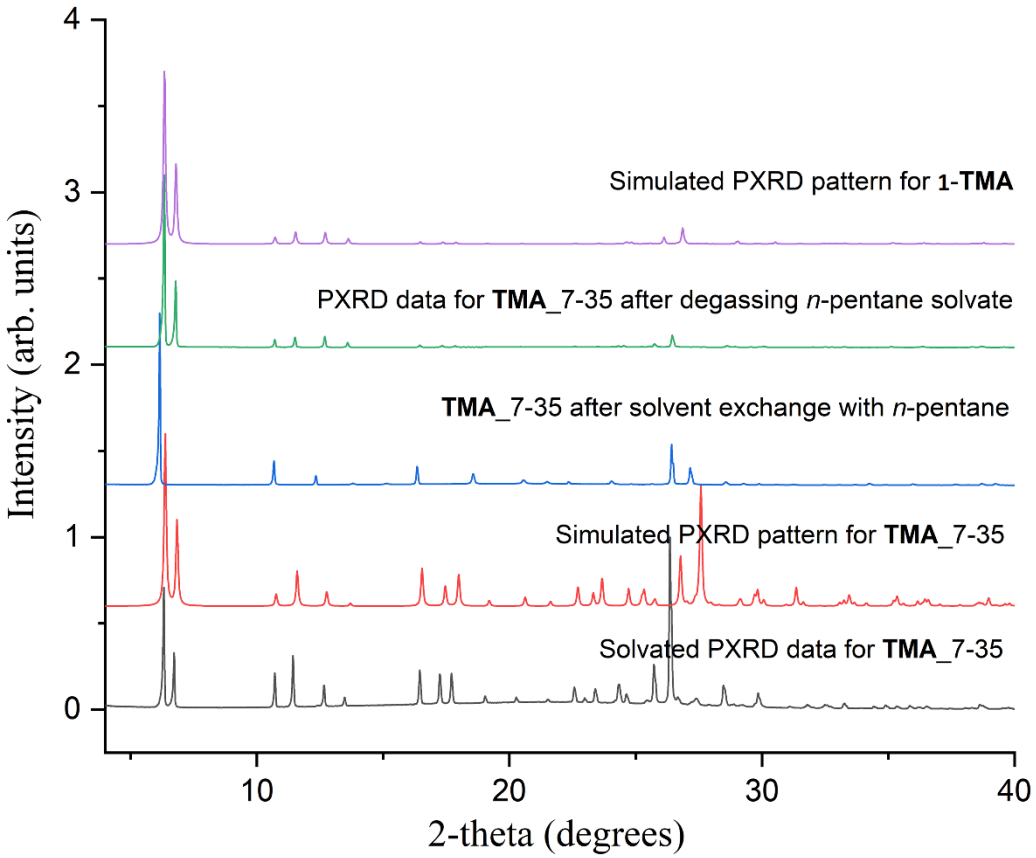

Figure 2.20. PXRD patterns of solvated PXRD data for **TMA**_7-35 (black), simulated PXRD pattern for **TMA**_7-35 (red); after exchanging with *n*-pentane (blue); after degassing the *n*-pentane exchanged sample at room temperature for 2 hrs (green); and the simulated PXRD pattern of the predicted low-density **TMA** phase, **1-TMA** (purple).

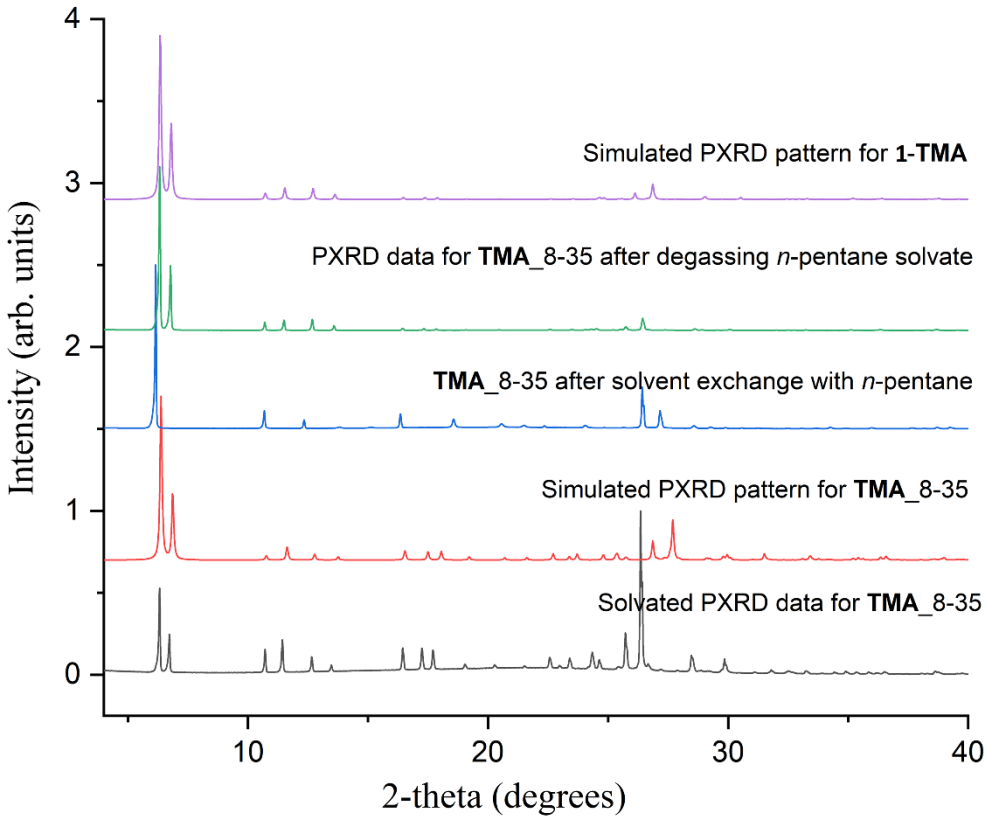

Figure 2.21. PXRD patterns of solvated PXRD data for **TMA**_8-35 (black), simulated PXRD pattern for **TMA**_8-35 (red); after exchanging with *n*-pentane (blue); after degassing the *n*-pentane exchanged sample at room temperature for 2 hrs (green); and the simulated PXRD pattern of the predicted low-density **TMA** phase, **1-TMA** (purple).

*3.3.3 Scale-up, solvent exchange, and activation of **TMA_2-33***

The crystallisation conditions that afforded **TMA**_2-33 were used to scale-up the preparation of the hexagonal **TMA** phase so that properties of the evacuated structure could be investigated. **TMA**_2-33 was simply chosen because large quantities (100s of mg) of crystals could be obtained from THF/*n*-butylbenzene after the solvents were evaporated at RT for 3-4 days. For the scale-up crystallisations, **TMA** (150 mg, 0.7 mmol) was dissolved in THF (10 mL) at room temperature. *n*-Butylbenzene (10 mL) was slowly layered on top of the THF solution through a needle and the solvents were allowed to evaporate at room temperature. After 3 days, crystal had formed in the glass vial (**TMA**_2-33) and the residual solvent was removed via syringe. *n*-Pentane

(20 mL) was added to fully immerse the crystals and the *n*-pentane solvent was exchanged every 12 hours for 5 days. ^{1}H NMR was used to determine the composition of the solvent molecules in the pores in the crystal structure (Figure 2.22). The single signal at 8.64 ppm showed only one type of aromatic proton signal, which proved the *n*-butylbenzene had been removed for the crystal pores. After exchanging the crystallisation solvents with the more volatile *n*-pentane, the crystals were then evacuated under vacuum at RT for two hours to obtain a new polymorph, δ-**TMA** (yield: 92 %).

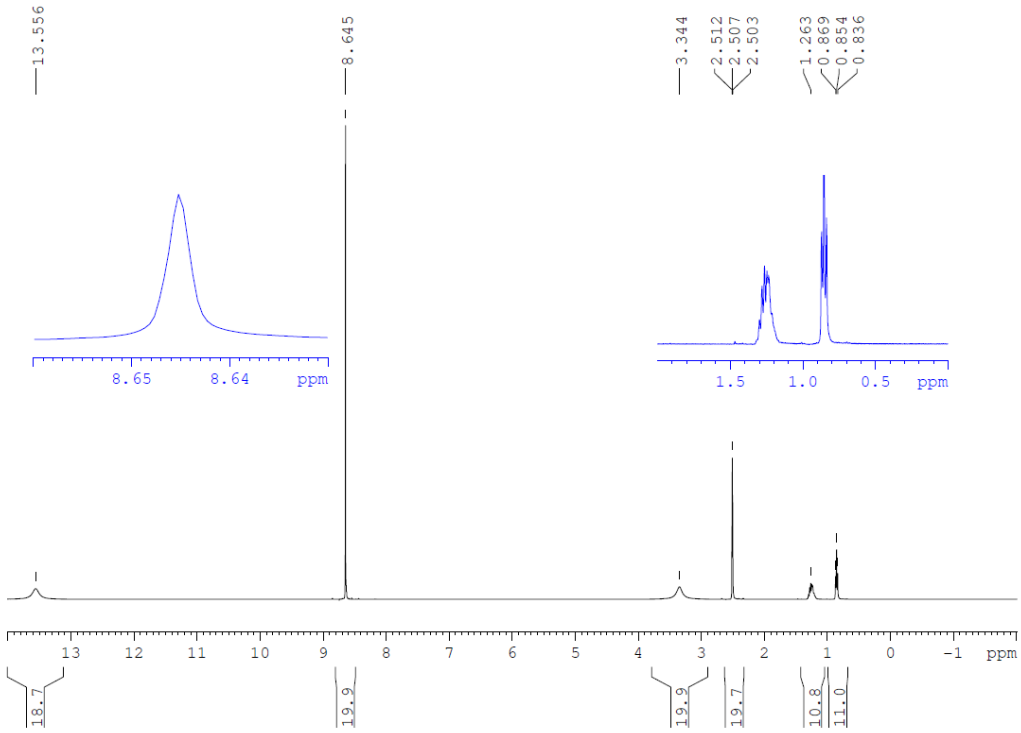

Figure 2.22. ^{1}H NMR spectrum (400 MHz, DMSO-d_6) of δ-**TMA**. The NMR spectra was assigned accordingly, **TMA** [δ (ppm): 8.64 (s, 3H, PhenylH) and 13.5 (s, 3H, COOH)], and *n*-pentane [δ (ppm): 1.26 (-CH_2) and 0.85 (-CH_3)]. The signals at 2.50 and 3.34 ppm are DMSO and H_2O, respectively.

The TGA plot of δ-**TMA**, recorded under a dry nitrogen gas flow after degassing the *n*-pentane exchanged crystals at room temperature for 1 h under dynamic vacuum showed no obvious mass loss before 200 °C. The TGA plot, therefore, indicated that *n*-pentane had been fully removed from the evacuated structure of δ-**TMA** after

activation at RT. The TGA plot also indicated that the material began to thermally decompose at 250 °C and was fully decomposed by 450 °C (Figure 2.23), which is comparable to the TGA plot of the as-received commercially sourced **TMA**.

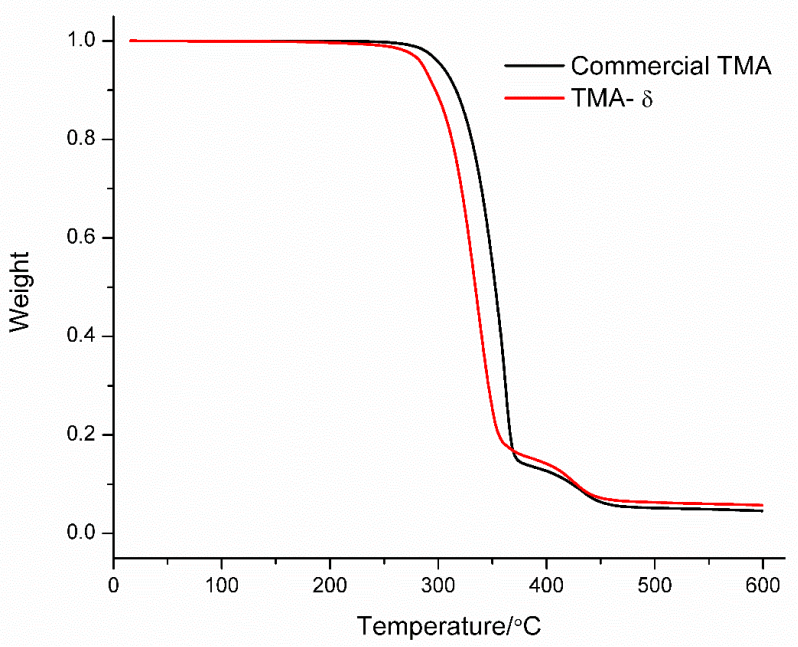

Figure 2.23. TGA plot of δ-**TMA**, recorded under a dry nitrogen gas flow after degassing the *n*-pentane exchanged crystals at room temperature for 1 h under dynamic vacuum (red). The TGA trace for commercially sourced **TMA** is shown in black.

The structure of δ-**TMA** was determined by SCXRD at 200 K, and *in-situ* crystal heating on the same δ-**TMA** crystal was undertaken by heating the crystal from 200 to 350 K and a second single crystal structure was determined at 350 K. δ-**TMA** has monoclinic *C2/m* space group symmetry and its asymmetric unit comprises one complete **TMA**. In the structure of δ-**TMA** recorded at 200 K, one **TMA** molecule formed three $R_2^2(8)$ hydrogen bonding motifs between the three neighboring **TMA** molecules which constructed a continuous honeycomb-like network (Figure 2.24b). The **TMA** molecules are stacked with an 'A-A' packing arrangement at a distance of 3.68 Å along the crystallographic *c* axis. The empty, solvent-accessible space (1.4 Å probe radius, 0.1 Å grid spacing) makes up approximately 27.5% of the unit cell

volume [433.30 Å^3 (V_{cell} = 1573.3 Å^3)]. In the structure of δ-**TMA** recorded at 350 K, δ-**TMA** has the same crystal symmetry and comparable unit cell parameters were determined. There was a small increase (0.07 Å) in the 'A-A' stacking distance between **TMA** molecules along the crystallographic *c* axis and the solvent-accessible space (1.4 Å probe radius, 0.1 Å grid spacing) of approximately 27.8% of the unit cell volume [449.48 Å^3 (V_{cell} = 1614.6 Å^3) was comparable. The slight expansion is likely caused by the 150 K increase in collection temperature, although within error the parameters are very similar.

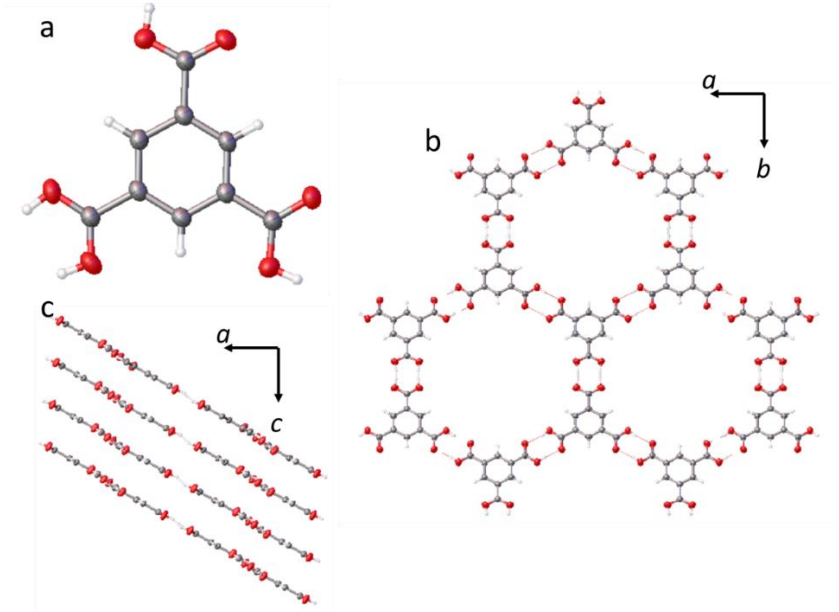

Figure 2.24. a) Displacement ellipsoid plot from the single crystal structure of δ-**TMA** (200 K). Ellipsoids are displayed at 50% probability. Atom labels are omitted for clarity. Grey: carbon; red: oxygen; white: hydrogen. b,c) Crystal packing of δ-**TMA** (200 K) viewed along [001] and [010]. Red: oxygen; grey: carbon; white: hydrogen.

The SCXRD structure of ***δ-TMA*** (200 K)

Crystal data for δ-**TMA** recorded at 200 K: Formula $C_9H_6O_6$, M = 210.14, monoclinic *C2/m*, colourless hexagonal shape crystals; a =26.075(2) Å, b = 16.4837(12) Å, c = 3.6749(3) Å, β = 95.076(2) °; V = 1573.3(2) Å^3; ρ = 0.887 g/cm^3; Z = 4; μ(Mo-Kα) = 0.077 mm^{-1}; F (000) = 432.0; crystal size = 0.15 × 0.14 × 0.09 mm; T = 200 (2) K. 8938 reflections measured (4.94 < 2θ < 53.37 °), 1723 unique (R_{int} = 0.043), 1324 ($I > 2\sigma(I)$); R_1 = 0.0406 for observed and R_1 = 0.0547 for all reflections; wR_2 = 0.1206 for all

reflections; max/min difference electron density = 0.209 and -0.230 e·Å^{-3}; data/restraints/parameters = 1723/0/75; GOF = 1.042; CCDC No. 1915307. For the displacement ellipsoid plot from the crystal structure, see Figure 2.24.

δ-TMA (350 K)

Crystal data for **δ-TMA** recorded at 350 K: Formula $C_9H_6O_6$, M = 210.14, monoclinic *C2/m*, colourless hexagonal shape crystals; a =26.240(5) Å, b = 16.529(3) Å, c = 3.7452(7) Å, β = 96.283(6)°; V = 1614.6(5) Å^3; ρ = 0.864 g/cm^3; Z = 4; μ(Mo-Kα) = 0.075 mm^{-1}; F (000) = 432.0; crystal size = 0.15 × 0.14 × 0.09 mm; T = 350 (2) K. 9783 reflections measured (4.93 < 2θ < 52.94 °), 1731 unique (R_{int} = 0.0397), 1183 ($I > 2\sigma(I)$); R_1 = 0.0423 for observed and R_1 = 0.0622 for all reflections; wR_2 = 0.1342 for all reflections; max/min difference electron density = 0.148 and -0.158 e·Å^{-3}; data/restraints/parameters = 1731/0/75; GOF = 1.020; CCDC No. 1915306. For the displacement ellipsoid plot from the crystal structure, see Figure 2.25.

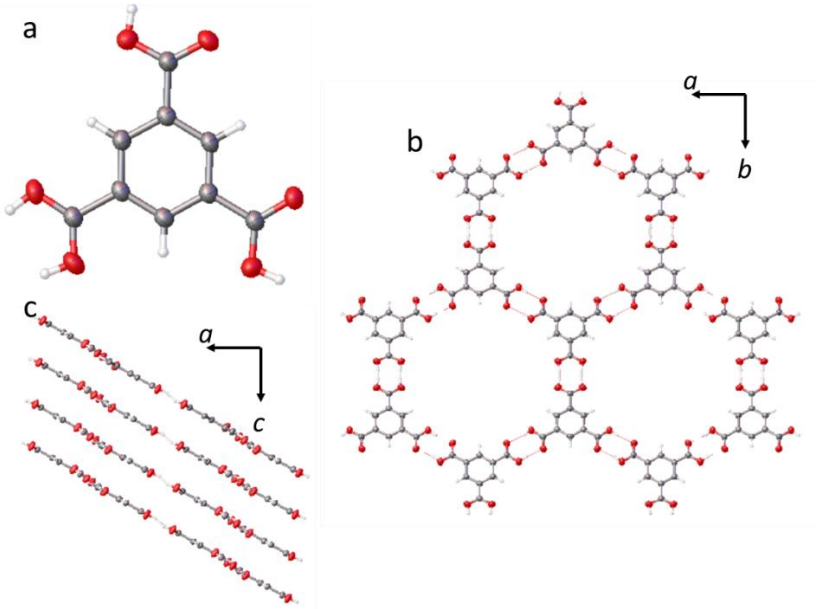

Figure 2.25. a) Displacement ellipsoid plot from the single crystal structure of **δ-TMA** (350 K). Ellipsoids are displayed at 50% probability. Atom labels are omitted for clarity. Grey: carbon; red: oxygen; white: hydrogen. b,c) Crystal packing of **δ-TMA** (350 K) viewing along [001] and [010]. Red: oxygen; grey: carbon; white: hydrogen.

*3.3.4 The stability and porosity of δ-**TMA** phase*

Variable temperature PXRD patterns of δ-**TMA** were recorded after degassing the *n*-pentane exchanged crystals at room temperature for 1 h under a dynamic vacuum to investigate its stability. In the variable temperature PXRD study, PXRD patterns were recorded from 70 °C because SCXRD had proven that δ-**TMA** had the same structure at 77 °C (350 K, Figure 2.25). PXRD patterns were recorded every 20 °C, after equilibrating the sample temperature for 10 minutes at each temperature. From the variable temperature PXRD study, it was found that δ-**TMA** was thermally stable up to 90 °C (Figure 2.26), while higher temperatures PXRD patterns revealed that δ-**TMA** transforms into the α-**TMA**[23] polymorph (Figure 2.26). This solid state transformation indicated that δ-**TMA** is metastable, as often observed for porous molecular crystals with low densities.

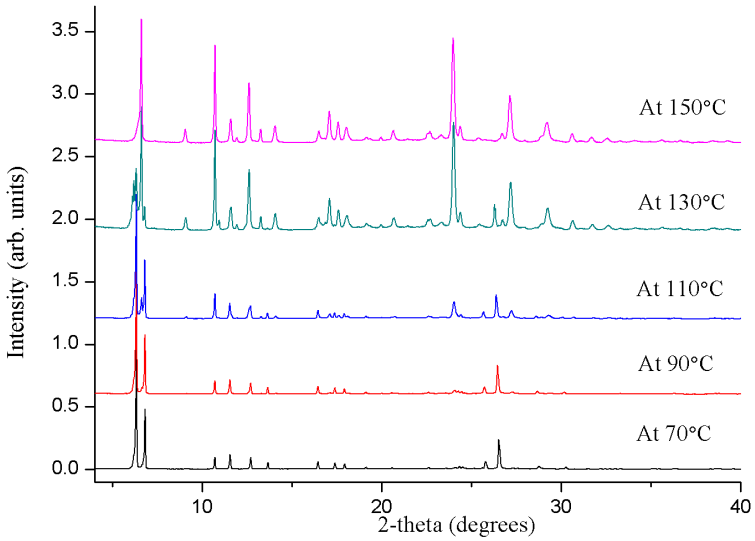

Figure 2.26. Variable temperature PXRD patterns that were recorded on an activated δ-**TMA** sample over the temperature range 70-150 °C. At 110 °C the δ-**TMA** structure was found to start to transform to the α- **TMA** polymorph.

A similar structural transformation was observed after subjecting δ-**TMA** to 6 hours under dynamic vacuum at room temperature (Figure 2.27), or after standing an activated sample in humid air for 13 hours (Figure 2.28), indicating that the phase transformation was not only thermally induced, although the temperature did appear

to increase the rate at which δ-**TMA** transformed into α-**TMA** (10 minutes at 130 °C *versus* 780 minutes at RT, Figure 2.26, 2.28).

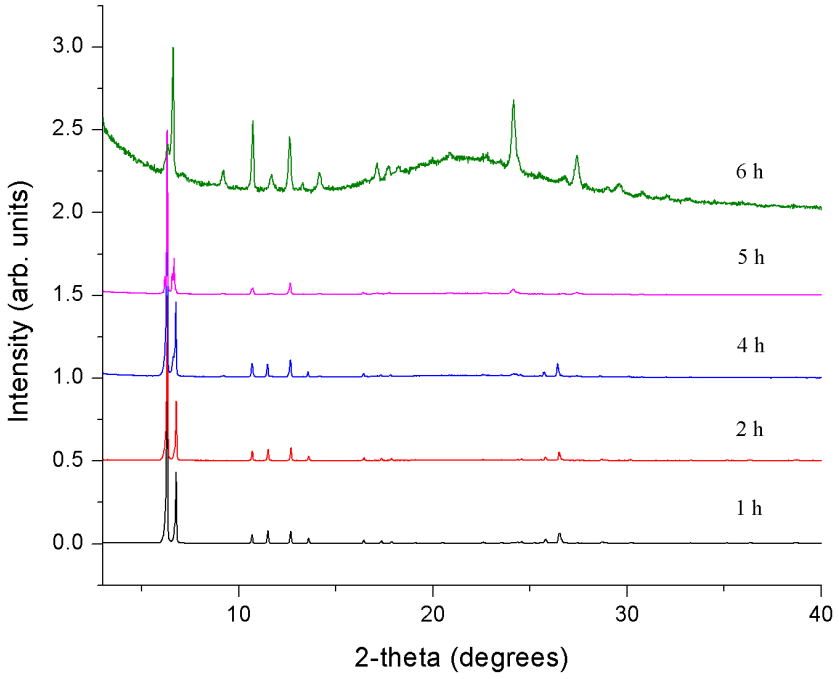

Figure 2.27. PXRD patterns for δ-**TMA**, recorded after degassing the sample under dynamic vacuum for between 1-6 h, at room temperature.

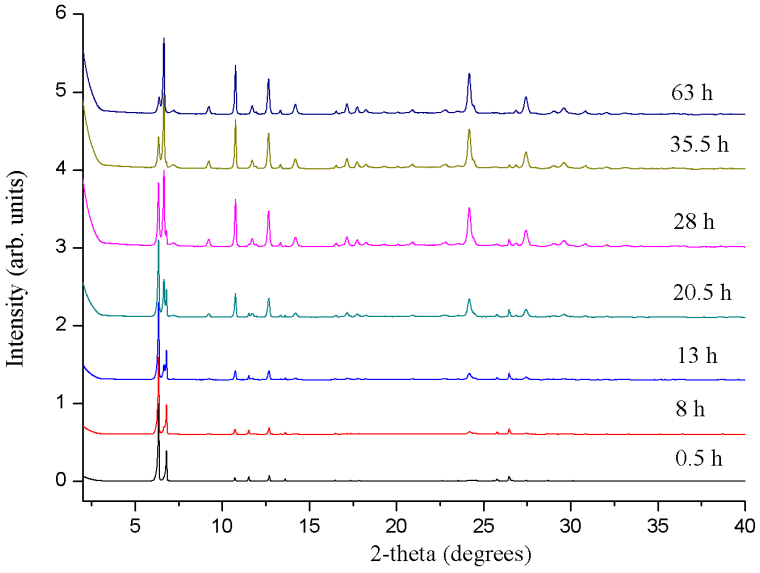

Figure 2.28. PXRD patterns for δ-**TMA**, recorded after standing the activated material in humid air at room temperature.

Based on PXRD data collected during the variable temperature studies and after

activating δ-**TMA**, we used the following condition to activate δ-**TMA** before determining its gas adsorption properties: 2 hrs dynamic vacuum at RT. From the N_2 sorption isotherms of δ-**TMA**, we found that δ-**TMA** is porous to nitrogen and has a SA_{BET} of 910 m^2 g^{-1} at 77.3 K (Figure 2.29). However, the PXRD pattern recorded after gas sorption analysis indicated that there was a small amount of the non-porous α-**TMA** polymorph in the sample (Figure 2.30).

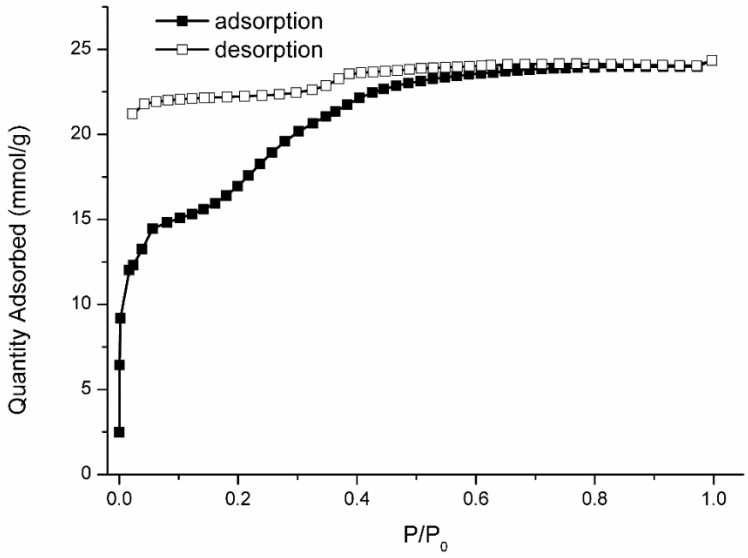

Figure 2.29. N_2 gas sorption isotherm for δ-**TMA** recorded at 77.3 K.

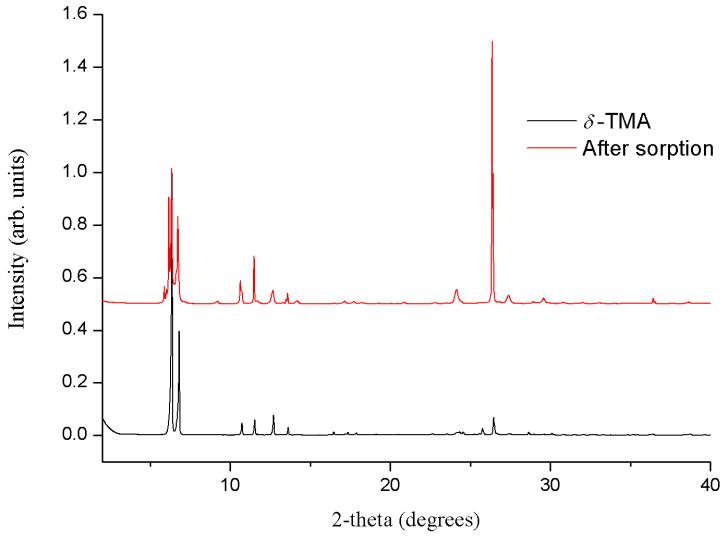

Figure 2.30. PXRD patterns of δ-**TMA** recorded before and after N_2 adsorption and desorption cycles. PXRD data collected post gas sorption analysis indicated that there was some of the α-**TMA** polymorph present in the sample.

*3.3.5 Comparison of δ-**TMA** phase with CSP results*

The experimental PXRD pattern of the activated δ-**TMA** material (red) was compared to the simulated PXRD pattern of the CSP structure **1-TMA** (blue), which revealed there to be a very close structural match (Figure 2.31a). A visual comparison between 15 molecules in these structures was also performed using Mercury CSD-Materials. In the structure comparison, only non-hydrogen atoms were included and a loose geometric tolerance (± 20 % in distance tolerance; ± 20 degrees in angle tolerance) was executed. The overlay of the predicted polymorph, **1-TMA** (blue) and the experimental δ-**TMA** structure (red) reveal the close structural match between these structures (Figure 2.31b), which was also found by comparing their unit cell parameters (Table 2.3).

Table 2.3. The cell parameters of predicted structure **1-TMA** (pred.) and experimental (expt.) δ-**TMA**.

	Space Group	***a*** **/Å**	***b*** **/Å**	***c*** **/Å**	***β*** **/°**	***V*** **/Å^3**
Pred.	*C*2/*m*	26.27	16.92	3.72	93.87	1651.8
Expt.	*C*2/*m*	26.08	16.48	3.68	95.08	1573.3

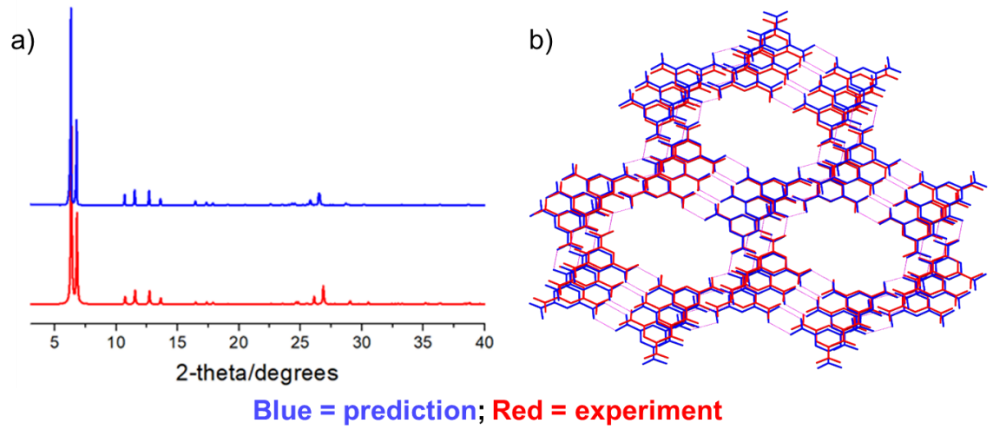

Figure 2.31. a) Comparison between predicted (**1-TMA)** and experimental (δ-**TMA**) PXRD patterns (the predicted structure is shown as **1-TMA** in Figure 2.5b); b) overlay of the predicted **1-TMA** (blue) and the experimental δ-**TMA** (red) structures. The experimental structure was determined after solvent exchange followed by activation of **TMA**_2-33.

*3.4 HT screening results of **ADTA***

Encouraged by the successful discovery of the porous δ-**TMA**, we applied CSP to explore if new crystal structures of another prototypical molecule, **ADTA**, could be discovered using the same workflow. The previously reported and non-porous crystal structure of **ADTA** features diamondoid nets of **ADTA** molecules that hydrogen-bonded together though $R_2^2(8)$ motifs between the carboxylic acid groups. Close packing of the diamondoid nets is then achieved via 5-fold interpenetration in the extended crystal structure (Figure 2.1, 2.3).

*3.4.1 Crystal structure prediction (CSP) of **ADTA***

For **ADTA**, six conformers were chosen for the CSP calculations (Figure 2.32). **ADTA2** was the lowest energy conformer, with the relative energies for **ADTA1**, **ADTA3**, **ADTA4**, **ADTA5**, and **ADTA6** found to be 2.77, 0.35, 1.76, 2.05, and 2.40 kJ/mol higher in energy, respectively. The only significant difference between **ADTA** conformers were the rotation angles of the carboxylic acid groups (Figure 2.32), which could lead to changes in the symmetry of the predicted hydrogen bonded networks or lead to these networks being distorted (Figure 2.1d). The six predicted conformers were therefore included in the CSP calculations.

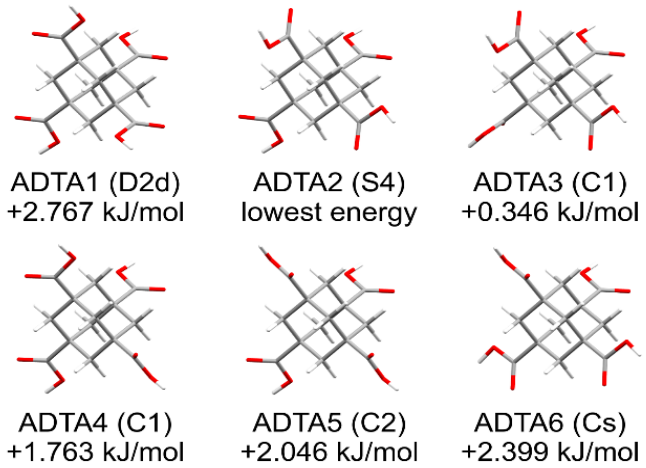

Figure 2.32. Conformers of **ADTA**. Points groups of all conformers are given in parentheses and calculated energies relative to the lowest energy conformer in the gas phase. Red: oxygen, grey: carbon, white: hydrogen.

The CSP map of **ADTA** is shown in Figure 2.33 and is colour coded to highlight structures with different numbers of unique hydrogen-bond networks that are interpenetrated in their extended crystal structures (Figure 2.3). All predicted **ADTA** crystal structures were analysed according to their hydrogen-bonded networks and degree(s) of interpenetration of these lattices within each crystal structure. This classification was performed by expanding a cluster of molecules consisting of all hydrogen-bonded molecules to each molecule in the unit cell and neighbouring cells, then repeating this process on the cluster 4 times. The resulting connectivity graph consisting of covalent and hydrogen bonds was then analysed for subgraphs (or connected components), with the number of these distinct subgraphs which passed through the unit cell providing the degree of lattice interpenetration. While most of the predicted structures have energy-density distributions that lie within the bulk of the predicted structures, the most stable predicted structures for each degree of interpenetration, from 5-fold (ρ = 1.57 g/cm^3) down to 2-fold (ρ = 0.324 g/cm^3) interpenetration, lie just below the low-energy 'leading edge' of the energy-density distribution. These low-lying predicted structures correspond to the lowest energy predicted structure of each level of interpenetration and are found at approximately equally-spaced intervals of density and they lose, on average, around 20 kJ/mol of lattice energy per lost degree of interpenetration of the hydrogen bonding networks (Figure 2.33). The energetic stability of these diamondoid hydrogen-bonded structures relative to other crystal packing arrangements is not as pronounced as the 'spike' of structures containing the new δ-polymorph, **1-TMA**, on the **TMA** landscape (Figure 2.5a). However, the $R_2^2(8)$ hydrogen-bonding motif provides greater stability than any other hypothetical crystal packing of similar density in the cases of 3-fold, 4-fold, and 5-fold interpenetration.

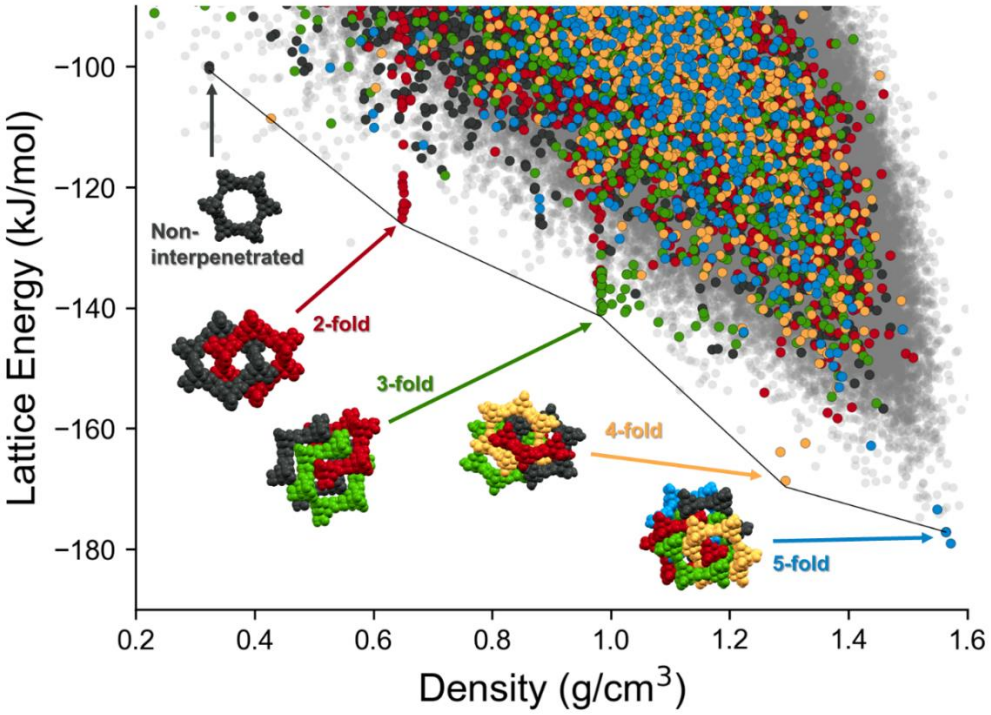

Figure 2.33. CSP landscape for **ADTA**. The different colours highlight the number of unique hydrogen-bond networks interpenetrated within each structure, blue: 5-fold; yellow: 4-fold; green: 3-fold; red: 2-fold interpenetrated. Light grey dots show structures that do not contain the diamondoid hydrogen bonding.

The predicted 4-fold interpenetrated structure is particularly stable, being located just 10.4 kJ/mol above the global minimum predicted 5-fold interpenetrated structure (and 4.8 kJ/mol above the known 5-fold crystal structure). The energy difference between known 5-fold structure and predicted structure is due to different condition which the known 5-fold structure was obtained at atmospheric pressure and the predicted structure was calculated at absolute vacuum. This falls within the usual energetic range of polymorphism in organic crystals[18,22], and the predicted structure should be accessible under the right crystallisation condition. A large number of predicted structures with 3-fold interpenetrated diamondoid hydrogen-bonded networks are found in the region around 1 g/cm^3 (cluster of green points in Figure 2.33). The many possibilities for 3-fold interpenetration, compared to higher degrees of interpenetration, can be rationalised by the number of available permutations for arriving at 3-fold interpenetrated structures by the removal of 2 networks from the 5-fold interpenetrated

structure. The relative positions of three diamondoid nets in the 3-fold interpenetrated structure also vary the number of possibilities available.

A non-interpenetrated diamondoid crystal structure was also found among the predicted structures, along the same roughly linear energy-density relationship as the lowest energy 2-fold, 3-fold, 4-fold and 5-fold interpenetrated forms. The non-interpenetrated structure was predicted to be 78.6 kJ/mol above the global minimum 5-fold network and had a density of 0.324 g/cm^3, in excellent agreement with the structure hypothesised by Ermer[35]. However, the CSP results show that, at such low densities, there are many energetically preferable structures with similar densities that feature different hydrogen-bonded networks. The presence of alternative, lower energy structures in this density region suggests that the non-interpenetrated structure is too unstable, so is unlikely to be observed. Moreover, even if it could be formed as a solvated structure, its position on the CSP landscape suggests that it might not occupy a sufficiently deep, isolated energy basin to be kinetically stable as an unsolvated structure.

*3.4.2 **ADTA** solubility test*

To determine the solubility of **ADTA** in the organic solvent library we used the following procedure: Initially, 1 mL of organic solvent was added to **ADTA** (~ 3 mg) at room temperature. If the **ADTA** was fully dissolved, more **ADTA** was added in ~ 1 mg portions and the total amount of **ADTA** added to the vial was recorded. The solubility of **ADTA** in each solvent was calculated in terms of mg/mL. The organic solvents which dissolved ≥ 3 mg/mL of **ADTA** and had boiling points < 120 °C, were chosen as good solvents for the crystallisation screen. The order of increased solubility of **ADTA** was: Methanol > THF, ethanol > 1,4-dioxane > 2-propanol > 1-propanol. The six ‘good solvents’; methanol, THF, ethanol, 1,4-dioxane, 2-propanol, 1-propanol, were used to prepare 3 mg/mL stock solutions of **ADTA** for the HT crystallisation screen. All of the solvents, which did not dissolve **ADTA** at a concentration ≥ 3 mg/mL, were used as anti-solvents (bad solvents) for the HT crystallisation experiment.

3.4.3 HT crystallisation screen

Stock solutions of **ADTA** (0.3 g, 0.96 mmol) in an organic solvent (100 mL), were prepared in each of the six good solvents at room temperature. For each crystallisation, a 2 mL portion of the **ADTA** stock solution was transferred into 38 different sample vials, loaded in racks on the Chemspeed platform at room temperature. A 2 mL portion of the 38 other solvents listed in Table 2 were then added into these vials to form 37 1:1 (*vol*:*vol*) binary solvent crystallisations, and 1 single 'good-solvent' crystallisation. The process was repeated for all five other 'good solvent' stock solutions. After mixing, the solvents were evaporated at room temperature over several days or weeks, resulting in **ADTA** crystallising in the vials. Using the predicted 3-, 4-, and 5- fold structures as a reference along with experimental PXRD data (Figure 2.34), 5 sets of conditions were found to lead to new **ADTA** crystal forms with 3-fold interpenetrated diamondoid hydrogen-bonded networks, 81 conditions led to 4-fold interpenetration, and 77 conditions led to 5-fold interpenetration. 22 conditions were also identified that appeared to give a phase mixture of 4- and 5-fold interpenetrated structures. The remaining conditions produced two amorphous samples, and 41 structures that could not be identified as one, or a mixture, of the 3-, 4-, or 5-fold structures by simply comparing PXRD patterns (Figure 2.35).

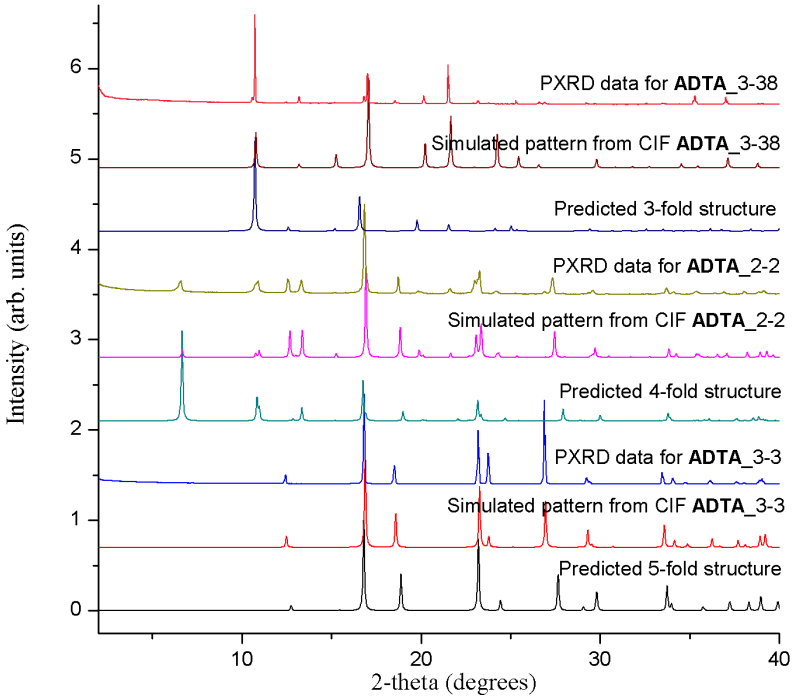

Figure 2.34. Experimental PXRD data from the HT crystallisation screen for **ADTA**_3-38, **ADTA**_2-2, and **ADTA**_3-3 *vs.* the simulated PXRD patterns for the predicted 3-, 4-, and 5-fold **ADTA** structures, and the simulated PXRD patterns for single-crystal structures **ADTA**_3-38 (3-fold), **ADTA**_2-2 (4-fold), and **ADTA**_3-3 (5-fold).

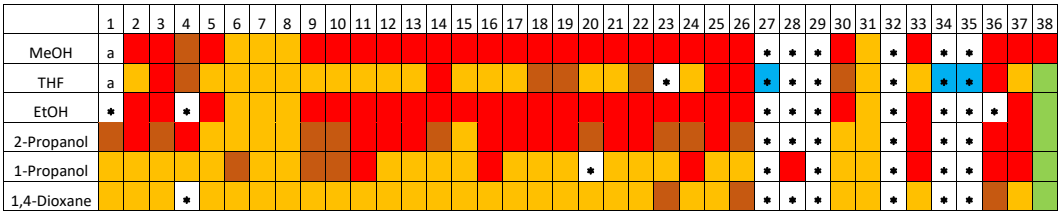

Figure 2.35. PXRD pattern map for **ADTA** from 228 crystallisation conditions. Red: 5-fold; maroon: 4/5-fold mixture; orange: 4-fold; green: 3-fold; and a: amorphous phase. The 41 conditions that could not be identified are starred. Of these 41 conditions, we determined that 3 had formed 2-fold structures by SCXRD (blue). The solvents 1-38 are numbered in Table 2.2.

*3.4.4 Single crystal structures of **ADTA***

*3.4.4.1 4-fold interpenetrated **ADTA (ADTA_2-2)***

ADTA_2-2 crystallised from THF solution in the tetragonal space group $I4_1/a$. The asymmetric unit in **ADTA**_2-2 comprises one complete **ADTA** molecule and disordered solvent that was modelled as ¼ of a THF molecule, $0.25(C_4H_8O)$ (Figure 2.36a). As a non-planar five-membered ring THF is conformationally flexible and it was found to be disordered over two positions in the crystal structure which are shown in Figure 2.37. In the extended structure, one **ADTA** molecule forms four $R_2^2(8)$ hydrogen bonding motifs to four neighboring **ADTA** molecules, which generates a continuous diamondoid network (Figure 2.36b). The diamondoid nets are then interpenetrated form a 4-fold interpenetrated structure with the disordered THF molecules trapped in small cavities between the **ADTA** molecules (Figure 2.36b). To show the packing more clearly, the four interpenetrated nets in **ADTA**_2-2 are shown in different colours in Figure 2.36d.

Crystal data for **ADTA**_2-2 (100 K): Formula $C_{14}H_{16}O_8 \cdot 0.25(C_4H_8O)$; M = 330.29, tetragonal $I4_1/a$, colourless block shape crystals; $a = b$ = 16.4008(15) Å, c = 22.397(2) Å; V = 6024.5(13) Å^3; ρ = 1.457 g/cm^3; Z = 16; μ(Mo-Kα) = 0.120 mm^{-1}; F (000) = 2784; crystal size = 0.12 × 0.12 × 0.11 mm; T = 100 (2) K. 40618 reflections measured ($4.97 < 2\theta < 58.27$ °), 4055 unique (R_{int} = 0.0493), 4055 ($I > 2\sigma(I)$); R_1 = 0.0549 for observed and R_1 = 0.0686 for all reflections; wR_2 = 0.1635 for all reflections; max/min difference electron density = 0.485 and -0.271 e·Å^{-3}; data/restraints/parameters = 4055/14/238; GOF = 1.135; CCDC No. 1915301.

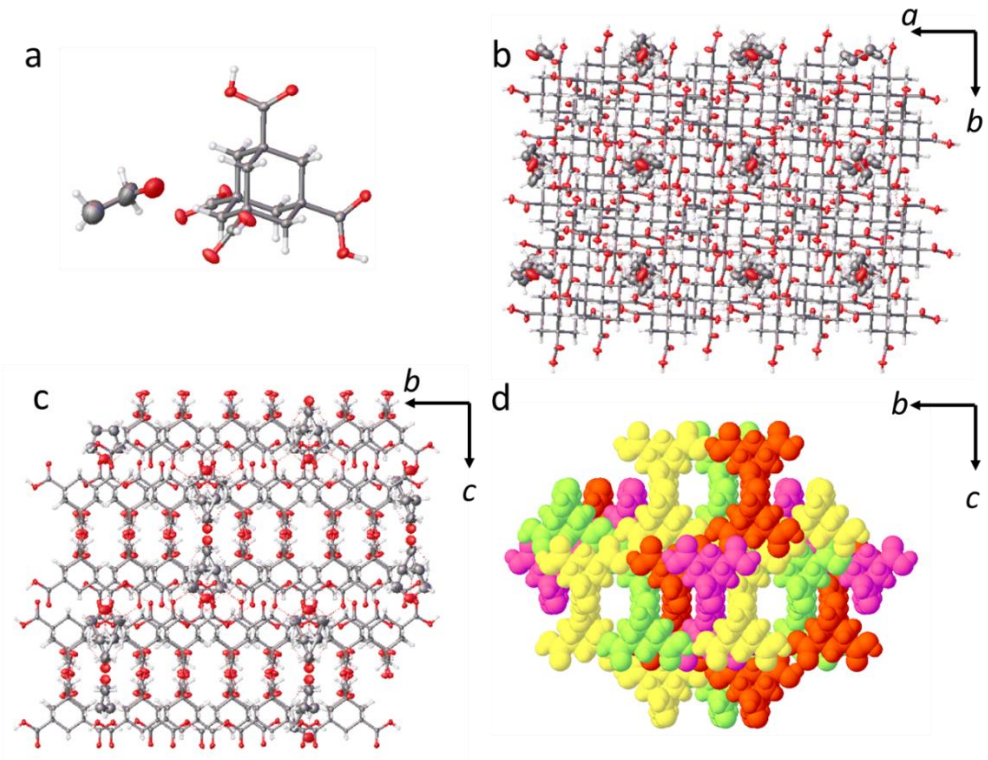

Figure 2.36. a) Displacement ellipsoid plot from the single crystal structure of **ADTA**_2-2. Each THF molecule was modelled a with 50% occupancy, ellipsoids are displayed at 50% probability. Atom labels are omitted for clarity. Grey: carbon; red: oxygen; white: hydrogen. Crystal packing of **ADTA**_2-2 viewed along [001] (b) and [100] (c). d) 4-fold interpenetrated **ADTA**_2-2 coloured with different diamondoid lattices. Red: oxygen; grey: carbon; white: hydrogen.

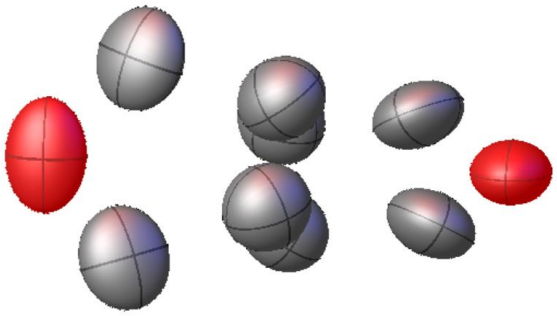

Figure 2.37. Displacement ellipsoid plot of disordered THF from the single crystal structure of **ADTA**_2-2. Each THF molecule was modelled with 50% occupancy, ellipsoids are displayed at 50% probability. Hydrogen atoms are omitted for clarity. Red: oxygen; grey: carbon.

The arrangement of **ADTA** molecules in **ADTA**_2-2 was compared to the 4-fold CSP structure that had the lowest predicted lattice energy. From the structure comparison, a root mean squared deviation (RMSD) in atomic positions of 0.28 Å was found for a cluster of 20 molecules, which was performed using Mercury CSD-Materials. In the structure comparison, only non-hydrogen atoms were included and a loose geometric tolerance (± 20 % in distance tolerance; ± 20 degrees in angle tolerance) was executed. It indicated that the observed and predicted crystal structures were closely matched. The structural overlay that is shown in Figure 2. 38 also shows the close match between **ADTA**_2-2 with the lowest energy 4-fold interpenetrated structure from the CSP calculations (Figure 2.38).

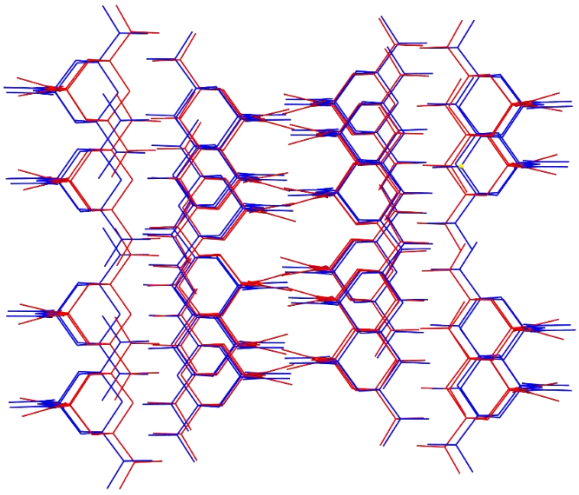

Figure 2.38. Comparison between predicted and experimental **ADTA**_2-2 4-fold interpenetrated structures, blue: prediction; red: experiment. Solvent molecules in the experimental 4-fold interpenetrated structures are hidden.

From the SCXRD, it appeared that the disordered THF molecules were trapped in the extrinsic cavities in **ADTA**_2-2 (Figure 2.36b). Attempts were therefore made to remove the THF solvent to determine the stability of the solvent-free structure. After **ADTA**_2-2 was crystallised from THF, *n*-pentane (20 mL) was added to the crystallisation in an attempt to exchange the THF solvent. A similar process to that used for the hexagonal **TMA** systems was used, with the *n*-pentane solvent being

exchanged every 12 hours for 5 days. Afterward, the PXRD pattern of the crystals that had been immersed in *n*-pentane, **ADTA**_2-2_pentane, was recorded (blue, Figure 2.39). However, the resulting PXRD pattern showed no obvious structural change compared to **ADTA**_2-2 (pink, Figure 2.39) and the SCXRD structure of **ADTA**_2-2-pentane showed that the THF molecules were still trapped in the 4-fold **ADTA** structure (Figure 2.36).

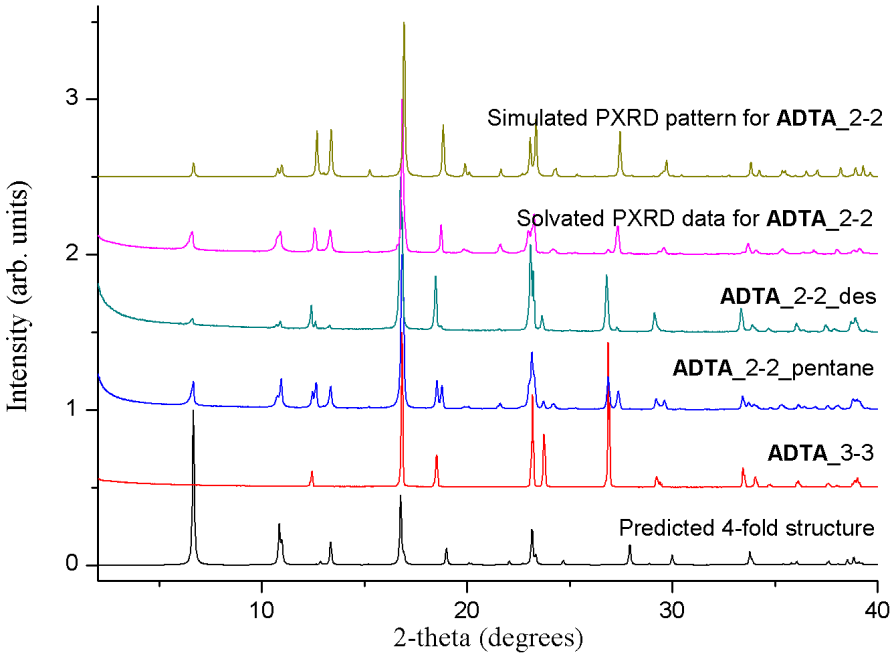

Figure 2.39. PXRD patterns of simulated from predicted 4-fold structure (black); simulated PXRD pattern of the experimental 5-fold structure **ADTA**_3-3 (red); experimental PXRD pattern for **ADTA**_2-2 that was recorded after attempting to exchanging the crystallisation solvent with *n*-pentane (blue); experimental PXRD pattern recorded after attempting to desolvate it at 100 °C under dynamic vacuum (**ADTA**_2-2_des, cyan); experimental PXRD data of solvated **ADTA**_2-2 (pink), simulated PXRD pattern from the single crystal structure, **ADTA**_2-2 recorded at 100 K (green).

Attempts were also made to thermally desolvate **ADTA**_2-2. Initially, **ADTA**_2-2 was heated at 100 °C under a dynamic vacuum. The resulting PXRD pattern did not show any obvious structural change (**ADTA**_2-2_des, cyan, Figure 2.39). A TGA plot recorded under a dry nitrogen gas flow showed that **ADTA**_2-2 did not start to lose

mass loss until ~ 210 °C (Figure 2.40). After heating **ADTA**_2-2 at 175 °C, the samples can still keep good crystallinity and the SCXRD showed a same structure with **ADTA**_2-2 and THF was still trapped in the structure. To ensure removal of THF solvent from the 4-fold structure, a sample of **ADTA**_2-2 was therefore heated at 210 °C for 2.5 h and NMR was then used to confirm there was no THF left in the sample (Figure 2.41). A DSC plot was recorded after desolvating **ADTA**_2-2 at 210 °C for 2.5 hrs and showed no obvious phase changes during the heating and cooling cycles (Figure 2.42). While the PXRD pattern of the sample after heating at 210 °C for 2.5 hrs is similar to the simulated PXRD pattern of **ADTA**_2-2 (Figure 2.43), structural changes were monitored in a subsequent variable temperature PXRD study (Figure 2.44). The variable temperature PXRD was performed on THF solvated **ADTA**_2-2 and showed a gradual transformation into the 5-fold interpenetrated structure at high temperature and that this transformation was complete at 350 °C, albeit with a small loss of crystallinity. The sample started to lose more crystallinity above 350 °C and it is caused by the decomposition of structure.

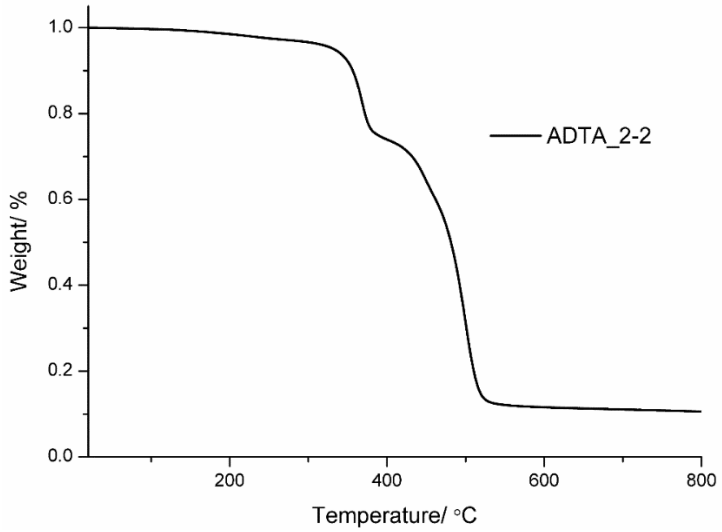

Figure 2.40. TGA plot for **ADTA**_2-2, recorded after degassing the sample at 100 °C for 10 hrs.

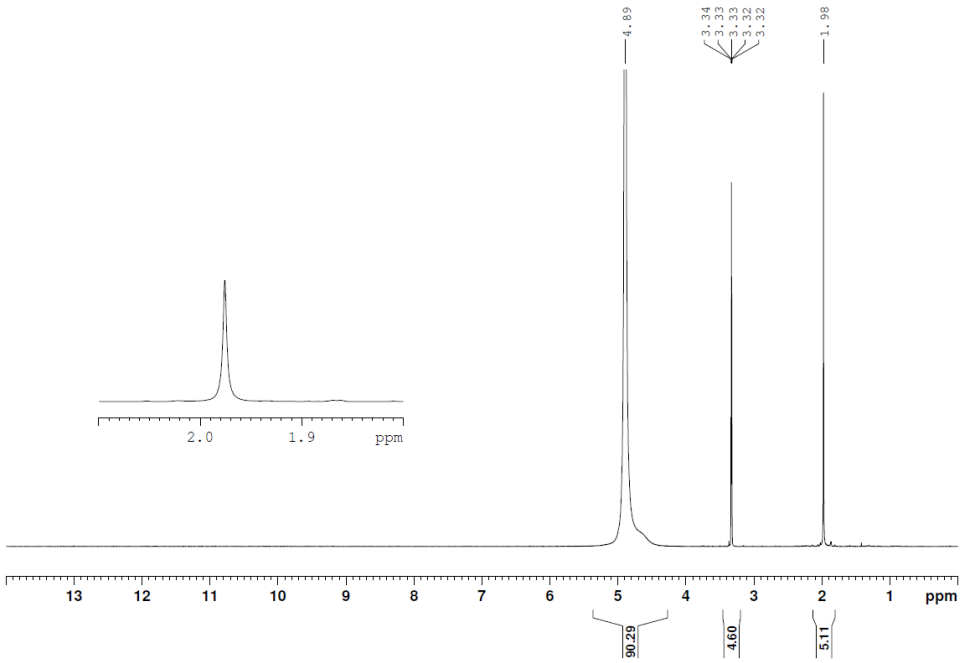

Figure 2.41. ^{1}H NMR spectrum (400 MHz, CD_3OD-d_4) of desolvated **ADTA**_2-2. **ADTA** [δ (ppm.) 1.98 (-CH_2)]. The signals at 3.33 and 4.89 ppm are CD_3OD and H_2O, respectively.

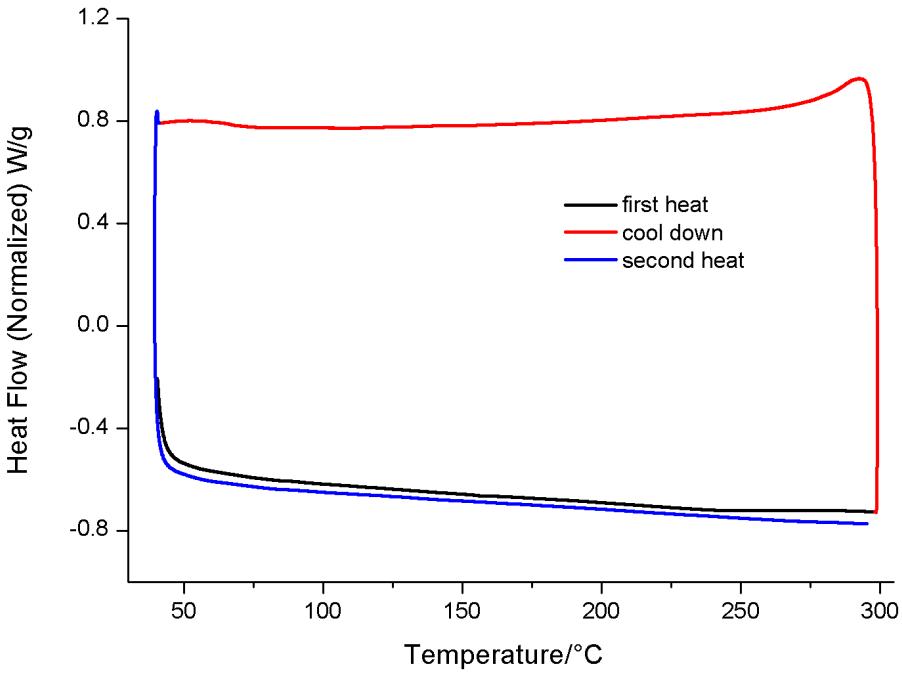

Figure 2.42. DSC plot of desolvated **ADTA**_2-2, recorded after heating crystalline materials of the THF solvate at 210 °C for 2.5 hrs.

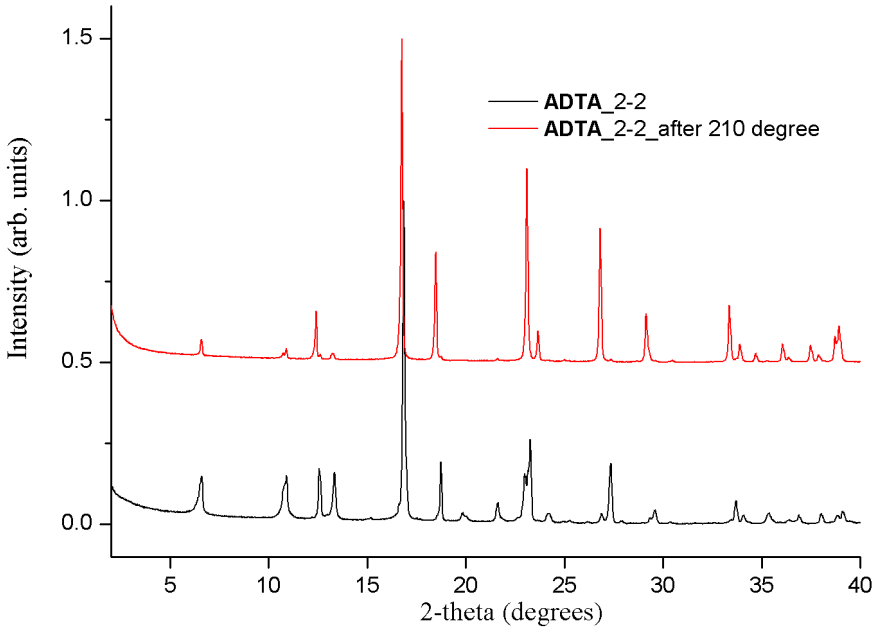

Figure 2.43. PXRD patterns for solvated **ADTA**_2-2 (black), and after heating **ADTA**_2-2 at 210 °C for 2.5 hrs. (red).

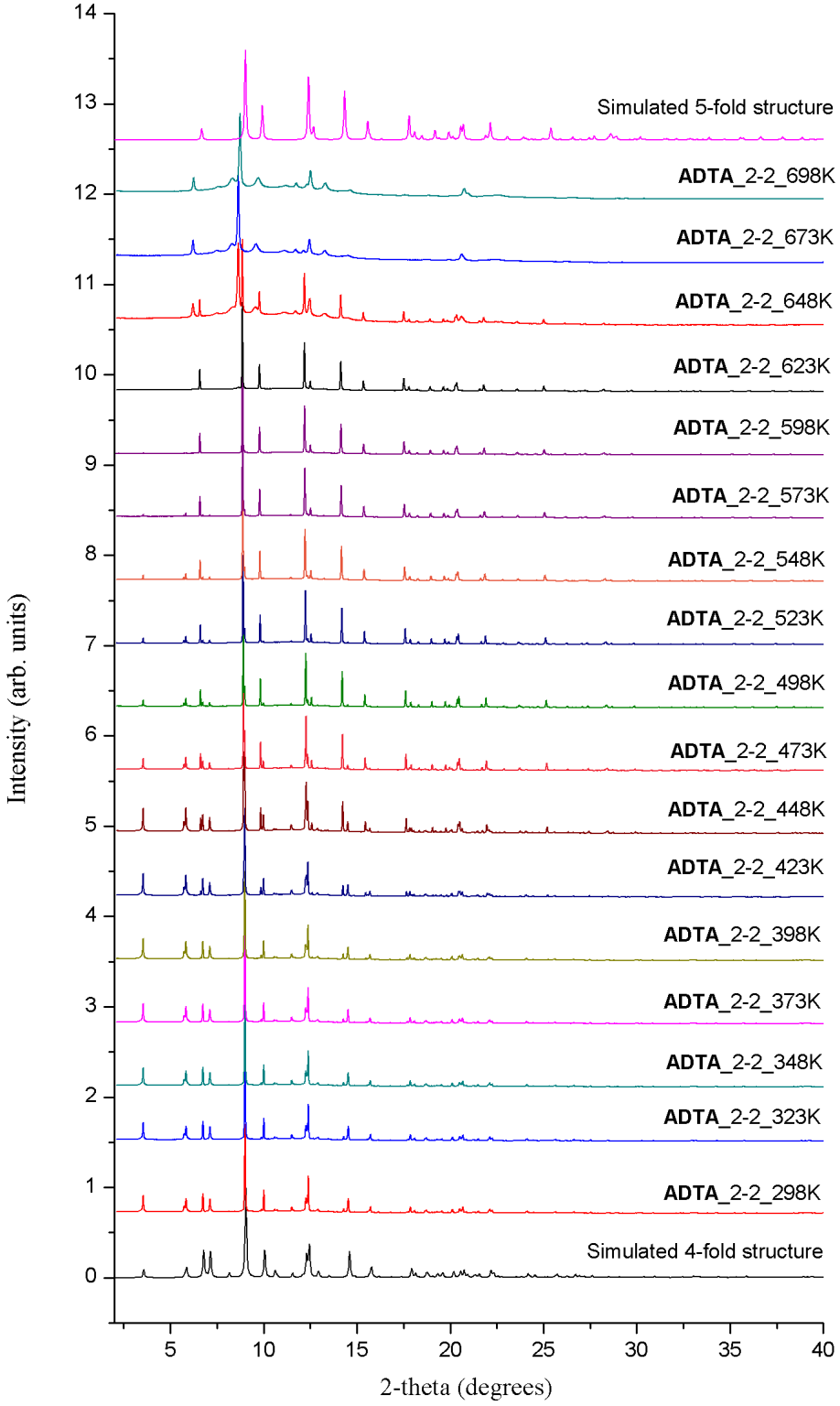

Figure 2.44. Variable temperature PXRD patterns for **ADTA**_2-2, recorded over the temperature range of 298–698 K. (λ = 0.825186 Å). PXRD patterns were recorded every 25 K, after equilibrating the sample at each temperature for 15 minutes.

*3.4.4.2 3-fold interpenetrated **ADTA***

The 3-fold structure was only clearly observed in the crystallisation screen when tetradecane was used as the anti-solvent (Figure 2.45). We characterised the 3-fold structure using the ethanol/tetradecane (**ADTA**_3-38) and dioxane/tetradecane (**ADTA**_7-38) crystallisation condition. In both 3-fold structures, disordered tetradecane solvent was found to occupy 1-D pores, rationalising the formation of the 3-fold structure with tetradecane in both instances, but we observed slight differences in crystallographic symmetry of the structures; *Fddd* for **ADTA**_3-38 *vs. I*4$_1$/*amd* for **ADTA**_7-38. This finding can also be explained by the tetradecane solvent, which appeared to be more ordered in the *Fddd* **ADTA**_3-38 structure and distorted the interpenetrated packing of diamondoid networks (Figure 2.45e, 2.46e).

ADTA_3-38

ADTA_3-38 crystallised from an ethanol and tetradecane solution in the orthorhombic space group *Fddd*. The asymmetric unit of **ADTA**_3-38 comprises one complete **ADTA** and disordered tetradecane solvent, 0.43($C_{14}H_{30}$) (Figure 2.45a). In the structure, one **ADTA** molecule forms four $R_2^2(8)$ hydrogen bonding motifs to four neighboring **ADTA** molecules to generate a continuous diamondoid network (Figure 2.45b, c). In the extended packing, the diamondoid nets are distorted, which creates an ~0.6 Å difference between the *b* and *c* unit cell dimensions. The **ADTA** nets are also interpenetrated to generate a 3-fold structure with 1-D channels running along the crystallographic *c* axis. Disordered tetradecane molecules were packed in the one-dimensional channels (Figure 2.45b) and their long alkyl chains are likely to have played an important role in the formation of the experimentally observed 3-fold structure (Figure 2.35), even though the methyl group positions could not be determined crystallographically (Figure 2.45e).

Crystal data for **ADTA**_3-38 (100 K): Formula $C_{14}H_{16}O_8 \cdot 0.43(C_{14}H_{30})$; M = 397.29, monoclinic *Fddd*, colourless block shape crystals; a =7.3713(11) Å, b = 22.951(4) Å, c = 23.585(4) Å; V = 3990.0(11) Å^3; ρ = 1.323 g/cm^3; Z = 8; μ(Mo-Kα) = 0.102 mm^{-1}; F (000) = 1703; crystal size = 0.11 × 0.08 × 0.05 mm; T = 100 (2) K. 8009 reflections measured (4.95 < 2θ < 52.75 °), 1028 unique (R_{int} = 0.0818), 628 ($I > 2\sigma(I)$); R_1 =

0.0634 for observed and R_1 = 0.1034 for all reflections; wR_2 = 0.2143 for all reflections; max/min difference electron density = 0.332 and -0.260 e·Å^{-3}; data/restraints/parameters = 1028/3/67; GOF = 1.039; CCDC No. 1915300.

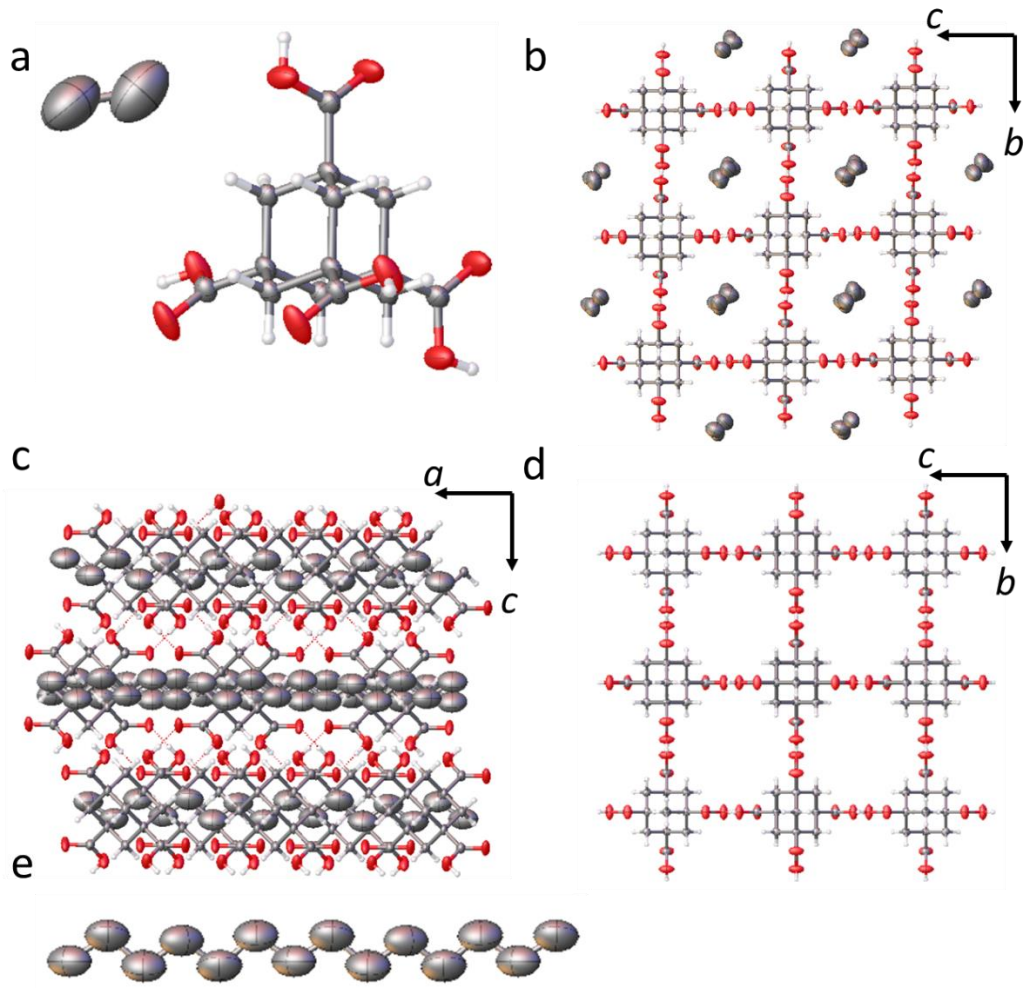

Figure 2.45. a) Displacement ellipsoid plot from the single crystal structure of **ADTA**_3-38. Ellipsoids are displayed at 50% probability. Labels are omitted for clarity. Grey: carbon; red: oxygen; white: hydrogen. b,c) Crystal packing of **ADTA**_3-38 viewed along [100] and [010]. d) 3-fold interpenetrated **ADTA**_3-38 viewed along [100] disordered carbon atoms are omitted for clarity. e) Displacement ellipsoid plot showing the disordered tetradecane in **ADTA**_3-38. Red: oxygen; grey: carbon; white: hydrogen.

ADTA_7-38

ADTA_7-38 crystallised from a 1,4-dioxane and tetradecane solution in the tetragonal space group $I4_1/amd$. The asymmetric unit of **ADTA**_7-38 comprises one complete **ADTA** and disordered solvent that was again modelled as tetradecane, $0.43(C_{14}H_{30})$ (Figure 2.46a). In the structure, one **ADTA** molecule formed four $R_2^2(8)$ hydrogen bonding motifs to four neighboring **ADTA** molecules to generate diamondoid nets that were interpenetrated to form a 3-fold structure (Figure 2.46b, c). The disordered tetradecane molecules were again stacked in one-dimensional channels in the 3-fold interpenetrated structure (Figure 2.46b). However, in comparison to the disordered tetradecane in **ADTA_3-38**, the tetradecane in **ADTA_7-38** appeared more disordered (Figure 2.46e). In **ADTA_7-38** the packing of **ADTA** molecules is symmetrically equivalent along the *a* and *b* unit cell directions and the *ab* plane is perpendicular to the 1-D solvent-filled channels. By comparison, in **ADTA_3-38** the *bc* plane is perpendicular to the solvent-filled 1-D channels and the *b* and *c* unit cell directions are inequivalent. It is therefore reasonable to assume that the ordering of tetradecane solvent ordering affected the crystal symmetry of **ADTA_3-38 and ADTA_7-38**.

Crystal data for **ADTA**_7-38 (100 K): Formula $C_{14}H_{16}O_8 \cdot 0.43(C_{14}H_{30})$; M = 397.29, tetragonal $I4_1/amd$, colourless block shape crystals; $a = b$ = 16.429(3) Å, c = 7.3580(12) Å; V = 1986.0(7) Å^3; ρ = 1.329 g/cm^3; Z = 4; μ(Mo-Kα) = 0.102 mm^{-1}; F (000) = 852; crystal size = 0.15 × 0.15 × 0.13 mm; T = 100 (2) K. 7390 reflections measured ($4.96 < 2\theta < 52.75$ °), 554 unique (R_{int} = 0.0598), 407 ($I > 2\sigma(I)$); R_1 = 0.0650 for observed and R_1 = 0.0842 for all reflections; wR_2 = 0.1993 for all reflections; max/min difference electron density = 0.241 and -0.242 e·Å^{-3}; data/restraints/parameters = 554/1/47; GOF = 1.135; CCDC No. 1915302.

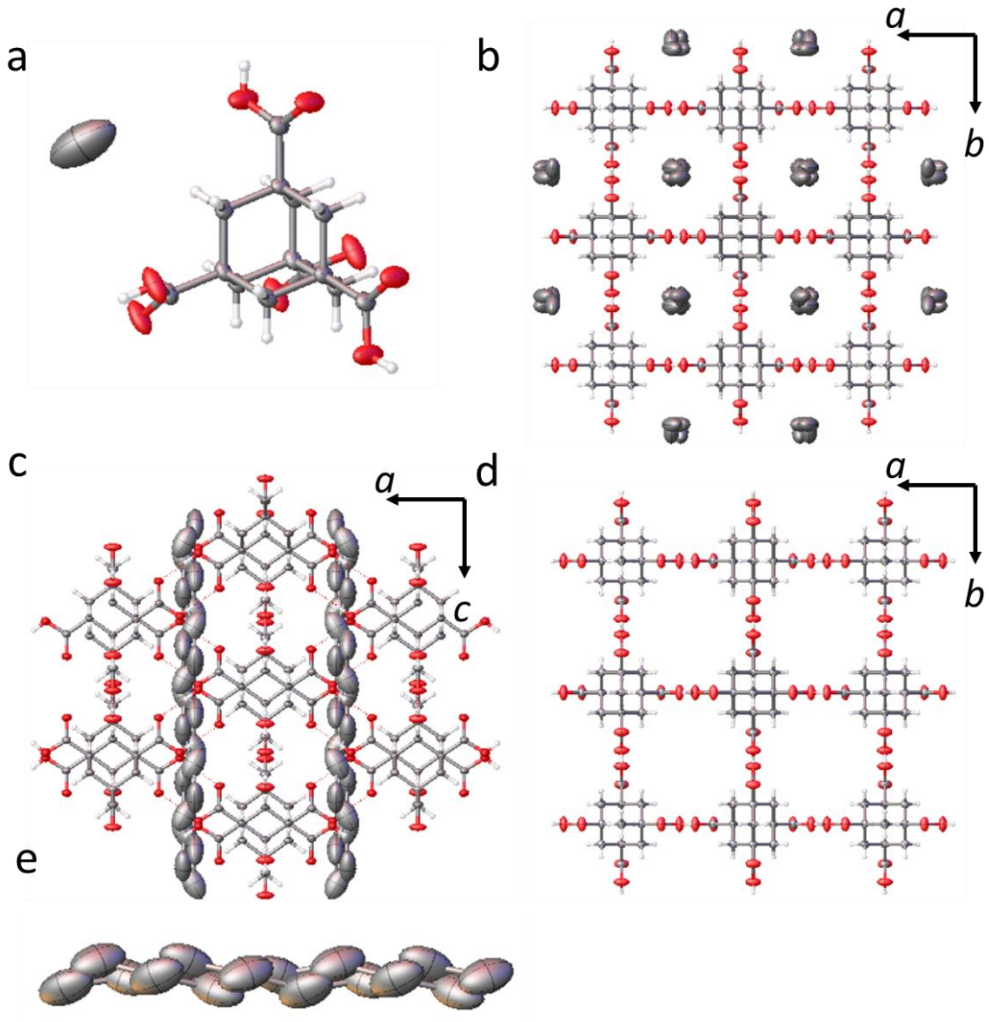

Figure 2.46. a) Displacement ellipsoid plot from the single crystal structure of **ADTA**_7-38. Each disordered carbon atom was modelled with 75% occupancy, ellipsoids are displayed at 50% probability. Labels are omitted for clarity. Grey: carbon; red: oxygen; white: hydrogen. b,c) Crystal packing of **ADTA**_7-38 viewed along [001] and [010]. d) 3-fold interpenetrated **ADTA**_7-38 viewed along [001]. Disordered carbon atoms were omitted for clarity. e) Displacement ellipsoid plot showing the disordered tetradecane in **ADTA**_7-38. Red: oxygen; grey: carbon; white: hydrogen.

A comparison of the **ADTA** atomic coordinates in the single crystal structure of **ADTA**_7-38 and the predicted 3-fold structure that had the lowest predicted lattice energy revealed an excellent agreement between the arrangements of **ADTA** molecules. The root means squared deviation (RMSD) for atomic positions of 0.28 Å

was found using a cluster of 20 molecules, and the excellent structural agreement between the two experimental and predicted structures is shown in Figure 2.47.

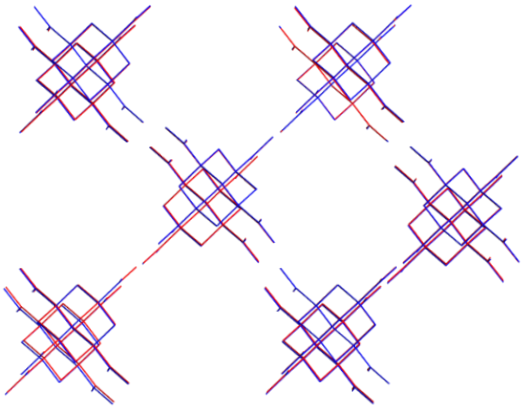

Figure 2.47. Comparison between predicted and experimental 3-fold interpenetrated **ADTA**_7-38, blue: prediction; red: experiment. Solvent molecules in the experimental 3-fold interpenetrated structures are hidden.

To determine the experimental stability of the 3-fold structures, solvated crystals of **ADTA**_3-38 were subjected to direct activation under vacuum at 100 °C. The materials were also activated by first exchanging the crystallisation solvent with *n*-pentane and then evacuating the solvent from the pores at room temperature. However, the 3-fold structures transformed in the solid state into the 5-fold structure after activation under both conditions (Figures 2.48). The 3-fold interpenetrated packing of **ADTA** could therefore not be isolated as solvent-free new polymorph.

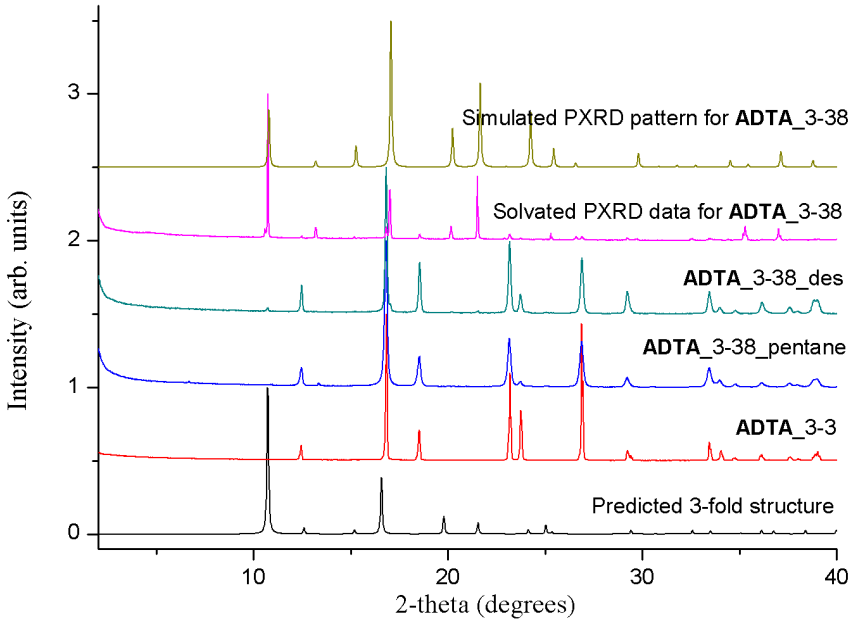

Figure 2.48. PXRD pattern from simulated the predicted 3-fold structure (black); simulated PXRD pattern of the experimental 5-fold structure **ADTA**_3-3 (red); experimental PXRD pattern for **ADTA**_3-38 that was recorded after attempting to exchanging with *n*-pentane (blue); experimental PXRD pattern recorded after attempting to desolvate the **ADTA**_3-38 at 100 °C under dynamic vacuum (**ADTA**_3-38_des, cyan); experimental PXRD data for solvated **ADTA**_3-38 (pink), simulated PXRD pattern from the single crystal structure, **ADTA**_3-38 recorded at 200 K (green).

*3.4.4.3 2-fold interpenetrated **ADTA***

The PXRD patterns from the HT crystallisation screen that could not be assigned to the 3-, 4-, or 5-fold structures were mostly crystallised from a series of structurally related bad solvents: *o*-xylene, *m*-xylene, *p*-xylene, mesitylene, 1,2-dimethoxybenzene, and 1,3-dimethoxybenzene (Figure 2.35) and were shown in Figure 2.49-2.54, which are grouped based on the bad solvent used. The PXRD patterns from *o*-xylene (**ADTA**_1-27, **ADTA**_2-27, **ADTA**_3-27, **ADTA**_4-27, **ADTA**_5-27, **ADTA**_6-27 and **ADTA**_1-27) were found to be similar with each other and they are different from the predicted 4-, and 5-fold structures (Figure 2.49). However, the PXRD patterns could not be classified as 2-fold or 3-fold structures using the CSP dataset. Also, the

problem of classification was found from other solvent systems because of the poor match between experimental patterns and predicted patterns in Figure 2.50-2.54. The structures of three typical samples (**ADTA**_2-27, **ADTA**_2-34 and **ADTA**_2-35) were therefore subjected to analysis by SCXRD to explore the degrees of interpenetration in the resulting structures.

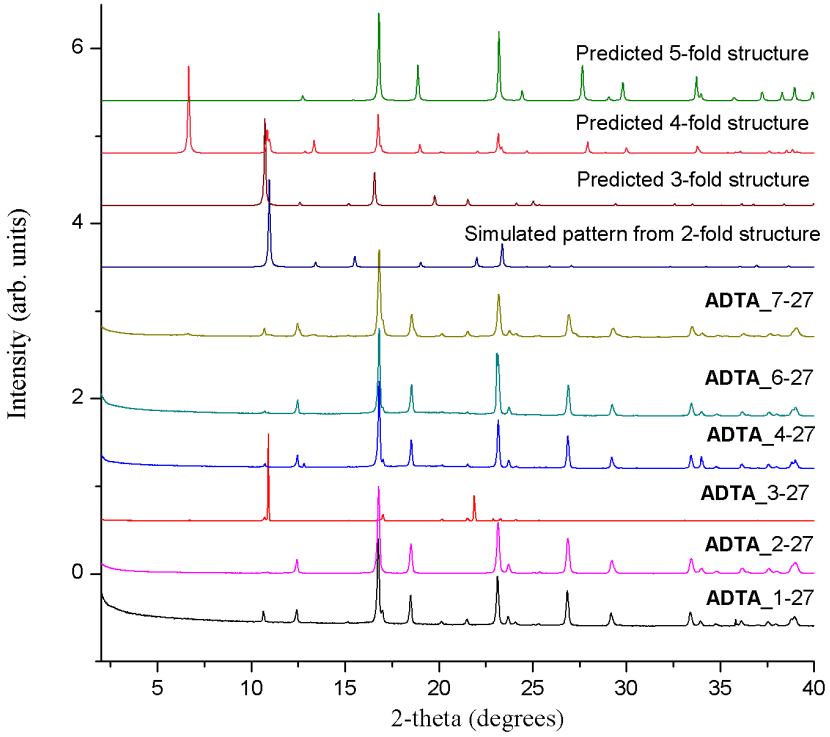

Figure 2.49. PXRD patterns of **ADTA** crystallised from the 6 good solvents (1: methanol, 2: THF, 3: ethanol, 4: 2-propanol, 6: 1-propanol, and 7: 1,4-dioxane) and the one anti-solvent *o*-xylene (27). The unground samples were air-dried on the PXRD plate before analysis.

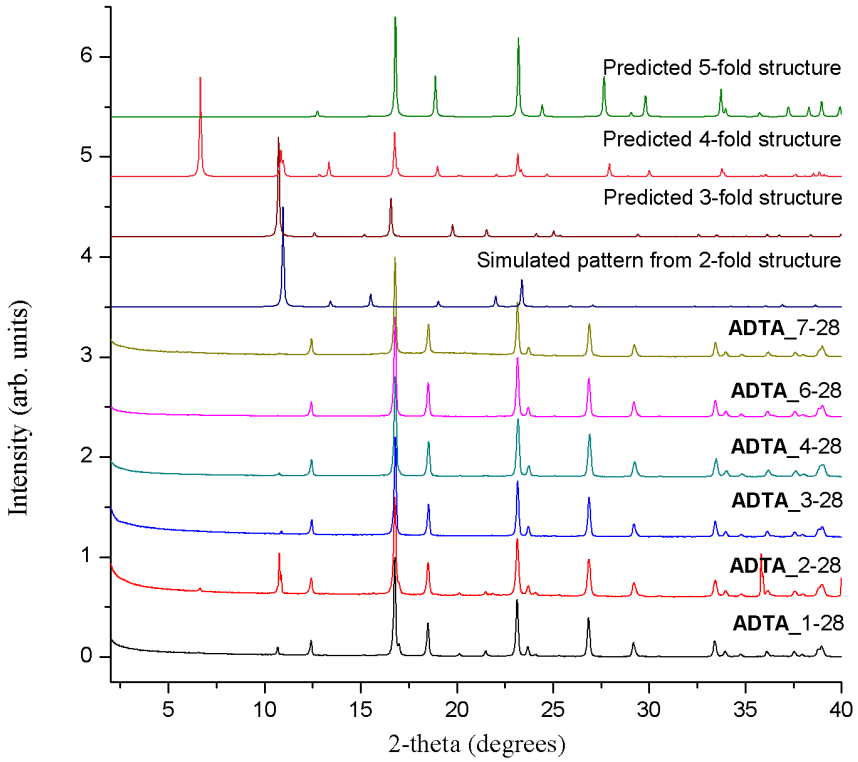

Figure 2.50. PXRD patterns of **ADTA** crystallised from the 6 'good solvents' (1: methanol, 2: THF, 3: ethanol, 4: 2-propanol, 6: 1-propanol, and 7: 1,4-dioxane) and the one anti-solvent *m*-xylene (28). The unground samples were air-dried on the PXRD plate before analysis.

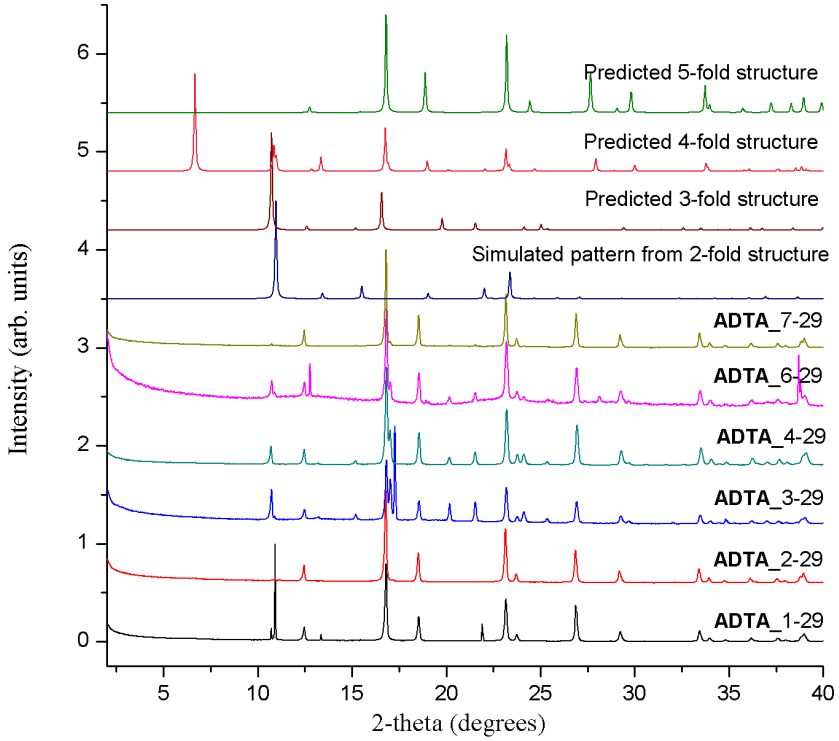

Figure 2.51. PXRD patterns of **ADTA** crystallised from the 6 'good solvents' (1: methanol, 2: THF, 3: ethanol, 4: 2-propanol, 6: 1-propanol, and 7: 1,4-dioxane) and the one anti-solvent *p*-xylene (29). The unground samples were air-dried on the PXRD plate before analysis.

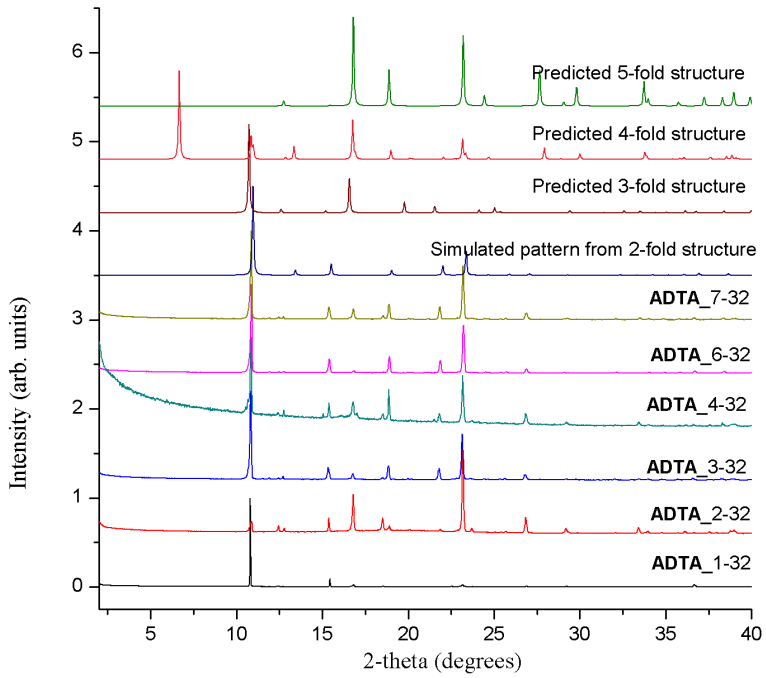

Figure 2.52. PXRD patterns of **ADTA** crystallised from the 6 'good solvents' (1: methanol, 2: THF, 3: ethanol, 4: 2-propanol, 6: 1-propanol, and 7: 1,4-dioxane) and the one anti-solvent mesitylene (32). The unground samples were air-dried on the PXRD plate before analysis.

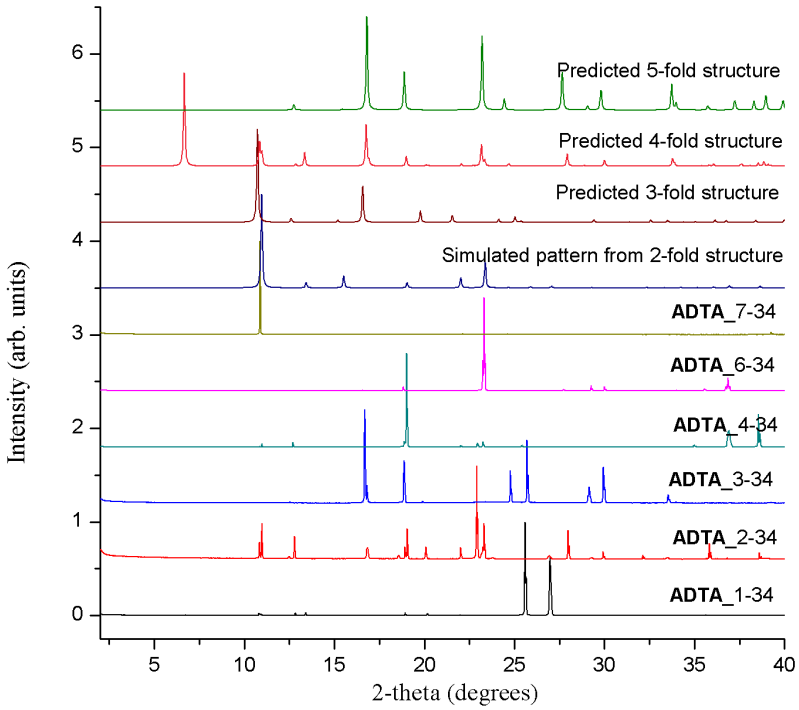

Figure 2.53. PXRD patterns of **ADTA** crystallised from the 6 'good solvents' (1: methanol, 2: THF, 3: ethanol, 4: 2-propanol, 6: 1-propanol, and 7: 1,4-dioxane) and the one anti-solvent 1,2-dimethoxybenzene (34). The unground samples were air dried on the PXRD plate before analysis.

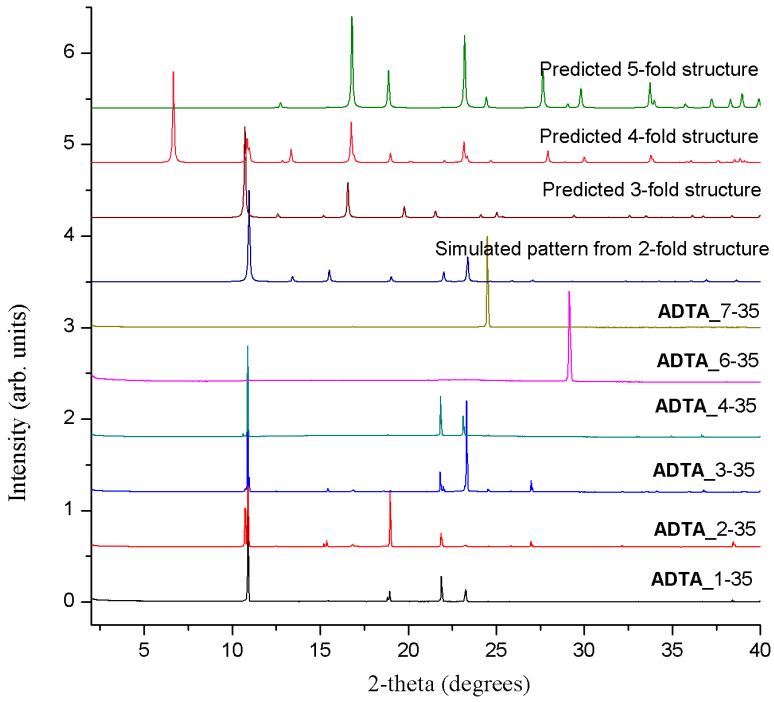

Figure 2.54. PXRD patterns of **ADTA** crystallised from the 6 'good solvents' (1: methanol, 2: THF, 3: ethanol, 4: 2-propanol, 6: 1-propanol, and 7: 1,4-dioxane) and the one anti-solvent 1,3-dimethoxybenzene (35). The unground samples were air-dried on the PXRD plate before analysis.

The THF crystallisations with the following bad solvents: *o*-xylene (**ADTA**_2-27), 1,2-dimethoxybenzene (**ADTA**_2-34), and 1,3-dimethoxybenzene (**ADTA**_2-35) were used to determine X-ray crystal structures for three of the unmatched phases. In the crystal structure of **ADTA**_2-34 (Figure 2.55), ordered 1,2-dimethoxybenzene between **ADTA** molecules were found, whereas the aromatic solvents in **ADTA**_2-27 (Figure 2.56) and **ADTA**_2-35 (Figure 2.57) were too disordered to accurately model in their crystal structures. However, all three structures, **ADTA**_2-27, **ADTA**_2-34, and **ADTA**_2-35, have the same underlying 2-fold interpenetrated structure. However, the crystallised 2-fold interpenetrated structures that we isolated experimentally did not have any exact matches on the CSP landscape. In the case of **ADTA**_2-34, there are two symmetrically inequivalent **ADTA** molecules in the structure, which was not considered in the CSP search. For **ADTA**_2-34, and **ADTA**_2-35 with 2-fold interpenetration of hydrogen bond networks, the absence of exact matches on the CSP

landscape can be rationalised by considering how the solvent content affects the packing of the diamondoid networks. Due to weak, non-directional interactions between interpenetrated hydrogen-bonded networks of **ADTA**, the solvent molecules have an important influence on their relative packing arrangements. In the CSP 2-fold structures, the diamondoid networks were more closely packed to maximise the intermolecular interaction between the two interpenetrated networks. By comparison, the solvent molecules in the experimental structures, which were not included in the CSP calculation, filled the gaps between the two interpenetrated networks. As a result, the packing arrangement on **ADTA** diamondoid networks in the predicted and experimental structures varied, with larger solvent-filled gaps found in the experimental hits, which meant no exact structural matches were found of the CSP landscape.

*The SCXRD structure of 2-fold **ADTA***

***ADTA**_2-34*

ADTA_2-34 crystallised from a THF and 1,2-dimethoxybenzene solution in the tetragonal space group $I4_1/a$. The asymmetric unit for **ADTA**_2-34 comprises two complete **ADTA** and ordered solvent molecules which were modelled as 1,3-dimethoxybenzene, $4(C_8H_{10}O_2)$ (Figure 2.55a). In **ADTA**_2-34, one **ADTA** molecule formed four $R_2^2(8)$ hydrogen bonding motifs between the four neighboring **ADTA** molecules to generate diamondoid networks that are interpenetrated to form a 2-fold structure (Figure 2.55c, d). The ordered 1,3-dimethoxybenzene molecules were stacked in the large pore of 2-fold interpenetrated structure (Figure 2.55b).

Crystal data for **ADTA**_2-34 (100 K): Formula $2(C_{14}H_{16}O_8)\cdot4(C_8H_{10}O_2)$; M = 1177.17, tetragonal $I4_1/a$, colourless block shape crystals; $a = b$ = 16.2380(2) Å, c = 22.3825(3) Å; V = 5901.65(17) Å^3; ρ = 1.325 g/cm^3; Z = 4; μ(Mo-Kα) = 0.103 mm^{-1}; F (000) = 2496; crystal size = 0.11 × 0.09 × 0.07 mm; T = 100 (2) K. 45910 reflections measured ($5.02 < 2\theta < 52.72$ °), 3006 unique (R_{int} = 0.0789), 2383 ($I > 2\sigma(I)$); R_1 = 0.0511 for observed and R_1 = 0.0639 for all reflections; wR_2 = 0.1421 for all reflections; max/min

difference electron density = 0.330 and -0.250 e·Å^{-3}; data/restraints/parameters = 3006/0/195; GOF = 1.064; CCDC No. 1915303.

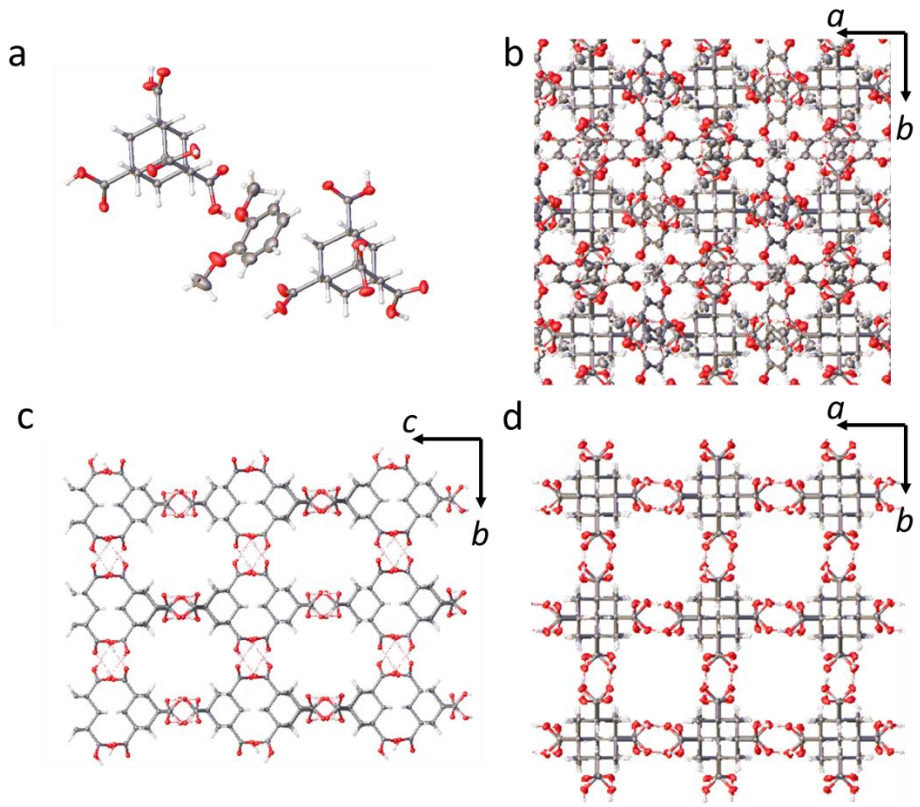

Figure 2.55. a) Displacement ellipsoid plot from the single crystal structure of **ADTA**_2-34. Ellipsoids are displayed at 50% probability. Atom labels are omitted for clarity. Grey: carbon; red: oxygen; white: hydrogen. b) Crystal packing of **ADTA**_2-34 viewed along [001]. c,d) 2-fold interpenetrated **ADTA**_2-27 viewed along [100] and [001] omitted solvents for clarity. Red: oxygen; grey: carbon; white: hydrogen.

ADTA_2-27

ADTA_2-27 crystallised from a THF and *o*-xylene solution in the cubic space group $Pn\bar{3}$. The asymmetric unit of **ADTA**_2-27 comprises one complete **ADTA** and disordered solvent which was tentatively modelled as oxygen, 8.75(O) (Figure 2.56a). In **ADTA**_2-27, one **ADTA** molecule formed four $R_2^2(8)$ hydrogen bonding motifs between the four neighboring **ADTA** molecules to generate diamondoid networks that are interpenetrated to form a 2-fold structure (Figure 2.56c, d). Disordered solvent

occupies the gaps between the diamondoid networks, but it was not possible to accurately model these solvent molecules (Figure 2.56b).

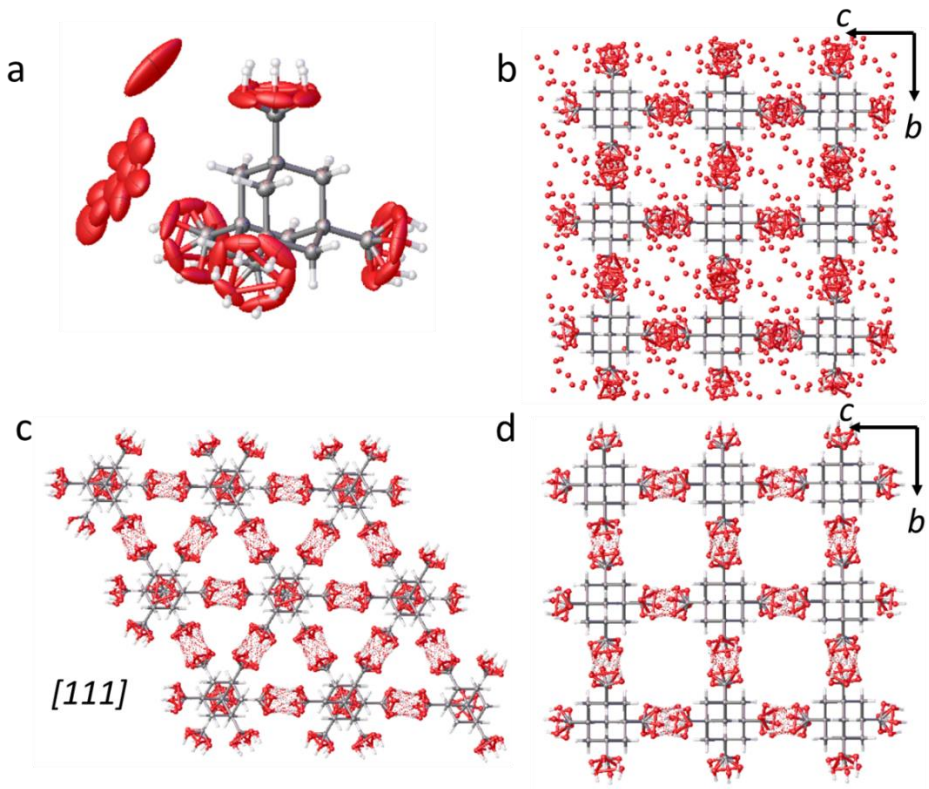

Figure 2.56. a) Displacement ellipsoid plot from the single crystal structure of **ADTA**_2-27. The oxygen atoms on the carboxylic acid group were disordered and modelled with 33.3% occupancy. Each disordered oxygen atom in the crystal pores was tentatively modelled with 25% occupancy, ellipsoids are displayed at 50% probability. Atom labels are omitted for clarity. Grey: carbon; red: oxygen; white: hydrogen. b) Crystal packing of **ADTA**_2-27 viewed along [100]. c,d) 2-fold interpenetrated **ADTA**_2-27 viewed along [111] and [100]; disordered oxygen atoms omitted for clarity. Red: oxygen; grey: carbon; white: hydrogen.

X-ray crystal structure refined with the TWINLAW [$\bar{1}$00 001 010] and BASF refined to 0.494. Crystal data for **ADTA**_2-27 (100 K): Formula $C_{14}H_{16}O_8 \cdot 8.75(O)$; M = 456.30, cubic $Pn\bar{3}$, colourless block shape crystals; $a = b = c$ = 14.4074(5) Å; V = 1484.4(2) Å^3; ρ = 1.021 g/cm^3; Z = 2; μ(Mo-Kα) = 0.097 mm^{-1}; F (000) = 476; crystal size = 0.40 × 0.39 × 0.38 mm; T = 100 (2) K. 15739 reflections measured (3.57 < 2θ < 60.94 °), 761

unique (R_{int} = 0.0579), 656 ($I > 2\sigma(I)$); R_1 = 0.0859 for observed and R_1 = 0.0928 for all reflections; wR_2 = 0.2255 for all reflections; max/min difference electron density = 0.338 and -0.420 e·Å^{-3}; data/restraints/parameters = 761/36/76; GOF = 1.196; CCDC No. 1915299.

ADTA_2-35

ADTA_2-35 crystallised from THF and 1,3-dimethoxybenzene solution in the tetragonal space group $P4_2/nnm$. The asymmetric unit of **ADTA**_2-35 comprises one complete **ADTA** and disordered solvent which were modelled as oxygen, 17.5(O) (Figure 2.57a). In **ADTA**_2-35, one **ADTA** molecule formed four $R_2^2(8)$ hydrogen bonding motifs between the four neighboring **ADTA** molecules to generate diamondoid networks that are interpenetrated to form a 2-fold structure (Figure 2.57c, d). Disordered solvent occupies the gaps between the diamondoid networks, but it was not possible to accurately model these solvent molecules (Figure 2.57b).

X-ray crystal structure refined with the TWINLAW [$\bar{1}$00 001 010] and BASF refined to 0.532. Crystal data for **ADTA**_2-35 (100 K): Formula $C_{14}H_{16}O_8 \cdot 17.5(O)$; M = 596.30, tetragonal $P4_2/nnm$, colourless block shape crystals; $a = b$ = 11.4331(8) Å, c = 11.4312(8) Å; V = 1494.2(2) Å^3; ρ = 1.325 g/cm^3; Z = 2; μ(Mo-Kα) = 0.134 mm^{-1}; F (000) = 616; crystal size = 0.14 × 0.11 × 0.11 mm; T = 100 (2) K. 17215 reflections measured (3.56 < 2θ < 52.72 °), 829 unique (R_{int} = 0.0453), 682 ($I > 2\sigma(I)$); R_1 = 0.0760 for observed and R_1 = 0.0860 for all reflections; wR_2 = 0.2009 for all reflections; max/min difference electron density = 0.177 and -0.39 e·Å^{-3}; data/restraints/parameters = 829/6/98; GOF = 1.142; CCDC No. 1915312.

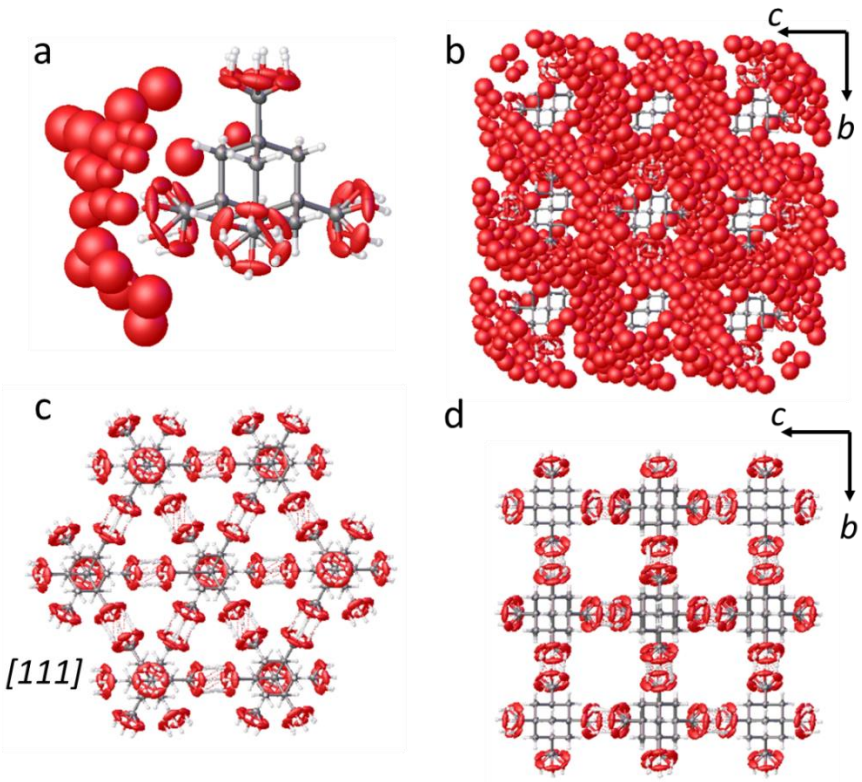

Figure 2.57 a) Displacement ellipsoid plot from the single crystal structure of **ADTA**_2-35. The oxygen atoms on the carboxylic acid group were disordered ad modelled with 33.3% occupancy. Each disordered oxygen atom in the solvent-filled pores was modelled with 25% occupancy, ellipsoids are displayed at 50 % probability. Atom labels are omitted for clarity. Grey: carbon; red: oxygen; white: hydrogen. b) Crystal packing of **ADTA**_2-35 viewed along [100]. c,d) 2-fold interpenetrated **ADTA**_2-35 viewed along [111] and [100]; disordered oxygen atoms are omitted for clarity. Red: oxygen; grey: carbon; white: hydrogen.

To characterise the experimental stability of the 2-fold structures, solvated crystals of **ADTA**_2-34, **ADTA**_2-35, and **ADTA**_2-27 were subjected to direct activation under vacuum at 100 °C. The materials were also activated by first exchanging the crystallisation solvent with *n*-pentane and then evacuated at room temperature. However, from both conditions, the 2-fold structures (**ADTA**_2-34, **ADTA**_2-35, and **ADTA**_2-27) transformed in the solid state into the 5-fold structure after activation

(Figure 2.58-2.60). Unfortunately, it was not possible to isolate solvent-free crystals of the 2-fold interpenetrated **ADTA** structures.

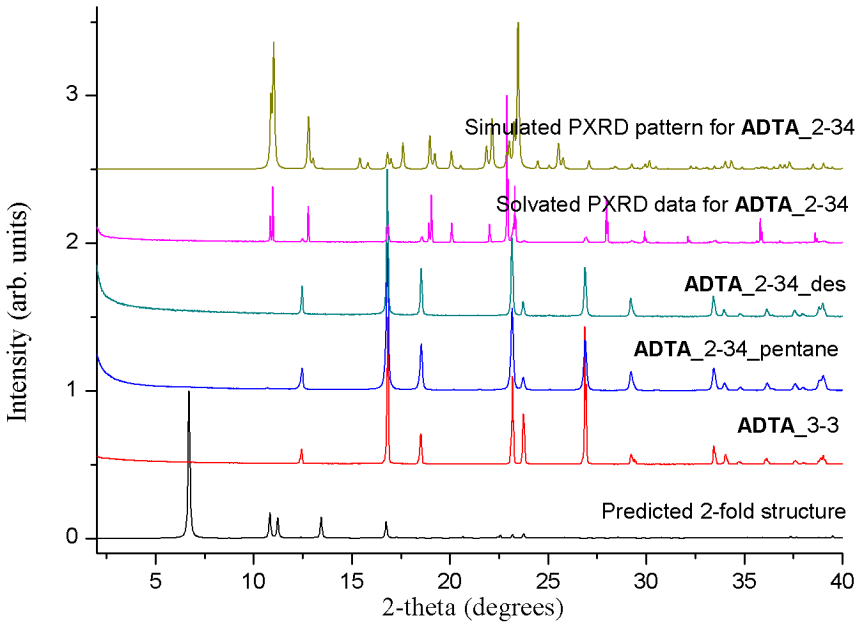

Figure 2.58. PXRD pattern from simulated from predicted 2-fold structure (black); 5-fold structure **ADTA**_3-3 (red); after *n*-pentane exchanged (blue); after degassed at 100 °C under dynamic vacuum (cyan); **ADTA**_2-34 (pink), simulated PXRD pattern from SCXRD (green).

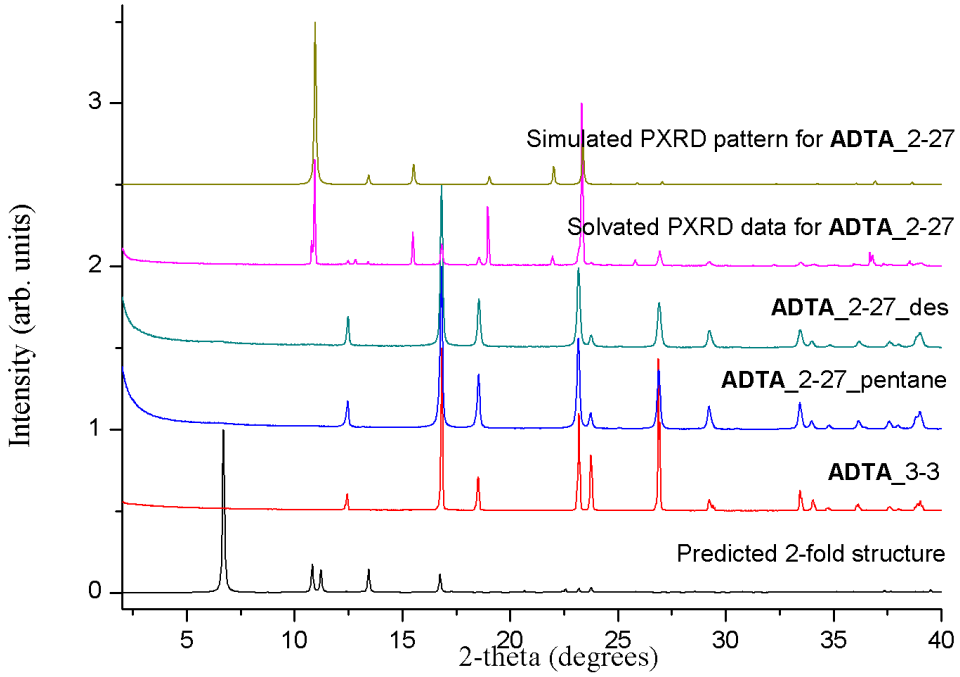

Figure 2.59. PXRD patterns recorded after activating **ADTA**_2-27: Simulated from predicted 2-fold structure (black); 5-fold structure **ADTA**_3-3 (red); after *n*-pentane exchanged (blue); after degassed at 100 °C under dynamic vacuum (cyan); solvated **ADTA**_2-27 (pink), simulated PXRD pattern from SCXRD (green).

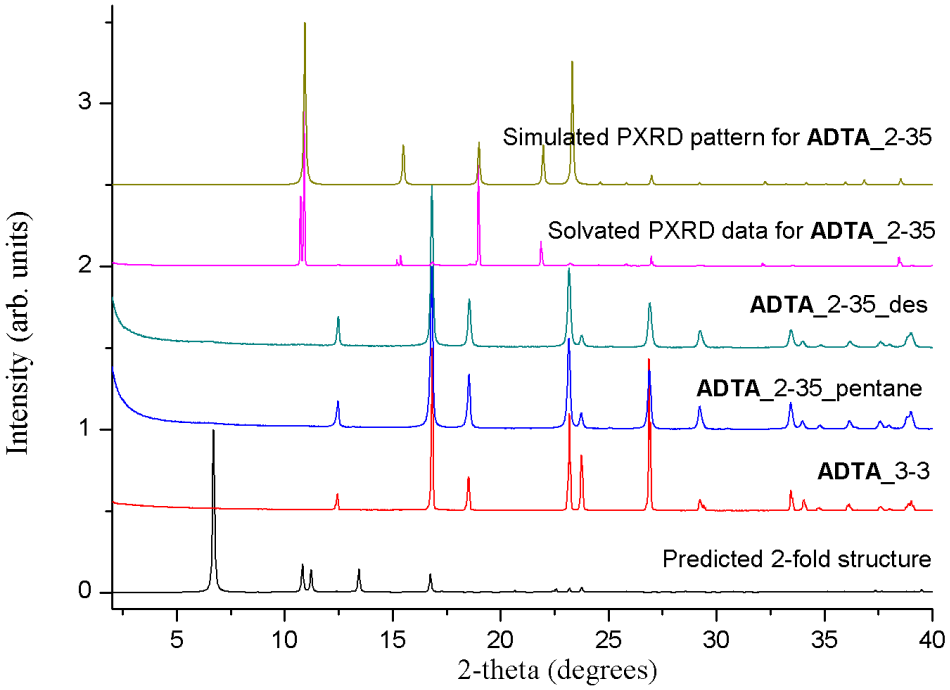

Figure 2.60. PXRD patterns recorded after activating **ADTA**_2-35: Simulated from predicted 2-fold structure (black); 5-fold structure **ADTA**_3-3 (red); after *n*-pentane exchanged (blue); after degassed at 100 °C under dynamic vacuum (cyan); solvated **ADTA**_2-35 (pink), simulated PXRD pattern from SCXRD (green).

Overall, the 5-, 4-, 3-fold interpenetration **ADTA** structures obtained experimentally correlate very well with the predicted structures in the CSP energy landscape. The new 4-, 3-fold experimental structures were found in the low energy, leading-edge, of the energy-density distribution of structures and match very well with their predictions. While the 2-fold structure was found experimentally, differences were found between the experimental packing of the diamondoid nets and the predicted packing in the CSP structures. Despite the 2-fold structural difference, 5-, 4-, 3-, and 2-fold structures were all found in low energy regions in the CSP landscape and were likewise observed experimentally. By contrast, the non-interpenetrated structure was much higher in energy and was not observed experimentally from any of the screened crystallisation conditions.

4. Conclusion

In summary, CSP calculations indicated that there were some promising unknown porous crystal structures for **TMA** and **ADTA** molecules that had not been uncovered experimentally. A number of these predicted phases (**1-TMA**, 3-fold and 4-fold interpenetrated **ADTA**) were subsequently discovered in the laboratory using a HT method that was developed to rapidly screen hundreds of different crystallisation conditions. Using a combination approach, it was showing that integrating CSP and experimental screening strategy greatly accelerated the discovery of these new materials: indeed, they would likely have remained undiscovered without this approach.

The hybrid computational and experimental approach allowed us to find new solvated porous structures for **TMA** and lower degrees of hydrogen bond network interpenetrated structures that supplement the known 5-fold form for **ADTA**. Furthermore, a desolvated porous polymorph of **TMA**, δ-**TMA**, with SA_{BET} = 910 m^2/g, was found by solvent exchanging one of these structures (**TMA**_2-33) with *n*-pentane. The stability of δ-**TMA** phase was also explored. The crystal structure of δ-**TMA** matched well with the lowest-energy predicted structure. Also, the experimental 3-, 4-, 5-fold interpenetrated structures of **ADTA** matched well with the predicted structures. More generally, the combination of CSP with HT crystallisation screening has the potential to aid the discovery of other porous molecular solids.

Despite their 3-D hydrogen-bonded networks, the **ADTA** structures were found to be far less stable than δ-**TMA**, indicating that a combination of hydrogen-bonded and other intermolecular interactions is important for stabilising porous crystal packings in hydrogen-bonded organic frameworks.

5. References

1. Cui, P. *et al.* Mining predicted crystal structure landscapes with high throughput crystallisation: Old molecules, new insights. *Chem. Sci*. **10**, 9988–9997 (2019).
2. Begley, T. P., Inglese, J. & Auld, D. S. High Throughput Screening (HTS) Techniques: Applications in Chemical Biology. *Wiley Encycl. Chem. Biol.* **5**, 233 (2008).

3. MacArron, R. *et al.* Impact of high-throughput screening in biomedical research. *Nat. Rev. Drug Discov.* **10**, 188–195 (2011).
4. Hertzberg, R. P. & Pope, A. J. High-throughput screening: New technology for the 21st century. *Curr. Opin. Chem. Biol.* **4**, 445–451 (2000).
5. Kitchen, D. B., Decornez, H., Furr, J. R. & Bajorath, J. Docking and scoring in virtual screening for drug discovery: Methods and applications. *Nat. Rev. Drug Discov.* **3**, 935–949 (2004).
6. Bleicher, K. H., Böhm, H. J., Müller, K. & Alanine, A. I. Hit and lead generation: Beyond high-throughput screening. *Nat. Rev. Drug Discov.* **2**, 369–378 (2003).
7. Shevlin, M. Practical High-Throughput Experimentation for Chemists. *ACS Med. Chem. Lett.* **8**, 601–607 (2017).
8. Greenaway, R. L. *et al.* High-throughput discovery of organic cages and catenanes using computational screening fused with robotic synthesis. *Nat. Commun.* **9**, 2849 (2018).
9. Kearsey, R. J., Alston, B. M., Briggs, M. E., Greenaway, R. L. & Cooper, A. I. Accelerated robotic discovery of type II porous liquids. *Chem. Sci.* **10**, 9454–9465 (2019).
10. Briggs, M. E. & Cooper, A. I. A perspective on the synthesis, purification, and characterisation of porous organic cages. *Chem. Mater.* **29**, 149–157 (2017).
11. Iuzzolino, L., McCabe, P., Price, S. L. & Brandenburg, J. G. Crystal structure prediction of flexible pharmaceutical-like molecules: density functional tight-binding as an intermediate optimisation method and for free energy estimation. *Faraday Discuss.* **211**, 275–296 (2018).
12. Neumann, M. A., Van De Streek, J., Fabbiani, F. P. A., Hidber, P. & Grassmann, O. Combined crystal structure prediction and high-pressure crystallisation in rational pharmaceutical polymorph screening. *Nat. Commun.* **6**, 7793 (2015).
13. Nyman, J. & Day, G. M. Static and lattice vibrational energy differences between polymorphs. *CrystEngComm* **17**, 5154–5165 (2015).
14. Woodley, S. M. & Catlow, R. Crystal structure prediction from first principles. *Nat. Mater.* **7**, 937–946 (2008).
15. Price, S. L. Computed crystal energy landscapes for understanding and predicting organic crystal structures and polymorphism. *Acc. Chem. Res.* **42**, 117–126 (2009).
16. Price, S. L. Is zeroth order crystal structure prediction (CSP_0) coming to maturity? What should we aim for in an ideal crystal structure prediction code? *Faraday Discuss.* **211**, 9–30 (2018).
17. Nyman, J. & Reutzel-Edens, S. M. Crystal structure prediction is changing from basic science to applied technology. *Faraday Discuss.* **211**, 459–476 (2018).
18. Pulido, A. *et al.* Functional materials discovery using energy-structure-function maps. *Nature* **543**, 657–664 (2017).
19. Jones, J. T. A. *et al.* Modular and predictable assembly of porous organic molecular crystals. *Nature* **474**, 367–371 (2011).
20. Sanderson, K. Model predicts structure of crystals. *Nature* **450**, 771 (2007).
21. Day, G. M. *et al.* Significant progress in predicting the crystal structures of small organic molecules - A report on the fourth blind test. *Acta Crystallogr. Sect. B Struct. Sci.* **65**, 107–125 (2009).
22. Day, G. M. & Cooper, A. I. Energy–Structure–Function Maps: Cartography for Materials Discovery. *Adv. Mater.* **30**, 1704944 (2018).

23. Duchamp, D. J. & Marsh, R. E. The crystal structure of trimesic acid (benzene-1,3,5-tricarboxylic acid). *Acta Crystallogr. Sect. B Struct. Crystallogr. Cryst. Chem.* **25**, 5–19 (1969).
24. Herbstein, F. H., Kapon, M. & Reisner, G. M. Catenated and Non-Catenated Inclusion Complexes of Trimesic Acid. *Incl. Phenom. Inorganic, Org. Organomet. Hosts* 211–214 (1987).
25. Herbstein, F. H., Kapon, M. & Reisner, G. M. Trimesic acid, its hydrates, complexes and polymorphism. VIII. Interstitial complexes of α- and (the hypothetical) γ-trimesic acid. *Acta Crystallogr. Sect. B* **41**, 348–354 (1985).
26. Sanchez-Sala, M., Vallcorba, O., Domingo, C. & Ayllón, J. A. A Flexible Hydrogen Bonded Organic Framework That Reversibly Adsorbs Acetic Acid: γ Trimesic Acid. *Cryst. Growth Des.* **18**, 6621–6626 (2018).
27. Vishweshwar, P., Beauchamp, D. A. & Zaworotko, M. J. An acetic acid solvate of trimesic acid that exhibits triple inclined interpenetration and mixed supramolecular homosynthons. *Cryst. Growth Des.* **6**, 2429–2431 (2006).
28. Dale, S. H. & Elsegood, M. R. J. Trimesic acid bis(N,N-dimethylformamide) solvate at 150 K. *Acta Crystallogr. Sect. E Struct. Reports Online* **59**, 127-128 (2003).
29. Berns, S., Hernández, G., Portillo, R. & Gutiérrez, R. Trimesic acid dimethyl sulfoxide solvate: Space group revision. *Acta Crystallogr. Sect. E Struct. Reports Online* **64**, 1366 (2008).
30. Fan, Z. Z., Li, X. H. & Wang, G. P. Trimesic acid dihydrate. *Acta Crystallogr. Sect. E Struct. Reports Online* **61**,45833 (2006).
31. Dale, S. H., Elsegood, M. R. J. & Richards, S. J. Step-wise dis-assembly of trimesic acid: Mono- and bis(methanol) solvates. *Chem. Commun.* **4**, 1278–1279 (2004).
32. Nath, K. G. *et al.* Crystal engineering in two dimensions: An approach to molecular nanopatterning. *J. Phys. Chem. C* **111**, 16996–17007 (2007).
33. Dmitriev, A., Lin, N., Weckesser, J., Barth, J. V. & Kern, K. Supramolecular assemblies of trimesic acid on a Cu(100) surface. *J. Phys. Chem. B* **106**, 6907–6912 (2002).
34. Chui, S. S. Y., Lo, S. M. F., Charmant, J. P. H., Orpen, A. G. & Williams, I. D. A chemically functionalizable nanoporous material [Cu3(TMA)2 (H2O)3](n). *Science.* **283**, 1148–1150 (1999).
35. Ermer, O. Fivefold-Diamond Structure of Adamantane-1,3,5,7-tetracarboxylic Acid. *J. Am. Chem. Soc.* **110**, 3747–3754 (1988).
36. Ermer, O. & Lindenberg, L. Double-Diamond Inclusion Compounds of 2,6-Dimethylydeneadamantane-1,3,5,7-tetracarboxylic Acid. *Helv. Chim. Acta* **74**, 825–877 (1991).
37. Zavakhina, M. S., Samsonenko, D. G., Yutkin, M. P., Dybtsev, D. N. & Fedin, V. P. Structure of a framework coordination polymer Zn 2(dmf)(H2O)(atc)].0.75DMF.0.5H 2O. *J. Struct. Chem.* **53**, 408–412 (2012).
38. Chen, B. *et al.* Cu2(ATC)·6H2O: Design of open metal sites in porous metal-organic crystals (ATC: 1,3,5,7-Adamantane Tetracarboxylate) [27]. *J. Am. Chem. Soc.* **122**, 11559–11560 (2000).
39. Davey, R. J., Brychczynska, M., Sadiq, G., Dent, G. & Pritchard, R. G. Crystallising trimesic acid from DMSO solutions-can crystallography teach us anything about the process of crystal nucleation? *CrystEngComm* **15**, 856–859 (2013).

40. Herbstein, F. H. & Marsh, R. E. The crystal structures of trimesic acid, its hydrates and complexes. II. Trimesic acid monohydrate–2/9 picric acid and trimesic acid 5/6 hydrate. *Acta Crystallogr. Sect. B Struct. Crystallogr. Cryst. Chem.* **33**, 2358–2367 (1977).
41. Chatterjee, S., Pedireddi, V. R., Ranganathan, A. & Rao, C. N. R. Self-assembled four-membered networks of trimesic acid forming organic channel structures. *J. Mol. Struct.* **520**, 107–115 (2000).
42. Herbstein, F. H. & Kapon, M. The crystal structures of trimesic acid, its hydrates and complexes. III. Trimesic acid–H 2 O–1,4-dioxane . *Acta Crystallogr. Sect. B Struct. Crystallogr. Cryst. Chem.* **34**, 1608–1612 (1978).
43. Kolotuchin, S. V. *et al.* Self-assembly of 1,3,5-benzenetricarboxylic (trimesic) acid and its analogues. *Chem. - A Eur. J.* **5**, 2537–2547 (1999).
44. Ermer, O. & Neudörfl, J. Comparative supramolecular chemistry of coronene, hexahelicene, and [18]crown-6: Hydrated and solvated molecular complexes of [18]crown-6 with 5-hydroxyisophthalic acid and related Di- and tricarboxylic acids. *Chem. - A Eur. J.* **7**, 4961–4980 (2001).
45. Ermer, O. & Neudörfl, J. Comparative supramolecular chemistry of coronene and hexahelicene: Helix alignment in crystalline complexes with trimesic acid (= benzene-1,3,5-tricarboxylic acid) and π-acceptor compounds). *Helv. Chim. Acta* **84**, 1268–1313 (2001).
46. Spek, A. L. Structure validation in chemical crystallography. *Acta Crystallogr. Sect. D Biol. Crystallogr.* **65**, 148–155 (2009).

Chapter 3

Hydrogen-Bonded Organic Frameworks Constructed by Adjustment of Carboxylic Acid Geometry

Contributions to this chapter

Peng Cui led the experimental work, crystallised all of the molecules, and interpreted the single crystal and powder X-ray diffraction data presented in this chapter. The 3-D electron diffraction data for 1,3,5-tri(4-carboxyphenyl) benzene was collected and processed by Erik Svensson Grape and Dr. A. Ken Inge. 3,3',3''-(Benzene-1,3,5-triyl) tripropiolic acid and 5'-(4-carboxy-2,3,5,6-tetrafluorophenyl)-2,2'',3,3'',5,5'',6,6''-octafluoro-[1,1':3',1''-terphenyl]-4,4''-dicarboxylic acid were synthesised by Dr. Christopher Kane. 4,4',4''-(1,3,3a[1],4,6,7,9-Heptaazaphenalene-2,5,8-triyl) tribenzoic acid was synthesised by Dr Xiaobo Li. SEM images were captured by Lunjie Liu. Sorption isotherms were measured by Rob Clowes.

1. Introduction

In Chapter 2, a predicted crystal structure of a porous hexagonal-pore phase of trimesic acid (δ-**TMA**) was found in the laboratory using an experimental high throughput (HT) crystallisation screen. Due to a combination of its weak intermolecular interactions and metastability, δ-**TMA** remained hidden for half a century. From the HT crystallisation screen, it was also found that the packing of **TMA** molecules was strongly influenced by guest solvents,[1] and while some of the structures had similar hydrogen-bonded frameworks, we and others have found different **TMA** phases with different hydrogen-bonded networks.[2–4] Here, in this chapter, five **TMA** analogues (**M1**-**M5**) with π-conjugated aromatic cores and comparable C_3-symmetry were chosen for crystallisation screens that were carried out in binary solvent mixtures (Figure 3.1). Where possible, single crystal structures were determined, including a HOF structure with the molecule **M2** that appeared to have mesopores. A HOF structure with **M3** was found to transform during the crystal activation procedure into a collapsed framework with much smaller pores. Three molecules that each had four carboxylic acids were also explored using the same approach (**M6**-**M8**, Figure 3.1). One of these molecules, **M6**, was previously reported by Biradha *et al*. to form clathrate-type solvated host crystal structures from phenolic

solvent[5], and based on these discoveries, two extended analogues, **M7** and **M8**, were chosen for this study. The crystal structures of **M7** and **M8** that were determined by SCXRD also showed these two molecules formed clathrate-type porous structures with HOF networks. The solvated structures of **M7** and **M8** were both crystallised from DMF/$CHCl_3$ system, and they had large 1-D pores that were activated after swapping the crystallisation solvent with *n*-pentane. However, while the porous HOF structures of **M7** and **M8** appeared to have some stability after activation their experimental porosities were found to be very low.

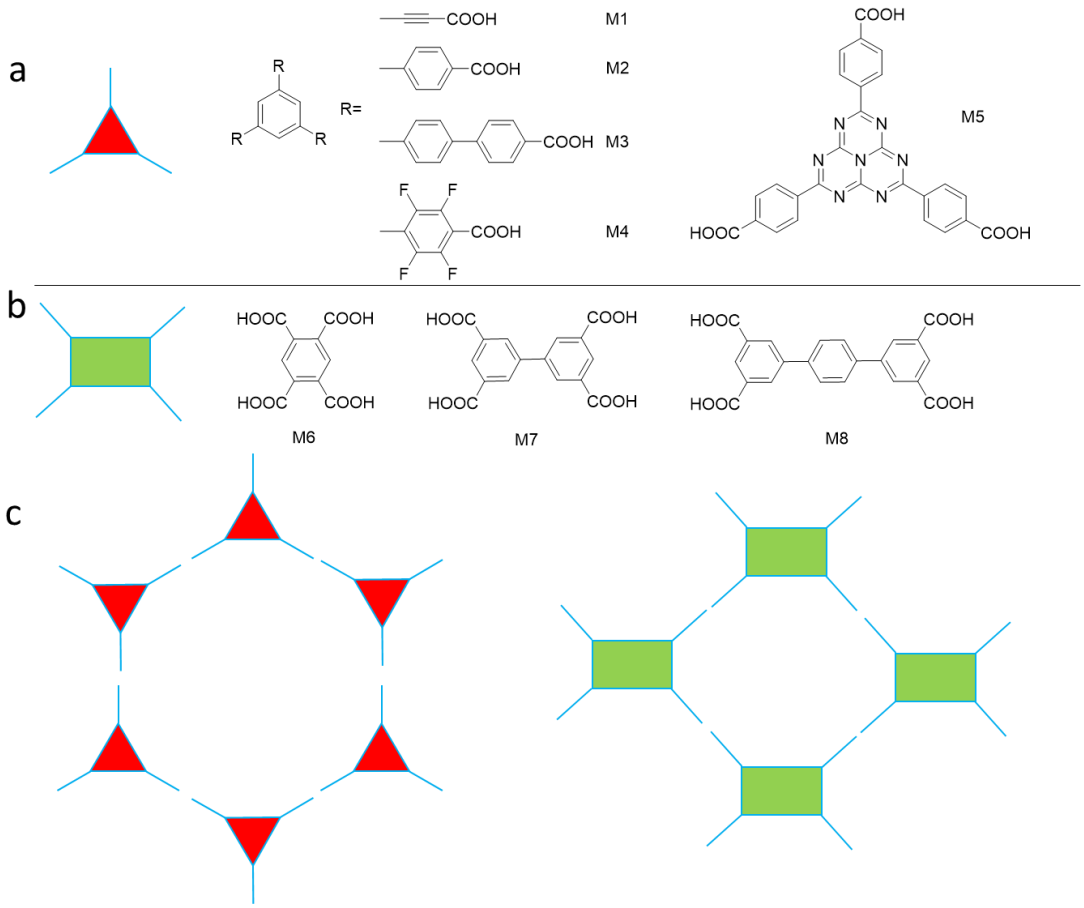

Figure 3.1. Chemical structures of, a) five molecules with three carboxylic acid groups, and b) three molecules with four carboxylic acid groups, which were investigated to determine if they form the continuous HOF structures shown in (c) through the formation of complementary $R_2^2(8)$ hydrogen bonding motifs.

2. Experiment results

*2.1 3,3',3''-(Benzene-1,3,5-triyl) tripropiolic acid (**M1**)*

The structure of 3,3',3''-(benzene-1,3,5-triyl) tripropiolic acid (**M1**, Figure 3.2a) was first reported by the Mertens group[6]. The reported crystal structure was crystallised from solvent evaporation of a mesitylene/ethanol/water mixture, and in the SCXRD structure, water molecules were incorporated into the hydrogen-bonded network. The inclusion of water molecules led to the formation of 12-membered hydrogen-bonded ring motifs between three carboxylic acid groups from three **M1** molecules and one water molecule (Figure 3.2c).

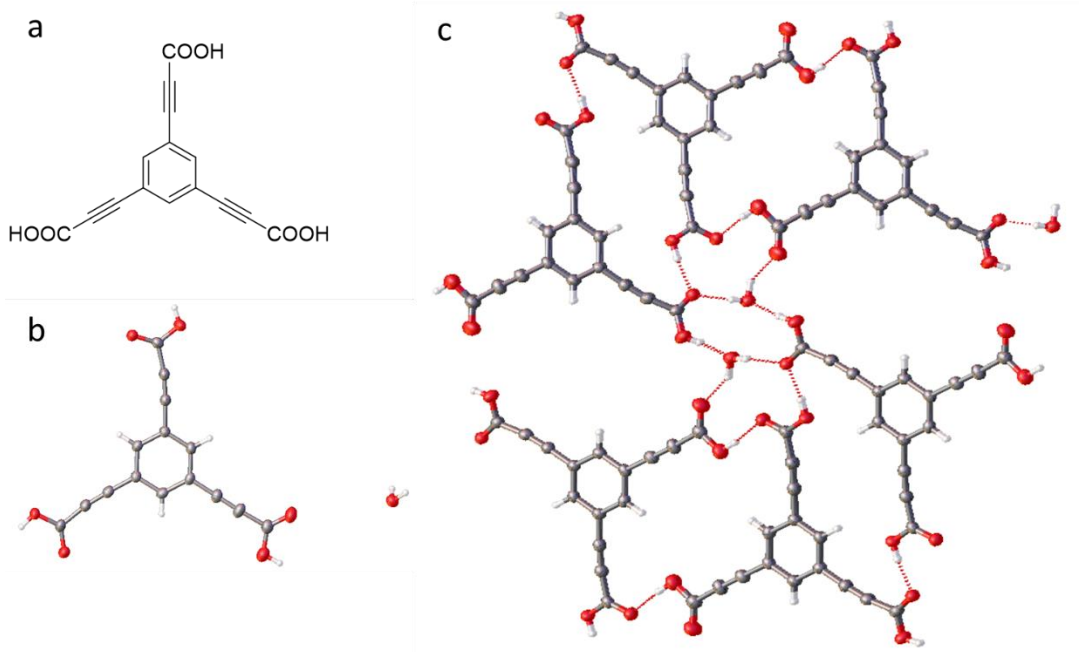

Figure 3.2. a) Chemical structure of **M1**. b) Displacement ellipsoid plot from the reported **M1** solvate[6], and c) the packing in the crystal structure viewed along *a* axis. Ellipsoids displayed at 50% probability level. Hydrogen bonds are shown with red dashed lines. Grey: carbon, red: oxygen, white: hydrogen.

To avoid the inclusion of water in the reported crystal structure of **M1**, attempts were made to crystallise **M1** from dry organic solvents. It was determined **M1** was soluble in THF (~ 2 mg/mL) and inspired by the conditions that yielded the porous **TMA**

structures discussed in Chapter 2, the following anti-solvents were screened: mesitylene, *n*-butylbenzene, 1,2-dimethoxybenzene, 1,3-dimethoxybenzene, and *n*-tetradecane. In the crystallisations, 2 mg of the **M1** molecule was dissolved in 1 mL of THF at RT. 1 mL of anti-solvent (mesitylene, *n*-butylbenzene, 1,2-dimethoxybenzene, 1,3-dimethoxybenzene, and *n*-tetradecane) was then added into separate THF solutions. Finally, the solvent mixtures were left to evaporate at RT. Light yellow needle-shaped crystals (**M1-1**) were obtained from THF/ *n*-tetradecane after 5 days, whereas light yellow powders were isolated from the other solvents systems.

M1-1 ($2C_{15}H_6O_6 \cdot (C_4H_8O)$) crystallised from THF and *n*-tetradecane solution in the triclinic space group $P\bar{1}$. The asymmetric unit for this phase comprises two complete **M1** molecules and one slightly disordered solvent molecule that was modelled as THF, C_4H_8O. The crystal data revealed that **M1-1** was a new solvated crystal structure in which one carboxylic acid group formed a hydrogen bond interaction with the THF molecule (**M1-1**, Figure 3. 3). The single crystal structure showed **M1** adopted a near-planar geometry with the propiolic acids in the same plan as the aromatic core. Although *n*-tetradecane was a guest solvent that generated a hexagonal porous structure with **TMA**[7], **M1** was found to form a non-porous crystal packing with the THF molecules interrupting $R_2^2(8)$ hydrogen bonding interactions between the **M1** molecules.

*2.1.1 The SCXRD structure of **M1-1***

Crystal data for **M1-1** (100 K): Formula $2C_{15}H_6O_6 \cdot (C_4H_8O)$; M = 636.50, triclinic $P\bar{1}$, transparent yellow needle-shaped crystals; a = 9.5713(7) Å, b = 11.2855(9) Å, c = 15.1191(12) Å, α = 74.114(2) °, β = 89.951(2) °, γ = 79.855(2) °; V = 1544.3(2) Å^3; ρ = 1.369 g/cm^3; Z = 4; μ(Mo-Kα) = 0.107 mm^{-1}; F (000) = 656; crystal size = 0.073 × 0.022 × 0.021 mm; T = 100 (2) K. 22126 reflections measured ($5.28 < 2\theta < 61.06$ °), 9371 unique (R_{int} = 0.0495), 6610 ($I > 2\sigma(I)$); R_1 = 0.0598 for observed and R_1 = 0.0894 for all reflections; wR_2 = 0.1531 for all reflections; max/min difference electron density = 0.508 and -0.352 e·Å^{-3}; data/restraints/parameters = 9371/0/508; GOF = 1.026.

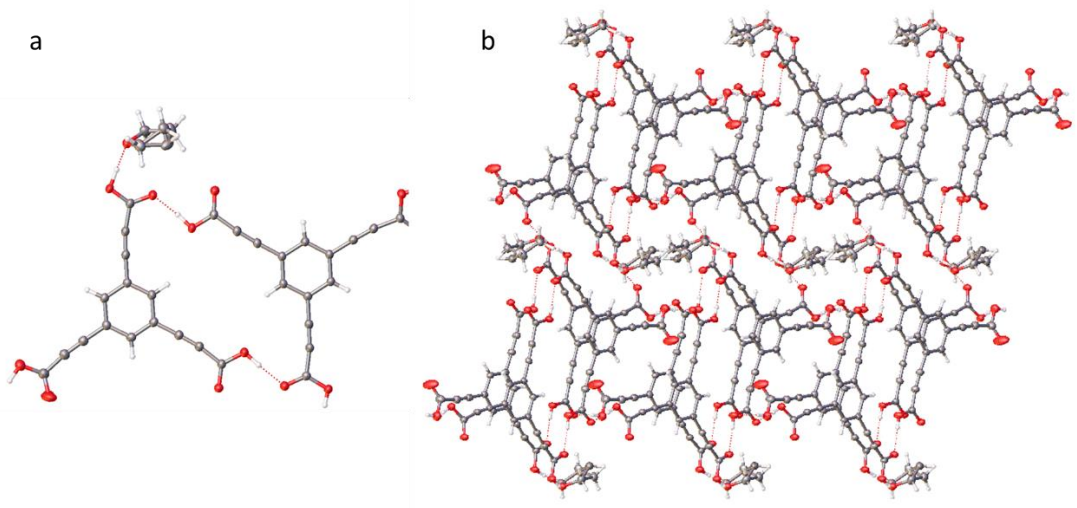

Figure 3.3. a) Displacement ellipsoid plot from the single crystal structure of **M1-1**. b) The packing in the crystal structure viewed along the *a* axis. Ellipsoids displayed at 50% probability level. Hydrogen bonds are shown as red dashed lines. Grey: carbon, red: oxygen, white: hydrogen.

*2.2 1,3,5-Tri(4-carboxyphenyl) benzene (**M2**)*

1,3,5-Tri(4-carboxyphenyl) benzene (**M2**, Figure 3.4a), which is an extended analogue of **TMA**, was also chosen as a new molecule to construct a continuous and topologically related HOF. Single crystal structures of **M2** have been reported previously, including an intricate 8-fold polycatenated assembly of hexagonal **M2** nets that was crystallised from ethanol and propanol or butanol (Figure 3.5).[4] The 8-fold polycatenated was found to have a BET surface area of 1095 m^2 g^{-1}, but at the start of this study, no non-interpenetrated HOF structures of **M2** were reported. Instead, **M2** has always been reported to form solvated or interpenetrated structures, with the latter being due to the large hexagonal pores between hexagonally packed **M2** creating large voids with plenty of space for interpenetration to occur (Figure 3.4c).[4,8–10] In an attempt to prevent interpenetration, a series of 1,3,5-tris(4-carboxyphenyl)arenes with functionalised central arene rings were also synthesised, crystallised, and reported. From their crystal structures, it was found that the crystal packings of **M2** analogues were influenced by the functional group on the central aromatic ring, which led to different stacking distances, interlayer offsets, and

degrees of catenation being observed.[11]

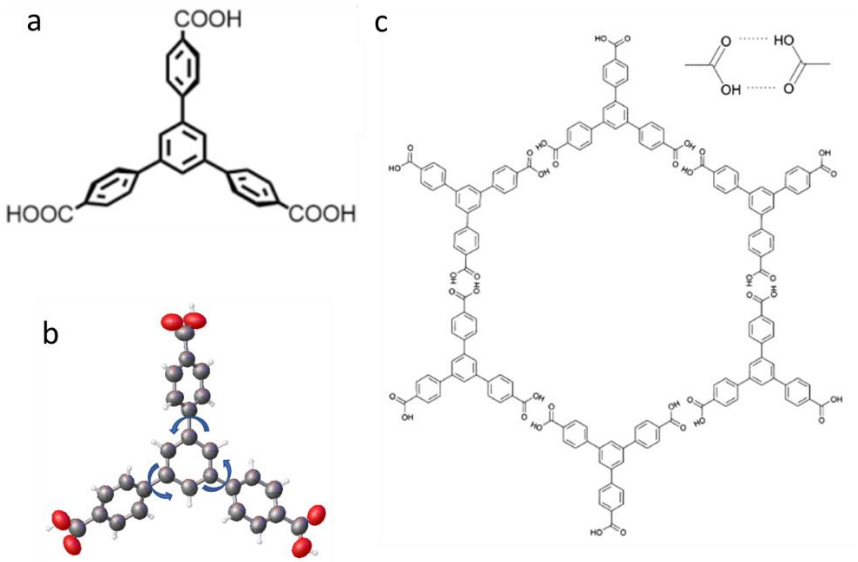

Figure 3.4. a) Chemical structure of **M2**; b) Displacement ellipsoid plot of **M2** from the single crystal structure of **M2-1**. Ellipsoids displayed at 50% probability level. Grey: carbon, red: oxygen, white: hydrogen. c) Formation of hexagonal packing with carboxylic acid dimer linkages in **M2** molecules.

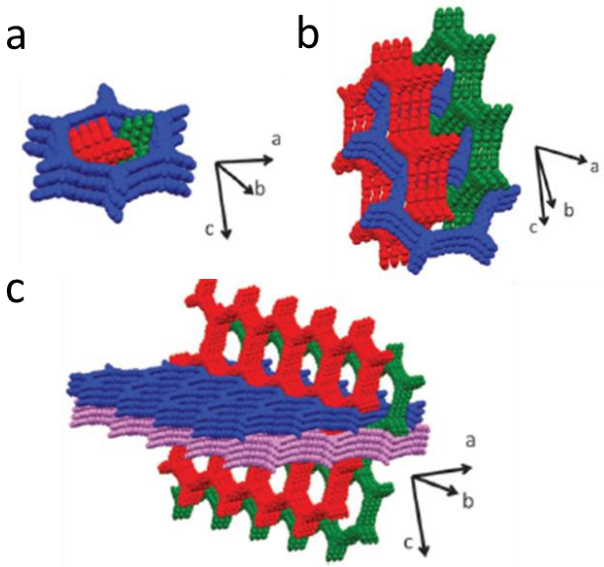

Figure 3.5. The crystal structure of the 8-fold interpenetrated **M2** HOF reported by Zentner *et al.*. a) Seven distinct HOF networks fit in the hexagonal pores (Figure 3.4c); b) 8-fold polycatenation; c) extended view of 8-fold polycatenation of hexagonal layers. Reprint from *Chem. Commun.*, 2015, 51, 11642-11645. Copyright from 2015 The Royal Society of Chemistry.

Here, **M2** was crystallised by slow evaporation of good-solvent/anti-solvent systems using a similar method to that developed for **TMA** discussed in Chapter 2. After performing a solubility test, **M2** (1 mg) was found to dissolve in the good solvents, THF (0.3 mL), and 1,4-dioxane (0.5 mL) at RT. In the crystallisation screen, 2 mg **M2** was dissolved in 1 mL of THF or 1,4-dioxane at RT. 1 mL of the anti-solvents, mesitylene, *n*-butylbenzene, 1,2-dimethoxybenzene, 1,3-dimethoxybenzene, and *n*-tetradecane, was then added into separate THF and 1,4-dioxane solutions. Finally, the solvent mixtures were left to evaporate at RT for 5-10 days to obtain crystals of **M2**. After 10 days, transparent colourless needle shape crystals were found to crystallise from the 1,4-dioxane/mesitylene system (**M2-1**, Figure 3.6). The crystals were too small for in-house data collection and instead were subjected to analysis with synchrotron radiation. Powders or very small needle shape crystals were obtained from the other systems and those crystals were even too small for synchrotron X-ray data analysis.

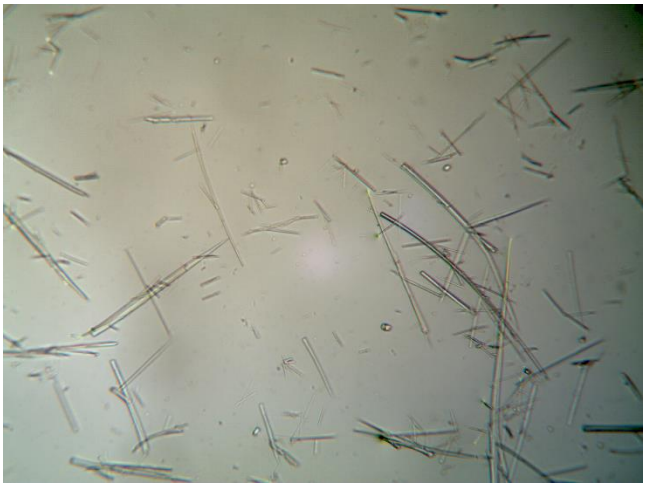

Figure 3.6. Optical photograph of **M2-1** recorded using a microscope.

M2-1 ($C_{27}H_{18}O_6$) crystallised from a 1,4-dioxane and mesitylene solution in the triclinic space group $P\bar{1}$. The asymmetric unit for **M2-1** comprises one complete **M2**. The single crystal data showed **M2** adopted a non-planar conformation, which was caused by a slight dihedral angle between the benzene core and adjoining benzene

rings (Figure 3.4b). The three dihedral angles varied and were found to be 23.8°, 34,2°, and 40.2°. In the crystal structure of **M2-1**, the 'A-A' packing style led to the formation of a 2.8 nm non-interpenetrated mesoporous hexagonal network of **M2** molecules (Figure 3.7a). The plane of **M2** molecules was offset, but the faces of the phenyl molecules were aligned in a parallel arrangement and the stacked of **M2** layers were separated by ~3.8 Å (Figure 3.7b). The $R_2^2(8)$ hydrogen bonding interactions were continuous and lead to the formation of a HOF structure with mesopores that made up approximately 54.3 % of the unit cell volume [1621.72 Å^3 (V_{cell} = 2985.1 Å^3)].

*2.2.1 The SCXRD structure of **M2-1***

Crystal data for **M2-1** (200 K): Formula $C_{27}H_{18}O_6$; M = 438.41, triclinic $P\bar{1}$, colourless needle shape crystals; a = 3.7658(4) Å, b = 29.691(3) Å, c = 30.402(3) Å, α = 61.631(9) °, β = 86.803(10) °, γ = 89.946(10) °; V = 2985.1(6) Å^3; ρ = 0.488 g/cm^3; Z = 2; μ(Mo-Kα) = 0.032 mm^{-1}; F (000) = 456; crystal size = 0.047 × 0.03 × 0.019 mm; T = 200 (2) K. 7649 reflections measured (2.96 < 2θ < 43.74 °), 4436 unique (R_{int} = 0.1058), 1313 ($I > 2\sigma(I)$); R_1 = 0.1051 for observed and R_1 = 0.1824 for all reflections; wR_2 = 0.3007 for all reflections; max/min difference electron density = 0.251 and -0.291 e·Å^{-3}; data/restraints/parameters = 4436/267/304; GOF = 0.81.

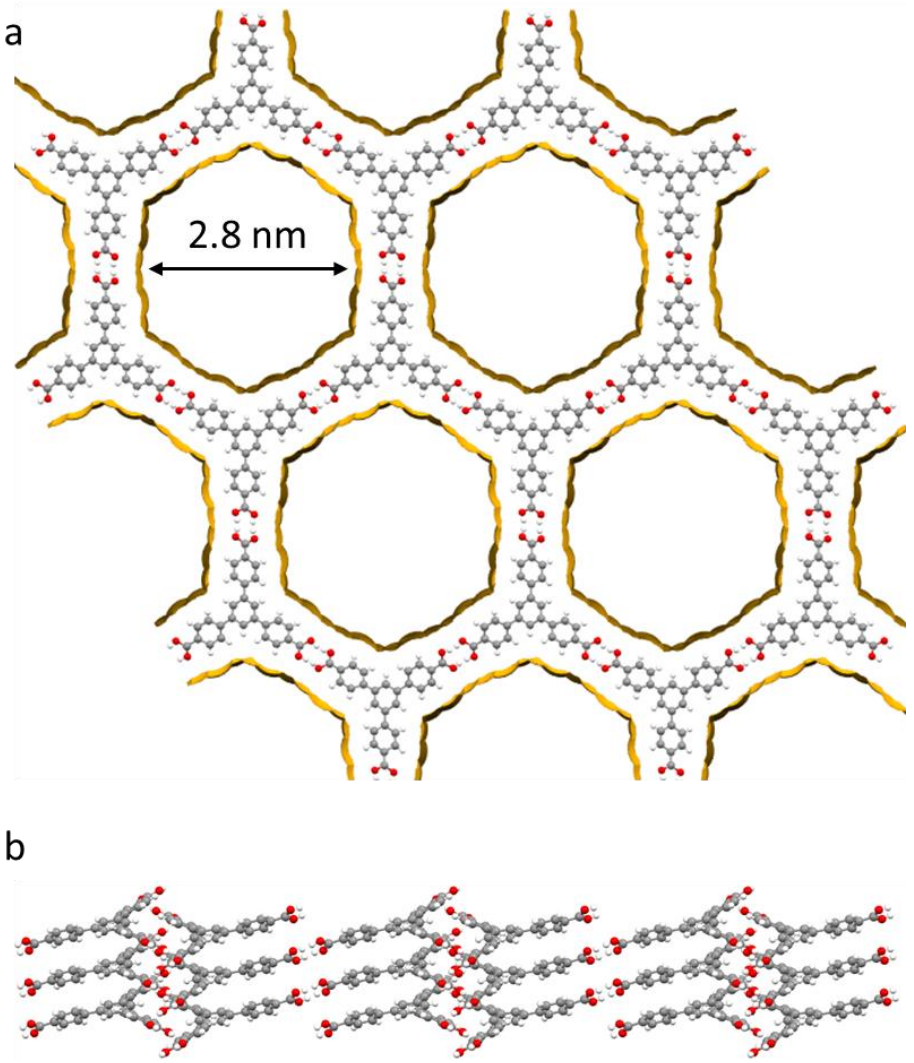

Figure 3.7. a) Crystal packing diagram of **M2-1** recorded at 200 K viewed along the *a* axis with the walls of the 1-D pores highlighted in yellow. The empty, solvent-accessible space (1.4 Å probe radius, 0.1 Å grid spacing). b) Viewed along the *b* axis. Grey: carbon, red: oxygen, white: hydrogen.

To evaluate the stability of **M2-1**, *n*-pentane was first used to exchange with the crystallisation solvents in the crystal pores. Initially, 1,4-dioxane and mesitylene were removed with a syringe and the crystals were immediately immersed in 10 mL of *n*-pentane. The *n*-pentane was refreshed every 12 hrs. After using *n*-pentane to exchange with the crystallisation solvents for 5 days, the crystals were degassed at RT for 2 hrs under a dynamic vacuum (yield: 89 %). The crystals (**M2-2**) appeared to lose some crystallinity during activation and the SEM images recorded afterward showed

they broke up into small pieces (Figure 3.8). After activation, the crystals of **M2-2** were too small for analysis by SCXRD, even using synchrotron radiation.

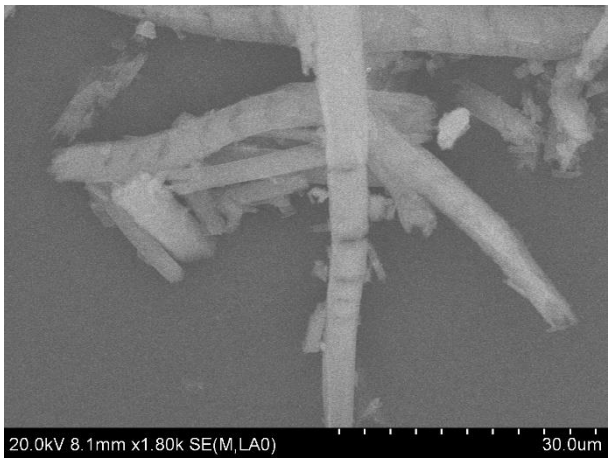

Figure 3.8. SEM image of **M2-2** recorded after crystal activation under dynamic vacuum. Scale bars are included in the bottom right corner of the SEM images.

*2.2.2 The ED structure of **M2-2***

Since small crystals of HOFs can be characterised by 3-D electron diffraction (3-D ED)[12], attempts were made to characterise the activated microcrystals of **M2-2** by 3-D ED. A crystal of **M2-2** was cooled to 97 K and collected by continuously tilting the sample stage. Data was collected using the software Instamatic,[13] and the acquired frames were then processed using XDS.[14] Reflection conditions were examined using the ED software package.[15] The structure was solved using SHELXT.[16] All the non-hydrogen atoms were located in the initial structure solution (Figure 3.9). The simulated PXRD pattern from the ED structure matched the experimental pattern well, and the structure comparison between **M2-1** and **M2-2** showed these structures had very similar cell parameters (Figure 3.10, 3.11). As there was no obvious change between the PXRD pattern and ED structure of **M2-2**, it appeared that **M2-1** maintained its structure during the crystal activation procedure.

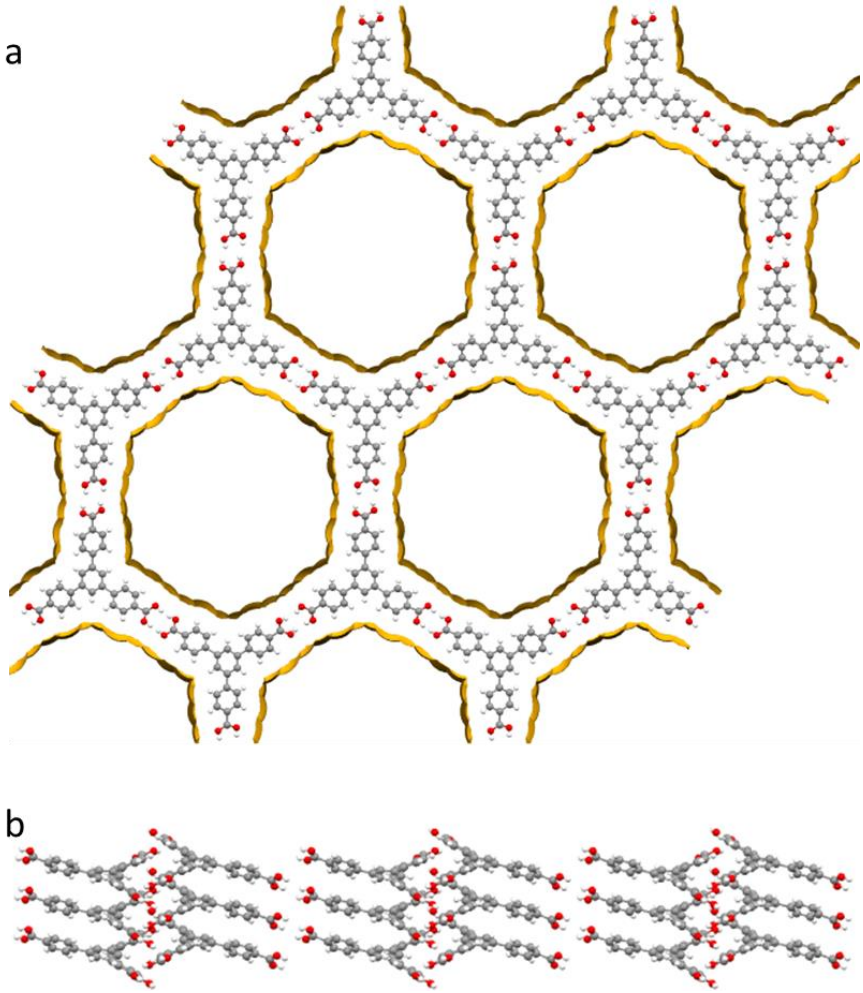

Figure 3.9. a) Crystal packing diagram of **M2-2** recorded at 97 K determined by 3-D ED and viewed along the *a* axis with the walls of the guest free 1-D empty pores highlighted in yellow. The empty, solvent-accessible space (1.4 Å probe radius, 0.1 Å grid spacing) makes up approximately 55.9 % of the unit cell volume [1869.19 $Å^3$ (V_{cell} = 3340.9 $Å^3$)]. b) Viewed along the *b* axis, the plane of **M2** molecules offset, but the faces of the phenyl molecules are aligned in a parallel arrangement and the stack of **M2** are separated by 3.910 Å

Electron diffraction single crystal data for **M2-2**: Formula $C_{27}H_{18}O_6$; M = 438.41, triclinic $P\bar{1}$, colourless needle shape crystals; a = 3.9100(8) Å, b = 30.780(6) Å, c = 31.920(6) Å, α = 119.52(3) °, β = 90.20(3) °, γ = 91.61(3) °; V = 3340.81(15) $Å^3$; ρ = 0.418 g/cm^3; Z = 2; λ = 0.0251 Å; T = 97 K; index ranges, $-3 \leq h \leq 3$, $-26 \leq k \leq 22$, $-27 \leq l \leq 24$; 6954 reflections measured, 3316 unique (R_{int} = 0.5384), completeness (to 1.16 Å resolution) = 73 %, R_1 (ED model) ($I > 2\sigma(I)$) = 0.5078.

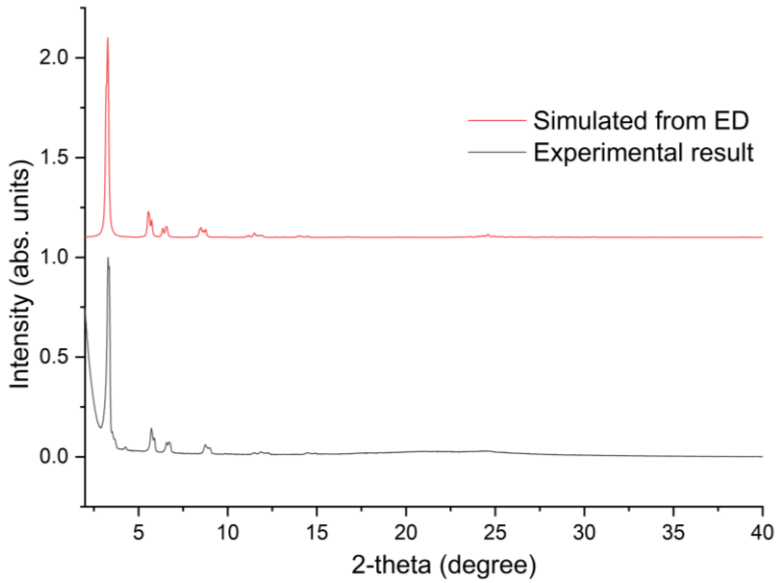

Figure 3.10. PXRD patterns of desolvated **M2-2** recorded at 298 K (black) and simulated pattern from ED structure recorded at 97 K (red).

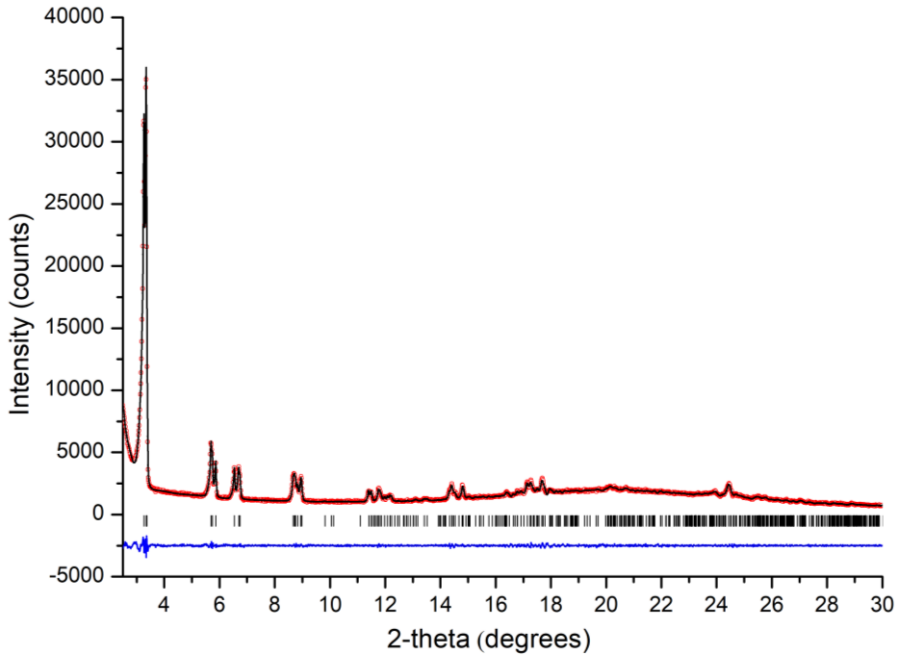

Figure 3.11. PXRD pattern fitting attempt of **M2-2** with Rietveld intensities using comparable structural parameters to those determine for **M2-1**. Red circles: experimental PXRD pattern, black line: fitting pattern, blue curve: difference between experimental and refinement, black bars: reflection positions, Rp = 2.44%, Rwp = 3.31%. ($P\bar{1}$, a = 7.972(4) Å, b = 30.808(1) Å, c = 30.099(8) Å, α = 61.238(2) °, β = 88.690(4) °, γ = 88.251(4) °; V = 6476.9(4) Å^3).

A DSC plot of **M2-2** recorded up to 300 °C showed no obvious phase transformations were evident up to this temperature (Figure 3.12). In the TGA plot of **M2-2** recorded after isolating the crystals from *n*-pentane, a ~40% weight loss was observed before 120 °C, which was attributed to a loss of *n*-pentane from the crystal pores (Figure 3.13). Then, no further weight loss steps were observed until 320 °C, which correlates with the DSC result (Figure 3.12). From the TGA plot, the compound was found to have fully decomposed by 630 °C.

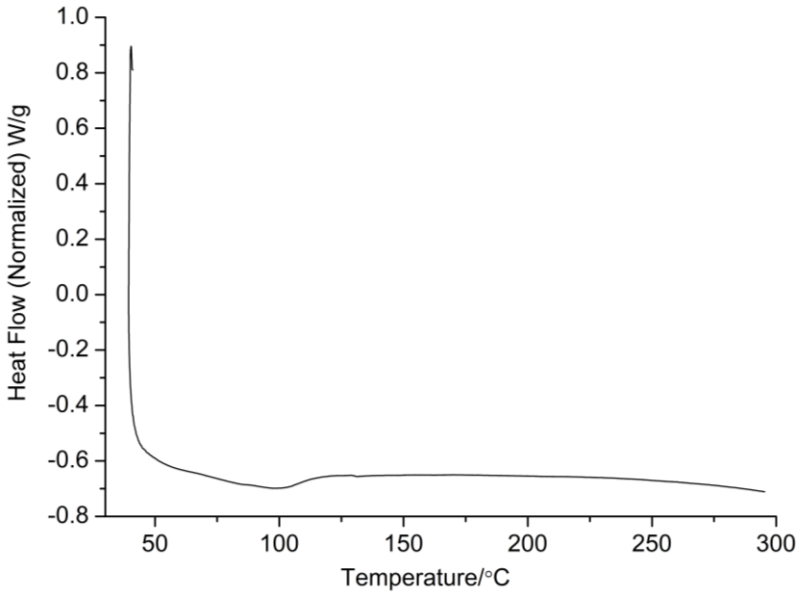

Figure 3.12. DSC plot for **M2-2** recorded over the temperature range 30 °C to 300 °C, using a single heat cycle. The DSC was recorded after removing the *n*-pentane solvent from the crystal pores of **M2-2** at RT under a dynamic vacuum for 2 hrs.

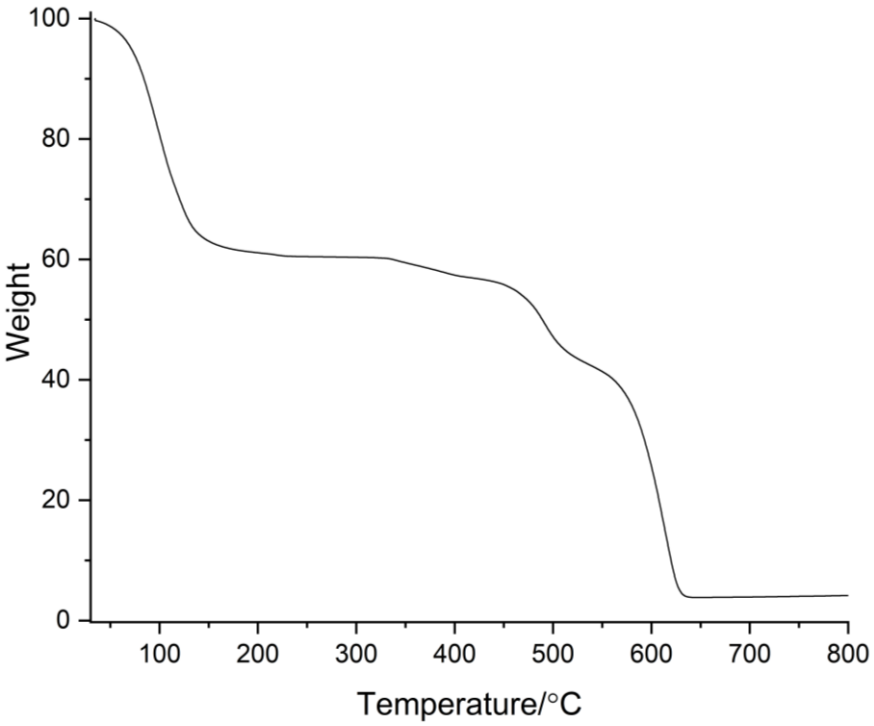

Figure 3.13. TGA plot for **M2-1** isolated directly from *n*-pentane and recorded over the temperature range 30 °C to 800 °C under a dry nitrogen gas flow.

Before the porosity of **M2-2** was measured, its stability under a dynamic vacuum was investigated. PXRD patterns recorded after degassing the sample for different amounts of time under dynamic vacuum at 298 K are stacked together in Figure 3.14. The PXRD patterns appeared to show no obvious change to the structure after degassing for 24 hrs. The PXRD patterns, therefore, indicated that **M2-2** was stable under dynamic vacuum conditions for at least 24 hrs.

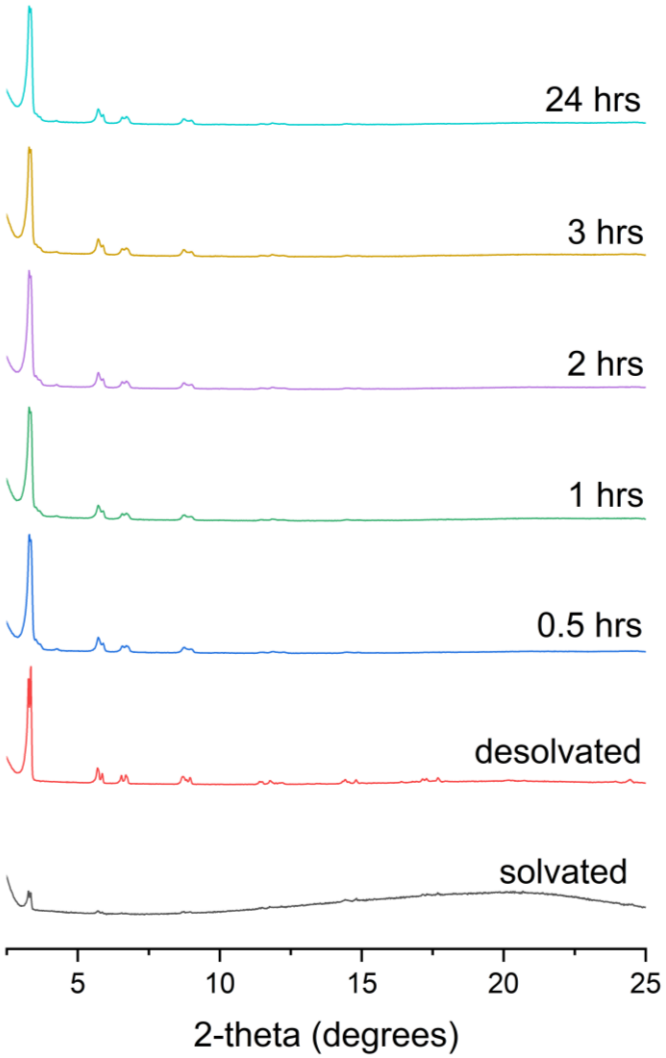

Figure 3.14. PXRD patterns of desolvated **M2-2** recorded after degassed the crystals for different times under dynamic vacuum at 298 K. The PXRD pattern of *n*-pentane solvated **M2-1** is shown at the bottom (black) and the PXRD pattern of desolvated **M2-2** that was recorded after removing the *n*-pentane solvent from the crystal pores of **M2-2** at RT under dynamic vacuum for 2 hrs (red).

The N_2 sorption isotherm for **M2-2** recorded at 77.3 K is shown in Figure 3.15. In the adsorption isotherm, there was a characteristic mesoporous step, but the BET surface area for **M2-2** was only 503 m^2 g^{-1}, which was much lower than expected, and even lower than the surface area of δ-**TMA** (chapter 2). In an attempt to improve the experimental surface area of **M2-2**, the crystals were activated using different conditions, including evacuation with supercritical CO_2, which has been shown to

maximise the potential capability of porous materials[17]. Despite attempting to activate **M2-2** using more gentle conditions the surface area did not improve. The pore size distribution plot of **M2-2** showed the pore width was mainly distributed around 2.8 nm, in agreement with the **M2-2** mesoporous structure (Figure 3.16). There was also a distribution smaller at 3.6 nm, which may be due to the packing of amorphous particles in **M2-2**. In the SEM images of **M2-2** (Figure 3.8) there were some non-crystalline particles present, and it was very hard to quantify the relative quantities of amorphous and crystalline particles. During the 3-D ED analysis, some particles did also not diffract, which proved non-crystalline particles were mixed in with **M2-2**. The existence of non-crystalline particles is likely to have contributed to the low adsorption capacity of **M2-2** and the pore width at 3.6 nm.

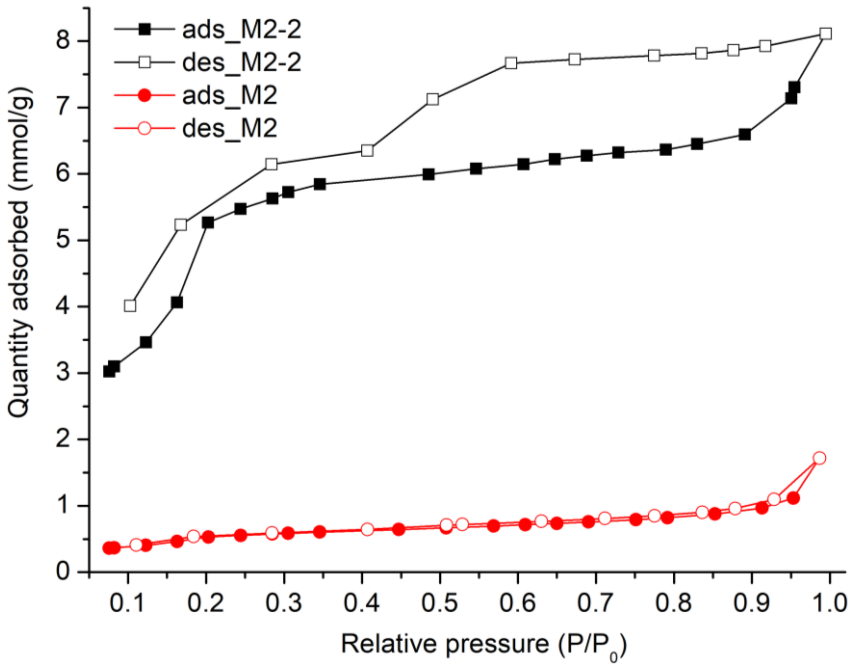

Figure 3.15. N_2 sorption isotherms for **M2-2** (black) and commercial **M2** (red) molecule recorded at 77 K.

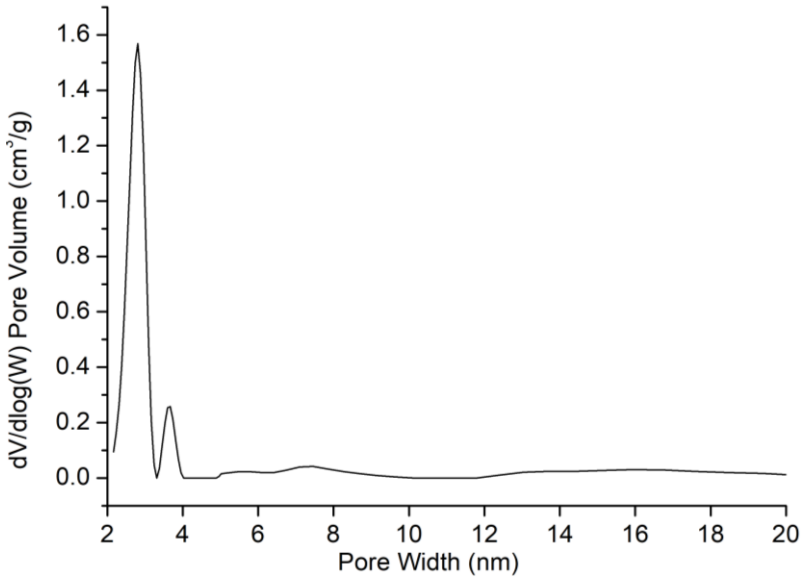

Figure 3.16. Pore size distribution plot for **M2-2** determined from it N2 sorption isotherm recorded at 77 K.

The PXRD pattern recorded after N_2 sorption showed no obvious change compared with **M2-2** (Figure 3.17), proving no obvious changes happened to **M2-2** during the sorption isotherms. However, the existence of unknown quantities of amorphous particles was not quantified during this study.

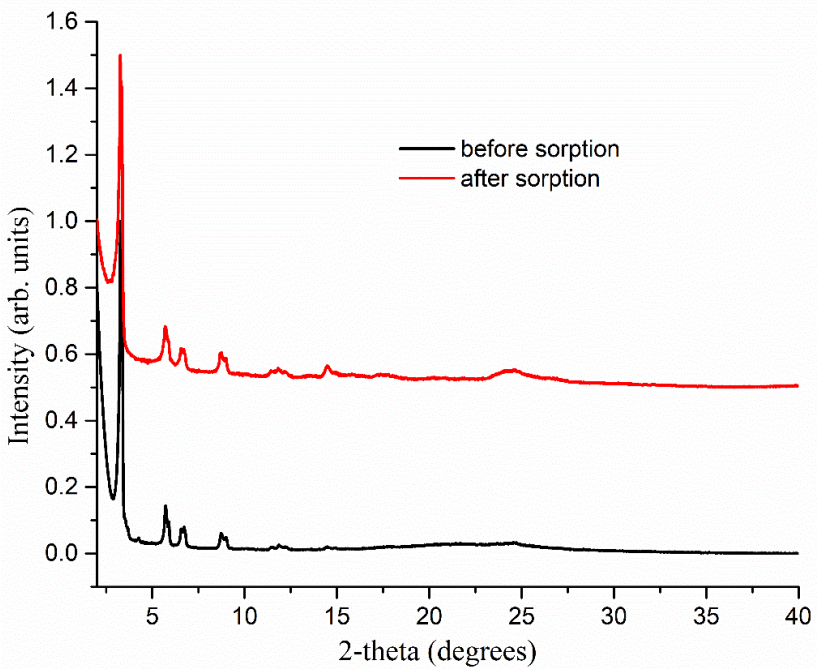

Figure 3.17. PXRD patterns of **M2-2** before (black) and after N_2 sorption (red).

2.3

*5''-(4'-((oxo-l3-methyl)-l3-oxidaneyl)-[1,1'-biphenyl]-4-yl)-[1,1':4',1'':3'', 1''':4''',1''''-quinquephenyl]-4,4''''-dicarboxylic acid (**M3**)*

Compared to **M2**, the molecule **M3** is an extended version that contains extra phenyl groups, and no single crystal structures of **M3** have yet been reported. To crystallise **M3**, 2 mg of the compound was dissolved in 1 mL THF at RT. Then 1 mL of the anti-solvents (mesitylene, *n*-butylbenzene, 1,2-dimethoxybenzene, 1,3-dimethoxybenzene, and *n*-tetradecane) was added into separate THF solutions. Finally, the solvent mixtures were left to evaporate at RT for 5 days to obtain crystal of **M3**. After 5 days, transparent colourless rod shape crystals were crystallised from THF and *n*-butylbenzene system (**M3-1**), and a suitable crystal was selected for analysis with synchrotron radiation. After 6-10 days, similar rod-shaped crystals were found to have crystallised from the other solvent systems.

M3-1 ($16(C_{45}H_{30}O_6)\cdot 2(H_2O)$) crystallised from a THF and *n*-butylbenzene solution in the orthorhombic space group *A*ea2. The asymmetric unit for **M3-1** comprises 16 complete **M3** molecules and disordered solvent molecules that were modelled as water, H_2O. The displacement ellipsoid plot of **M3** from the single crystal structure of **M3-1** shows **M3** is not a planer molecule but instead possesses a bowl-like shape (Figure 3.18).

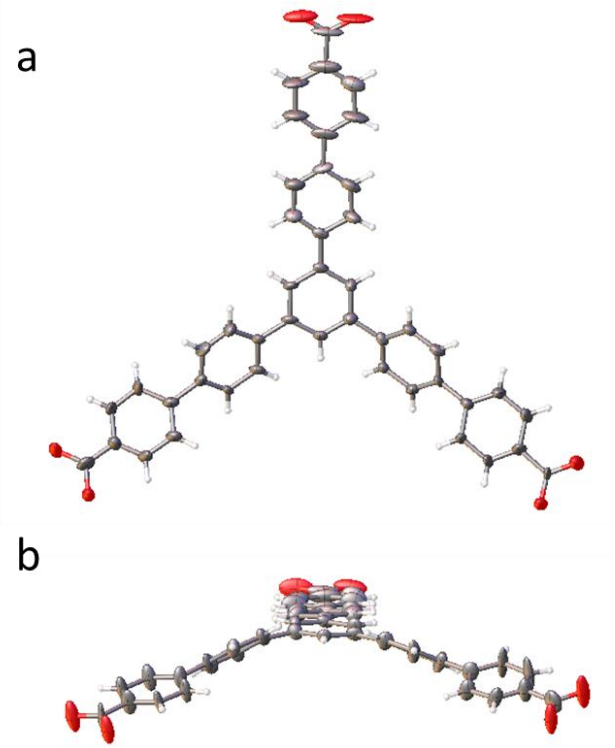

Figure 3.18. Displacement ellipsoid plot of **M3** from the single crystal structure of **M3-1**. a) front view; b) side view. Ellipsoids displayed at 50% probability level. Grey: carbon, red: oxygen, white: hydrogen.

The SCXRD structure of **M3-1** showed adjacent **M3** molecules interconnected through double $R_2^2(8)$ hydrogen bonds to form a regular hexagonal honeycomb net (**hcb**) (Figure 3.19a). The **hcb** honeycomb net in **M3-1** was curved because of the bowl-like structure of the **M3** molecule (Figure 3.19b) and the large cavity in the hexagonal motif was filled by interwoven **hcb** honeycomb nets to generate a complex two-dimensional (2-D) layered structure. In total ten honeycomb nets were interwoven into one **hcb** honeycomb net to form an 11-fold interpenetrated structure (Figure 3.20). A rectangular pore was observed in **M3-1** viewed along *a* axis (Figure 3.22a). Disordered solvents were found to occupy the 21.8 Å × 12.7 Å size pores, which makes up approximately 27.2 % of the unit cell volume [46402.32 Å^3 (V_{cell} = 170501 Å^3)].

*2.3.1 The SCXRD structure of **M3-1***

Crystal data for **M3-1** (100 K): Formula 16($C_{45}H_{30}O_6$)·2(H_2O); M = 10699.2,

orthorhombic *A*ea2, colourless cuboid shape crystals; a = 114.3226(3) Å, b = 42.9191(10) Å, c = 34.7492(10) Å, V = 170501.2(8) Å^3; Z = 128; crystal size = 0.134 × 0.063 × 0.039 mm; T = 100 (2) K. 49320 reflections measured (1.50 < 2θ < 50.14 °), R_{int} = 0.0563, R_1 = 0.0906 for observed and R_1 = 0.1462 for all reflections; wR_2 = 0.3803 for all reflections; max/min difference electron density = 0.9 and -0.7 e·Å^{-3}; restraints/parameters = 0/7874; GOF = 1.527.

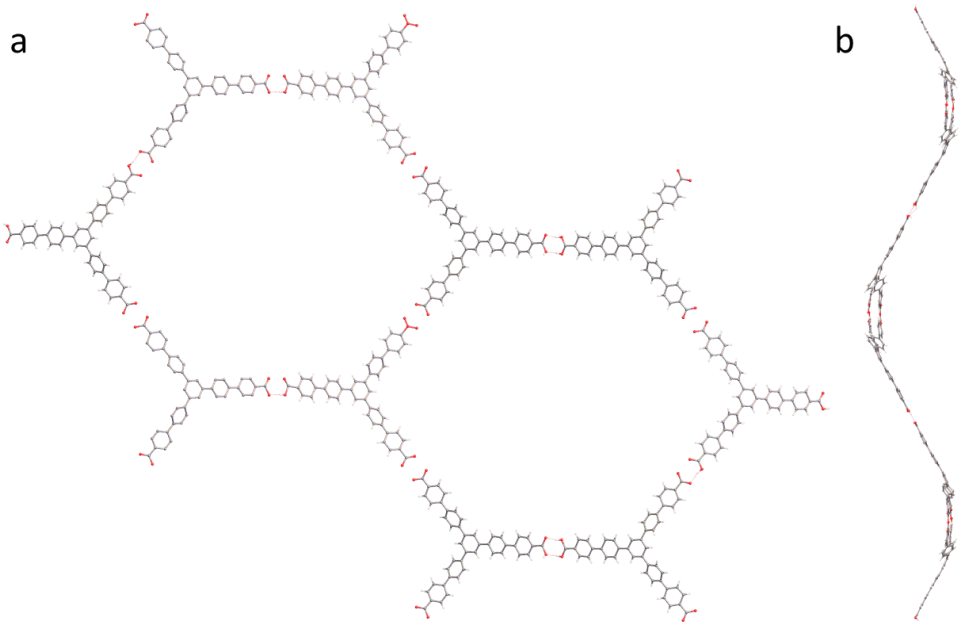

Figure 3.19. a) The hydrogen-bonded **hcb** honeycomb nets in the single crystal structure of **M3-1**, viewed along the *c* axis, and b) *b* axis. Disordered solvents are omitted for clarity. Grey: carbon, red: oxygen, white: hydrogen.

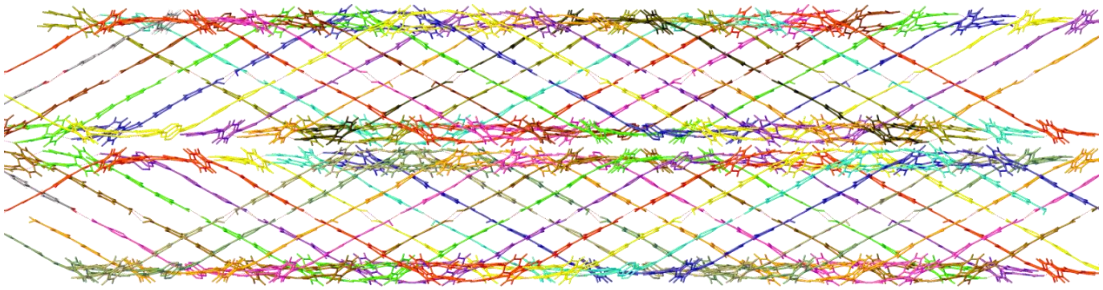

Figure 3.20. Wireframe packing of entangled **hcb** honeycomb nets in the single crystal structure of **M3-1** viewed along the *b* axis showing the 11-fold interpenetrated structure. The **hcb** honeycomb nets shown in Figure 3.19 are shown in different colours.

Before evacuating the solvent from the pores of **M3-1**, the crystallisation was first exchanged with *n*-pentane. This was achieved by removing the THF and *n*-butylbenzene using a syringe before immersing the crystals in 10 mL *n*-pentane. The *n*-pentane was refreshed every 12 hrs, and after using *n*-pentane to exchange the crystallisation solvents for 5 days, the sample was finally and degassed at RT for 2 hrs under dynamic vacuum (yield: 92 %). The structure of the activated crystals, **M3-2**, was determined with SCXRD.

M3-2 ($C_{45}H_{30}O_6$) had monoclinic *C*2/c space group symmetry and its asymmetric unit comprises one complete **M3** molecule. On analysis of the crystal structure, it was found that **M3-2** had a different network of $R_2^2(8)$ hydrogen bonding interactions to that found in the solvated **M3-1** structure (Figure 3.21a). In **M3-2**, each **M3** molecule formed $R_2^2(8)$ hydrogen bonding dimers to two neighbouring **M3** molecules, while the third $R_2^2(8)$ hydrogen bonding dimer was lost from the HOF structure during the solvent exchange or after activation steps. In the structure of **M3-2**, the basic hydrogen-bonded network is shown in Figure 3.21a and the network still appears to have a wave-shape topology because of the bowl-like shaped **M3** molecule.

*2.3.2 The SCXRD structure of **M3-2***

Crystal data for **M3-2** (100 K): Formula $C_{45}H_{30}O_6$; M = 666.69, monoclinic *C*2/c, colourless cuboid shape crystals; a = 40.267(4) Å, b = 6.9824(4) Å, c = 27.338(3) Å; β= 103.388(7) °, V = 7477.5(12) Å^3; ρ = 1.184 g/cm^3; Z = 8; μ(Mo-Kα) = 0.074 mm^{-1}; F (000) = 2784; crystal size = 0.12 × 0.02 × 0.02 mm; T = 100 (2) K. 14257 reflections measured (3.17 < 2θ < 49.72 °), 5314 unique (R_{int} = 0.1333), 1938 (I > 2σ(I)); R_1 = 0.2796 for observed and R_1 = 0.3625 for all reflections; wR_2 = 0.6039 for all reflections; max/min difference electron density = 0.771 and -0.458 e·Å^{-3}; data/restraints/parameters = 5314/684/463; GOF = 1.530.

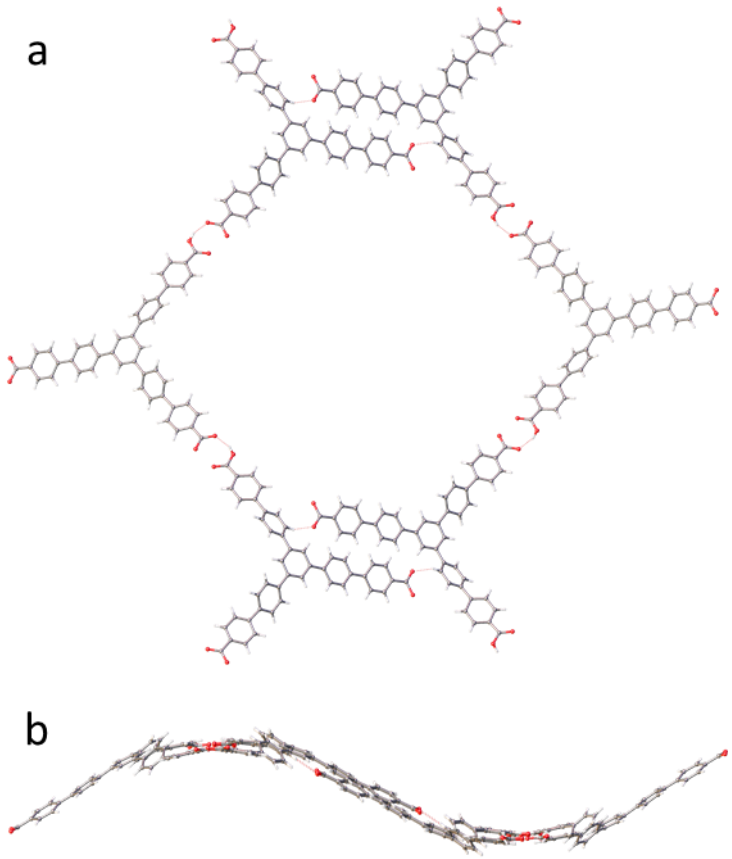

Figure 3.21. a) The hydrogen-bonded network in **M3-2** found in the SCXRD viewed along *c* axis; b) side view showing the wave-like topology of the network. Grey: carbon, red: oxygen, white: hydrogen.

In **M3-2**, the adjacent **M3** molecules were interconnected through two complementary $R_2^2(8)$ hydrogen-bonded motifs that formed part of the hexagonal honeycomb **hcb** net found in the **M3-1** structure. However, the third carboxylic acid unit in **M3-2** was disconnected, and instead, two biphenyl arms of **M3** were arranged in a close-packed aligned arrangement. The rearrangement caused the **hcb** hydrogen-bonded net found in **M3-1** to shrink to the smaller network shown in Figure 3.21, which led to the pore between six **M3** molecules in **M3-2** to decrease to 10.1 Å × 6.9 Å, which is only 22.79 % of the size of the pores in **M3-1** (Figure 3.22b). The smaller pores in **M3-2** make up approximately 6.2 % of the unit cell volume [461.68 Å^3 (V_{cell} = 7477.48 Å^3)]. Structural comparison between the SCXRD structures of **M3-1** and **M3-2** revealed that the closer packing of **M3** molecules in **M3-2** led the pores to shrink (Figure 3.22).

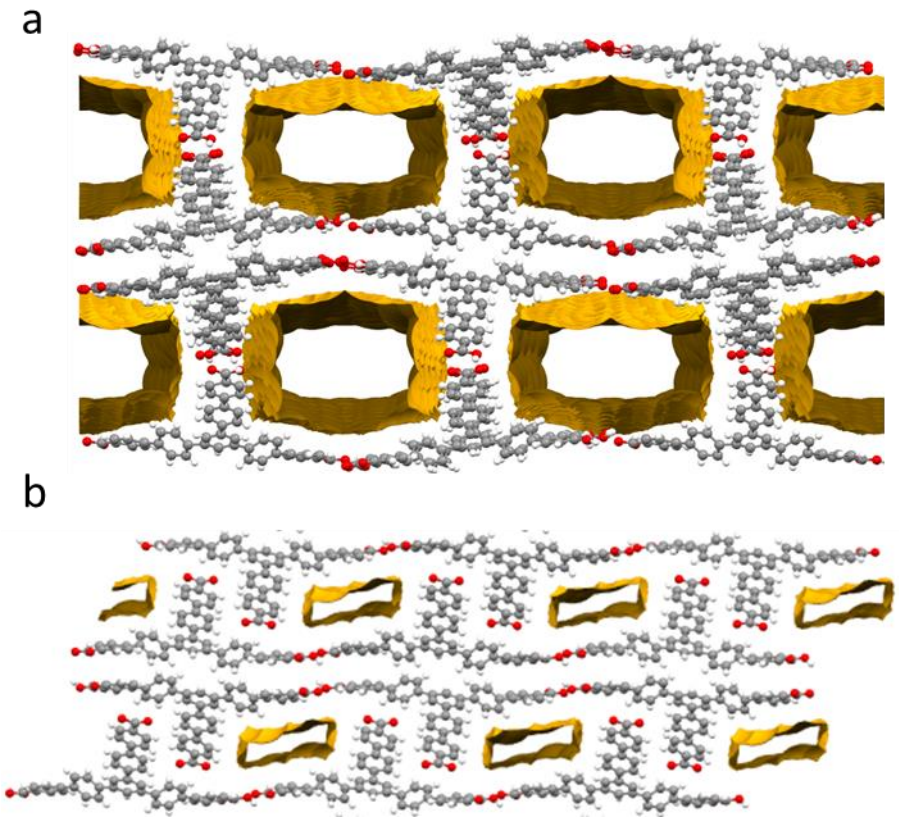

Figure 3.22. a) Crystal packing diagram of **M3-1** recorded at 100 K and viewed along the *a* axis with the walls of the guest free 1-D empty pores highlighted in yellow. The disordered solvents are omitted for clarity. The empty, solvent-accessible space (1.4 Å probe radius, 0.1 Å grid spacing). b) Crystal packing diagram of **M3-2** recorded at 100 K viewed along the *b* axis with the walls of the guest free 1-D empty pores highlighted in yellow. The empty, solvent-accessible space (1.4 Å probe radius, 0.1 Å grid spacing). Grey: carbon, red: oxygen, white: hydrogen.

*2.4 5'-(4-carboxy-2,3,5,6-tetrafluorophenyl)-2,2'',3,3'',5,5'',6,6''-octafluoro-[1,1':3',1''-terphenyl]-4,4''-dicarboxylic acid (**M4**)*

Although **M2** crystallised from dioxane and mesitylene to form a porous HOF with apparent mesopores the activated structure, **M2-2**, had a low BET surface area. In **M2-2**, the HOF layers were only stabilised by relatively weak intermolecular interaction, and to investigate if this accounted for the lack of stability and porosity, a

new co-crystal to increase the interaction between the HOF layers was designed. The idea was to use fluorinated and non-fluorinated aromatics because they are known to form electrostatically stabilised π-π-stacking motifs in molecular crystals[18,19]. 5'-(4-carboxy-2,3,5,6-tetrafluorophenyl)-2,2",3,3",5,5",6,6"-octafluoro-[1,1':3',1"-terphenyl]-4,4"-dicarboxylic acid (**M4)** was therefore designed, and the initial plan was to grow a co-crystal of **M2** and **M4** (Figure 3. 23), which would have a similar structure to **M2-2**, but with stronger interactions between fluorated aromatic arms of **M4** and aromatic in the arms of **M2** in the pore walls. The idea was to sandwich HOF layers of **M2** (Figure 3.4c) between layers of **M4** in an "A-B" stacking arrangement.

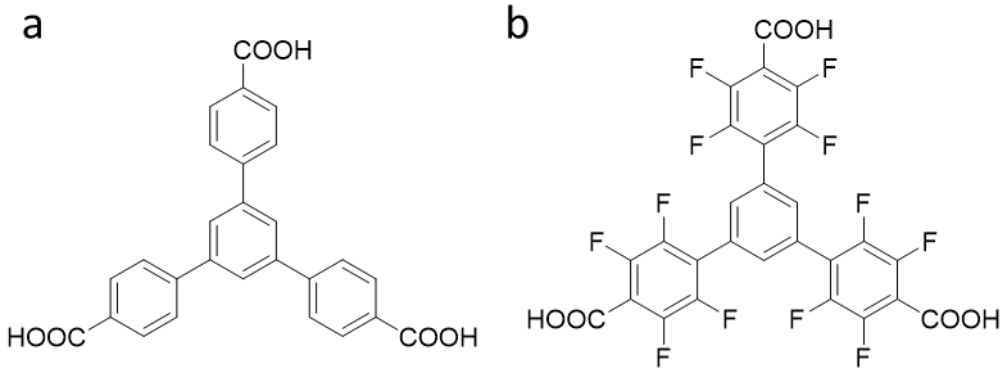

Figure 3.23. The structure of **M2** (a) and **M4** (b).

The same crystallisation conditions that afforded the non-interpenetrated **M2-1** structure (1,4-dioxane/mesitylene) were also used to co-crystallise **M2** and **M4** because **M4** is soluble in 1,4-dioxane (Figure 3. 7). The following process was used: 2 mg of **M2** and 3 mg of **M4** were dissolved in 2 mL of 1,4-dioxane at RT. 2 mL of mesitylene was then added into the 1,4-dioxane solution and the solvent mixture was left to evaporate at RT for 7 days. The resulting **M2-M4** particles that were isolated by filtration were found to contain very small needle-shaped crystals that were too small and of inadequate quality for single-crystal structure analysis, despite attempting data collections with synchrotron radiation. SEM images of the **M2-M4** particles showed a combination of poorly crystalline needle-like particles with rough edges and particles with spherical-like morphologies (Figure 3.24). The PXRD pattern of the **M2-M4** particles showed some similarities to the PXRD pattern of **M2-1**

(Figure 3.25) which cannot be determined to co-crystal or a mixture of **M2** and **M4**. The porosity of the **M2-M4** particles was also investigated. The nitrogen sorption isotherm recorded at 77 K indicated that the BET surface area of **M2-M4** was only 50 m^2 g^{-1} and the isotherm showed a limited nitrogen sorption and there is sharp increasement at P/P0 =1 due to the capillary condensation. It did not show a mesoporous step in the adsorption isotherm (Figure 3.26). Due to the unclear and non-porous structure of **M2-M4** particles, **M4** was instead crystallised in pure from 1,4-dioxane/mesitylene.

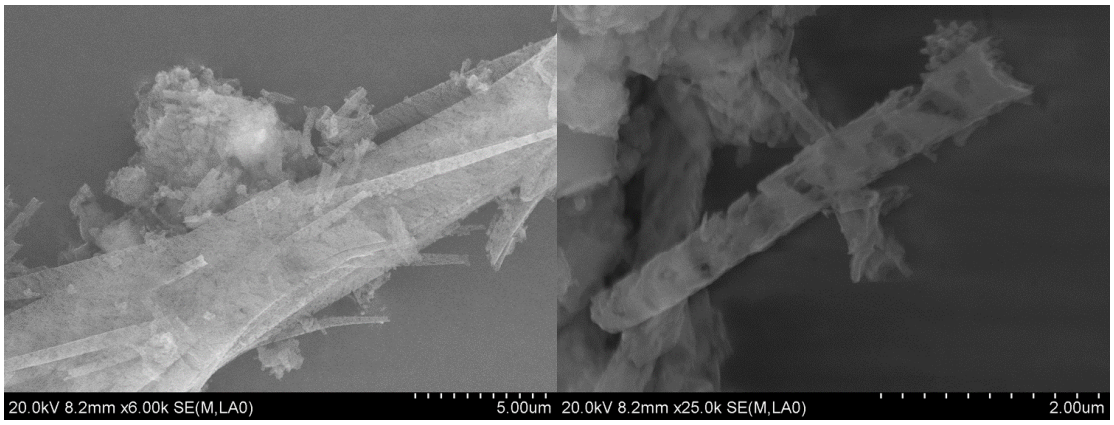

Figure 3.24. SEM image of the particles from the crystallisation of **M2** and **M4** in 1,4-dioxane/mesitylene system. Scale bars are included in the bottom right corner of the SEM images.

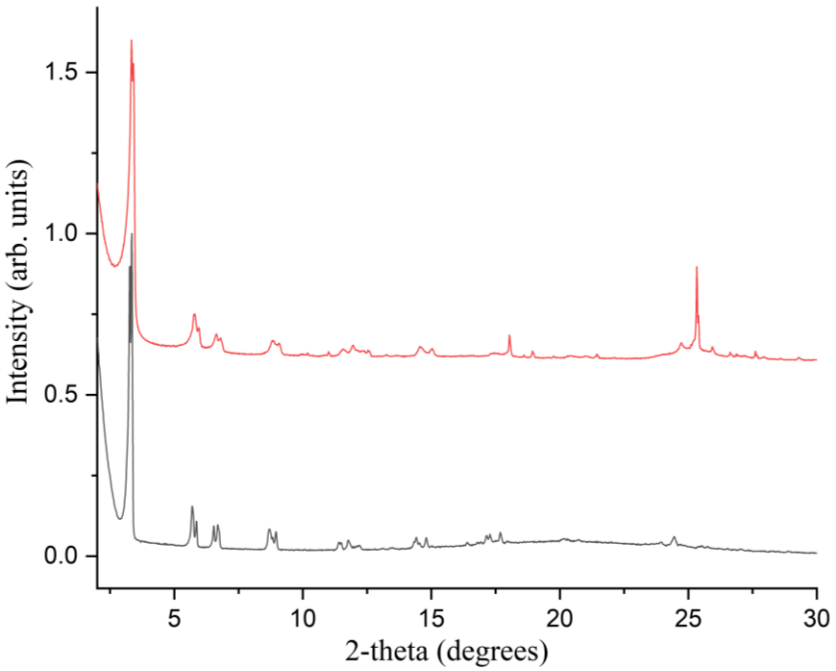

Figure 3.25. PXRD patterns of **M2-1** (black) and **M2-M4** (red).

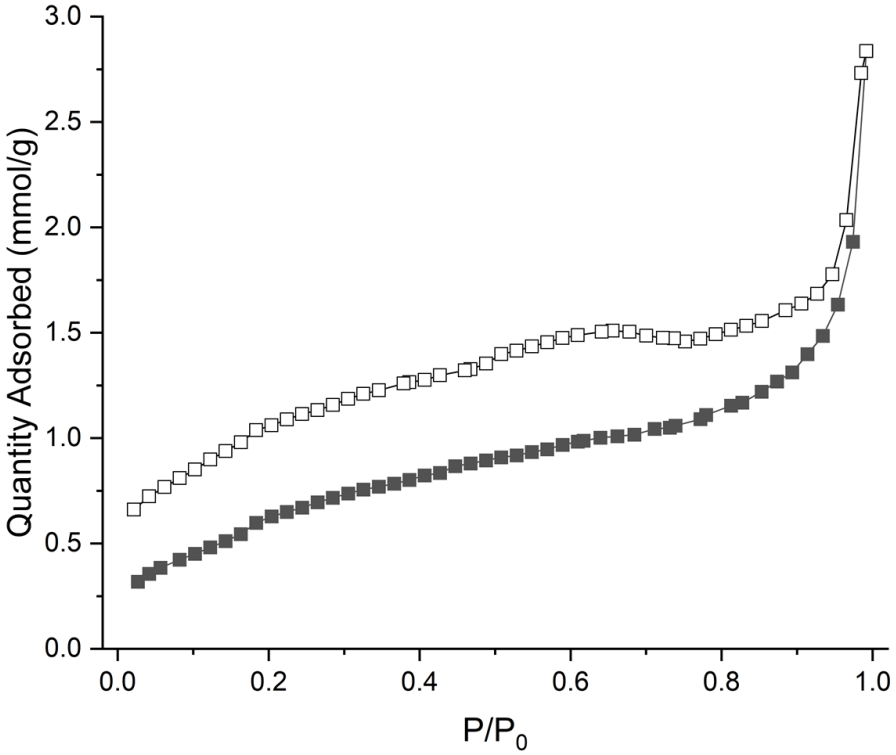

Figure 3.26. Nitrogen sorption isotherm of **M2-M4** recorded at 77 K.

To crystallise **M4** from 1,4-dioxane/mesitylene the following process was used. 2 mg of **M4** was dissolved in 2 mL of 1,4-dioxane at RT. 2 mL of mesitylene was then

added into 1,4-dioxane solution and the solvent mixture was left to evaporate at RT for 7 days. From the crystallisation, transparent colourless needle-shaped crystals of **M4-1** ($C_{27}H_6O_6F_{12}$·2($C_4H_8O_2$)) were isolated that had crystallised in the monoclinic *C*2/c space group. The asymmetric unit for **M4-1** comprises one complete **M4** and two ordered solvent molecules that were modelled as dioxane, $C_4H_8O_2$. The single crystal data of **M4-1** showed that **M4** was a twisted molecule and two dioxane molecules formed hydrogen bonds with two of the carboxylic acid groups of **M4** (**M4-1**, Figure 3.27). The three dihedral angles between the benzene core and tetrafluorophenyl group are 39.5°, 48.6° and 49.2°, and although **M2** and **M4** possessed similar molecular structures, the single crystal structures that were crystallised from the same condition were different. 1,4-Dioxane formed hydrogen bonds with the carboxylic acid group in **M4-1**, which interrupted the $R_2^2(8)$ hydrogen bonding interactions between **M4** molecules. This could be due to differences in the H atom donor strength in **M4**, caused by the aromatic rings being fluorinated, which could explain why the idealised '**M2-M4**' co-crystal could not be grown from dioxane/mesitylene.

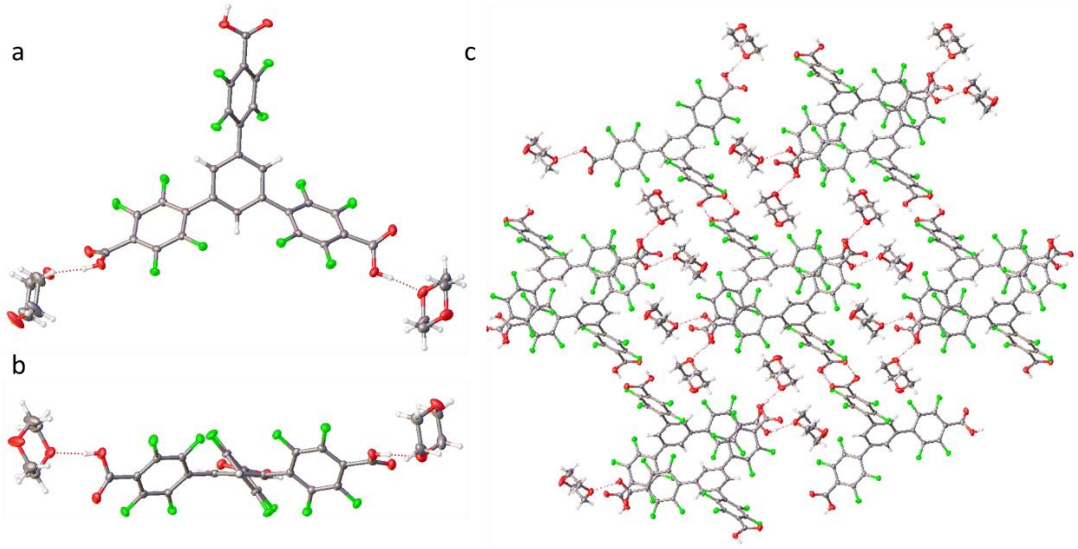

Figure 3.27. a,b) Displacement ellipsoid plot from the single crystal structure of **M4-1**. c) The packing of **M4-1** viewed along *b* axis. Ellipsoids displayed at 50% probability level. The hydrogen bonds are shown with red dashed lines. Grey: carbon, red: oxygen, white: hydrogen, green: fluorine.

*2.4.1 The SCXRD structure of **M4-1***

Crystal data for **M4-1** (100 K): Formula $C_{27}H_6O_6F_{12}\cdot 2(C_4H_8O_2)$; M = 636.50, monoclinic $C2/c$, colourless needle shape crystals; a = 34.4948(19) Å, b = 7.0851(4) Å, c = 31.2678(17) Å, β = 117.163(10) °; V = 6799.0(7) Å^3; ρ = 1.623 g/cm^3; Z = 8; μ(Mo-Kα) = 0.160 mm^{-1}; F (000) = 3360; crystal size = 0.062 × 0.035 × 0.03 mm; T = 100 (2) K. 19120 reflections measured (4.76 < 2θ < 65.98 °), 7475 unique (R_{int} = 0.0405), 6599 ($I > 2\sigma(I)$); R_1 = 0.0576 for observed and R_1 = 0.0635 for all reflections; wR_2 = 0.1475 for all reflections; max/min difference electron density = 0.555 and -0.431 e·Å^{-3}; data/restraints/parameters = 7475/0/520; GOF = 1.135.

*2.5 4,4',4''-(1,3,3a1,4,6,7,9-Heptaazaphenalene-2,5,8-triyl) tribenzoic acid (**M5**)*

4,4',4''-(1,3,3a1,4,6,7,9-Heptaazaphenalene-2,5,8-triyl) tribenzoic acid (**M5**) has been used to synthesise MOFs.[20] The heptazine core is conjugated and the molecule has also recently been studied as a photocatalyst,[21,22] including after being crystallised from methanol (PFC-42).[23] In the reported crystal structure of PFC-42, each molecule interacts with two neighbouring molecules through two O–H···O hydrogen bonds and this motif extends into a one-dimensional layer (Figure 3.28a). Adjacent 2-D layers stack in an 'A-B' mode through intermolecular π-π interactions (Figure 3.28b) and **M5** is densely packed in PFC-42.

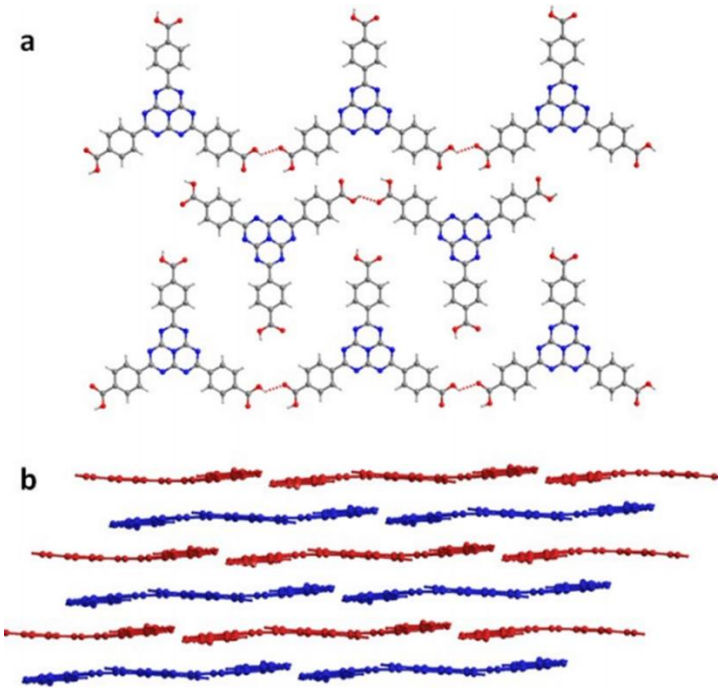

Figure 3.28. a) Reported crystal structure of PFC-42. Blue: N, red: O, grey: C. b) the 'A-B' packing mode of PFC-42 viewed along the *b*-axis. Reprint from *J. Mater. Chem. A*, **9**, 4687-4691, 2021. Copyright from 2021, Royal Society of Chemistry.

Here, **M5** was crystallised from other solvent systems to explore if different polymorphs could be isolated. 2 mg of **M5** was dissolved in 1 mL THF at RT, then 1 mL of the anti-solvents (mesitylene, *n*-butylbenzene, 1,2-dimethoxybenzene, 1,3-dimethoxybenzene, and *n*-tetradecane) were added into separate THF solutions. Finally, the solvent mixture was left to evaporate at RT. Luminous yellow needle shape crystals (**M5-1**) were obtained from THF/ 1,3-dimethoxylbenzene after 5 days and light-yellow powders were obtained from the other solvents systems.

M5-1 ($C_{27}H_{15}N_7O_6 \cdot (H_2O)$) crystallised from a THF and 1,3-dimethoxylbenzene solution in the triclinic space group $P\bar{1}$. The asymmetric unit for **M5-1** comprises one complete **M5** and one disordered solvent molecule that was modelled as water, H_2O. The SCXRD structure showed **M5** adopted a near-planar conformation (Figure 3.29a) and water molecule was found to be incorporated into the structure. In the structure, two carboxylic acid groups incorporated with water, and only one carboxylic acid could form $R_2^2(8)$ hydrogen bonding dimer with the adjacent **M5** molecule, which

formed a 16.9 Å × 13.9 Å size pore (Figure 3.29b). PXRD patterns for **M5-1** were recorded after the residual solvents in the crystallisation vial were removed with a syringe and the wet **M5-1** was transferred into PXRD plate without further preparation.

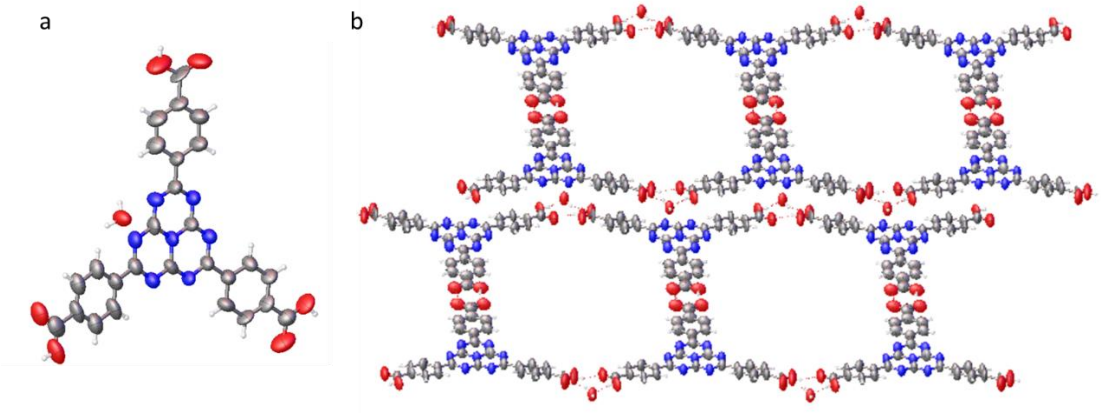

Figure 3.29. a) Displacement ellipsoid plot from the single crystal structure of **M5-1**. Ellipsoids displayed at 50% probability level. b) Crystal packing diagram of **M5-1** recorded at 100 K viewed along the *a* axis. Hydrogen bonds are shown with red dash lines. Grey: carbon, red: oxygen, white: hydrogen, blue: nitrogen.

The experimental PXRD pattern of **M5-1** was similar to the simulated pattern from the single crystal structure of **M5-1** but there were some addition peaks, and the diffraction pattern was quite noisy, which may indicate that the sample had low crystallinity (Figure 3.30). To evacuate the crystallisation solvent from the pores of **M5-1**, *n*-pentane was first used to exchange with the crystallisation solvent, and the same procedure that was used to activate **M2-1** was also used for **M5-1**. For **M5-1**, the *n*-pentane exchange was carried out for 5 days and the sample was then degassed under dynamic vacuum for 2 hrs at RT. **M5-1** was also degassed under dynamic vacuum for 12 hrs at 100 °C without carrying out the *n*-pentane solvent exchange first. After activation using both conditions, PXRD patterns of the activated **M5** materials were recorded, and both PXRD patterns showed **M5-1** lost some crystallinity during crystal activation (Figure 3.30). While the PXRD pattern recorded after the *n*-pentane exchange was similar to the **M5-1** solvate, the PXRD patterns recorded after

activation indicated **M5** transformed into a new phase after activation. Unfortunately, it was not possible to determine the desolvated structure of **M5** because of its low crystallinity. The water molecule in the framework was likely removed during activation, which could have led to the structure collapsing. To avoid the inclusion of water incorporated in the **M5-1** structure, anhydrous THF was used for the crystallisation of **M5**, but the same **M5-1** structure was obtained, possibly because the compound was not fully dry at the start of the crystallisation.

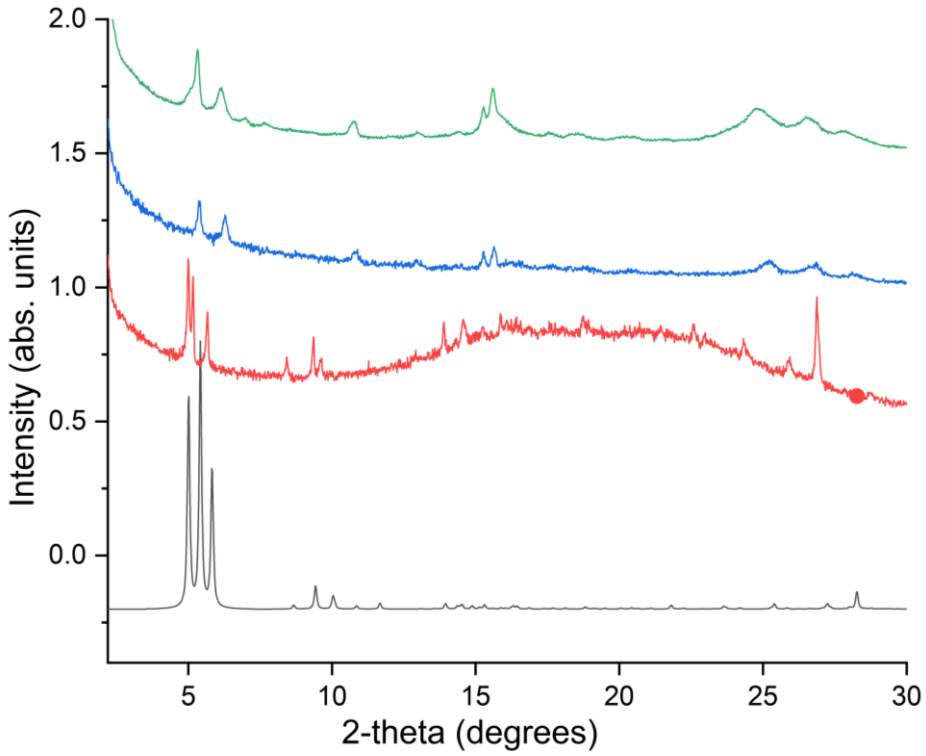

Figure 3.30. PXRD pattern simulated from the single crystal structure of **M5-1** (black), experimental PXRC for wet **M5-1** (red), experimental PXRD patterns are degassing the material under dynamic vacuum for 12 hrs at 100 °C (blue), and after degassing the *n*-pentane exchanged material (green).

*2.5.1 The SCXRD structure of **M5-1***

Crystal data for **M5-1** (100 K): Formula $C_{27}H_{15}N_7O_6 \cdot (H_2O)$; M = 551.47, triclinic $P\bar{1}$, transparent yellow needle shape crystals; a = 6.2794(6) Å, b = 17.813(3) Å, c = 19.1089(17) Å, α = 110.948(13) °, β = 95.233(9) °, γ = 99.027(2) °; V = 1946.2(4) Å^3; ρ = 0.941 g/cm^3; Z = 2; μ(Mo-Kα) = 0.066 mm^{-1}; F (000) = 568; crystal size = 0.4 ×

0.07 × 0.05 mm; T = 100 (2) K. 8604 reflections measured (3.87 < 2θ < 38.29 °), 3416 unique (R_{int} = 0.1117), 1585 ($I > 2\sigma(I)$); R_1 = 0.0867 for observed and R_1 = 0.1309 for all reflections; wR_2 = 0.2438 for all reflections; max/min difference electron density = 0.262 and -0.256 e·Å^{-3}; data/restraints/parameters = 3416/3/376; GOF = 1.159.

*2.6 1,2,4,5-benzenetetracarboxylic acid (**M6**)*

The first crystal structure of 1,2,4,5-benzenetetracarboxylic acid (**M6**) was reported in 1971 by Takusagawa who found a water solvate.[24] Afterward, a methanol solvate of **M6** was reported, which transformed into the water solvate at ambient atmosphere. The reported MeOH slovate can also transform into desolvated structure at dry atmosphere or by heating[25].

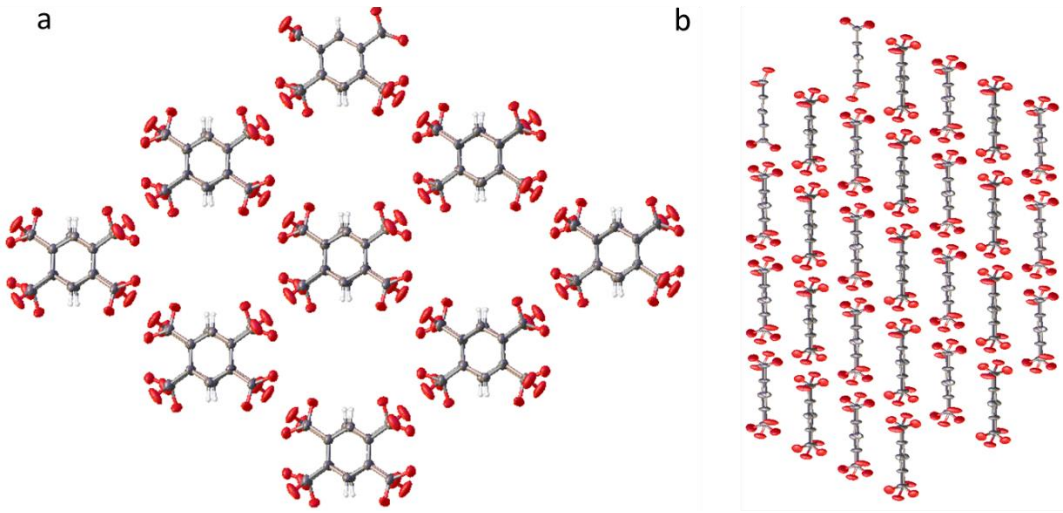

Figure 3.31. a) The reported crystal packing diagram of **M6** viewed along the *c* axis. The solvents are disordered and omitted for clarity. b) The same structure viewed along the *b* axis, the planes of **M6** molecules are aligned in a parallel arrangement and the layers of **M6** are separated by 3.74 Å. Hydrogen bonds are shown with red dashed lines. Grey: carbon, red: oxygen, white: hydrogen.

M6 was also reported to form a clathrate-type solvated structure by Biradha group[5] by crystallising **M6** from phenolic or methyl phenolic (Figure 3.31a). The structure contains a $R_2^2(8)$ hydrogen bonding interactions constructed the framework, which when viewed along the along *c* axis reveals that the **M6** molecular are packed in an

aligned arrangement. In the solvated crystal structure, the layers of **M6** are separated by 3.74 Å (Figure 3.31), indicating the layer are close enough to form π-π stacking interactions.

In this study, 5 mg of **M6** was dissolved in 1 mL THF at RT, then 1 mL of the anti-solvents, *o*-xylene, *p*-xylene, mesitylene, *n*-butylbenzene, 1,2-dimethoxylbenzene and 1,3-dimethoxylbenzene, were added into separate THF solutions. The solvent mixtures were left to evaporate at RT for 5 days which afforded colourless block shape crystals.

Single crystals were obtained from four of the crystallisation conditions screened, and SCXRD revealed that the crystals from THF/*o*-xylene, THF/*p*-xylene, THF/mesitylene THF/ *n*-butylbenzene, and THF/1,3-dimethoxylbenzene all had the same structure (**M6-1**, Figure 3.32). Here, the crystal structure of **M6-1**, isolated from THF/*p*-xylene. is described. **M6-1** ($C_{10}H_6O_8 \cdot 2(H_2O)$) crystallised from THF and *p*-xylene solution in the triclinic space group $P\bar{1}$. The asymmetric unit for **M6-1** comprises half **M6** molecule and one water. In this structure, the carboxylic acid group formed two types of hydrogen bonds, one with a water molecule and another with the adjacent carboxylic acid from a neighbouring **M6** molecule (Figure 3.32).

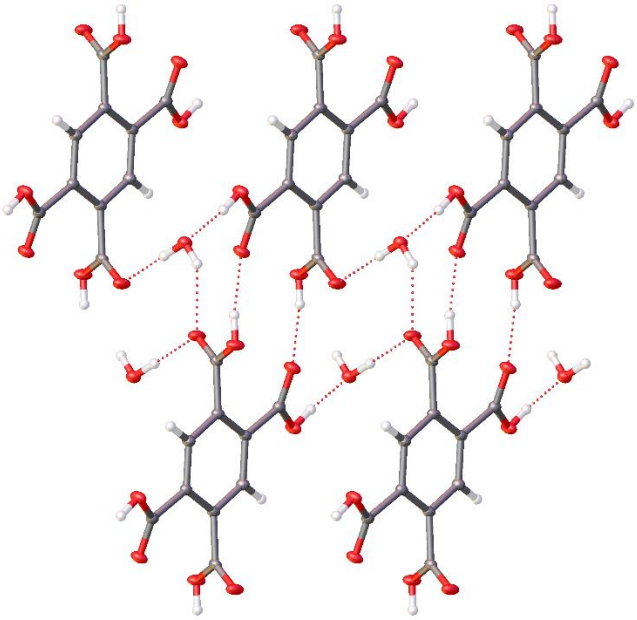

Figure 3.32. Crystal packing diagram of **M6-1** recorded at 100 K viewed along *a* axis. Hydrogen bonds are shown as red dashed lines. Grey: carbon, red: oxygen, white: hydrogen.

*2.6.1 The SCXRD structure of **M6-1***

Crystal data for **M6-1** (100 K): Formula $C_{10}H_6O_8 \cdot 2(H_2O)$; M = 290.18, triclinic $P\bar{1}$, colourless block shape crystals; a = 5.4568(8) Å, b = 6.3717(6) Å, c = 9.1080(9) Å, α = 71.947(8) °, β = 88.744(10) °, γ = 72.875(10) °; V = 286.90(6) Å^3; ρ = 1.680 g/cm^3; Z = 1; μ(Mo-Kα) = 0.156 mm^{-1}; F (000) = 150; crystal size = 0.035 × 0.032 × 0.012 mm; T = 100 (2) K. 1785 reflections measured (4.83 < 2θ < 60.57 °), 1330 unique (R_{int} = 0.0225), 1183 ($I > 2\sigma(I)$); R_1 = 0.0330 for observed and R_1 = 0.0369 for all reflections; wR_2 = 0.0898 for all reflections; max/min difference electron density = 0.352 and -0.216 e·Å^{-3}; data/restraints/parameters = 1330/3/99; GOF = 1.069.

Despite repeating the crystallisation with anhydrous THF and degassing **M6** under dynamic vacuum for 12 hrs at 100 °C water was still found in the **M6-1** structure after repeating the crystallisation. However, a different structure of **M6** was crystallised from THF/1,2-dimethoxylbenzene (**M6-2**, Figure 3.33). **M6-2** ($C_{10}H_6O_8 \cdot C_7$)) crystallised from a THF and 1,2-dimethoxylbenzene solution in the monoclinic space group $C2$. The asymmetric unit for **M6-2** comprises two halves of two **M6** molecules and disordered solvent that was modeled as C_7 since the OMe groups could not be located. In the structure of **M6-2**, the disordered solvent molecule appeared to template the formation of a small pore located between **M6** molecules that are stacked in an 'A-B' arrangement. The distance between the adjacent **M6** layers in the structure is 3.79 Å, indicating there are offset π-π stacking interactions between the **M6** layers. The $R_2^2(8)$ hydrogen bonding interactions constructed the framework with the clathrate shape (Figure 3.1c). Initially, before attempting to evacuate the 1-D pores in the **M6-2** structure, *n*-pentane solvent exchanges were used in an attempt to replace the disordered solvent in the crystal structure. However, after exchanging crystallisation solvent with the *n*-pentane solvent for 5 days, the disordered 1,2-dimethoxylbenzene solvent molecule was still located in the crystal pores, and **M6-2** had the same structure and crystal symmetry. Attempts were therefore made to desolvate **M6-2** by heating the crystals to 110 °C in a vacuum oven for 24 hrs. Despite using this energetically more intensive evacuation process, the disordered solvent

molecules remained in the crystal pores of **M6-2**. One possible reason is that there are strong interactions between the **M6** HOF in the A-B packed structure and the 1,2-dimethoxylbenzene molecules.

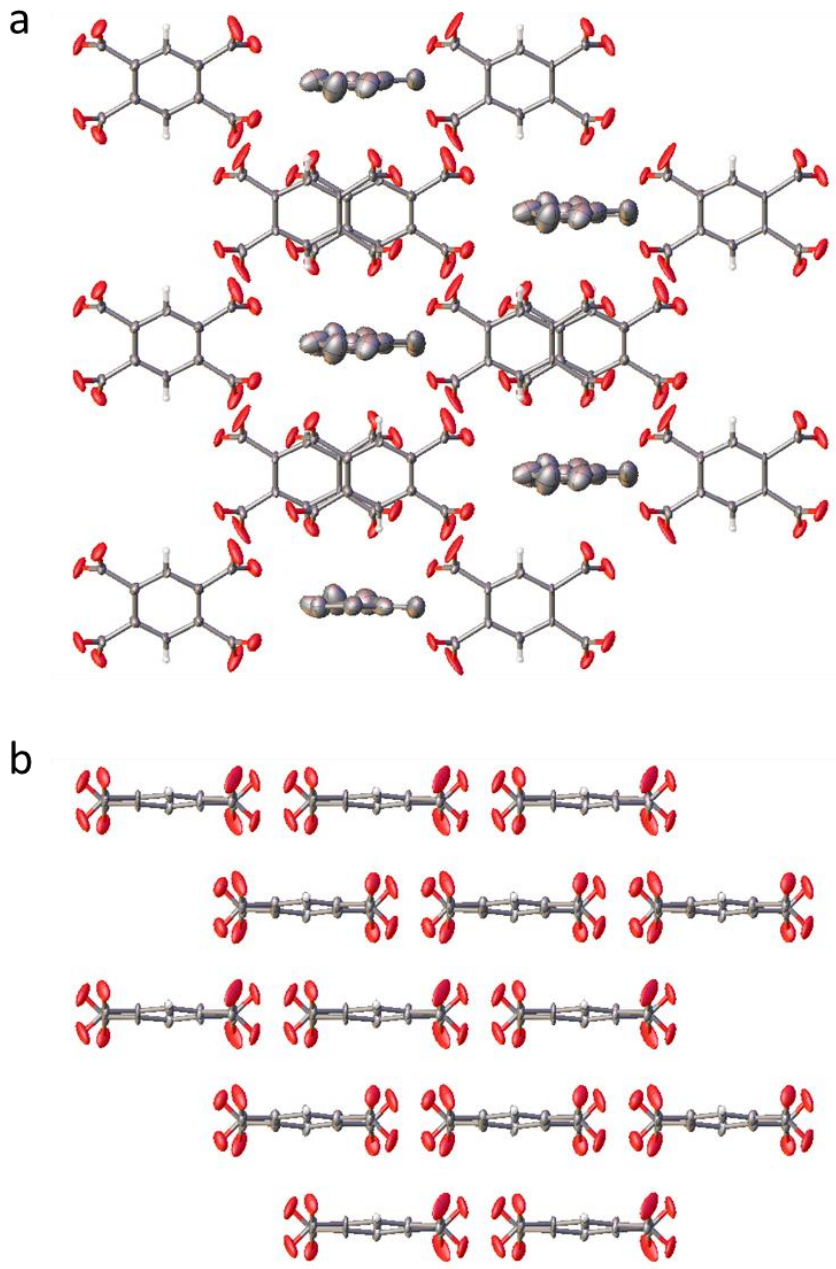

Figure 3.33. a) Crystal packing diagram of **M6-2** recorded at 292 K viewed along *c* axis with the positions of the disordered solvent molecules in the crystal pores shown. b) **M6-2** viewed along the *a* axis showing the **M6** molecules that are stacked in an offset arrangement and are separated by 4.33 Å. The disordered solvents are omitted from (b) for clarity. Grey: carbon, red: oxygen, white: hydrogen.

*2.6.2 The SCXRD structure of **M6-2***

Crystal data for **M6-2** (292 K): Formula $C_{10}H_6O_8 \cdot C_7H_8O$ M = 319.22, monoclinic $C2$, colourless block shape crystals; a = 10.4068(6) Å, b = 16.0662(8) Å, c = 8.6627(6) Å, β = 108.140(7) °; V = 1376.40(15) Å^3; ρ = 1.540 g/cm^3; Z = 4; μ(Mo-Kα) = 0.130 mm^{-1}; F (000) = 644; crystal size = 0.033 × 0.028 × 0.015 mm; T = 292 (10) K. 2609 reflections measured (2.4020 < 2θ < 30.0490 °), 2101 unique (R_{int} = 0.0131), 2039 (I > 2σ(I)); R_1 = 0.0867 for observed and R_1 = 0.0973 for all reflections; wR_2 = 0.2852 for all reflections; max/min difference electron density = 0.655 and -0.918 e·Å^{-3}; data/restraints/parameters = 2101/130/227; GOF = 1.246.

2.7 Biphenyl-3,3',5,5'-tetra-carboxylic acid (M7)

In a previous study, a 3-fold interpenetrated biphenyl-3,3',5,5'-tetra-carboxylic acid (**M7**) was reported to crystallise under hydrothermal conditions on cooling from 503 K.[26] In the structure, all four carboxylic acid groups of **M7** form the classic cyclic $R_2^2(8)$ hydrogen-bond motif to neighbouring molecules (Figure 3.34a). There is also a twist in the central C-C bond, which results in a corrugated structure (Figure 3.34c), and the supramolecular structure of this material comprises a mutually interwoven 3-fold interpenetrated form.

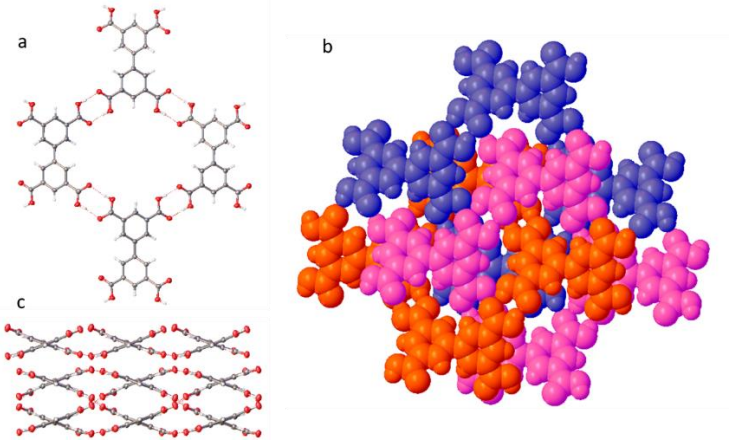

Figure 3.34. a) The four-membered hydrogen-bonded rings that generate a HOF net with a **sql** topology in the previously reported structure of **M7**, grey: C, red: O, white: H; b) The reported 3-fold interpenetrated structure of **M7**. The **sql** motifs are coloured in red, pink, and blue; c) the packing of 3-fold interpenetrated form viewed along the c axis.

Here, efforts were made to grow a non-interpenetrated structure of **M7** resembling the crystal structure of **M6-2**, which has 1-D pores (Figure 3.31). Initially, 1 mg of **M7** molecule was dissolved in 1 mL DMF in a small vial at RT. The vial was then inserted into a larger vial that contained 10 mL of anti-solvent. Here, the low boiling point organic solvents, $CHCl_3$, methanol, diethyl ether, ethyl acetate, and acetone, were used in the crystallisation procedure, and the small vials were left open to let the anti-solvents diffuse into the DMF solution. At the same time, the larger vial was sealed and left at RT. After two weeks, transparent colourless needle shape crystals (**M7-1**) crystallised from DMF/$CHCl_3$ system, but no particles were found in the other vials.

The crystals from DMF/$CHCl_3$ condition were characterised by SCXRD (**M7-1**). **M7-1** ($C_{16}H_{10}O_8 \cdot 5(H_2O)$) crystallised in the orthorhombic space group *P*nna and asymmetric unit comprises half of one **M7** molecule and disordered solvent, which was tentatively modelled as water, H_2O. In the solvated single crystal structure, **M7** was found to be non-planar (Figure 3.35a), which is similar to the **M7** conformed reported 3-fold interpenetrated structure (Figure 3.34c). The dihedral angle between the two benzene rings was calculated to be 42.6° in the solvated **M7-1** structure (Figure 3.35b).

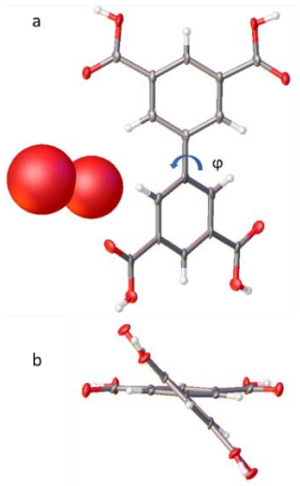

Figure 3.35. a) Displacement ellipsoid plot of **M7** in the single crystal structure of **M7-1**. Ellipsoids are displayed at the 50% probability level. The dihedral angles are shown with the symbol, φ. b) Side view of **M7** showing the twisted conformation. Grey: carbon, red: oxygen, white: hydrogen.

The $R_2^2(8)$ hydrogen bonding interactions constructed the framework (Figure 3.36a). The single crystal structure of **M7-1** viewed along *b* axis showed the **M7** molecules were packed in an 'A-B' stacking mode and there was an 0.95 Å offset between the **M7** layers. While the plane of **M7** molecules was offset, the faces of the phenyl molecules are aligned in a parallel arrangement and the stacks of **M7** are separated by 3.59 Å in solvated structure **M7-1** (Figure 3.36b). The disordered solvents occupy the 1-D pore, which was too disordered to accurately model as refined as disordered water.

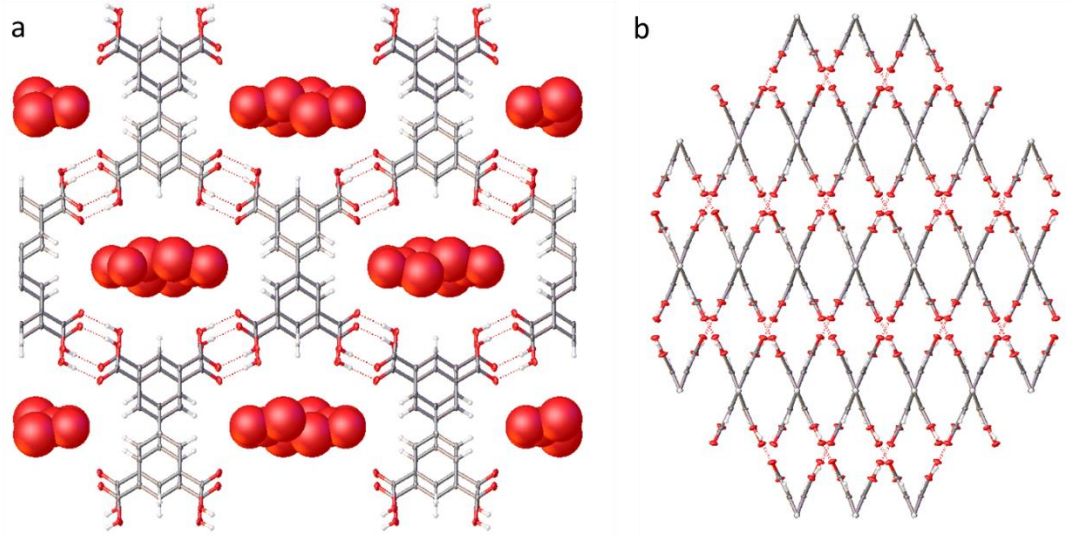

Figure 3.36. a) Crystal packing diagram of **M7-1** recorded at 100 K and viewed along the *b* axis, disordered solvents occupy the pore and were modelled as water. b) **M7-1** viewed along the *c* axis, the planes of **M7** molecules are aligned in a parallel arrangement and the stacks of **M7** are separated by 3.6 Å. Hydrogen bonds are shown with red dashed lines. Grey: carbon, red: oxygen, white: hydrogen.

*2.7.1 The SCXRD structure of **M7-1***

Crystal data for **M7-1** (100 K): Formula $C_{16}H_{10}O_8 \cdot 5(H_2O)$; M = 410.24, orthorhombic *P*nna, colourless block shape crystals; a = 15.2243(19) Å, b = 7.1637(13) Å, c = 17.5962(19) Å; V = 1919.1(5) Å^3; ρ = 1.420 g/cm^3; Z = 4; μ(Mo-Kα) = 0.128 mm^{-1}; F (000) = 840; crystal size = 0.032 × 0.022 × 0.019 mm; T = 100 (2) K. 9135 reflections measured (4.63 < 2θ < 54.18 °), 2073 unique (R_{int} = 0.0904), 1464 ($I > 2\sigma(I)$); R_1 =

0.1266 for observed and R_1 = 0.1626 for all reflections; wR_2 = 0.3632 for all reflections; max/min difference electron density = 0.792 and -0.485 e·Å^{-3}; data/restraints/parameters = 2073/0/123; GOF = 1.090.

As usual, *n*-pentane was used to exchange the crystallisation solvents in the pore before activating **M7-1**. To evacuate the pore of **M7-1**, the DMF and chloroform crystallisation solvents were removed with a syringe and 10 mL *n*-pentane was added to fully immerse the crystals. The *n*-pentane was refreshed every 12 hrs, and after using *n*-pentane to exchange the solvents for 5 days the crystals were degassed at RT for 2 hrs under dynamic vacuum to afford the activated crystals, **M7-2** (yield: 78 %).

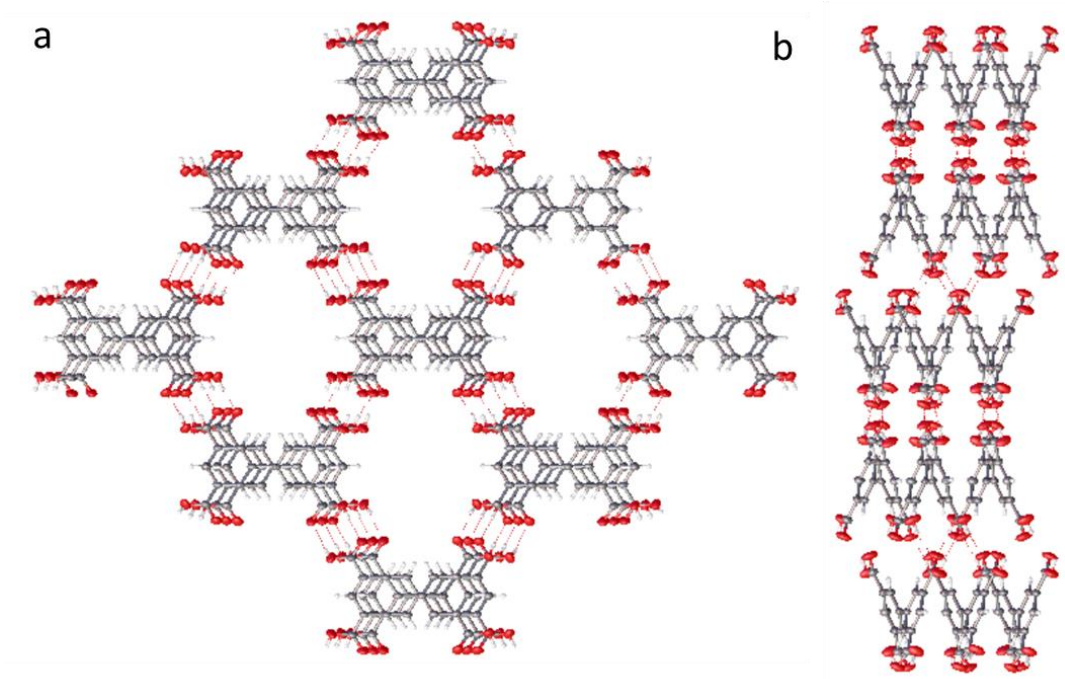

Figure 3.37. a) Crystal packing diagram of **M7-2** recorded at 292 K viewed along the *a* axis. b) **M7-2** viewed along the *c* axis, the planes of **M7** molecules are aligned in a parallel arrangement and the stacks of **M7** are separated by 3.69 Å. Hydrogen bonds are shown with red dashed lines. Grey: carbon, red: oxygen, white: hydrogen.

The structure of the activated phases, **M7-2**, was determined by SCXRD, which showed a non-interpenetrated porous structure was formed after activation (Figure

3.37). During the crystal activation, the dihedral angle between the two-benzene rings reduced from 42.6 ° in solvated **M7-1** to 35.1 ° in desolvated **M7-2**. In addition, the layers of **M7** molecules were observed to slide along the *c* axis, which led to an 'A-B-C' packing mode in the desolvated structure. The desolvated structure also possessed a 10.4 Å × 8.6 Å sized 1-D pore.

*2.7.2 The SCXRD structure of **M7-2***

M7-2 ($C_{24}H_{15}O_{12}$) had monoclinic *C*2/c space group symmetry and the asymmetric unit for this phase comprises one and a half **M7** molecules. Crystal data for **M7-2** (292 K): Formula $C_{24}H_{15}O_{12}$; M = 495.36, monoclinic *C*2/c, colourless block shape crystals; a = 10.8099(14) Å, b = 31.530(2) Å, c = 18.506(2) Å; β = 104.929(12) °; V = 6094.7(12) Å^3; ρ = 1.080 g/cm^3; Z = 8; μ(Mo-Kα) = 0.089 mm^{-1}; F (000) = 2040; crystal size = 0.052 × 0.016 × 0.012 mm; T = 292 (4) K. 6396 reflections measured (3.42 < 2θ < 61.15 °), 4163 unique (R_{int} = 0.028), 4014 ($I > 2\sigma(I)$); R_1 = 0.1209 for observed and R_1 = 0.1519 for all reflections; wR_2 = 0.3991 for all reflections; max/min difference electron density = 0.952 and -0.512 e·Å^{-3}; data/restraints/parameters = 4163/2/332; GOF = 1.487.

Although the desolvated **M7-2** structure has large 1-D channels (Figure 3.38) its nitrogen sorption isotherm at 77 K revealed the structure had low porosity and the BET surface area was only 15 m^2 g^{-1} (Figure 3.39). The PXRD of **M7-2** recorded after the gas sorption isotherm showed that there was a small structural rearrangement, but the pattern was still similar to the simulated PXRD of **M7-2** (Figure 3.40). The reason for the low BET surface area determine for **M7-2** might be similar to what happened for **M2-2**, and an unquantifiable amount of amorphous particles may have been present in the sample, which led to its having a low BET surface area.

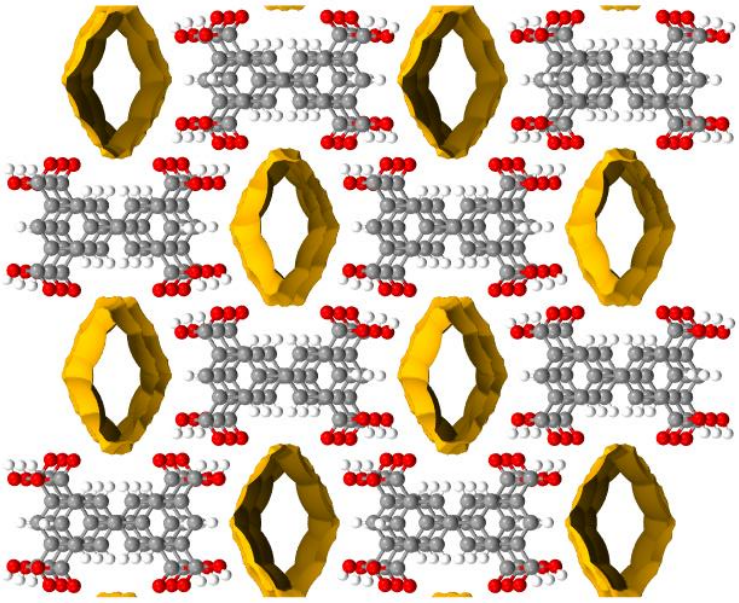

Figure 3.38. Crystal packing diagram of **M7-2** recorded at 292 K viewed along the *a* axis with the walls of the guest free 1-D pores highlighted in yellow. The empty, solvent-accessible space (1.4 Å probe radius, 0.1 Å grid spacing). The pore makes up approximately 13.3 % of the unit cell volume [809.60 Å^3 (V_{cell} = 6094.61 Å^3)].

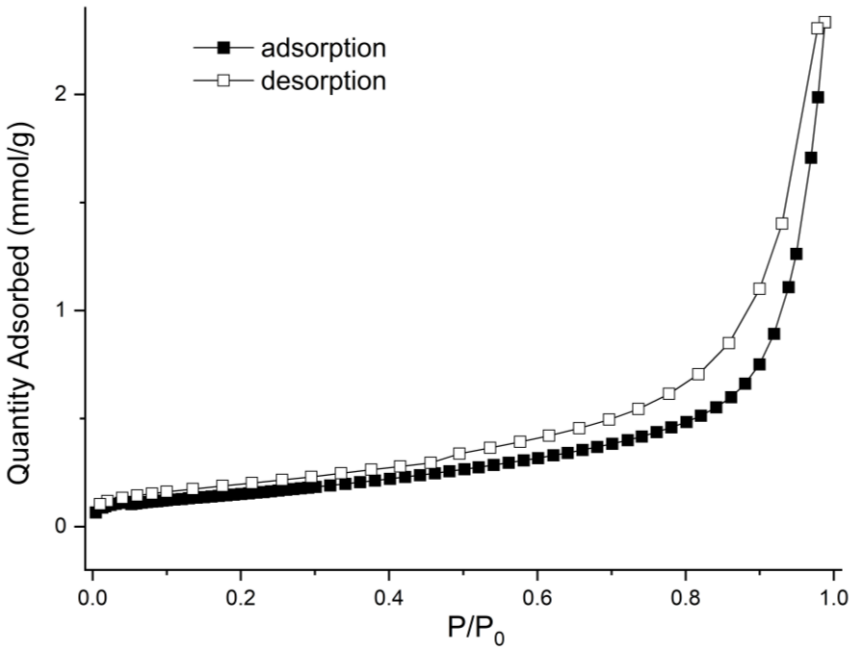

Figure 3.39. The N_2 sorption isotherm of **M7-2** that was recorded at 77 K.

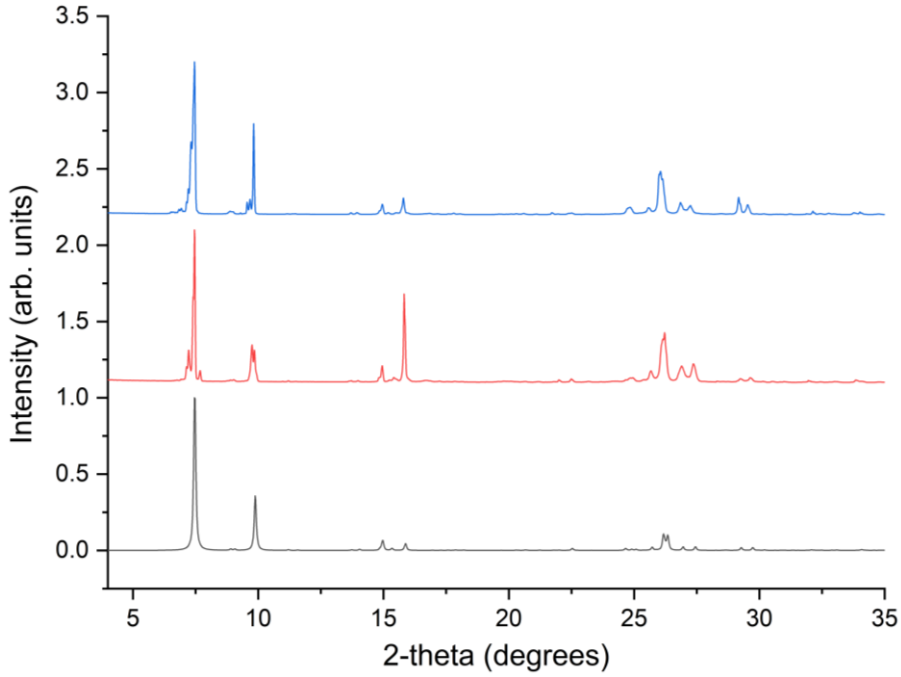

Figure 3.40. PXRD patterns of **M7-2**. Black: simulation from the single crystal structure recorded at 292 K; red: **M7-2** after activation; blue: **M7-2** after the N_2 sorption test.

*2.8 [1,1':4',1"] Terphenyl- 3,3",5,5"-tetracarboxylic acid (**M8**)*

In section 2.7, a non-interpenetrated solvated structure of **M7** was obtained from DMF/$CHCl_3$ condition. Inspired by this structure, an extended analogue, [1,1′:4′,1″] terphenyl- 3,3″,5,5″-tetracarboxylic acid (**M8**), was crystallised using the same conditions.

Here, 1 mg of **M8** was dissolved in 1 mL of DMF in a small vial at RT. This vial was then inserted into a larger vial that contained 10 mL of $CHCl_3$. The vial was left at RT for two weeks and afterward, transparent colourless needle shape crystals of **M8-1** were found in the vial and analysed by SCXRD. **M8-1** ($C_{22}H_{14}O_8 \cdot 16(H_2O)$) crystallised in the monoclinic space group *C*2/c and the asymmetric unit for this phase comprises half **M8** and disordered solvent that was modelled as water, H_2O. The single crystal structure of **M8-1** showed **M8** adopted a non-planar conformation and the dihedral angles between the central benzene and the two lateral phenyl group are 31.4 ° and 35.9 ° (Figure 3.41).

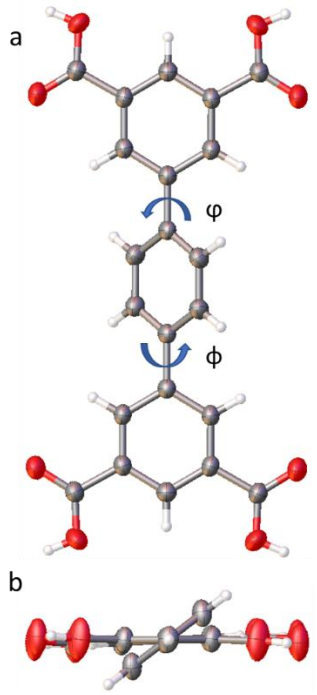

Figure 3.41. a) Displacement ellipsoid plot of **M8** from the single crystal structure of **M8-1** recorded at 100 K. Ellipsoids are displayed at 50% probability level. The dihedral angles are shown with φ and ϕ symbols. b) Side view of **M8** in **M8-1** showing its twisted conformation. Grey: carbon, red: oxygen, white: hydrogen.

The $R_2^2(8)$ hydrogen bonding interactions constructed the framework (Figure 3.42a). Viewing the single crystal structure of **M8-1** along the *a* axis revealed the **M8** molecules were packed in an 'A-B' arrangement and they are offset by 0.74 Å along the *b* axis. The stack of adjacent layers of **M8** are separated by 3.67 Å in solvated structure **M8-1** (Figure 3.42b). Disordered solvents occupy the 1-D pore, and these were modelled as water.

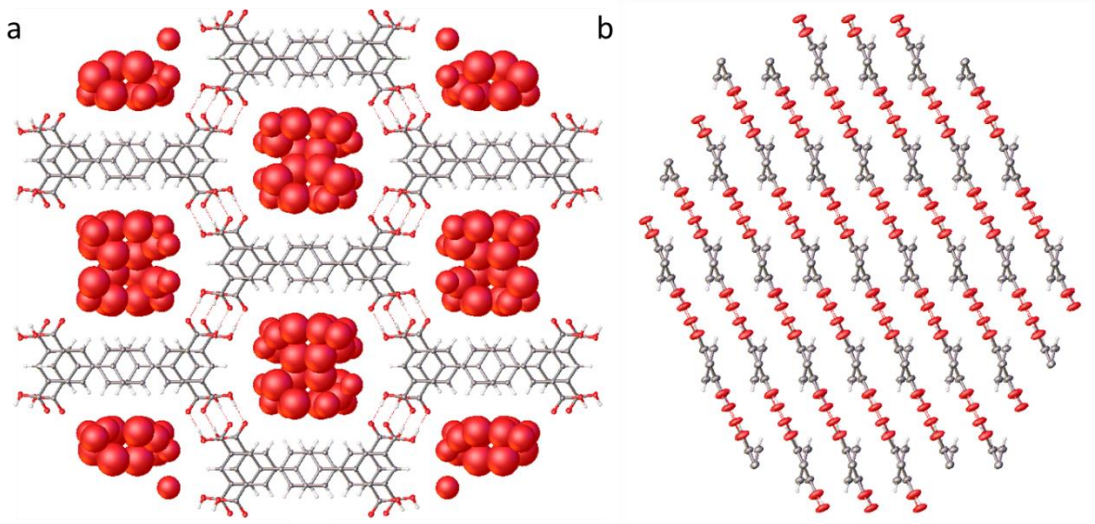

Figure 3.42. a) Crystal packing diagram of **M8-1** recorded at 100 K from SCXRD viewed along the *a* axis with disordered solvents occupied in the pore which were determined to oxygen. b) Viewed along the *b* axis, the planes of **M8** molecules are aligned in a parallel arrangement and the stacks of **M8** are separated by 3.67 Å. Hydrogen bonds are shown with red dashed lines. Grey: carbon, red: oxygen, white: hydrogen.

*2.8.1 The SCXRD structure of **M8-1***

Crystal data for **M8-1** (100 K): Formula $C_{22}H_{14}O_8 \cdot 16(H_2O)$; M = 662.33, monoclinic $C2/c$, colourless block shape crystals; a = 7.1875(3) Å, b = 26.3293(13) Å, c = 14.8068(5) Å, β = 92.178(3) °; V = 2800.0(2) Å^3; ρ = 1.571 g/cm^3; Z = 4; μ(Mo-Kα) = 0.149 mm^{-1}; F (000) = 1352; crystal size = 0.042 × 0.026 × 0.02 mm; T = 100 (2) K. 4319 reflections measured (5.35 < 2θ < 59.67 °), 3431 unique (R_{int} = 0.0257), 2671 (I > 2σ(I)); R_1 = 0.0801 for observed and R_1 = 0.0935 for all reflections; wR_2 = 0.2731 for all reflections; max/min difference electron density = 0.739 and -0.700 e·Å^{-3}; data/restraints/parameters = 3431/0/174; GOF = 1.059.

To evaluate the stability and porosity of **M8-1**, *n*-pentane was again used to exchange with the crystallisation solvents in the pores. Firstly, DMF and chloroform were removed with a syringe and the crystals were then immersed in 10 mL of *n*-pentane. The *n*-pentane was refreshed every 12 hrs and after exchanging the solvent for 5 days. Finally, the crystals were degassed at RT for 2 hrs under a dynamic vacuum (yield:

80 %). The activated crystal structure, **M8-2**, was analysed by SCXRD. **M8-2** ($C_{22}H_{14}O_8$) had monoclinic space group *C*2/c and the asymmetric unit for this phase comprises half of one **M8** molecule. The structure of **M8-2** showed no obvious change after activation (Figure 3.43) and the desolvated structure possessed 12.4 Å × 11.3 Å sized 1-D pores (Figure 3.44).

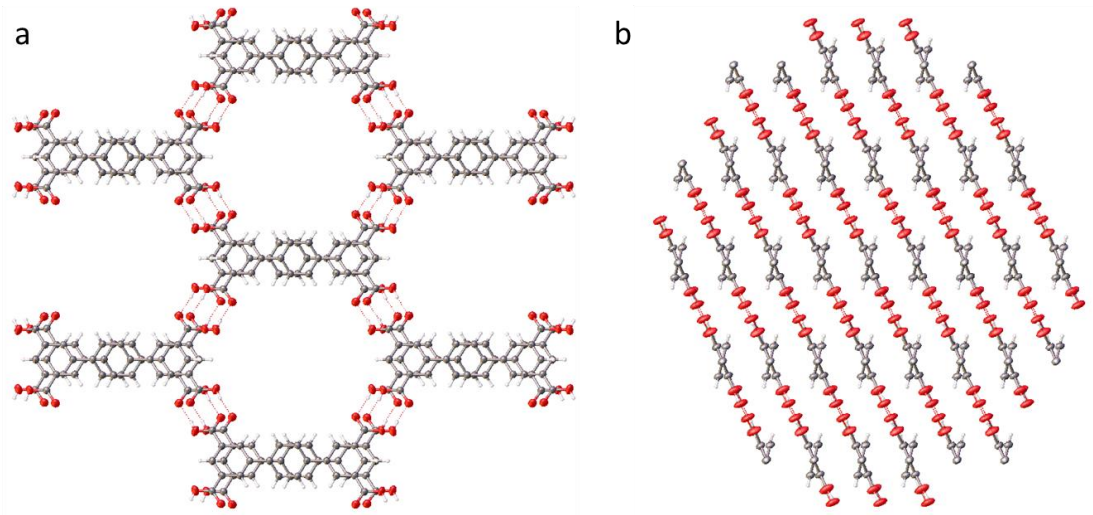

Figure 3.43. a) Crystal packing diagram of **M8-2** recorded at 291 K viewed along the *a* axis. b) **M8-2** viewed along the *b* axis, the planes of **M8** molecules are aligned in a parallel arrangement and the stacks of **M8** molecule are separated by 3.68 Å. Hydrogen bonds are shown with red dashed lines. Grey: carbon, red: oxygen, white: hydrogen.

*2.8.2 The SCXRD structure of **M8-2***

Crystal data for **M8-2** (291 K): Formula $C_{22}H_{14}O_8$; M = 402.30, monoclinic *C*2/c, colourless block shape crystals; a = 7.3463(3) Å, b = 26.5578(10) Å, c = 15.1916(6) Å, β = 92.149(4) °; V = 2961.8(2) Å^3; ρ = 0.902 g/cm^3; Z = 4; μ(Mo-Kα) = 0.070 mm^{-1}; F (000) = 824; crystal size = 0.05 × 0.032 × 0.019 mm; T = 291 (2) K. 4562 reflections measured (5.35 < 2θ < 58.79 °), 3582 unique (R_{int} = 0.0190), 2637 (I > 2σ(I)); R_1 = 0.0861 for observed and R_1 = 0.1084 for all reflections; wR_2 = 0.2916 for all reflections; max/min difference electron density = 0.665 and -0.551 e·Å^{-3}; data/restraints/parameters = 3582/0/140; GOF = 1.180.

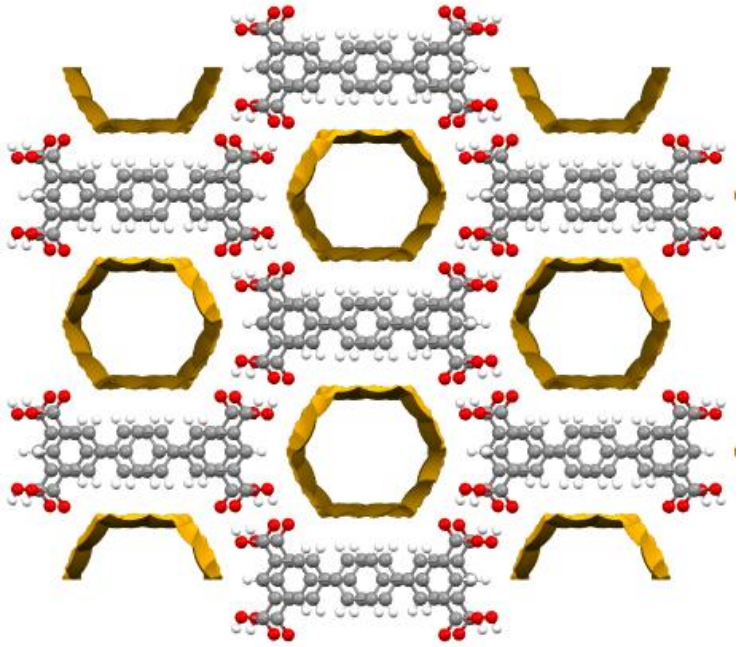

Figure 3.44. Crystal packing diagram of **M8-2** recorded at 291 K viewed along *a* axis with the walls of the guest free 1-D pores highlighted in yellow. The empty, solvent-accessible space (1.4 Å probe radius, 0.1 Å grid spacing). The pore makes up approximately 23.2 % of the unit cell volume [686.32 Å^3 (V_{cell} = 2961.8 Å^3)]. Grey: carbon, red: oxygen, white: hydrogen.

The desolvated **M8-2** structure indicated it would be a porous polymorph (Figure 3.44). Before the nitrogen sorption isotherm was recorded, **M8-2** was degassed at RT for 12 hrs (**M8-2_degas**). The single crystal structure of **M8-2_degas** was also determined. The single crystal structure of **M8-2_degas** showed the **M8** layers slid into a new arrangement after degassing, and this led to a new 'A-B-C-D' packing arrangement of **M8** layers, which decreased the porosity **M8-2_degas** compared to that found in **M8-2** (Figure 3.45). An **M8** conformational change also occurred during the degassing procedure, and this caused the **sql** HOF net to change from being planar layers into adopting wave-like layers (Figure 3.46).

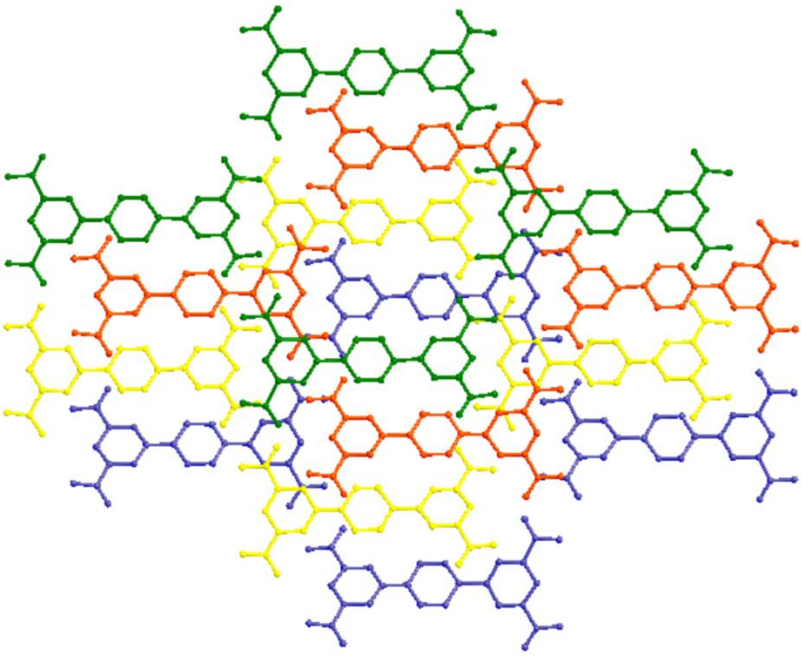

Figure 3.45. The crystal structure of **M8-2_degas**, which has an 'A-B-C-D' packing mode. The different layers are coloured with green, red, yellow, and blue.

Unfortunately, the N_2 sorption isotherm for **M8-2** recorded at 77 K showed the sample had a limited BET surface area (30 m^2 g^{-1}), which is not unsurprising because of the phase transformation (Figure 3.47). The structural transformation of **M8-2** that was observed after degassing proved it was a metastable polymorph and like δ-**TMA** discussed in chapter 2 lost porosity after transforming.

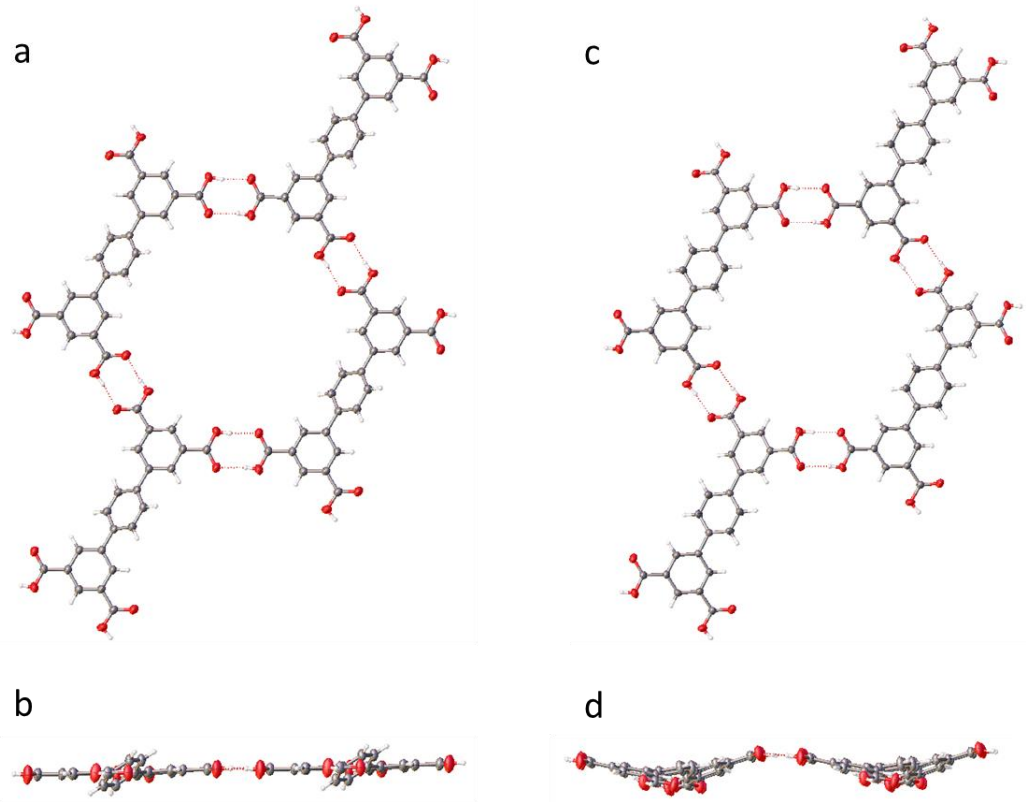

Figure 3.46. The **sql** net in **M8-2** (a) and side view (b); the **sql** net in **M8-2_degas** (c) and side view (d). Hydrogen bonds are shown with red dashed lines. Grey: carbon, red: oxygen, white: hydrogen.

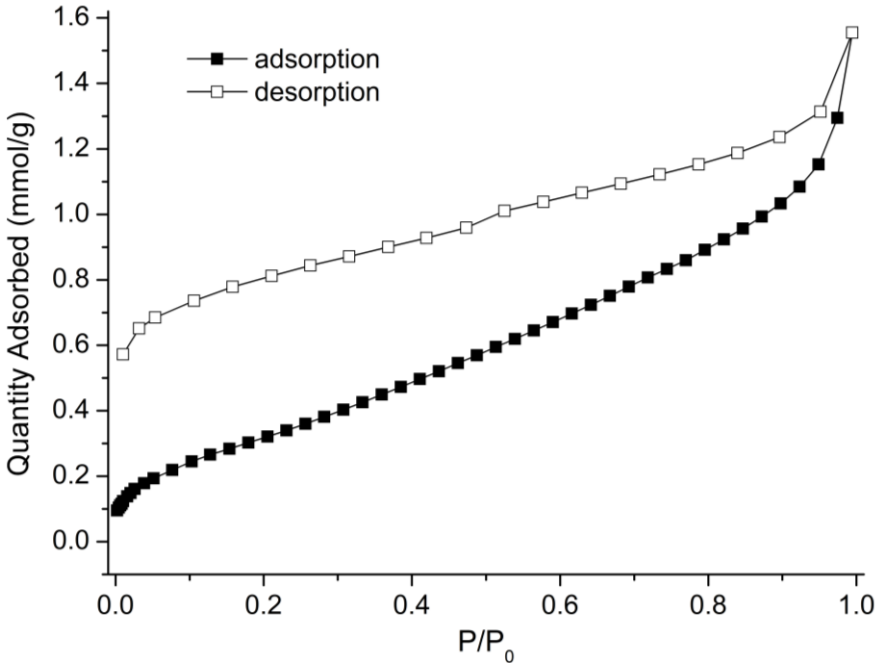

Figure 3.47. The N_2 sorption isotherm of **M8-2_degas** that was recorded at 77 K.

3. Conclusion

In this chapter, five carboxylic acid molecules with 3-fold symmetry (**M1**-**M5**) were crystallised from different binary solvent mixtures to afford a series of new HOF structures. By exploring the experimental single crystal structures, it was found that THF formed hydrogen bonds with the carboxylic acid in **M1**, which generated a non-porous solvate, **M1-1**. By contrast, a mesoporous HOF was constructed by crystallising **M2** from dioxane/mesitylene, and 3-D ED was used to determine the desolvated structure. **M2-2** is a rare example in mesoporous HOF[27,28] and was found to have a HOF structure that is similar to δ-**TMA** but with much larger pores. However, the experimental surface area of **M2-2** was much lower than anticipated, and this was likely to be due to the presence of non-crystalline particles in the same sample. A structure transform was found to occur during the activation of **M3-1** and this led to the formation of a desolvated structure, **M3-2**, with smaller pores. Although **M4** was crystallised from the same conditions as **M2-1**, 1,4-dioxane was found to form hydrogen bonds to two of the carboxylic acid groups of **M4**, which prevented the formation of a continuous HOF. The high conjugated molecule, **M5**, formed a large pore structure (**M5-1**) with water incorporated in the HOF structure. The crystallisation behavior of three four substituted carboxylic acid analogues (**M6**-**M8**) were also explored. The porous clathrate structures of **M7** and **M8** were obtained from the evacuation of **M7-1** and **M8-1** by solvent exchange with *n*-pentane. However, unquantifiable amounts of amorphous particles and the observed structure transformations during crystal activation limited the BET surface areas of the activated **M7** and **M8** HOFs.

The HOFs studied in this chapter were the start of a larger study that was interrupted by the COVID pandemic. The preliminary results show interlayer interaction, as well as network topology, are important for stabilising HOFs[29–31]. For the 2-D HOFs, the layers were found to slide during the activation procedure, and this was found to lead to the frameworks collapsing. Preventing 2-D HOFs from sliding during crystal activation is an important consideration, and in the next chapter, a stable HOF was

constructed by using a new strategy to solve this challenge.

4. References

1. Wang, B., Lin, R.-B., Zhang, Z., Xiang, S. & Chen, B. Hydrogen-Bonded Organic Frameworks as a Tunable Platform for Functional Materials. *J. Am. Chem. Soc.*,**142**, 14399-14416 (2020).
2. Li, Y. L. *et al.* Record Complexity in the Polycatenation of Three Porous Hydrogen-Bonded Organic Frameworks with Stepwise Adsorption Behaviors. *J. Am. Chem. Soc.* **142**, 7218–7224 (2020).
3. Cui, P. *et al.* Mining predicted crystal structure landscapes with high throughput crystallisation: Old molecules, new insights. *Chem. Sci.* **10**, 9988–9997 (2019).
4. Zentner, C. A. *et al.* High surface area and Z′ in a thermally stable 8-fold polycatenated hydrogen-bonded framework. *Chem. Commun.* **51**, 11642–11645 (2015).
5. Rajput, L., Jana, N. & Biradha, K. Carboxylic acid and phenolic hydroxyl interactions in the crystal structures of co-crystals/clathrates of trimesic acid and pyromellitic acid with phenolic derivatives. *Cryst. Growth Des.* **10**, 4565–4570 (2010).
6. Münch, A. S., Katzsch, F., Weber, E. & Mertens, F. O. R. L. Synthesis, spectroscopic characterisation and structural investigation of a new symmetrically trisubstituted benzene derivative: 3,3′, 3″-(Benzene-1,3,5-triyl)tripropiolic acid. *J. Mol. Struct.* **1043**, 103–108 (2013).
7. Herbstein, F. H., Kapon, M. & Reisner, G. M. Catenated and Non-Catenated Inclusion Complexes of Trimesic Acid. *Incl. Phenom. Inorganic, Org. Organomet. Hosts* 211–214 (1987).
8. Baek, S. Bin *et al.* High-temperature in situ crystallographic observation of reversible gas sorption in impermeable organic cages. *Proc. Natl. Acad. Sci. U. S. A.* **112**, 14156–14161 (2015).
9. Weber, E. *et al.* New trigonal lattice hosts: Stoicheiometric crystal inclusions of laterally trisubstituted benzenes-X-ray crystal structure of 1,3,5-tris-(4carboxyphenyl) benzene·dimethyrformamide. *J. Chem. Soc. Perkin Trans. 2* 1251–1257 (1988).
10. Yoon, T. U. *et al.* Efficient separation of C2 hydrocarbons in a permanently porous hydrogen-bonded organic framework. *Chem. Commun.* **54**, 9360–9363 (2018).
11. Lai, H. W. H., Wiscons, R. A., Zentner, C. A., Zeller, M. & Rowsell, J. L. C. Supramolecular Assembly of Tris(4-carboxyphenyl)arenes: Relationship between Molecular Structure and Solid-State Catenation Motifs. *Cryst. Growth Des.* **16**, 821–833 (2016).
12. Cui, P. *et al.* An Expandable Hydrogen-Bonded Organic Framework Characterised by Three-Dimensional Electron Diffraction. *J. Am. Chem. Soc.* **142**, 12743–12750 (2020).
13. Stef Smeets; Bin Wang; Magdalena O. Cichocka; Jonas Ångström; Wei Wan. Instamatic. (2018).
14. Kabsch, W. XDS. *Acta Crystallogr. Sect. D Biol. Crystallogr.* **66**, 125–132 (2010).
15. Wan, W., Sun, J., Su, J., Hovmöller, S. & Zou, X. Three-dimensional rotation electron diffraction: software RED for automated data collection and data processing. *J. Appl. Crystallogr.* **46**, 1863–1873 (2013).
16. Sheldrick, G. M. A short history of SHELX. *Acta Crystallogr. Sect. A Found. Crystallogr.* **64**, 112–122 (2008).
17. He, Y. *et al.* Activation of a gamma–cyclodextrin–based metal–organic framework using supercritical carbon dioxide for high–efficient delivery of honokiol. *Carbohydr. Polym.* **235**,

(2020).

18. Shen, Q. J., Wei, H. Q., Zou, W. S., Sun, H. L. & Jin, W. J. Cocrystals assembled by pyrene and 1,2- or 1,4-diiodotetrafluorobenzenes and their phosphorescent behaviors modulated by local molecular environment. *CrystEngComm* **14**, 1010–1015 (2012).
19. Collings, J. C. *et al.* Arene-perfluoroarene interactions in crystal engineering 8: Structures of 1:1 complexes of hexafluorobenzene with fused-ring polyaromatic hydrocarbonsyz. *New J. Chem.* **26**, 1740–1746 (2002).
20. Ke, Y., Collins, D. J., Sun, D. & Zhou, H. C. (10,3)-a Noninterpenetrated Network Built From a Piedfort Ligand Pair. *Inorg. Chem.* **45**, 1897–1899 (2006).
21. Ullah, N., Chen, S., Zhao, Y. & Zhang, R. Photoinduced Water-Heptazine Electron-Driven Proton Transfer: Perspective for Water Splitting with g-C3N4. *J. Phys. Chem. Lett.* **10**, 4310–4316 (2019).
22. Wu, C. *et al.* Mesoporous Polymeric Cyanamide-Triazole-Heptazine Photocatalysts for Highly-Efficient Water Splitting. *Small* **16**, 2003162 (2020).
23. Li, T. *et al.* Integrating Active C3N4 Moieties in Hydrogen-bonded Organic Frameworks for Efficient Photocatalysis. *J. Mater. Chem. A*, **9**, 4687-4691 (2021).
24. Takusagawa, F., Hirotsu, K. & Shimada, A. The Crystal and Molecular Structure of Pyromellitic Acid Dihydrate (Benzene-1,2,4,5-tetracarboxylic Acid Dihydrate). *Bull. Chem. Soc. Jpn.* **44**, 1274–1278 (1971).
25. Fujii, K., Ashida, Y., Uekusa, H., Guo, F. & Harris, K. D. M. Selective transformation pathways between crystalline forms of an organic material established from powder X-ray diffraction analysis. *Chem. Commun.* **46**, 4264–4266 (2010).
26. Coles, S. J., Holmes, R., Hursthouse, M. B. & Price, D. J. Biphenyl-3,3′,5,5′-tetracarboxylic acid. *Acta Crystallogr. Sect. E Struct. Reports Online* **58**, o626–o628 (2002).
27. Ma, K. *et al.* Ultrastable Mesoporous Hydrogen-Bonded Organic Framework-Based Fiber Composites toward Mustard Gas Detoxification. *Cell Reports Phys. Sci.* **1**, 100024 (2020).
28. Wang, B. *et al.* A novel mesoporous hydrogen-bonded organic framework with high porosity and stability. *Chem. Commun.* **56**, 66–69 (2019).
29. Hisaki, I. *et al.* Docking Strategy To Construct Thermostable, Single-Crystalline, Hydrogen-Bonded Organic Framework with High Surface Area. *Angew. Chemie - Int. Ed.* **57**, 12650–12655 (2018).
30. Hisaki, I. *et al.* Hexaazatriphenylene-Based Hydrogen-Bonded Organic Framework with Permanent Porosity and Single-Crystallinity. *Chem. - A Eur. J.* **23**, 11611–11619 (2017).
31. Hisaki, I., Nakagawa, S., Tohnai, N. & Miyata, M. A C3-symmetric macrocycle-based, hydrogen-bonded, multiporous hexagonal network as a motif of porous molecular crystals. *Angew. Chemie - Int. Ed.* **54**, 3008–3012 (2015).

Chapter 4

An Expandable Hydrogen-Bonded Organic Framework Characterised by Three-Dimensional Electron Diffraction

The work reported herein is published in Cui *et al.*, *J. Am. Chem. Soc.*, **2020**, *142*, 12743-12750.[1]

Contributions to this chapter

Peng Cui crystallised the **ABTPA** molecule and led the experimental work. 3-D electron diffraction data was collected and processed by Erik Svensson Grape and Dr. A. Ken Inge. Dr. Peter R. Spackman and Prof. Graeme M. Day performed crystal structure prediction (CSP) calculations. Peng Cui, Dr. Marc A. Little, and Dr. Yue Wu interpreted single crystal and powder X-ray diffraction data. SEM images were captured by Lunjie Liu. Methane sorption was measured by Rob Clowes.

1. Abstract

A molecular crystal of a 2-D hydrogen-bonded organic framework (HOF) that undergoes an unusual pore expansion after removing solvent from the crystal pores during activation was discovered. The HOF was constructed with 5',5""-(anthracene-9,10-diyl) bis (([1,1'3',1"-terphenyl]-4,4"-dicarboxylic acid)) (**ABTPA)**, which has a conformationally flexible π-conjugated anthracene core that stabilises interlayer HOF packing and adapts its molecular conformation during crystal activation. The activated HOF structure (**ABTPA-2**) was characterised by single-crystal three-dimensional electron diffraction (3-D ED) because its crystals were too small for conventional single-crystal X-ray diffraction (SCXRD). The activated structure, **ABTPA**-2, revealed **ABTPA** uses out-of-plane anthracene units as adaptive structural anchors. These units change orientation to generate a lower density framework material in the **ABTPA-2** which has robust dynamic porosity (SA_{BET} = 1183 m^2 g^{-1}). The underlying energetics behind the phase transition was clarified by crystal structure prediction (CSP).

2. Introduction

Porous organic molecular crystals contain different types of non-covalent interactions that compete during crystallisation. Controlling intermolecular packing in porous organic molecular crystals is important because their resulting crystal structures often exhibit polymorph-specific physisorption properties.[2–5] If the non-covalent

interactions in porous organic molecular crystals are weak, then is it quite common for their structures to undergo structural transformations during crystal activation. For example, their structures can collapse or transform as the structure stabilising crystallisation solvent is removed from their crystal pores. Such structural transformations often lead to the loss of single crystallinity, and frequently the loss of porosity. It is difficult to characterise such transformations, particularly for flexible systems, because microcrystals are often formed by these transformations, although the same can also happen if the structure does not collapse entirely. Determining the activated structures of porous organic molecular crystals can, therefore, be extremely challenging, but characterising their activated structures is often important for rationlising their materials properties.

Porous organic cages (POCs) have been reported to transform during crystal activation.[6–9] For example, Mastalerz reported a shape-persistent cage compound that bears a cavity of a minimum inner diameter of 2.6 nm, which after removing solvent molecules is mesoporous and has a surface area of 3758 m^2 g^{-1}. However, the desolvated structure could not be determined by PXRD or SCXRD and the crystal packing in the activated crystals was different to that in the solvated crystals.[7] Other examples of POCs, for which the desolvated cage structure could not be determined include **CC20**, which was reported by Teng *et al.* in 2019.[8] The [8+12] POC, **CC20**, was observed to different solvatomorphs by SCXRD, which contain some distinctly shaped cages due to the changes in the shape of **CC20** upon partial desolvation and/or reorientation of the cages.

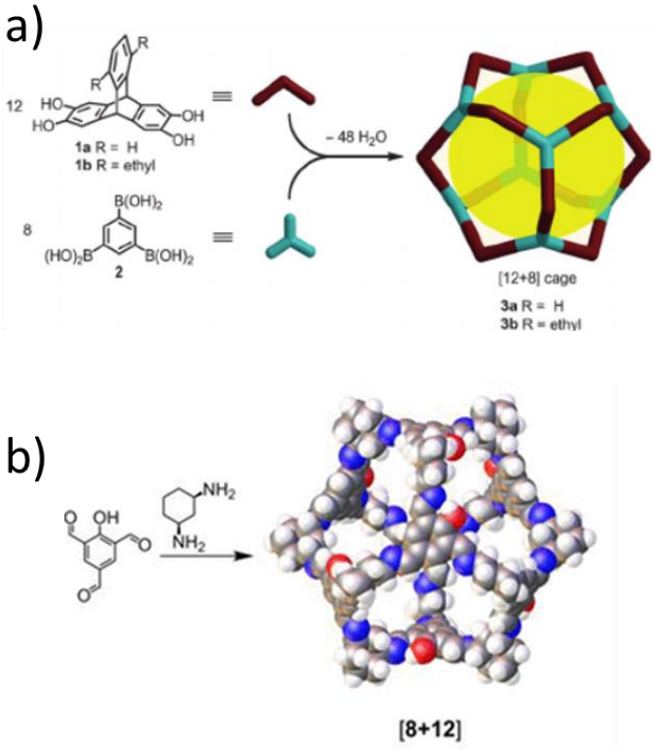

Figure 4.1. a) Synthesis of POC reported by Zhang *et al.*. Reprinted from *Angew. Chem. Int. Ed.* 2014, 53, 1516 –1520. Copyright from 2014 Wiley-VCH. b) synthesis **CC20** reported by Teng *et al.*. Reprinted from *Cryst. Growth Des.*, 2006, 6, 2429–2431. Copyright from 2006 American Chemical Society.

HOFs possess extended networks and porous structures that often undergo structural transformations during activation.[2,10–12] For example, the tetrahedral diaminotriazine based **HOF-1**[2,13] reported by Chen *et al.* (Figure 4.2a) transformed into a selectively-porous crystalline phase whose structure could not be determined after thermal activation. A series of porous triptycene-based 3-D HOFs reported by Stoddart *et al* that were found to feature different interpenetrated forms transformed into undetermined structures after activation.[10,11] (Figure 4.2b, c). While a 2-D HOF reported by Hisaki *et al.* transformed its structure during activation due and formed a new phase that could not be determined by X-ray diffraction alone (Figure 4.2d).[12]

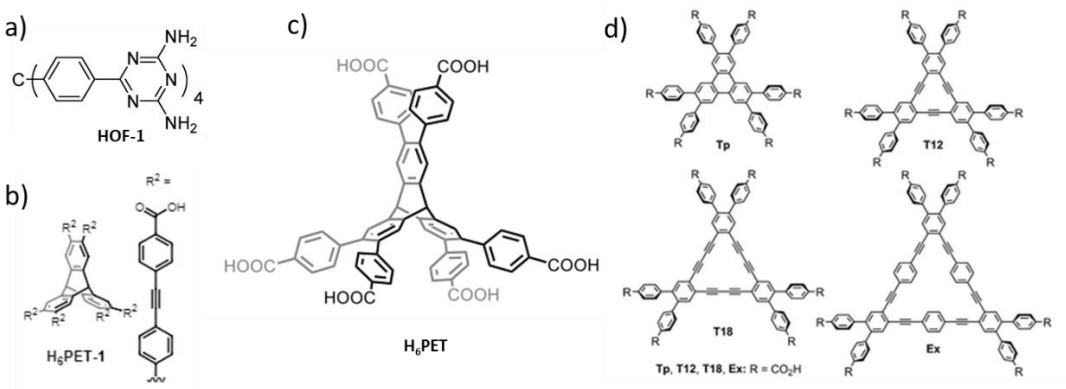

Figure 4.2. A series of organic building blocks were used to construct porous HOFs.

In chapter 2, CSP was introduced as a method to predict energetically stable porous molecular crystals. However, it is still challenging to use CSP to discover the porous structures of conformationally flexible molecules. The reason is the expanded configurational space made available by molecular flexibility, combined with the need to locate all relevant structures in a wide energy range, to allow for the energetic effects of solvent stabilisation on crystallisation outcome.[4,14] For example, a highly solvatomorphic porous organic cage, **CC1**, was crystallised in different solvent systems (Figure 4.3). The solvated structures that contain different crystal packing motifs are stabilised with the respect to the desolvated **CC1** by up to 133.8 kJ mol^{-1}.[14]

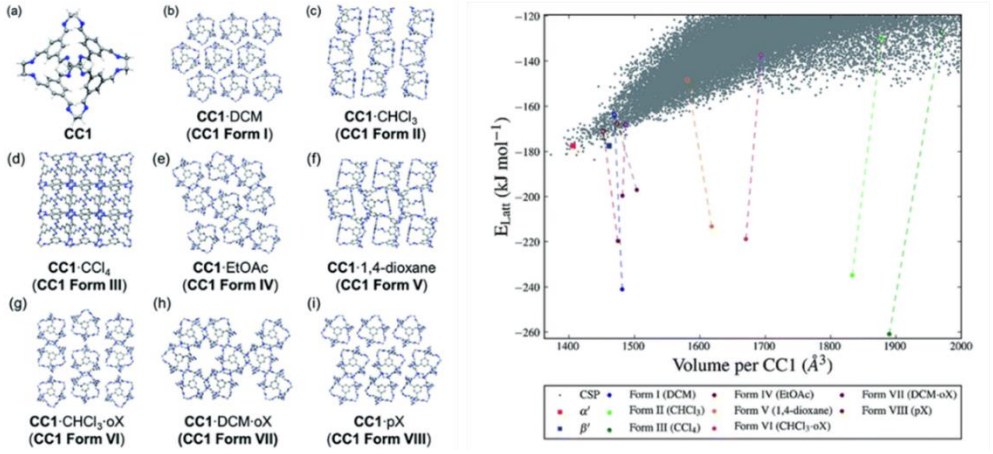

Figure 4.3. Experimental crystal structures of the solvatomorphs (left) and the CSP energy landscape of **CC1** (right) showing the calculated lattice energies of the desolvated structures (Forms I–VIII, unfilled circles) and after solvent stabilisation (filled circles). Reprinted from *Faraday Discuss.*, 2018, 211, 383-399. Copyright from 2018 Royal Society of Chemistry.

Conformationally flexible molecules have been explored in lower throughput and computationally more expensive CSP calculation, such as flexible pharmaceuticals where only hundreds of crystal structures were been predicted.[15,16] For example, axitinib, which is a conformationally flexible pharmaceutical molecule was used in CSP calculation where only one molecule was in the asymmetric unit. Only the minimizing energy conformers were performered while varying one of the 7 torsion angles at a time. The four known polymorphs were all identified (Figure 4.4).[16]

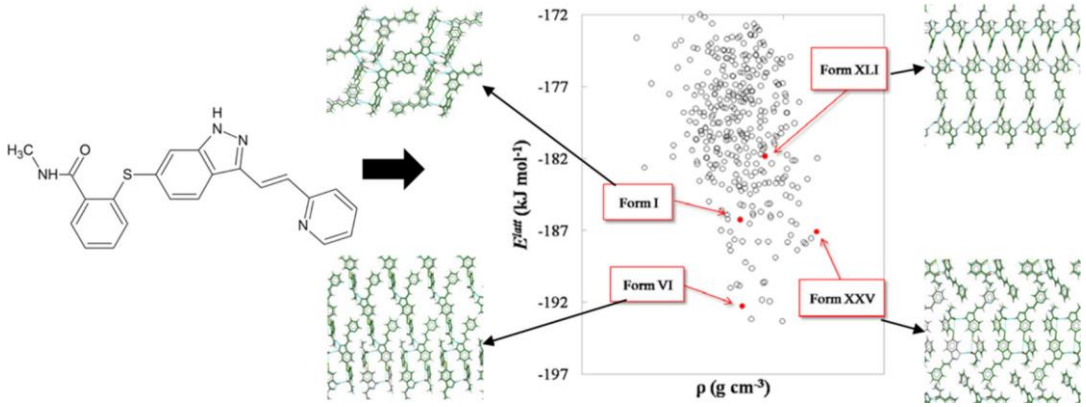

Figure 4.4. The molecular structure and CSP landscape for axitinib showing its four known polymorphs. Reprinted from *Chemical Engineering Science*, 2015, 121, 60–76. Copyright from 2015 Elsevier.

In this chapter, the CSP landscape **ABTPA** (Figure 4.5b) was calculated using a lower-cost approach, which was achieved using an ensemble of rigid gas-phase conformers and a force field description of intermolecular interactions, without allowing for full molecular conformational flexibility during CSP calcualtions.[4,17–21]

2.1 Reported organic materials based on flexible anthracene core

A series of compounds that are structurally related to **ABTPA** (Figure 4.5) have crystal structures deposited in the Cambridge Structural Database. The compounds are listed in Table 4. 1, where R = the functional groups in the reported structures and the dihedral angles ϕ and ψ are listed as those between the plane of the anthracene unit and the plane of the diphenyl units in the 9- and 10-positions. Analysis of the reported crystal structures revealed that the dihedral angles ϕ and ψ ranged between 63.7 ° to

89.7 °, and was dependent on a range of factors, including the R groups, type of structure (e.g. MOF *vs.* molecular crystal), and collection temperature. The ϕ and ψ dihedral angles also varied in some of the structures if parts of the molecule resided in different chemical environments. In comparison to more typical 2-D carboxylic acid molecules, such as trimesic acid (**TMA**, chapter 2), the **ABTPA** molecule possesses out-of-plane anthracene units that could influence interlayer 2-D stacking (Figure 4.5, 4.6). It was envisaged that the out-of-plane anthracene unit would anchor the packing of 2-D layers and prevent them from sliding. For example, as shown for **TMA** in chapter 2, without such kind of out-of-plane anchors, 2-D honeycomb networks of **TMA** were easily able to slide and cause the structure to collapse. **ABTPA** is also different from the 3-D molecules, such as adamantane carboxylic acid (**ADTA**, chapter 2), which usually formed tetrahedral hydrogen-bonded networks.

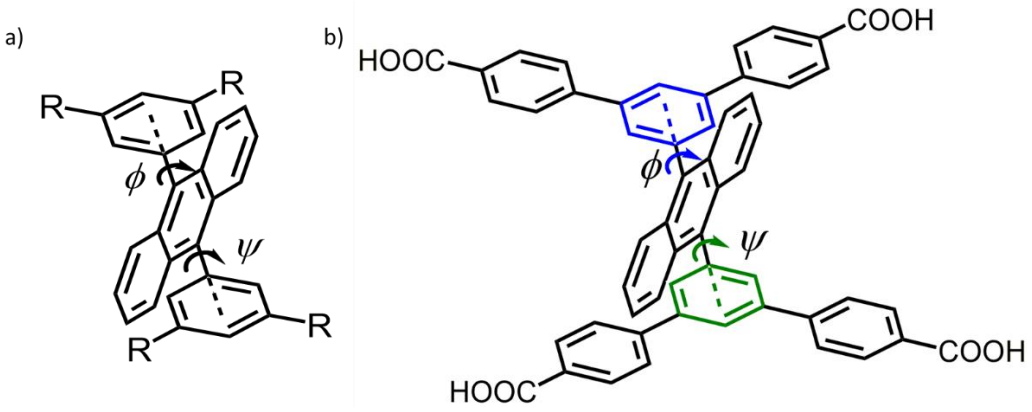

Figure 4.5. a) Schematic representation of molecules that are structurally related to **ABTPA**. The dihedral angles ϕ and ψ between the plane of the anthracene unit and the plane of the diphenyl units in the 9- and 10-positions in these crystal structures are listed in Table 4.1. b) **ABTPA** molecule that was studied in this chapter.

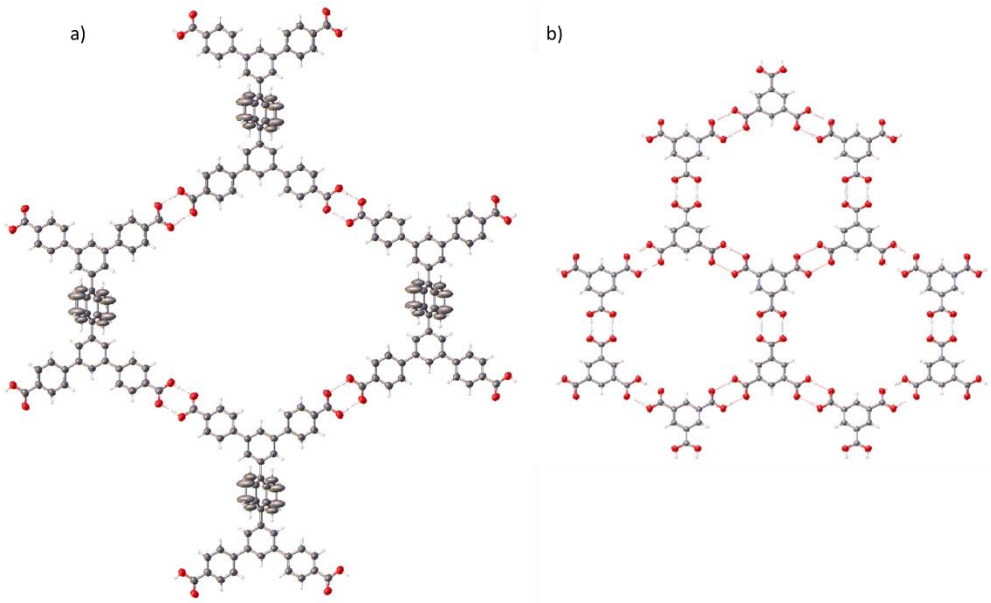

Figure 4.6. a) Schematic of a hypothetical single 2-D hydrogen-bonded layer constructed with **ABTPA**, the anthracene is rotated out of the 2-D hydrogen-bonded plane; b) schematic representation of a single 2-D hydrogen-bonded layer constructed with **TMA**.

Table 4.1. The angle between the plane of the anthracene unit and the plane of the diphenyl units in the 9- and 10-positions for series of compounds that are structurally related to **ABTPA**.[22-38]

CSD code	CCDC No.	Materials form	R=	ϕ	ψ	Reference
DABFIV	1134886	Organic	-OH	83.8	81.1	
DEKLEN	1499823	MOF	$-COO^-$	78.7	78.7	[22]
DEKLEN01	1499824	MOF	$-COO^-$	89.1	89.2	[22]
DEKMOY	1499825	MOF	$-COO^-$	70.5	70.6	[22]
DEKMOY01	1499829	MOF	$-COO^-$	68.7	68.8	[22]
DEKNOZ	1499830	MOF	$-COO^-$	68.2	68.3	[22]
DEKNUF	1499831	MOF	$-COO^-$	67.9	67.9	[22]
DEZHIA	220731	Organic	-OH	77.5	77.5	[23]

DEZHOG	220732	Organic	-OH	85.9	85.9	[23]
DEZHUM	220733	Organic	-OH	79.3	79.3	[23]
DEZJAU	220734	Organic	-OH	66.3	66.3	[23]
DEZJEY	618381	Organic	-OH	78.6	78.6	[23]
FUTDII	682384	MOF	$-COO^-$	85.6	85.6	[24]
KIHXOR	1818275	Organic	-COOH	70.5	70.4	[25]
PICWED	1233039	Organic	-OH	82.8	82.4	[26]
PICWIH	1233040	Organic	$-CH_3$	83.8	83.8	[26]
POYBIP	714754	Organic	-OH	74.6	74.7	[27]
POYBOV	714755	Organic	-OH	86.7	71.1	[27]
PUNZIH	1239552	Organic	-OH	86.9	86.9	[28]
QACMOY	727912	Organic	-OH	89.3	73.0	[29]
QACMUE	727913	Organic	-OH	70.7	70.7	[29]
QACNAL	727914	Organic	-OH	63.7	63.7	[29]
RATPEH	1246943	Organic	-OH	88.1	89.4	[30]
RICBEM	939459	MOF	-phenylCOO^-	79.8	79.8	[31]
TENKIG	1268993	Organic	-OH	83.8	83.8	[32]
TENKOM	1268994	Organic	-OH	89.7	89.7	[32]
TENKUS	1268995	Organic	-OH	75.6	75.6	[32]
TENLAZ	1268996	Organic	-OH	75.9	75.9	[32]
TIFLUQ	632059	Organic	-phenylOH	74.6	74.6	[33]
TIFMAX	632060	Organic	-phenylOH	71.3	71.3	[33]
TIFMEB	632061	Organic	-phenylOH	77.7	77.7	[33]
TIFMIF	632062	Organic	-phenylOH	80.0	80.0	[33]
WONKEQ	690241	Metal complex	-C=N	77.2	77.2	[34]
XITYOP	678724	MOF	$-COO^-$	71.7	71.7	[35]

YOGKEM	988120	MOF	-COO$^-$	76.1	76.1	[36]
YOGKIQ	988121	MOF	-COO$^-$	70.5	70.5	[36]
YOGKOW	988122	MOF	-COO$^-$	88.9	88.9	[36]
ZAZLER	1309926	Organic	-OH	74.5	74.5	[37]

3. Initial CSP calculation with 63 low energy conformations

3.1 63 unique conformers

An ensemble of 63 unique conformers with low relative conformational energies was used in CSP calculations to assess **ABTPA**'s ability to form porous frameworks (Figure 4.7b). The relative energy difference of these conformers is within 1 kJ mol^{-1} and their dihedral angles ranged from 73.94 ° to 89.88 °. From the initial CSP landscape, it was not immediately obvious which of the predicted packing modes might be discovered by experiment, and the preliminary CSP results did not show any regions with low-energy porous structures in local minima (Figure 4.8).

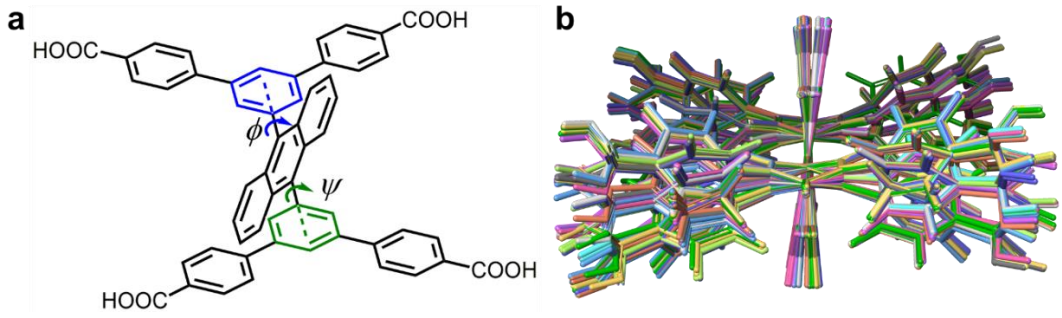

Figure 4.7. a) Structure of **ABTPA**; the dihedral angles ϕ and ψ between the anthracene plane and adjacent phenyl group planes are indicated; b) an overlay plot of the 63 unique low energy conformations used in the initial CSP calculations. The conformers are aligned to minimise the total root-mean-square deviation (RMSD) with the lowest energy conformer.

3.2 Leading Edge Structures

Although no obvious porous structures with relatively low energy were observed in

the initial CSP landscape that was calculated with 63 low energy conformers the leading-edge structures in the CSP landscape were explored. Initially, all structures were separated within 100 kJ/mol of the global minimum into 50 bins by their density (resulting in a bin width of roughly 0.16 g/cm^3). Within each bin, structures within 7 kJ/mol of the lowest energy structure of that bin were kept – these structures make up the 'leading edge' set of 233 crystal structures which were coloured by predicted accessible surface areas in Figure 4. 8. Predicted structures with square lattice (**sql**) packings (Figure 4.9), which were constructed by fully satisfied $R_2^2(8)$ hydrogen bonds were observed in the area of the lower density structures along the low energy leading edge of the CSP landscape (Figure 4.10). Most of the **sql** packed structures contained 1-D pore networks and significant accessible surface areas. While porous lower density structures have an energetic penalty in CSP, these phases can often be formed experimentally as they are stabilised by solvent interactions.[4,14]

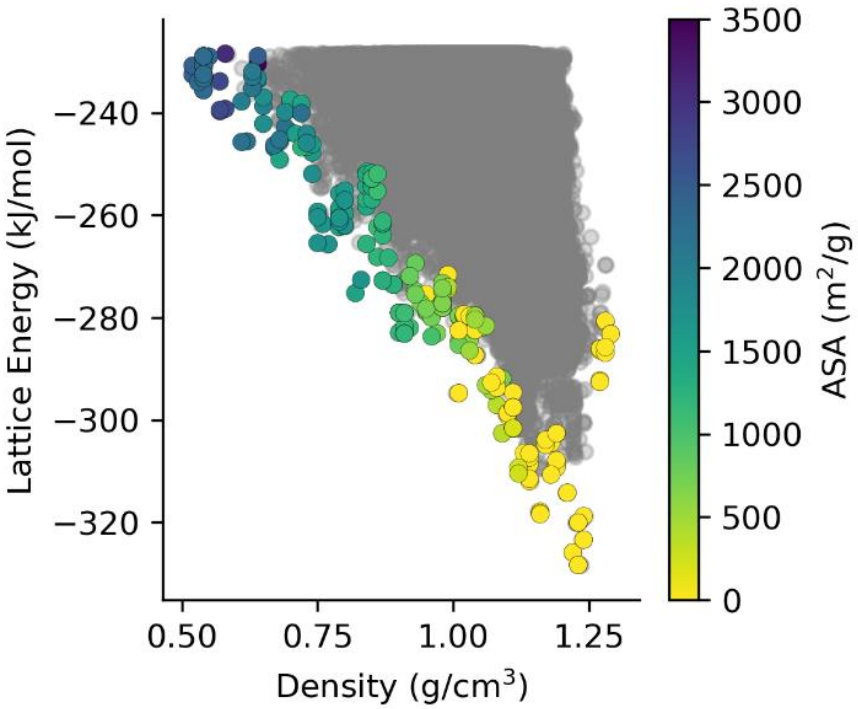

Figure 4.8. Energy-structure-function (ESF) map for predicted **ABTPA** conformers (grey). The leading-edge structures are colour coded by accessible surface areas (m^2/g), calculated using a probe radius of 1.7 Å.

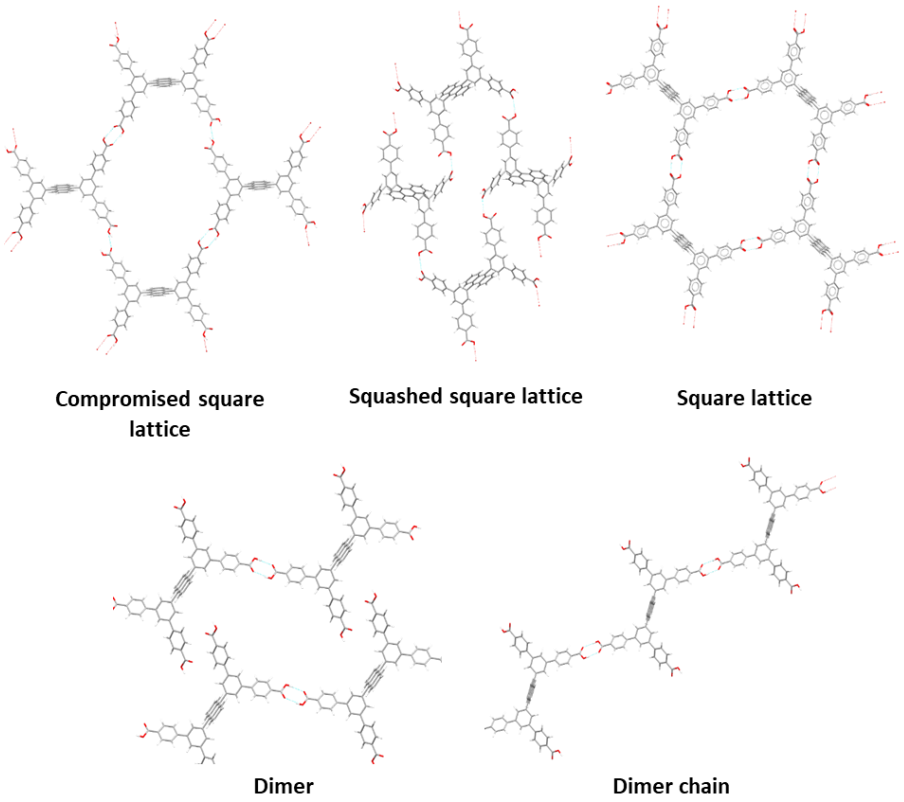

Figure 4.9. Examples of the hydrogen bond motifs that were found in the initial CSP dataset.

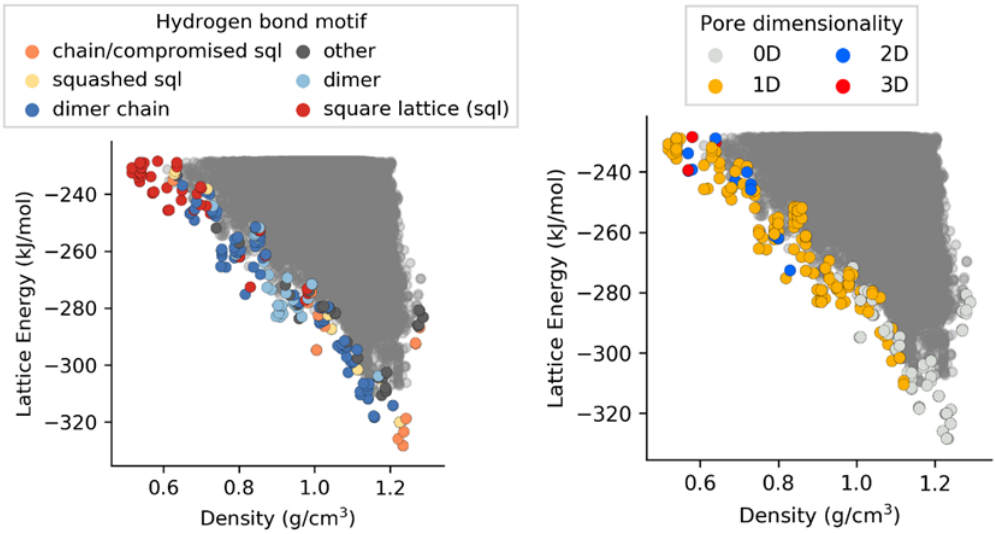

Figure 4.10. Energy vs. density plot for CSP calculations on an initial set of 63 conformers, with points on the 'leading edge' coloured by (left) their hydrogen bonding packing motif (Figure 4) and (right) by the dimensionality of the pores, calculating using a probe radius of 1.7 Å.

4. Experiment and result discussion

*4.1 Crystallisation and single crystal structure of **ABTPA-1***

ABTPA showed poor solubility in organic solvents, possibly because of its π-conjugated system. After a solubility test, **ABTPA** was found to dissolve THF (~ 2 mg mL^{-1}) and 1,4-dioxane (~ 1 mg mL^{-1}). THF was used as a good solvent to crystallise **ABTPA** according to the following procedure:

ABTPA (10 mg, 12.3 mmol) was dissolved in THF (5 mL) in a 20 mL glass sample vial and then 5 mL several different anti-solvents (mesitylene, n-butylbenzene, 1,2-dimethoxybenzene, 1,3-dimethoxybenzene) was added to the solution. The vial was left uncapped at room temperature (RT) to allow the crystallisation solvent to slowly evaporate. After 5 – 7 days, **ABTPA** was crystallised on the wall and bottom of the vial. In these four conditions, only small needle-shaped crystals (**ABTPA-1**) were obtained from THF/1,2-dimethoxybenzene that were large enough for SCXRD.

The solvated crystals were characterised by synchrotron SCXRD at 100 K (Figure 4.11). In the solvated crystal structure, **ABTPA-1**, the carboxylic acid groups of **ABTPA** direct the structure of a HOF net with a **sql** topology (Figure 4.11c). Four-membered hydrogen-bonded rings are formed via cooperative $R_2^2(8)$ hydrogen bonding interactions at an O-H•••O distance of 2.625(2) Å. The angle between the plane of the 2-D hydrogen-bonded network and the plane of the anthracene unit in **ABTPA-1** is 76(3)°. Each 4-membered hydrogen-bonded ring has two out-of-plane anthracene units that prevent the interpenetration of the 2-D hydrogen-bonded layers. A biphenyl analog of **ABTPA** without these anthracene units, for example, was shown to crystallise as a 5-fold interpenetrated structure.[39] In the extended crystal structure of **ABTPA-1**, the **sql** hydrogen-bonded layers are stacked along [010] through the formation of offset, face-to-face, π-π stacking interactions between the anthracene units in neighboring 2-D hydrogen-bonded layers, at a repeat distance of 5.0 Å (Figure 4.11d). This packing arrangement generates an open pore structure in **ABTPA-1** along the [001] direction, which is full of disordered solvent molecules.

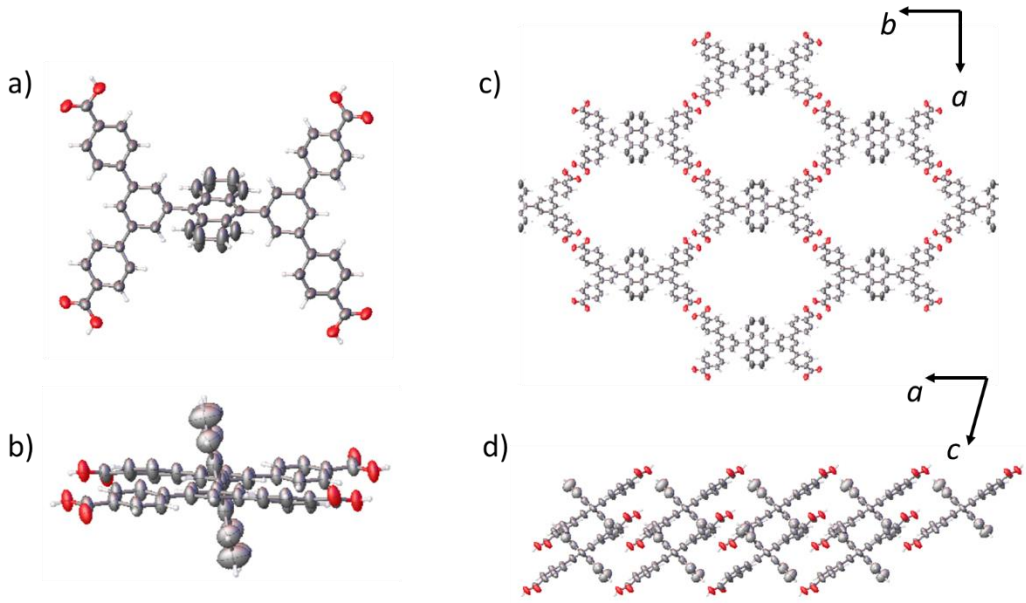

Figure 4.11. a) Displacement ellipsoid plot from the single crystal structure of **ABTPA**-1. b) Side view of **ABTPA-1**. c) Crystal packing of **ABTPA-1** viewed along [001]. d) Crystal packing of **ABTPA-1** viewed along [010]. Ellipsoids are displayed at 50 % probability. Labels were omitted for clarity. Grey: carbon; red: oxygen; white: hydrogen.

Crystal data for **ABTPA-1**: Formula $(C_{54}H_{34}O_8)\cdot 2(C_4H_8O)\cdot 2(C_8H_{10}O_2)$; M = 1231.34, Monoclinic $C2/m$, light yellow needle shaped crystals; a = 20.3444(9) Å, b = 34.8402(10) Å, c = 5.0204(2) Å, β = 103.926(4)° ; V = 3453.9(2) Å^3; ρ = 1.184 g/cm^3; Z = 2; $\mu(\lambda$ = 0.6889 Å) = 0.075 mm^{-1}; F (000) = 1300; crystal size = 0.20 x 0.03 x 0.03 mm; T = 100(2) K; 12499 reflections measured ($1.149 < \theta < 26.572$), 3800 unique (R_{int} = 0.0801), 1821 ($I > 2\sigma(I)$); R_1 = 0.0754 for observed and R_1 = 0.1151 for all reflections; wR_2 = 0.2333 for all reflections; max/min difference electron density = 0.233 and -0.220 e·Å^3; data/restraints/parameters = 3800/21/143; GOF = 1.076. CCDC: 1977891. Due to disorder, solvent molecules in the large interconnected 1-D pores could not be accurately modelled. A solvent mask was applied during the final refinement cycles.[40]

The experimental PXRD pattern of **ABTPA-1** was also compared to the simulated pattern from the CIF file (Figure 4.12). To prepare solvated **ABTPA-1** for PXRD, the residual THF and 1,2-dimethoxybenzene solvents were removed from the vial with a

syringe. The wet **ABTPA-1** was transferred onto the PXRD plate and its PXRD pattern was recorded at RT for 60 mins. For the simulated PXRD pattern of **ABTPA-1**, the diffraction pattern peak intensity from $2\theta = 15°$ was multiplied by 10 for clarity. A close structural match was observed by comparing the low angle regions of the PXRD patterns, although solvent molecules that could not be resolved in **ABTPA-1** and difference in collection temperature may have contributed to the differences at a higher angle.

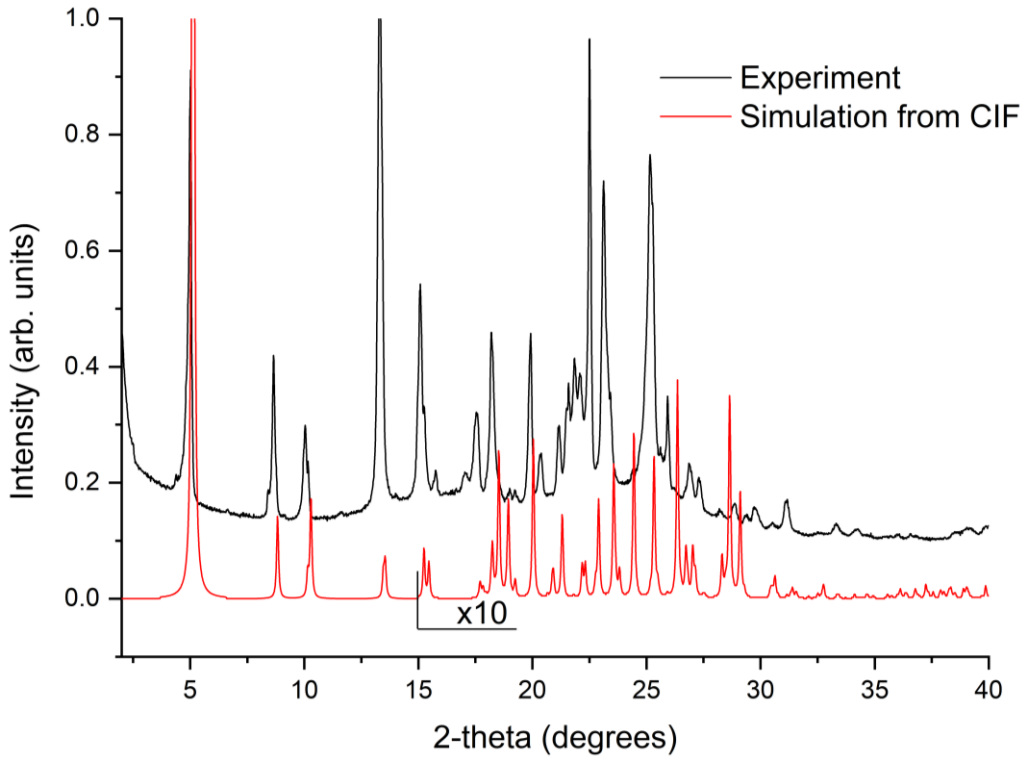

Figure 4.12. Experimental PXRD pattern of solvated **ABTPA-1** (λ = 1.54184 Å), shown above the simulated PXRD pattern from the solvent masked single crystal structure of **ABTPA-1**. For the simulated PXRD pattern of **ABTPA-1**, the diffraction pattern peak intensity was multiplied by 10 from $2\theta = 15°$. Also, Pawley method was used to refine the PXRD pattern that collected from synchrotron (Figure 4.13).

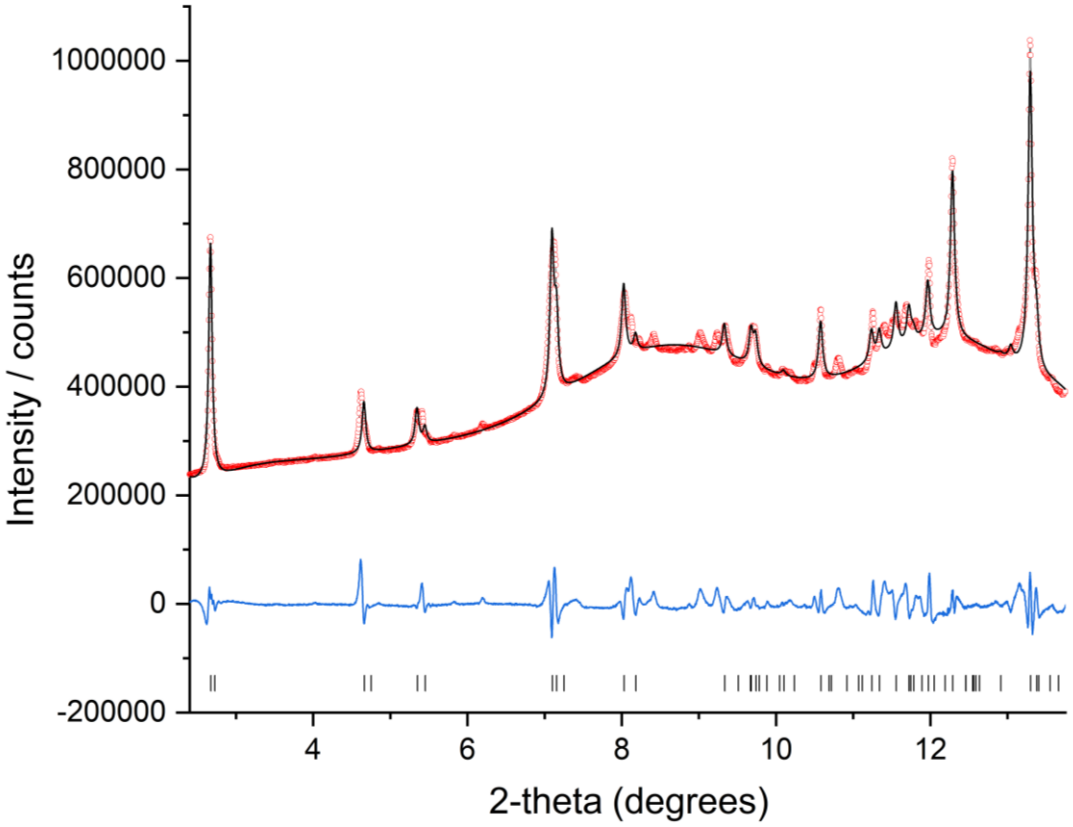

Figure 4.13. PXRD pattern fitting of **ABTPA-1** with Pawley refinement (λ = 0.825186 Å). Red circles: experimental PXRD pattern from synchrotron, black line: fitting pattern, blue curve: difference between experimental and refinement, black bars: reflection positions, R_p = 2.346%, R_{wp} = 2.998% (*C*2/*m*, *a* = 20.12010(5) Å, *b* = 35.00322(4) Å, *c* = 5.00715(7) Å, β = 103.05752(2)°, *V* = 3435.19764(1) Å^3).

*4.2 Crystallisation and single crystal structure of **ABTPA-2***

Residual 1,2-dimethoxybenzene and THF crystallisation solvent covering crystals of **ABTPA-1** (10 mg) in a 20 mL sample vial was removed using a syringe. Acetone (10 mL) was then added to fully immerse the crystals and the vial was capped. After 12 hours, the acetone solvent was removed using a syringe and replaced with fresh acetone solvent (10 mL). This process was repeated every 12 hours for 5 days. The acetone exchanged crystals were degassed at RT under a dynamic vacuum for 2 hrs to obtain the activated material, **ABTPA-2**. Yield: 98 %.

PXRD patterns that were recorded after exchanging the crystallisation solvent with

acetone (**ABTPA-acetone,** Figure 4.14) and then after degassing the crystals under dynamic vacuum at RT (**ABTPA-2,** Figure 4.15) showed that an obvious phase change occurred during the degassing step. Pawley refinements were used to refine the PXRD patterns of **ABTPA-acetone** and **ABTPA-2**.

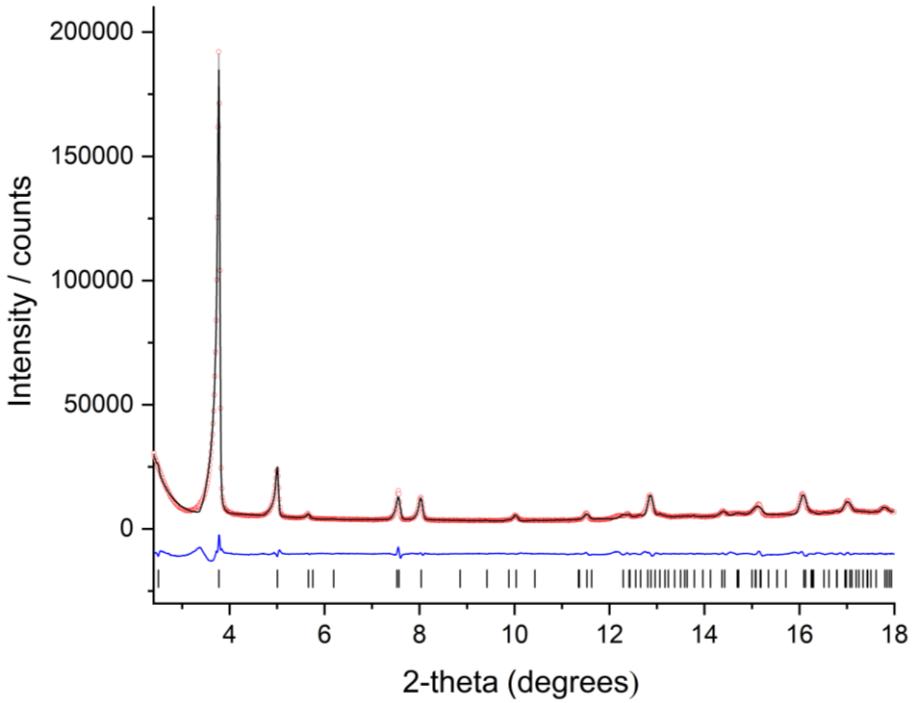

Figure 4.14. PXRD pattern fitting of **ABTPA-acetone** with Pawley refinement (Cu-kα). Red circles: experimental PXRD pattern, black line: fitting pattern, blue curve: difference between experimental and refinement, black bars: reflection positions, R_p = 3.51%, R_{wp} = 5.10% ($P2_1/c$, a = 35.29789(2) Å, b = 31.24071(4) Å, c = 7.27175(2) Å, β = 92.66608(5)°, V = 8010.10195(3) Å^3).

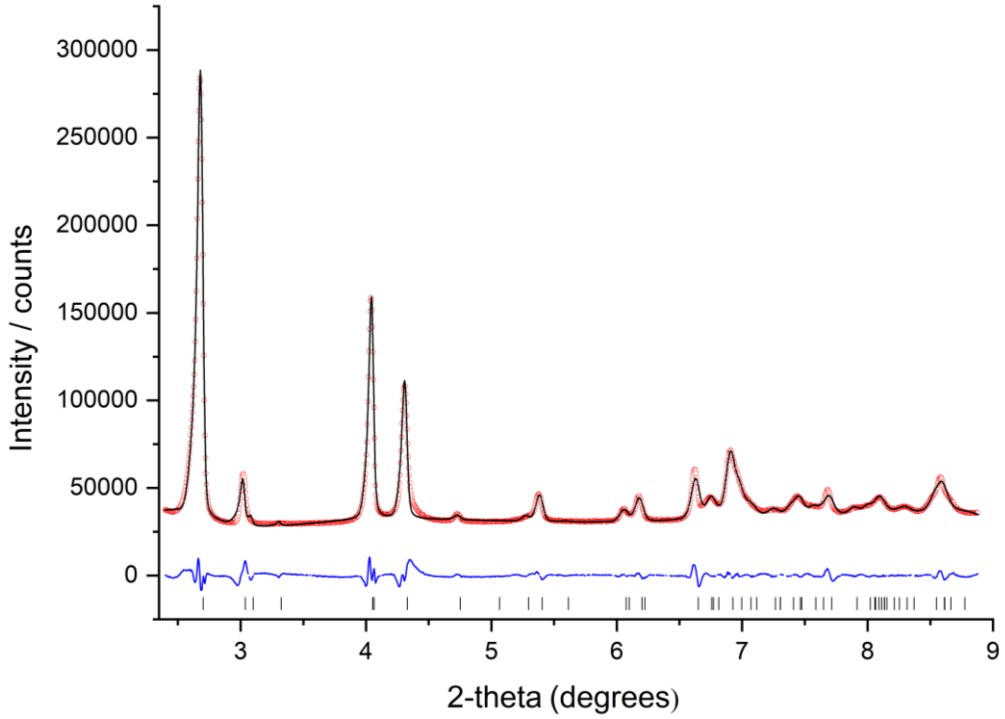

Figure 4.15. PXRD pattern fitting of **ABTPA-2** with Pawley refinement (λ = 0.825186 Å). Red circles: experimental PXRD pattern, black line: fitting pattern, blue curve: difference between experimental and refinement, black bars: reflection positions, R_p = 2.345%, R_{wp} = 3.683% ($P2_1/c$, a = 35.091130(2) Å, b = 31.147111(4) Å, c = 7.187532(2) Å, β = 94.10248(5)°, V = 7835.752(3) Å^3).

The crystals of **ABTPA-1** broke up during the transformation and became too small for analysis by SCXRD, even using synchrotron radiation. The SEM images showed the activated crystals (**ABTPA-2**) were micron-sized (Figure 4.16), and it is therefore not surprising that even synchrotron X-ray data was too weak for determine the structure of **ABTPA-2**.

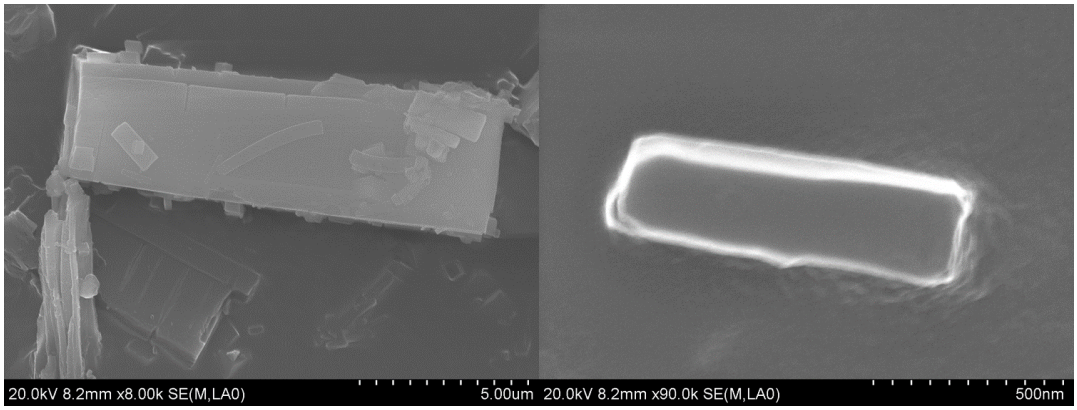

Figure 4.16. SEM images of **ABTPA-2** with different magnifications. Scale bars are included in the bottom right corner of the SEM images.

To determine the structure of **ABTPA-2,** 3-D electron diffraction (ED) was introduced because of its shorter wavelength (x 10^{-3} nm) and stronger scattering power than X-ray diffraction. 3-D ED makes it possible to acquire three-dimensional reciprocal space data for crystals that are too small for conventional single-crystal X-ray diffraction (SCXRD) methods.[41] Various techniques have been developed such as continuous rotation electron diffraction (cRED),[42–44] automated diffraction tomography (ADT),[45,46] and microcrystal electron diffraction (MicroED).[47] cRED is a method that the diffraction data is collected by combining electron beam tilt at many very small steps, with rotation of the crystal in a few but large steps.[42] The ADT data is acquired through sequentially tilting a selected crystal around an arbitrary crystallographic axis with a variable tilt step down to 0.1°, which includes a large number of high-index reflections.[45,46] With the same principle, MicroED data are collected as a movie as the crystal is continuously rotated by the microscope stage.[47] Moreover, the collection of 3-D ED data on crystals previously considered too beam-sensitive has been made possible recently through advances in detector technology and software development,[29,41,48] as illustrated by studies on metal-organic frameworks (MOFs),[49,50] proteins,[47,51] and covalent-organic frameworks (COFs).[52–54] For example, a porous cobalt tetraphosphonate MOF with 1-D channels, Co-CAU-36, was determined by cRED and the organic molecules in the pores are also located using the cRED data (Figure 4.17).[50]

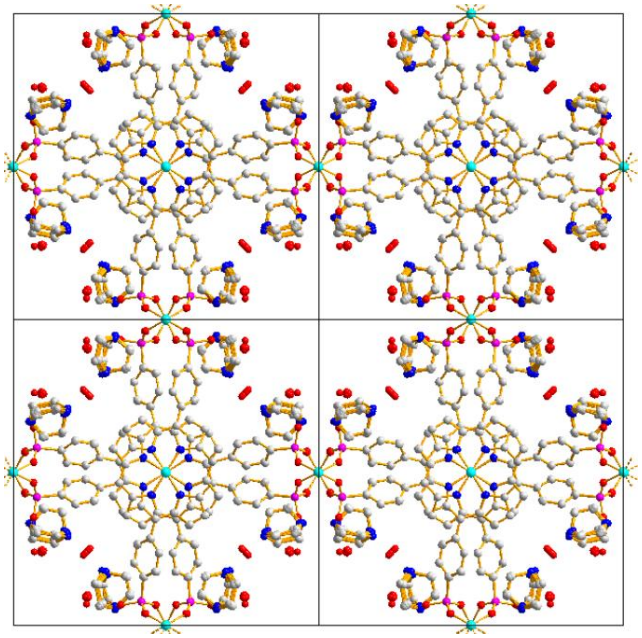

Figure 4.17. The structure of Co-CAU-36 MOF determined by 3-D ED. Grey: carbon; red: yellow; blue: nitrogen; pink: phosphorus; cyan: cobalt. Reprint from *Chem. Eur.J.*, 2018, 24, 17429 –17433. Copyright from 2018 Wiley-VCH.

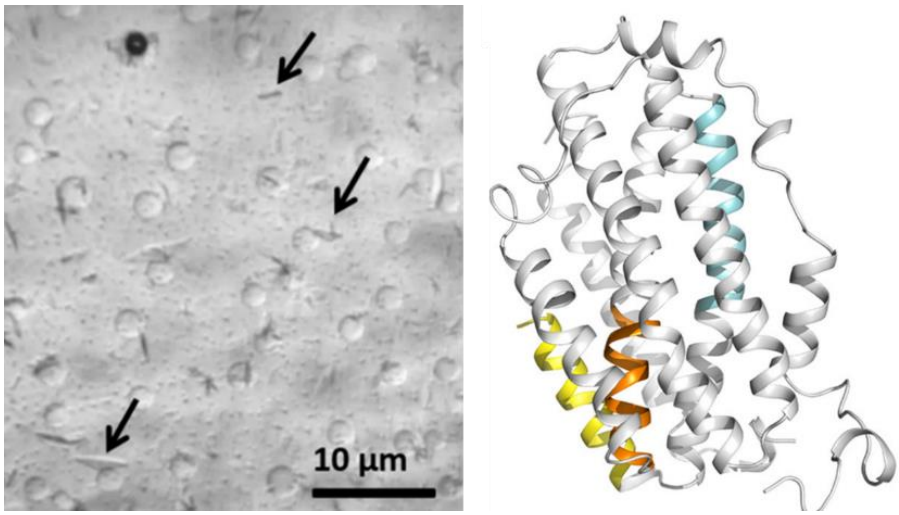

Figure 4.18. The R2lox microcrystals (pointed out by arrows) that were characterised by 3-D ED, viewed under an optical microscope and the overall structure solved by MicroED. Reprint from *Sci. Adv.*, 2019, 5, eaax4621. Copyright from 2019 American Association for the Advancement of Science.

MicroED was usually applied to redetermine the protein structures that have already

been solved by SCXRD.[47] But in 2019, it was first used to solve a new protein structure, an R2lox enzyme (Figure 4.18).[51] Microcrystalline COFs with strong covalent linages (B-O, C-N, and B-N) between building units have also be determined with ED. The first COF (COF-320) structure that was solved with ED was reported in 2013 (Figure 4.19a),[52] and now other COFs, including COF-300 and COF-505 were characterised with 3-D ED (Figure 4.19b, c).[53,54]

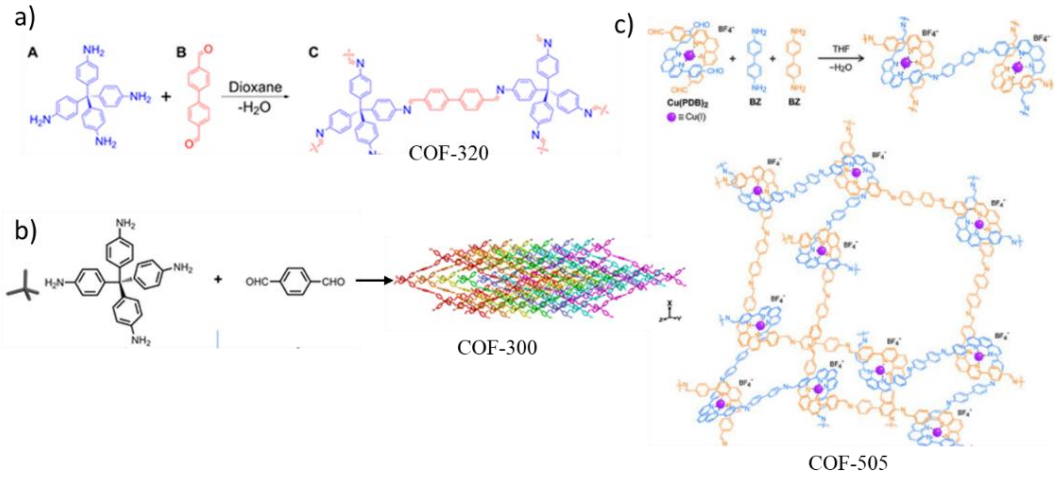

Figure 4.19. a) The structure of COF-320 determined by 3-D ED. Reprint from *J. Am. Chem. Soc.*, 2013, 135, 44, 16336–16339. Copyright from 2013 American Chemical Society. b) The structure of COF-300. Reprint from *J. Am. Chem. Soc.*, 2018, 140, 22, 6763–6766. Copyright from 2018 American Chemical Society. c) The structure of COF-505. Reprint from Science, 2016, 351, 365-369. Reprint from 2016 American Association for the Advancement of Science.

Here, 3-D ED was combined with crystal structure prediction to understand the structural transformation of a flexible HOF. This is also the first time that 3-D ED has been used in the determination of porous HOF materials.

3-D ED data was collected by continuously tilting a 0.5 μm crystal cooled to 97 K by the collaborators from Stockholm University (Dr A Ken Inge and Erik Svensson Grape, Figure 4.20). Data was collected using the software Instamatic,[55] and the acquired frames were then processed using XDS.[56] Reflection conditions were examined using the RED software package.[43] The structure was solved using

SHELXT.[57] All the non-hydrogen atoms were located in the initial structure solution (Figure 4.21).

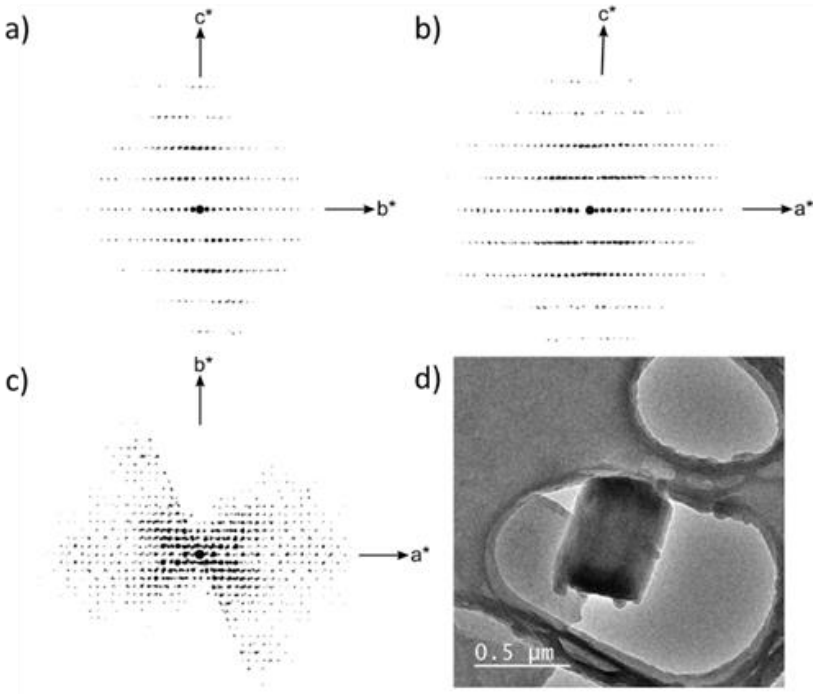

Figure 4.20. Two-dimensional slices cut from the three-dimensional reciprocal space lattice showing the (a) 0kl, (b) h0l, and (c) hk0 planes; (d) low magnification TEM image of crystallite (**ABTPA-2**) used here for data collection and processing.

In the desolvated crystal structure, **ABTPA-2**, the carboxylic acid groups of **ABTPA** direct the structure of a HOF net with a **sql** topology which is the same as **ABTPA-1**. Four-membered hydrogen-bonded rings are formed via cooperative $R_2^2(8)$ hydrogen bonding interactions at an O-H•••O distance of 2.739(2) Å. The angle between the plane of the 2-D hydrogen-bonded network and the plane of the anthracene unit in **ABTPA-2** is 71.4(2) °. Each 4-membered hydrogen-bonded ring has two out-of-plane anthracene units that prevent the interpenetration of the 2-D hydrogen-bonded layers (Figure 4.21).

In the extended crystal structure of **ABTPA-2**, the **sql** hydrogen-bonded layers are stacked along [100] through the formation of offset, edge-to-face, CH-π stacking interactions between the anthracene units in neighboring 2-D hydrogen-bonded layers.

This packing arrangement generates an open pore structure in **ABTPA-2** along the [001] direction.

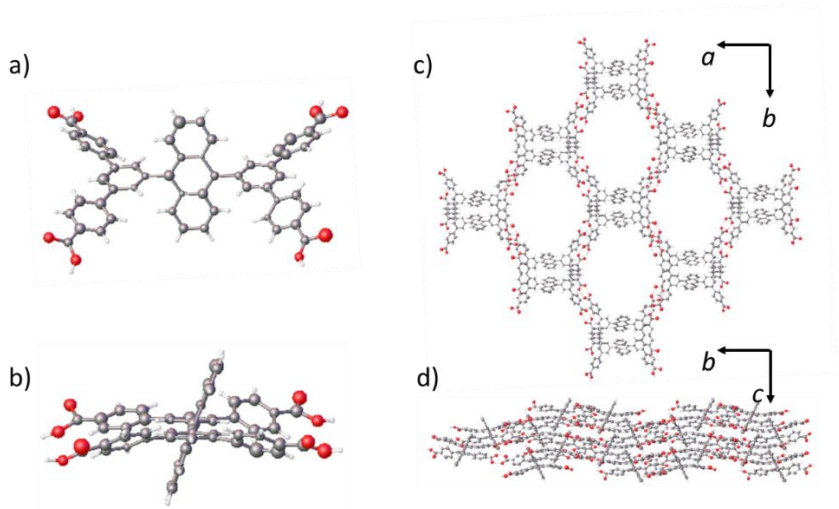

Figure 4.21. a) Displacement ellipsoid plot from the 3-D ED structure of **ABTPA-2**. b) Side view of **ABTPA-2**. c) Crystal packing of **ABTPA-2** viewed along [001]. d) Crystal packing of **ABTPA-2** viewed along [100]. Labels were omitted for clarity. Grey: carbon; red: oxygen; white: hydrogen.

Electron diffraction single crystal data for **ABTPA-2**: Formula ($C_{54}H_{34}O_8$); M = 810.86, Monoclinic $P2_1/c$, light yellow cuboid shaped crystals; a = 36.20(3) Å, b = 32.39(3) Å, c = 7.30(3) Å, β = 92.52(4)° ; V = 8550(19) Å^3; ρ = 0.63 g/cm^3; Z = 4; λ = 0.0251 Å; T = 97 K; rotation range = 107.30° (-42.74° – 64.56°); index ranges: -32 ≤ h ≤ 24, -26 ≤ k ≤ 20, -5 ≤ l ≤ 6; 8319 reflections measured, 4168 unique (R_{int} = 0.2237), completeness (to 1.1 Å resolution) 62.7 %, R_1 (ED model) ($I > 2\sigma(I)$) = 0.311.

The experimental PXRD pattern of **ABTPA-2** was compared with the simulated pattern from 3-D ED to prove the accuracy of the ED model (Figure 4.22). The experimental PXRD pattern of **ABTPA-2** was recorded after activating the acetone solvated crystals at RT under vacuum (Figure 4.22, black), shown above the simulated PXRD pattern from the ED structure, **ABTPA-2** (Figure 4.22, red). For both PXRD patterns, the diffraction peak intensity was multiplied by 10 from 2θ = 6° for clarity. The good match also proved the accuracy of the ED model for **ABTPA-2**.

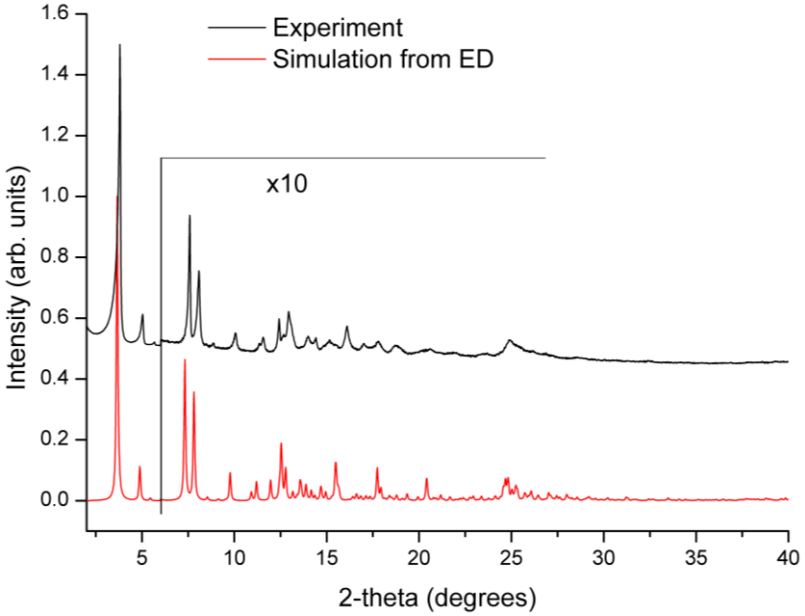

Figure 4.22. Experimental PXRD pattern of **ABTPA-2** (black), and the simulated PXRD pattern from the ED structure of **ABTPA-2** (red). For both PXRD patterns, the diffraction peak intensity was multiplied by 10 from $2\theta = 6°$.

A full Rietveld refinement of the **ABTPA-2** structure against the synchrotron powder X-ray diffraction data is displayed in Figure 4.23 to further validate the ED model. During the Rietveld refinement, all six peripheral aromatic rings were allowed to rotate freely, but the carbon-carbon distances in the aromatic rings were constrained to be equal. All carbon-oxygen bond distances, carbon-carbon distances between carboxylates and the aromatic rings, and the carbon-carbon bond distances between rings were also constrained to be equal. Additional soft distance restraints were applied to oxygen-oxygen distances between hydrogen-bonded carboxylic acid groups, and the carboxylic acid groups were allowed to rotate but the hydrogen-bonded carboxylic acid groups were refined with a co-planar restraint. After the refinement a good structural match between the 3-D ED and Rietveld refinement structural model (see Figure 4.24 for the structural comparison). However, due to the differences in the collection temperature (97 K for 3-D ED versus 298 K powder X-ray diffraction data) and the overestimation of cell parameters for the electron diffraction data, these structures are not directly comparable.

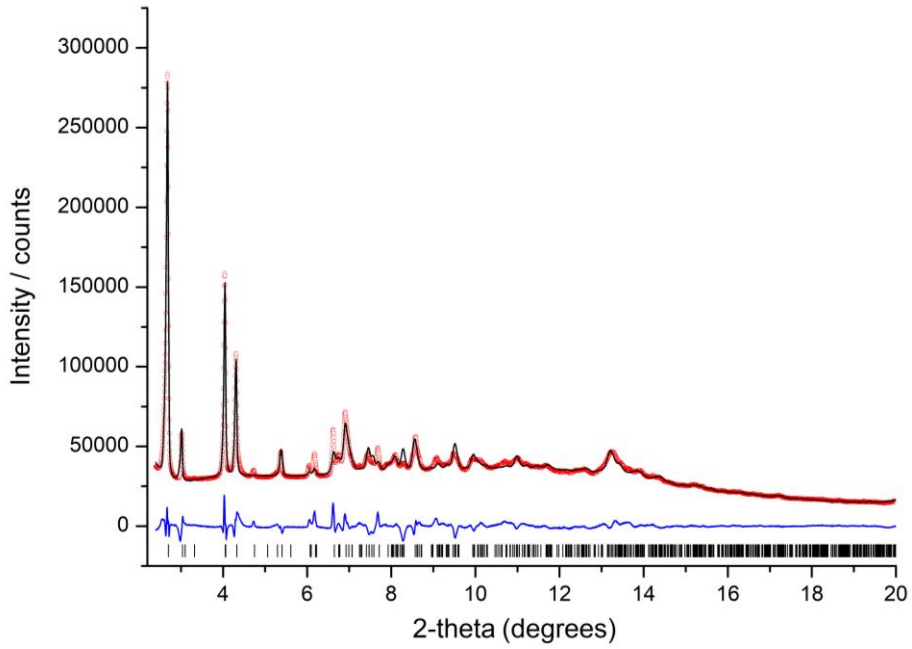

Figure 4.23. PXRD pattern fitting of **ABTPA-2** after a Rietveld refinement, using the 3-D ED structure as a starting model (λ = 0.825186 Å). Red circles: experimental PXRD pattern, black line: fitting pattern, blue curve: difference between experimental and refinement, black bars: reflection positions, R_p = 2.925%, R_{wp} = 4.585%. ($P2_1/c$, a = 35.120(6) Å, b = 31.145(4) Å, c = 7.213(1) Å, β = 94.78(1) °, V = 7862(2) Å^3).

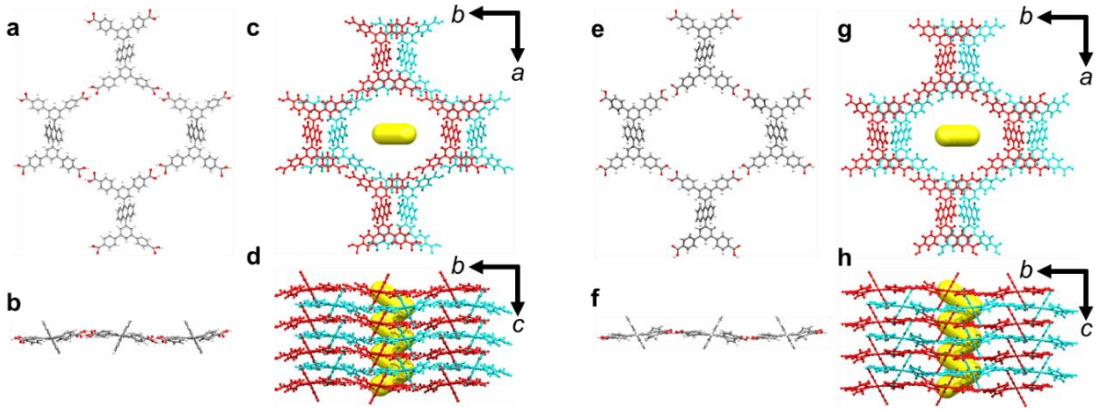

Figure 4.24. a-d) The ED structure of **ABTPA-2**; a) The 4-membered rings with **sql** topology. b) The side viewed along [100]. c) The packing of **sql** layers viewed along [001]. d) The herringbone arrangement viewed along [100]. e-h) The Rietveld structure of **ABTPA-2**; e) The 4-membered hydrogen-bonded rings generated a same HOF net with **sql** topology with ED structure. f) The side viewed along [100]. g) The packing of **sql** layers viewed along [001]. h) The arrangement viewed along [100].

The 3-D ED structure and Rietveld structure were compared with each other in Figure 4.24 to show the close match and prove the accuracy of the 3-D ED model.

Table 4.2. Unit cell parameter for **ABTPA** structures determined from X-ray and 3-D ED data.

	ABTPA-1	**ABTPA-1[a]**	**ABTPA-acetone[a,b]**	**ABTPA-2[c]**	**ABTPA-2[d]**
***T* [K]**	100	298	298	97	298
Space group	*C*2/*m*	*C*2/*m*	$P2_1/c$	$P2_1/c$	$P2_1/c$
***a* [Å]**	20.34(9)	20.12(1)	35.29(1)	36.20(3)	35.12(6)
***b* [Å]**	34.84(1)	35.00(1)	31.24(1)	32.39(3)	31.15(4)
***c* [Å]**	5.02(2)	5.00(1)	7.27(1)	7.30(3)	7.21(11)
***β* [°]**	103.93(4)	103.06(2)	92.7(2)	92.52(4)	94.78(12)
Volume [Å^3]	3453(2)	3435(2)	8010(9)	8550(3)	7862(2)
Z	2	2	4	4	4
HOF framework density (g/cm^3)	0.78	0.78	0.67	0.63	0.66
Void volume per ABTPA [Å^3][e]	551			859	790

[a] Cell parameters from PXRD data recorded at 298 K. [b] **ABTPA**-acetone: **ABTPA-1** was subjected to crystallisation solvent exchanges with acetone for 5 days, before the PXRD pattern was recorded in air at 298 K. [c] Cell parameters from 3-D ED structure recorded at 97 K. [d] Unit cell parameters determined for **ABTPA-2** from the Rietveld refinement shown in Figure 4.23. [e] calculated using 1.2 Å probe and 0.15 Å grid spacing.

Remarkably, the reorientation of 2-D HOF layers in **ABTPA-2** results in the crystal structure undergoing a framework expansion during crystal activation, decreasing the

skeleton density of the HOF from 0.78 in **ABTPA-1** to 0.63 g/cm^3 in **ABTPA-2**, and increasing the total void volume per **ABTPA** molecule from 551 to 859 Å^3 (Table 4.2).

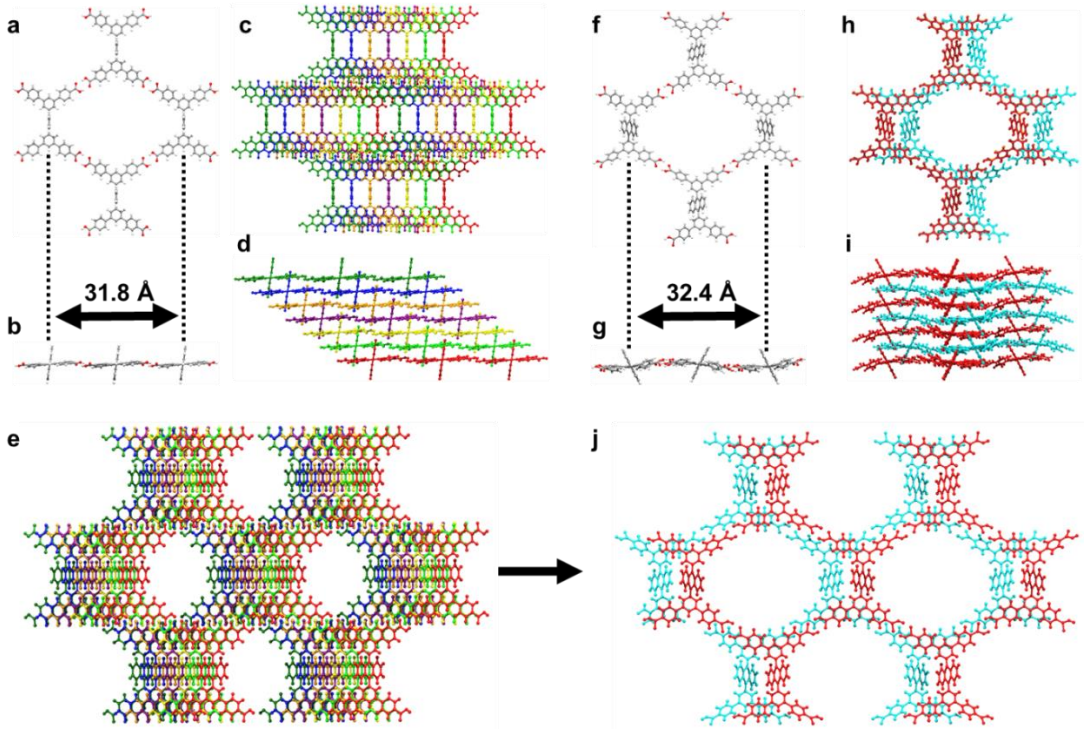

Figure 4.25. a) In the **ABTPA-1** single crystal structure, the 4-membered hydrogen-bonded rings generate a HOF net with a **sql** topology. b) The **sql** HOF nets feature out-of-plane anthracene units. c, d) In **ABTPA-1**, the **sql** HOF nets are stacked in an offset arrangement viewed along [103] (c); viewed along [010] (d), via offset π-π interactions between the anthracene units, to generate a packing motif which repeats every seven layers. e) This packing arrangement of **ABTPA** molecules in **ABTPA-1** generates 1-D solvent-filled pores viewed along [001]. (f, g, h, i) In the Rietveld refined **ABTPA-2** structure that used synchrotron PXRD data collected at 298 K, the **sql** HOF layers have a different geometry and the anthracene units are packed in a herringbone arrangement viewed along [100] (i). j) The alternating packing of **sql** HOF layers in **ABTPA-2** generates a 1-D pore viewed along [001].

The crystal packing in the Rietveld refined **ABTPA-2** structure is distinct from that in **ABTPA-1** (Figure 4.25, e → j). In **ABTPA-2**, the 2-D hydrogen-bonded nets have the same underlying **sql** topology, but the geometry of the HOF layers is different (Figure 4.25, b → g), with the carboxylic acid groups rotated out of plane to their adjacent ring to better satisfy the H-bonding network. In **ABTPA-2** the 2-D HOF layers are packed in an A-B stacking arrangement, with the anthracene units packed in a herringbone-type arrangement when viewed along the [100] direction (Figure 4.25, d → 2i).

*4.3 Crystallisation and single crystal structure of **ABTPA-3***

Besides exchanging the crystallisation solvent in **ABTPA-1** with acetone, *n*-pentane was also exchanged directly with the crystallisation solvent before the pores were evacuated under vacuum. To achieve this, the residual 1,2-dimethoxybenzene and THF crystallisation solvent covering crystals of **ABTPA-1** (10 mg) in a 20 mL sample vial was removed using a syringe. *n*-Pentane (10 mL) was then added to fully immerse the crystals and the vial was capped. After 12 hours, the *n*-pentane solvent was removed using a syringe and replaced with fresh *n*-pentane solvent (10 mL). This process was repeated every 12 hours for 5 days. The *n*-pentane exchanged crystals were degassed at RT under dynamic vacuum for 2 hrs to obtain the activated material, **ABTPA-3**. Yield: 98 %.

The crystals of **ABTPA-1** also broke up during activation of the *n*-pentane exchanged phase and became too small for analysis by SCXRD, even using synchrotron radiation. The SEM images showed the size of the activated crystals (**ABTPA-3**) were only a few micrometers (Figure 4.26), revealing why it was difficult to collect suitable 4. single crystal X-ray data for **ABTPA-3**.

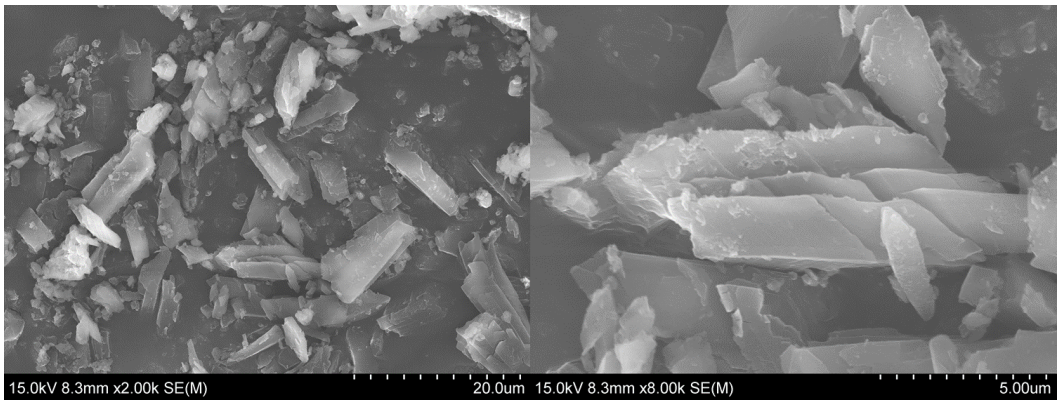

Figure 4.26. SEM images of **ABTPA-3** at different magnifications. Scale bars are included in the bottom right corner of the SEM images.

Instead, 3-D ED data was collected for **ABTPA-3** by continuously tilting a 0.5 µm crystal cooled to 97 K. During the ED collection, the thin plate crystal (Figure 4.27a) was used to determine the structure while some large particles cannot diffract (Figure 4.27b). There were also non-crystalline particles in **ABTPA-3**, which proved it was a mixture crystalline and amorphous particle.

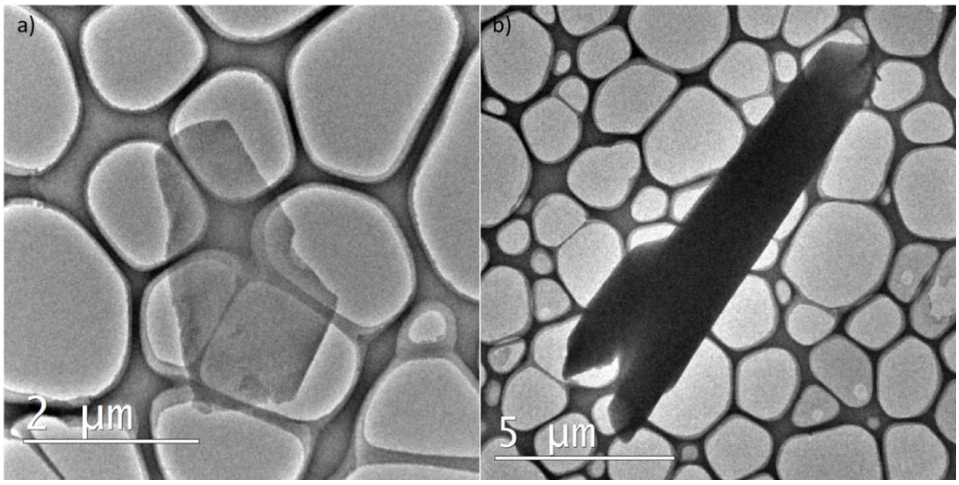

Figure 4.27. TEM images of **ABTPA-3** at different magnifications. a) Images of the **ABTPA-3** crystal used for 3-D ED structure determination, b) image of a larger particle that was found to be amorphous. Scale bars are included in the bottom left corner of the TEM images.

The 3-D ED structure of **ABTPA-3** revealed that **ABTPA-1** transforms into a

different structure following activation via the *n*-pentane solvated crystals (Figure 4.28). After the *n*-pentane exchange procedure, water molecules were found in the resulting hydrogen bonded structure. Water molecules in **ABTPA-3** disrupted the $R_2^2(8)$ hydrogen bonding motifs between **ABTPA** molecules and meant that it did not have a comparable **sql** hydrogen bonded network to that found in **ABTPA-1** and **ABTPA-2**.

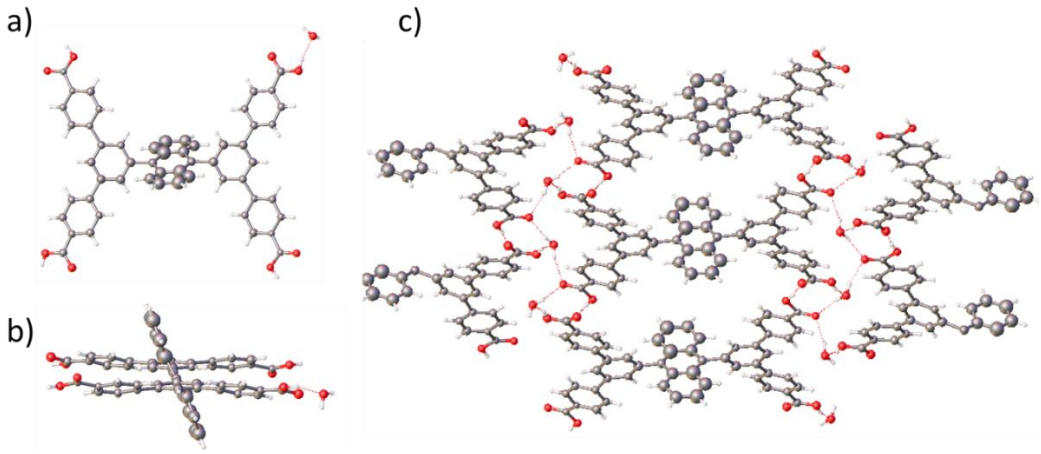

Figure 4.28. a) Displacement ellipsoid plot from the 3-D ED structure of **ABTPA-3**. b) Side view of **ABTPA-3**. c) Crystal packing of **ABTPA-3** viewed along [100]. Labels are omitted for clarity. Atom colours, grey: carbon; red: oxygen; white: hydrogen.

3-D ED single crystal data for **ABTPA-3**: Formula ($C_{54}H_{34}O_8$ $2H_2O$); M = 846.84, Monoclinic $P2_1/c$, light yellow cuboid shaped crystals; a = 7.16(3) Å, b = 39.62(3) Å, c = 8.34(3) Å, β = 95.9(4)° ; V = 2357(9) Å^3; Z = 2; λ = 0.0251 Å; T = 97 K; rotation range = 94.62° (-61.48° – 33.14°); index ranges: -7 ≤ h ≤ 8, -45 ≤ k ≤ 41, -9 ≤ l ≤ 8; 5283 reflections measured, 2740 unique (R_{int} = 0.1016), completeness (to 0.8 Å resolution) 64.3 %, R_1 (ED model) ($I > 2\sigma(I)$) = 0.3292.

The experimental PXRD pattern of **ABTPA-3** was not a direct match to the simulated PXRD pattern from 3-D ED, although there were some similarities (Figure 4.29). The experimental PXRD pattern of **ABTPA-3** was measured at RT after activating the *n*-pentane solvated crystals at RT under vacuum for 1 hour (Figure 4.29, red), in contrast to the 3-D ED structure that was recorded at 97 K and is shown above the

simulated PXRD pattern from the ED structure, **ABTPA-3** (Figure 4.29, black). The difference in collection temperature may have accounted for some of the differences. The broadening of several peaks in the experimental PXRD **ABTPA-3** also indicated it had lower crystallinity than **ABTPA-1** and **ABTPA-2**. Because **ABTPA-3** contains water in its hydrogen-bonded network that was not included in the CSP calculations its structure was not predicted. Only **ABTPA-1** and **ABTPA-2** are therefore discussed in the following sections of this chapter.

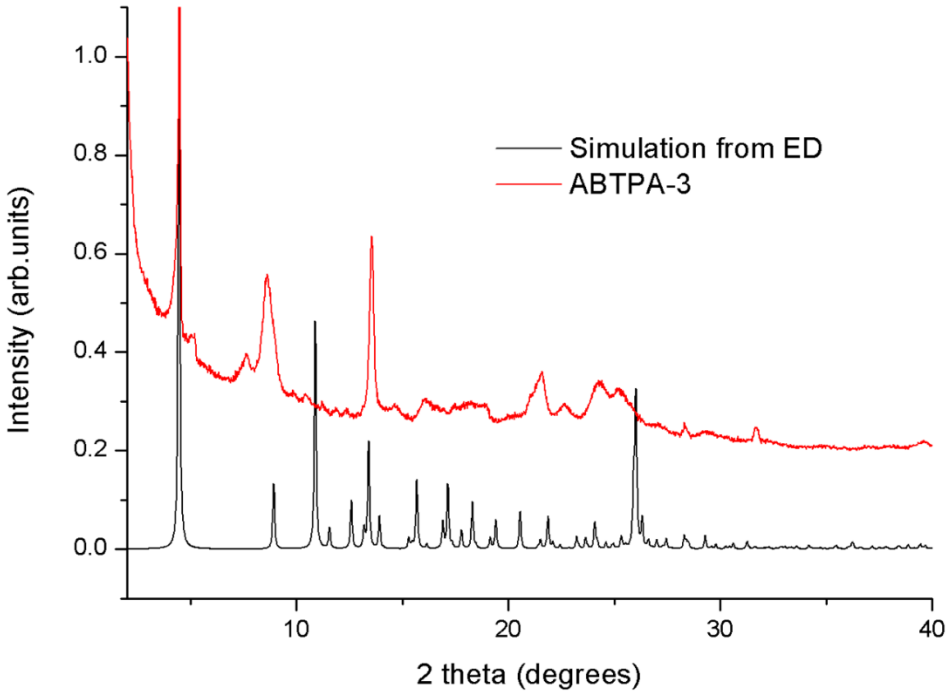

Figure 4.29. Experimental PXRD pattern of solvated **ABTPA-3** (red), shown above the simulated PXRD pattern from the 3-D ED structure of **ABTPA-3** (black).

*4.4 **ABTPA-1** and **ABTPA-2** on CSP map*

No good match for the experimental solvated structure, **ABTPA-1**, was found on the initial CSP landscape, which was calculated using an ensemble of 63 predicted low energy conformers. This was thought to be due to insufficient conformational sampling rather than an inadequacy in the energy models used. Additional conformer searches were therefore performed using the experimental conformers in **ABTPA** found in **ABTPA-1** as a starting point.

Additional conformers were optimised by extracting the 3-D geometry from the experimental crystal structures and optimizing, subject to a) no constraints, b) constraining the arene-arene dihedral angles φ and ψ, and c) constraining all arene-arene and arene-carboxylic dihedral angles. All other degrees of freedom (e.g. bond lengths, torsion angles etc.) were free to refine in these optimisations. Details about the optimised conformers are shown in Table 4.3.

Table 4.3. Relative conformational energies for **ABTPA-1** and **ABTPA-2** with fixed at different conditions and accompanying dihedral angles (ordered by relative energy).

Conformer	**Relative Energy (kJ/mol)**	**Dihedral Angle (ψ)**	**Dihedral Angle (ϕ)**
ABTPA-1 (opt. fixing 2 dihedrals)	0.143	75.49	76.21
ABTPA-2 opt.	0.780	80.50	80.51
ABTPA-2 (opt. fixing 2 dihedrals)	2.639	71.63	72.21
ABTPA-2 (opt. fixing all dihedrals)	11.869	71.63	72.21
ABTPA-1 (opt. fixing all dihedrals)	26.008	75.49	76.21

Further CSP calculations were performed using the restrained conformations of **ABTPA** that were based on the experimental conformer in **ABTPA-1**. The predicted crystal structure in the new CSP dataset that matches with **ABTPA-1** stands out as having low energy in the CSP map relative to other structures of similar density (Figure 4.30). The new conformer was missed in the initial conformer search due to its significant internal molecular strain (~26 kJ/mol relative to the gas phase conformers), highlighting the challenge of accounting for **ABTPA**-**ABTPA** or **ABTPA**-solvent interactions in the CSP of flexible molecules.

As with **ABTPA-1**, gas-phase optimisation of the **ABTPA** conformation found in

ABTPA-2 was performed with and without restricting the torsional angles. Free optimisation of the experimental conformer in **ABTPA-2** found an additional gas-phase minimum that was not sampled in the original CSP set. This freely optimised conformer was ~0.7 kJ/mol above the minimum energy conformation. Fixing only the two dihedral angles ϕ & ψ adjacent to the anthracene core resulted in a molecular energy ~2.6 kJ/mol above the minimum energy conformer, while optimisation restricting all the arene−arene and arene−carboxylic acid dihedrals resulted in a higher molecular strain of ~11.9 kJ/mol. In contrast to what was found with **ABTPA-1**, all the optimised conformer variations of **ABTPA-2** result in CSP predicted structures with the same packing as the experimental structure, albeit with significant strain to the hydrogen bonding for the less constrained conformations. Despite the increasing molecular energy, the total crystal energy is lowered as more constraints are applied to intramolecular dihedrals (Figure 4.30).

While **ABTPA-1** and **ABTPA-2** appear to have similar lattice energies (**ABTPA-1** is approximately ~1kJ/mol lower in energy than **ABTPA-2** when adjusted for intramolecular energy). The transformation from **ABTPA-1** to **ABTPA-2** may be explained by considering the relative internal molecular strain of **ABTPA** in each of the crystal structures, ~ 26 kJ/mol in **ABTPA-1** vs ~ 12 kJ/mol in **ABTPA-2**. Therefore, it is plausible that the framework expansion may be triggered by the release of strain in the **ABTPA** conformer.

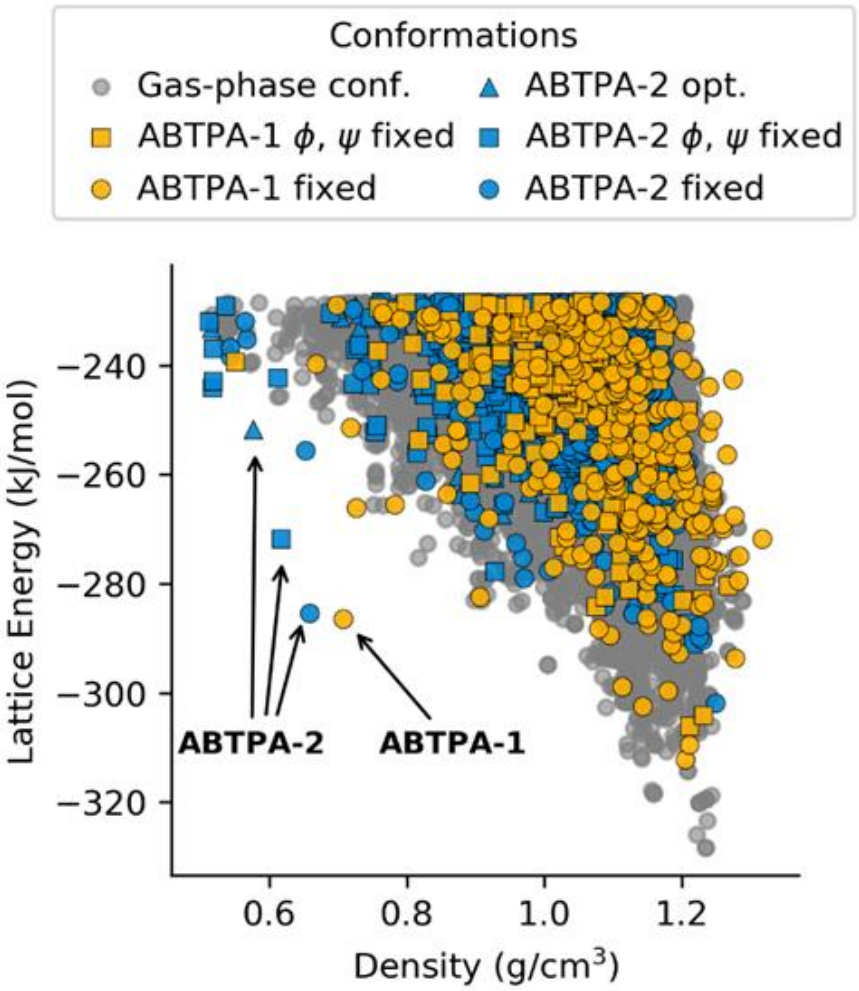

Figure 4.30. CSP map for initial **ABTPA** conformers (grey), and various gas-phase optimisations of the experimental conformations in **ABTPA-1** (orange) and **ABTPA-2** (blue). Angles ϕ and ψ refer to the arene-arene dihedral angles adjacent to the anthracene core. **ABTPA-1** fixed, and **ABTPA-2** fixed refer to conformations in which all arene-arene and arene-carboxylic acid dihedrals were fixed from the conformations in the experimental crystal structures. Note that free optimisation of the conformer from **ABTPA-1** resulted in one of the low-energy conformations from the initial CSP calculations, hence its absence from the labeling.

The CSP results demonstrate the importance of the incorporation of molecular flexibility into the CSP procedure. When rigid molecule CSP with gas-phase predicted conformers was used, the observed packing barely stood out on the energy-density landscape, while a small deviation facilitated significantly improved hydrogen

bonding, which more than compensating for the intramolecular strain associated with the conformational change. It should be noted, however, that even performing rigid molecule CSP on the ensemble of conformations is computationally demanding, particularly when the crystal structure landscape needs to be sampled up to relatively high energies, which is required when searching for porous crystal structures. The incorporation of accurate intramolecular flexibility models for systems with 6 or more internal degrees of freedom with sub-kJ/mol accuracy is an immense challenge due to the higher dimensionality of the search space and greater demands on the energy model, illustrating the current limitations of these *a priori* predictive methods.

*4.5 Porosity, stability, and flexibility of **ABTPA-2***

To determine the porosity of **ABTPA-2**, a N_2 sorption isotherm was recorded at 77 K after activation of **ABTPA-2** at 120 °C for 12 hrs. Activated **ABTPA-2** has a BET surface area of 1183 m^2 g^{-1} and a pore size of 1.8 nm (Figure 4.31a), which agrees with the crystal structure. The permanent porosity of **ABTPA-2** was also characterised by methane sorption at 115 K. From the CH_4 sorption isotherm (Figure 4.31b), **ABTPA-2** was found to adsorb 12.68 mmol g^{-1} of CH_4 at saturation at 115 K, which proved **ABTPA-2** was a stable and porous HOF structure with better stability than δ-**TMA**.

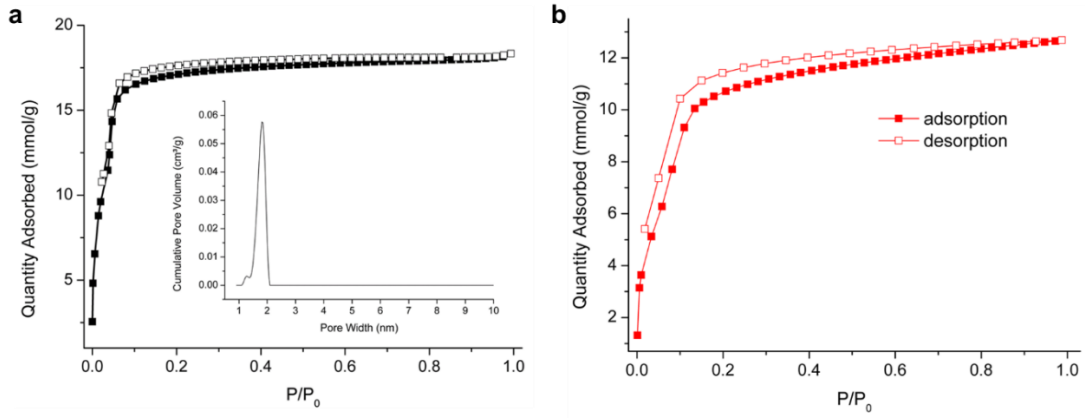

Figure 4.31. a) N_2 sorption isotherms for **ABTPA-2** recorded at 77 K and the pore width distribution for this sample. b) CH_4 sorption isotherm for **ABTPA-2** recorded at 115 K.

The stability of **ABTPA-2** was also investigated by variable temperature (VT) PXRD, thermogravimetric analysis (TGA), and differential scanning calorimetry (DSC). The VT-PXRD data, collected between RT and 175 °C, revealed that **ABTPA-2** undergoes a negative area thermal expansion,[58,59] with the 2-D **sql** HOF layers contracting along the *ab* plane (Figure 4.32-4.34). At the same time, it undergoes an interlayer expansion along *c*, indicating a rippling of the 2-D HOF layers upon heating (Figure 4.34).

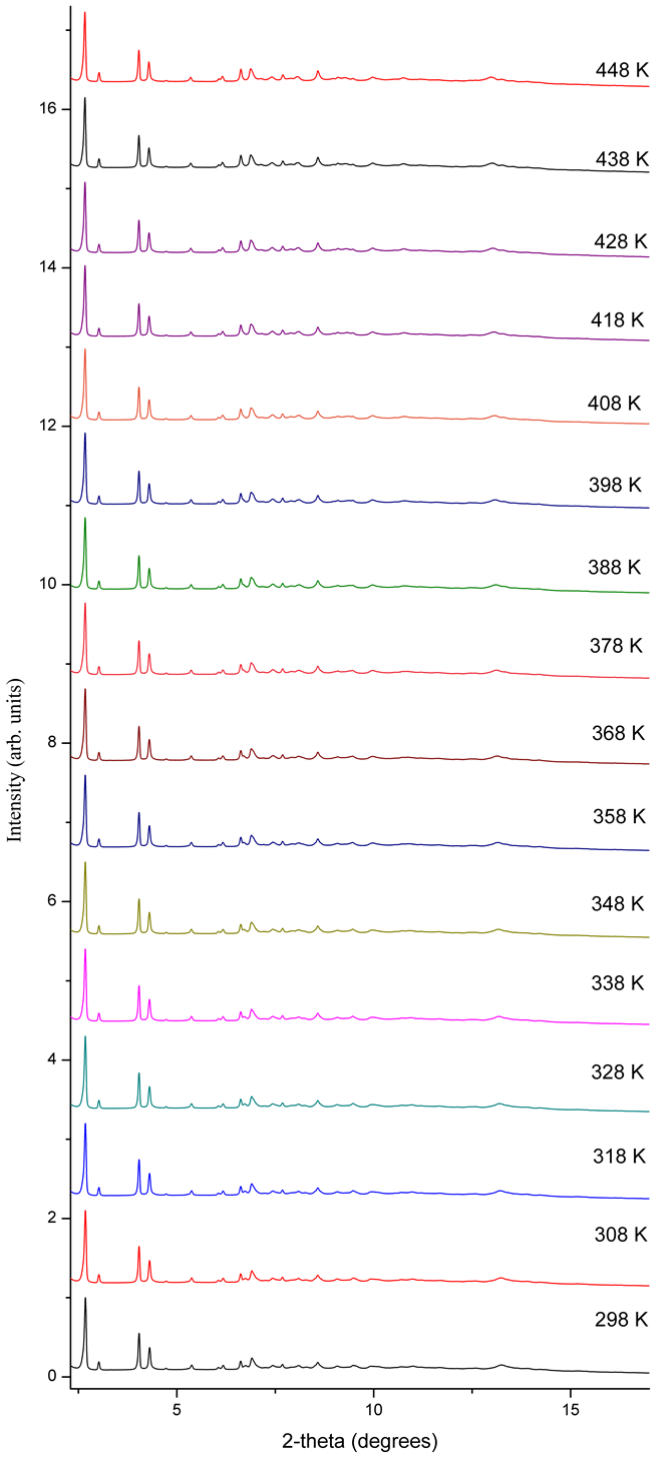

Figure 4.32. Variable temperature PXRD patterns for **ABTPA-2**, recorded over the temperature range 298–448 K. (λ = 0.825186 Å). PXRD patterns were recorded every 10 K, after equilibrating the sample temperature for 10 minutes. Recorded after removing the acetone solvent from the crystal pores of **ABTPA-2** at RT under dynamic vacuum.

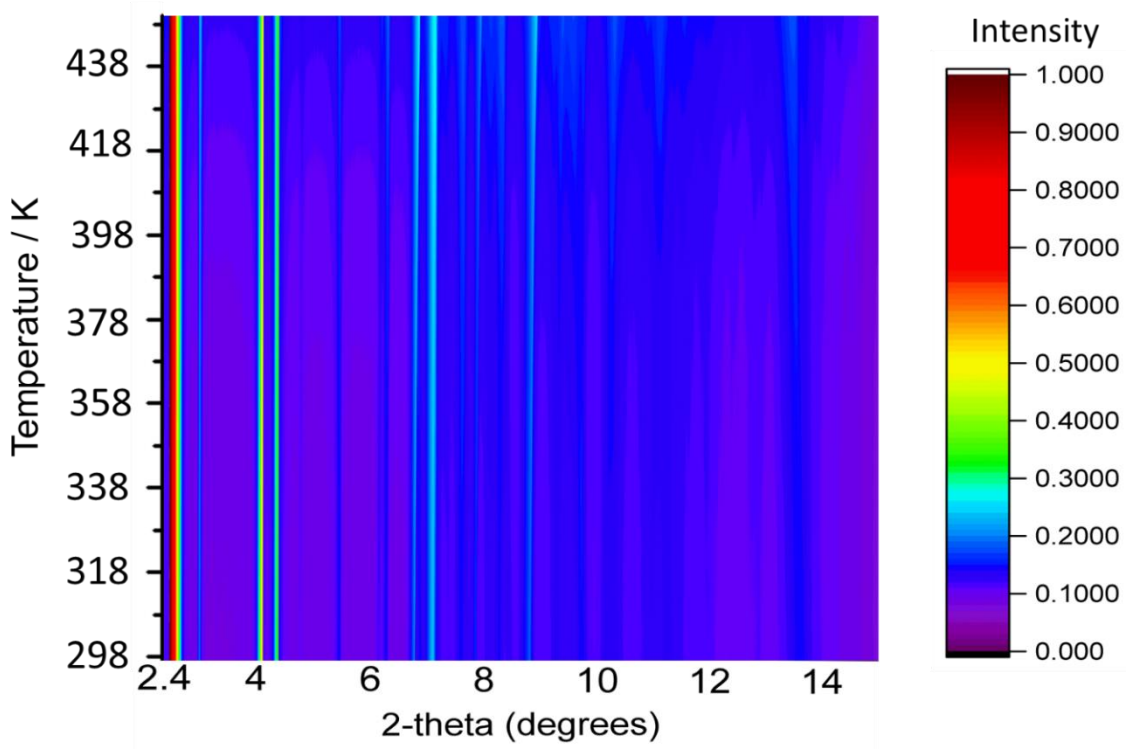

Figure 4.33. Surface plot of VT-PXRD patterns of **ABTPA-2** recorded over the temperature range 298–448 K. Recorded after removing the acetone solvent from the crystal pores of **ABTPA-2** at RT under dynamic vacuum. Variable temperature PXRD patterns for **ABTPA-2**, recorded over the temperature range 298–448 K. (λ = 0.825186 Å). PXRD patterns were recorded every 10 K, after equilibrating the sample temperature for 10 minutes.

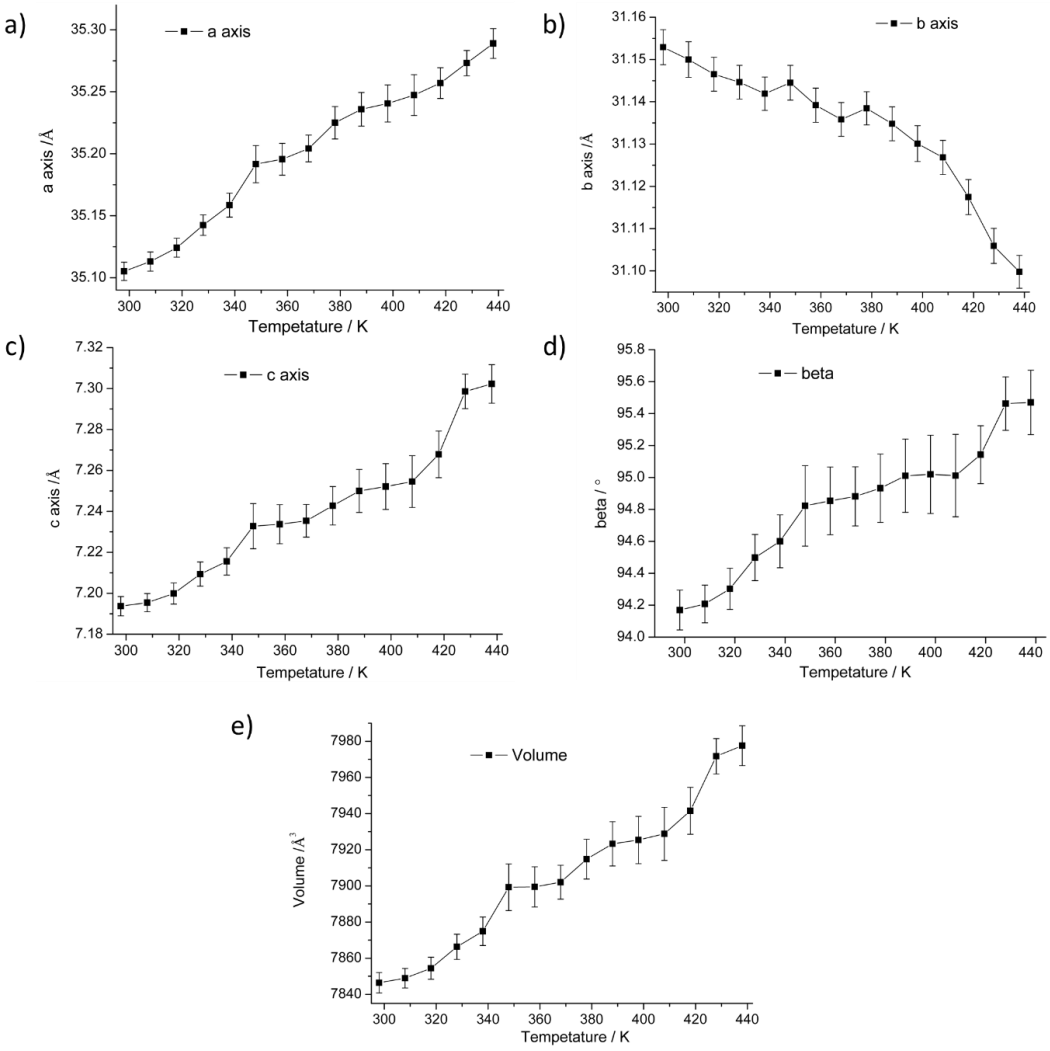

Figure 4.34. Change in unit cell parameter for **ABTPA-2** recorded over the VT-PXRD temperature range 298–448 K; (a) *a*-axis, (b) *b*-axis, (c) *c*-axis, (d) *β* angle, and (e) volume. Data points were recorded every 10 K. The change in unit cell parameters as the temperature was increased indicate that the 2-D hydrogen-bonded layers contract along *b*, whilst at the same time, the herringbone packing of anthracene extends along *c*.

DSC was recorded from RT to 300 °C after removing the acetone solvent from the crystal pores of **ABTPA-2** at RT under dynamic vacuum for 2 hrs and the plot showed a pure phase of **ABTPA-2**. No phase changed happening during heating to 300 °C. It also showed **ABTPA-2** no evidence of any phase changes until 300 °C at least (Figure 4.35).

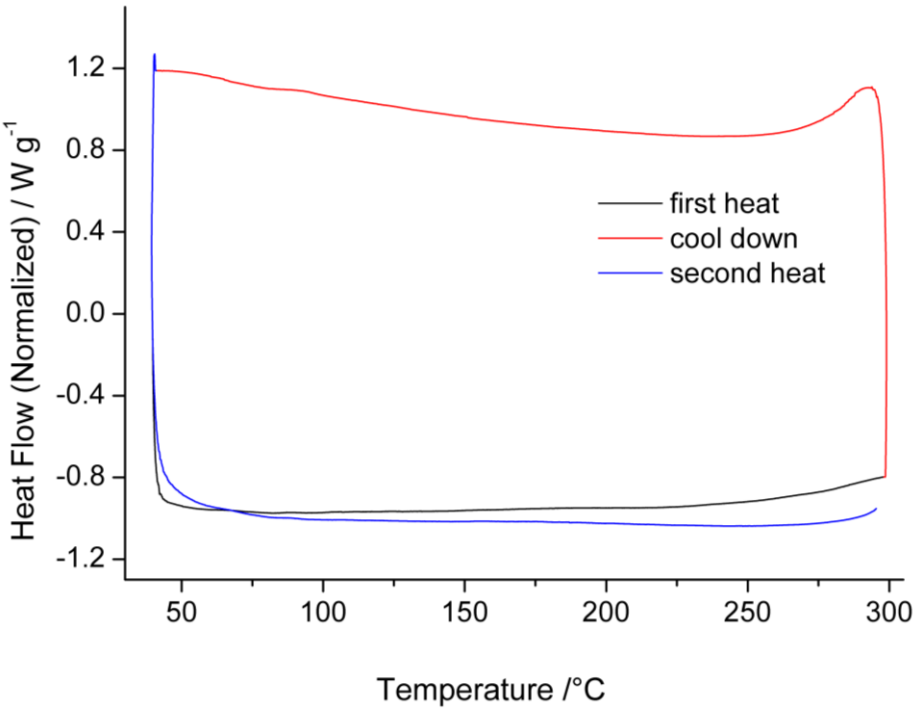

Figure 4.35. DSC plot for **ABTPA-2** recorded over the temperature range 30 °C to 300 °C, using heat-cool-heat cycle procedure. Black: first heating procedure from 30 °C to 300 °C; red: cooling from 300 °C to 30 °C; blue: second heating procedure from 30 °C to 300 °C.

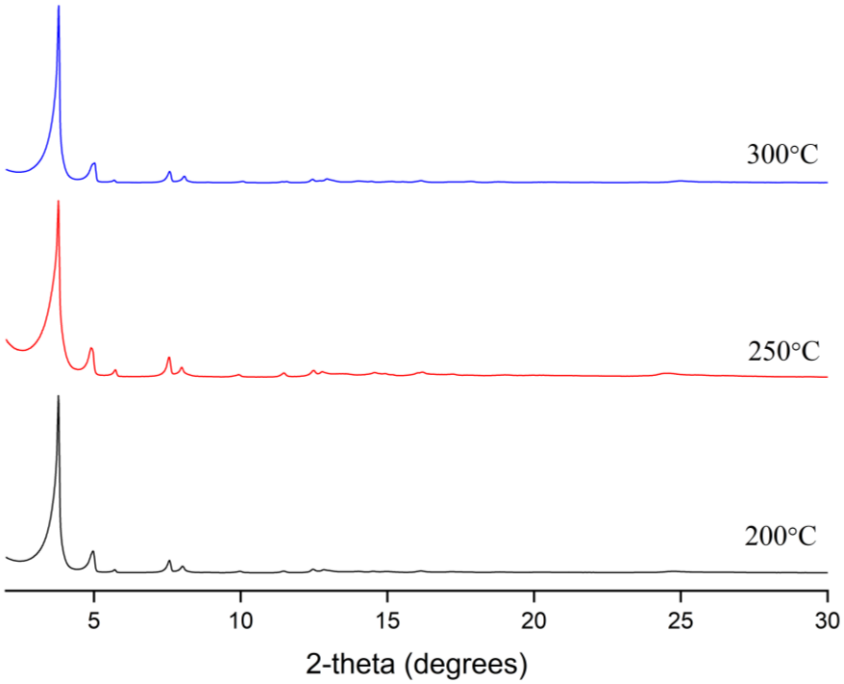

Figure 4.36. PXRD patterns for **ABTPA-2**, recorded after heating an activated sample at 200 °C (bottom, black), 250 °C (middle, red), and 300 °C (top, blue) for 1 h at each temperature.

PXRD patterns were also recorded after heating **ABTPA-2** to 200 °C, 250 °C, and 300 °C for 1h (Figure 4.36). There was no obvious change with the three PXRD patterns and it indicated that the structure remains crystalline, and the same phase is preserved over this temperature range (Figure 4.36). The VT PXRD patterns proved **ABTPA-2** was a stable 4. and porous HOF structure that has much better stability than *δ*-**TMA**. TGA was also collected after removing the acetone solvent from the crystal pores of **ABTPA-2** at RT under dynamic vacuum for 2 hrs from RT to 800 °C under air condition. From the TGA plot shown in Figure 4.37, there is no weight loss until 350 °C, and the onset of the decomposition starts at about 350 °C. After 590 °C, **ABTPA-2** was fully decomposed.

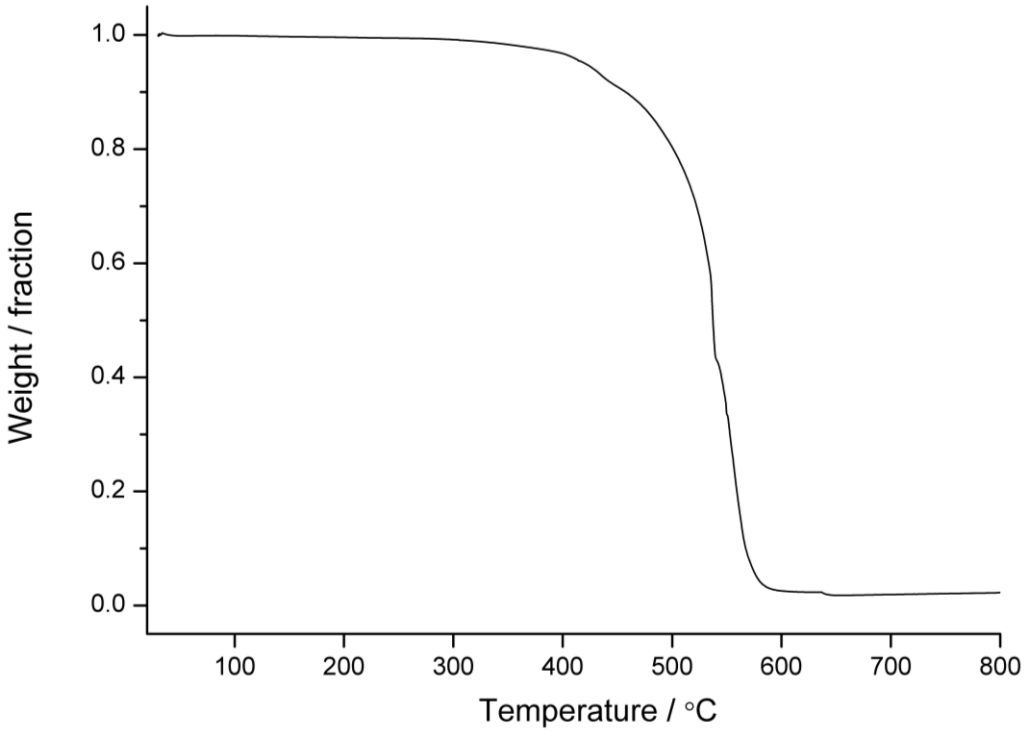

Figure 4.37. TGA plot for **ABTPA-2** recorded under a dry air flow.

The flexibility of **ABTPA-2** was also investigated after immersing the activated material in different aromatic organic solvents. The existence of phenyl group in aromatic organic solvents would lead to the conformation change by π-π interaction. 10 mg **ABTPA-2** was immersed in mesitylene (**2**), toluene (**3**), *m*-xylene (**4**), *n*-butylbenzene (**5**) 1,3-dimethoxybenzene (**6**), *p*-xylene (**7**), *o*-xylene (**8**), and 1,2-dimethoxybenzene (**9**) for 1 day at RT (Figure 4. 38f). After immersing in solvents for 1 day, PXRD patterns were recorded on suspensions in capillaries in the aromatic solvents. It was envisaged that the aromatic solvents might interact with the HOF to trigger a flexible framework response. In all the PXRD patterns there were strong backgrounds, which because of the presence of solvents in the capillaries. The PXRD patterns showed that **ABTPA-2** maintains the same structure but there are still some small structural changes in different patterns (Figure 4.37). After fitting the solvated PXRD patterns, assuming the structure and symmetry remained the same, different cell parameters were obtained. There are bigger errors in PXRD patterns recording from *o*-xylene (**8**) and *n*-butylbenzene (**5**) were due to the poor quality of these patterns than from the other solvents. From the cell parameters, the volume expanded

in most solvents (**4-9**). This indicated that **ABTPA-2** is dynamic and can adapt its structure to accommodate these guests in the crystal pore while retaining the extended packing of molecules in **ABTPA-2** (Figure 4.38).

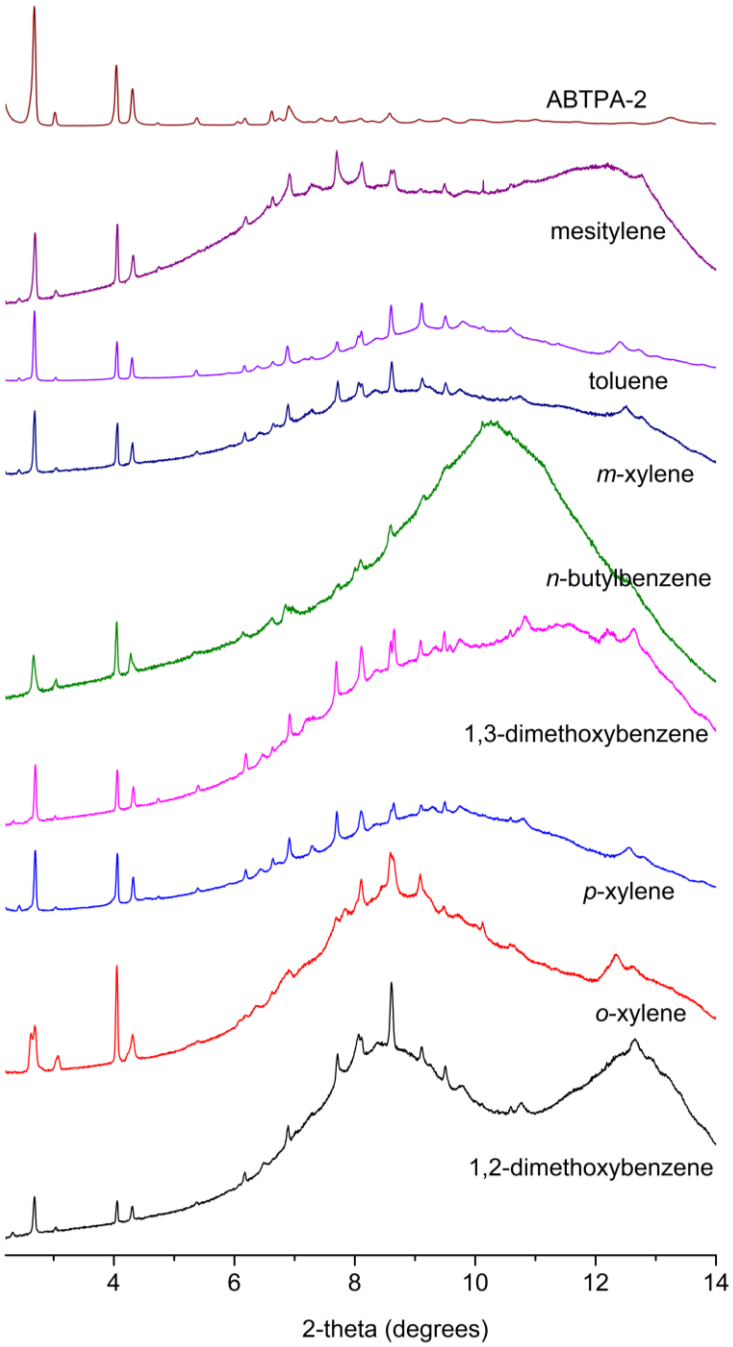

Figure 4.38. PXRD patterns recorded after immersing activated crystals of **ABTPA-2** in 8 different aromatic solvents for 24 hrs at RT. The order of mesitylene (**2**), toluene (**3**), *m*-xylene (**4**), *n*-butylbenzene (**5**), 1,3-dimethoxybenzene (**6**), *p*-xylene (**7**), *o*-xylene (**8**), and 1,2-dimethoxybenzene (**9**) corresponding with the order of solvents in Figure 4.39 (f).

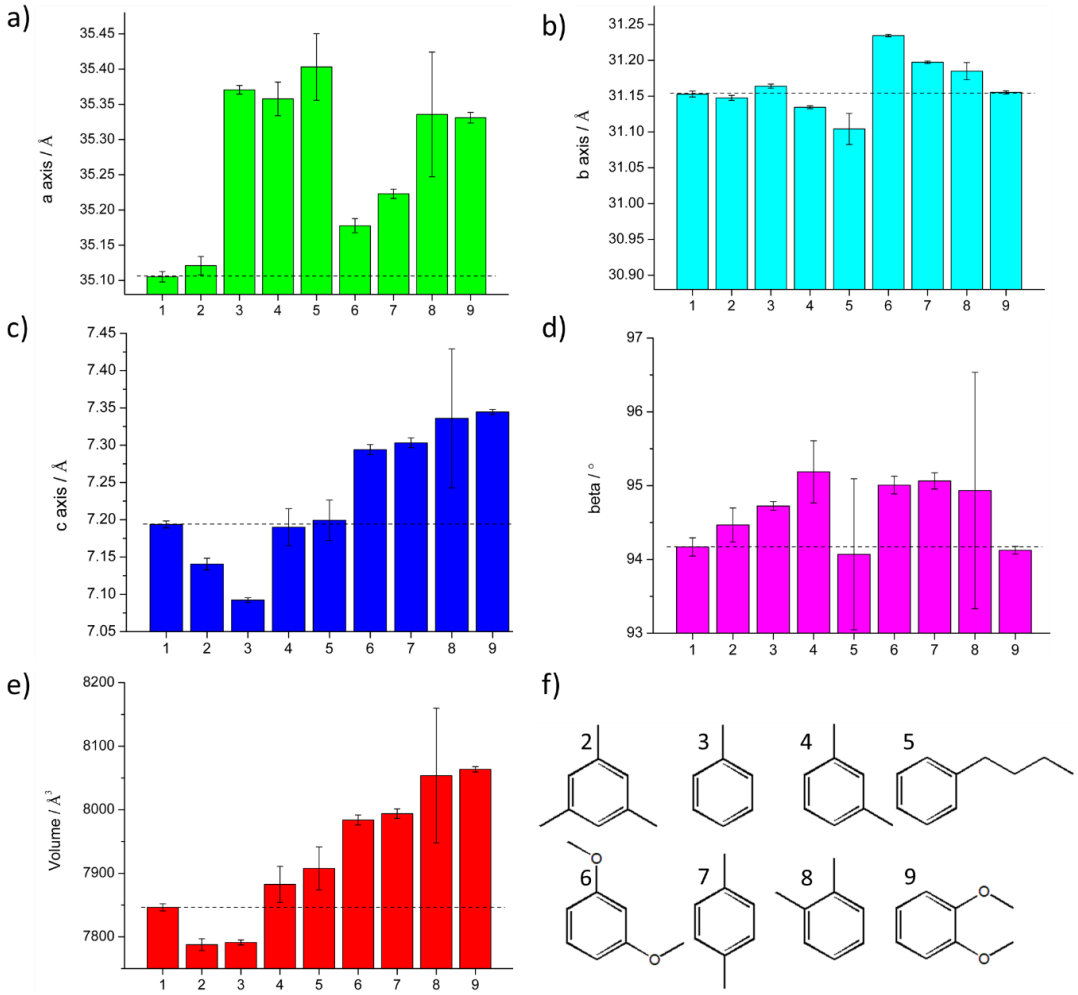

Figure 4.39. Change in unit cell parameter for **ABTPA-2**; (a) *a*-axis, (b) *b*-axis, (c) *c*-axis, (d) β angle, and (e) volume, after immersing activated crystals of **ABTPA-2** (#1 in plots a → e) in 8 different aromatic solvents (f, #2-9 in plots a → e) for 24 hrs at RT.

5. Conclusion

In summary, **ABTPA-2** is a dynamic 2-D HOF material with anthracene units that can adapt its conformation in response to changes in the chemical environment in the crystal pores. As well as stabalising porous crystal packings the anthracene units respond to external stimuli, such as guest absorption and changes in sample temperature. In response to crystal activation, the **ABTPA** molecules changed their conformation, which lead to a highly unusual structural change in which the structure expanded after desolvation of the crystal pores. There are already some previous

reports about the flexible porous solids can adapt their pore structures to generate additional functionalities. For example, some materials have a gate-opening type response during guest adsorption,[2,60–67] and some MOFs have even been shown to exhibit negative gas adsorption transitions.[68,69] By contrast, this study showed that the molecular structure of a HOF adapts during activation to initiate a structural expansion. From this discovery, the chemical analogs of **ABTPA** might also be promising to exhibit similar behavior as HOF materials. Importantly, the expandable behavior can be explained by computational calculation in this study. It was achieved by calculating the effect of crystal packing on conformational strain in predicted HOF materials and identifying structural pairs on the crystal structure landscape that represent routes for the relaxation of high intramolecular strain via a structural transformation to a less strained structure.

In this study, 3-D ED was used for the first time to solve a porous HOF structure, **ABTPA-2**. More broadly, the successful discovery of expandable **ABTPA-2** proved that 3-D ED is an accurate method to determine the structure of porous organic molecular solids rapidly. Especially, 3-D ED is an ideal supplement of SCXRD, which is essential when the crystals are too small for more conventional diffraction methods. In the future, 3-D ED will become an important new tool in crystalline materials discovery.

6. References

1. Cui, P. *et al.* An Expandable Hydrogen-Bonded Organic Framework Characterised by Three-Dimensional Electron Diffraction. *J. Am. Chem. Soc.* **142**, 12743–12750 (2020).
2. He, Y., Xiang, S. & Chen, B. A Microporous Hydrogen-Bonded Organic Framework for Highly Selective C 2 H 2 /C 2 H 4 Separation at Ambient Temperature. *J. Am. Chem. Soc.* **133**, 14570–14573 (2011).
3. Mastalerz, M. & Oppel, I. M. Rational Construction of an Extrinsic Porous Molecular Crystal with an Extraordinary High Specific Surface Area. *Angew. Chemie Int. Ed.* **51**, 5252–5255 (2012).
4. Pulido, A. *et al.* Functional materials discovery using energy–structure–function maps. *Nature* **543**, 657–664 (2017).
5. Little, M. A. & Cooper, A. I. The Chemistry of Porous Organic Molecular Materials. *Adv. Funct. Mater.* , **30** 1909842 (2020).
6. Zhang, G., Presly, O., White, F., Oppel, I. M. & Mastalerz, M. A shape-persistent quadruply interlocked giant cage catenane with two distinct pores in the solid state. *Angew. Chemie Int.*

Ed. **53**, 5126–30 (2014).

7. Zhang, G., Presly, O., White, F., Oppel, I. M. & Mastalerz, M. A permanent mesoporous organic cage with an exceptionally high surface area. *Angew. Chemie* **53**, 1516–20 (2014).
8. Teng, B. *et al.* Synthesis of a Large, Shape-Flexible, Solvatomorphic Porous Organic Cage. *Cryst. Growth Des.* **19**, 3647–3651 (2019).
9. Hasell, T. *et al.* Controlling the crystallisation of porous organic cages: molecular analogs of isoreticular frameworks using shape-specific directing solvents. *J. Am. Chem. Soc.* **136**, 1438–48 (2014).
10. Li, P. *et al.* Interpenetration Isomerism in Triptycene-Based Hydrogen-Bonded Organic Frameworks. *Angew. Chemie Int. Ed.* **58**, 1664–1669 (2019).
11. Li, P. *et al.* Assembly of a Porous Supramolecular Polyknot from Rigid Trigonal Prismatic Building Blocks. *J. Am. Chem. Soc.* **141**, 12998–13002 (2019).
12. Hisaki, I. *et al.* A Series of Layered Assemblies of Hydrogen-Bonded, Hexagonal Networks of C3-Symmetric π-Conjugated Molecules: A Potential Motif of Porous Organic Materials. *J. Am. Chem. Soc.* **138**, 6617–6628 (2016).
13. Brunet, P., Simard, M. & Wuest, J. D. Molecular Tectonics. Porous Hydrogen-Bonded Networks with Unprecedented Structural Integrity. *J. Am. Chem. Soc.* **119**, 2737–2738 (1997).
14. McMahon, D. P. *et al.* Computational Modelling of Solvent Effects in a Prolific Solvatomorphic Porous Organic Cage. *Faraday Discuss.* **211**, 383–399 (2018).
15. Mortazavi, M. *et al.* Computational polymorph screening reveals late-appearing and poorly-soluble form of rotigotine. *Commun. Chem.* **2**, 70 (2019).
16. Vasileiadis, M., Pantelides, C. C. & Adjiman, C. S. Prediction of the crystal structures of axitinib, a polymorphic pharmaceutical molecule. *Chem. Eng. Sci.* **121**, 60–76 (2015).
17. Jones, J. T. A. *et al.* Modular and predictable 4. assembly of porous organic molecular crystals. *Nature* **474**, 367–371 (2011).
18. Slater, A. G. *et al.* Reticular synthesis of porous molecular 1D nanotubes and 3D networks. *Nat. Chem.* **9**, 17 (2016).
19. Slater, A. G. *et al.* Computationally-Guided Synthetic Control over Pore Size in Isostructural Porous Organic Cages. *ACS Cent. Sci.* **3**, 734–742 (2017).
20. Pyzer-Knapp, E. O. *et al.* Predicted crystal energy landscapes of porous organic cages. *Chem. Sci.* **5**, 2235–2245 (2014).
21. Cui, P. *et al.* Mining predicted crystal structure landscapes with high throughput crystallisation: Old molecules, new insights. *Chem. Sci.* **10**, 9988–9997 (2019).
22. Sawaki, T., Endo, K., Kobayashi, K., Hayashida, O. & Aoyama, Y. Catalysis by Organic Solids. Stereoselective Intramolecular Ene Reaction of Citronellal Promoted by Microporous Molecular Crystals Having an Extensive Hydrogen-Bonded Network. *Bull. Chem. Soc. Jpn.* **70**, 3075–3079 (1997).
23. Yan, Y. *et al.* Porous Metal–Organic Polyhedral Frameworks with Optimal Molecular Dynamics and Pore Geometry for Methane Storage. *J. Am. Chem. Soc.* **139**, 13349–13360 (2017).
24. Li, X., Zhen, L., Fan, Y., Fan, X. & Zeng, Q. Crystal Engineering Based on Polymeric Hydrogen-Bonded Supramolecules by Self-Assembling of 9, 10-Bis(3,5-dihydroxyphenyl)anthracene and 2,2′,4,4′- Tetrahydroxybenzophenone with Bipyridines. *Int. J. Mol. Sci.* **8**, 241–258 (2007).

25. Ma, S., Simmons, J. M., Sun, D., Yuan, D. & Zhou, H.-C. Porous Metal-Organic Frameworks Based on an Anthracene Derivative: Syntheses, Structure Analysis, and Hydrogen Sorption Studies. *Inorg. Chem.* **48**, 5263–5268 (2009).
26. Lü, J. *et al.* Polycatenated 2D Hydrogen-Bonded Binary Supramolecular Organic Frameworks (SOFs) with Enhanced Gas Adsorption and Selectivity. *Cryst. Growth Des.* **18**, 2555–2562 (2018).
27. Kobayashi, K., Endo, K., Aoyama, Y. & Masuda, H. Hydrogen-bonded network formation in organic crystals as effected by perpendicular and divergent hydroxyl groups: The crystal structure of a bisresorcinol derivative of anthracene. *Tetrahedron Lett.* **34**, 7929–7932 (1993).
28. Imai, Y. *et al.* Charge-transfer host system composed of 9,10-bis(3,5-dihydroxyphenyl)anthracene and methylviologen. *Tetrahedron* **65**, 3740–3744 (2009).
29. Dewa, T., Endo, K. & Aoyama, Y. Dynamic Aspects of Lattice Inclusion Complexation Involving a Phase Change. Equilibrium, Kinetics, and Energetics of Guest-Binding to a Hydrogen-Bonded Flexible Organic Network. *J. Am. Chem. Soc.* **120**, 8933–8940 (1998).
30. Kinuta, T. *et al.* Complexation behaviour of a CT complex composed of 9,10-bis(3,5-dihydroxyphenyl)anthracene and viologen derivatives. *Supramol. Chem.* **22**, 221–227 (2010).
31. Endo, K. *et al.* Catalysis by Organic Solids. Stereoselective Diels−Alder Reactions Promoted by Microporous Molecular Crystals Having an Extensive Hydrogen-Bonded Network. *J. Am. Chem. Soc.* **119**, 4117–4122 (1997).
32. Gole, B., Bar, A. K., Mallick, A., Banerjee, R. & Mukherjee, P. S. An electron rich porous extended framework as a heterogeneous catalyst for Diels–Alder reactions. *Chem. Commun.* **49**, 7439 (2013).
33. Aoyama, Y. *et al.* Crystal Engineering of Stacked Aromatic Columns. Three-Dimensional Control of the Alignment of Orthogonal Aromatic Triads and Guest Quinones via Self-Assembly of Hydrogen-Bonded Networks. *J. Am. Chem. Soc.* **118**, 5562–5571 (1996).
34. Akimoto, K. *et al.* Ladder type supramolecular assembly and gas adsorption profile under reduced pressure based on hydrogen bonded m-tetraphenyl derivative of anthracene. *Tetrahedron* **63**, 6887–6894 (2007).
35. Akimoto, K. *et al.* A porous coordination architecture assembled by silver triflate and 9,10-bis(3,5-dicyano-1-phenyl)anthracene and its gas adsorption profile. *Tetrahedron Lett.* **49**, 7361–7363 (2008).
36. Ma, S. *et al.* Metal-Organic Framework from an Anthracene Derivative Containing Nanoscopic Cages Exhibiting High Methane Uptake. *J. Am. Chem. Soc.* **130**, 1012–1016 (2008).
37. Konstas, K., Taupitz, K. F., Turner, D. R., Kennedy, D. F. & Hill, M. R. A new family of zinc metal–organic framework polymorphs containing anthracene tetracarboxylates. *CrystEngComm* **16**, 8937–8940 (2014).
38. Endo, K. *et al.* Guest-Binding Properties of Organic Crystals Having an Extensive Hydrogen-Bonded Network: An Orthogonal Anthracene-Bis(resorcinol) Derivative as a Functional Organic Analog of Zeolites. *J. Am. Chem. Soc.* **117**, 8341–8352 (1995).
39. Hu, F. *et al.* An Ultrastable 4. and Easily Regenerated Hydrogen-Bonded Organic Molecular Framework with Permanent Porosity. *Angew. Chemie Int. Ed.* **56**, 2101–2104 (2017).
40. Spek, A. L. PLATON SQUEEZE: a tool for the calculation of the disordered solvent

contribution to the calculated structure factors. *Acta Crystallogr. Sect. C, Struct. Chem.* **71**, 9–18 (2015).

41. Gemmi, M. *et al.* 3D Electron Diffraction: The Nanocrystallography Revolution. *ACS Cent. Sci.* **5**, 1315–1329 (2019).
42. Zhang, D., Oleynikov, P., Hovmöller, S. & Zou, X. Collecting 3D electron diffraction data by the rotation method. *Zeitschrift für Krist.* **225**, (2010).
43. Wan, W., Sun, J., Su, J., Hovmöller, S. & Zou, X. Three-dimensional rotation electron diffraction: software RED for automated data collection and data processing. *J. Appl. Crystallogr.* **46**, 1863–1873 (2013).
44. Cichocka, M. O., Ångström, J., Wang, B., Zou, X. & Smeets, S. High-throughput continuous rotation electron diffraction data acquisition {\it via} software automation. *J. Appl. Crystallogr.* **51**, 1652–1661 (2018).
45. Mugnaioli, E., Gorelik, T. & Kolb, U. "Ab initio" structure solution from electron diffraction data obtained by a combination of automated diffraction tomography and precession technique. *Ultramicroscopy* **109**, 758–765 (2009).
46. Kolb, U., Krysiak, Y. & Plana-Ruiz, S. Automated electron diffraction tomography - development and applications. *Acta Crystallogr. Sect. B* **75**, 463–474 (2019).
47. Nannenga, B. L., Shi, D., Leslie, A. G. W. & Gonen, T. High-resolution structure determination by continuous-rotation data collection in MicroED. *Nat. Methods* **11**, 927–930 (2014).
48. Goerigk, L. *et al.* A look at the density functional theory zoo with the advanced GMTKN55 database for general main group thermochemistry{,} kinetics and noncovalent interactions. *Phys. Chem. Chem. Phys.* **19**, 32184–32215 (2017).
49. Wang, Y. *et al.* Elucidation of the elusive structure and formula of the active pharmaceutical ingredient bismuth subgallate by continuous rotation electron diffraction. *Chem. Commun.* **53**, 7018–7021 (2017).
50. Wang, B. *et al.* A Porous Cobalt Tetraphosphonate Metal-Organic Framework: Accurate Structure and Guest Molecule Location Determined by Continuous-Rotation Electron Diffraction. *Chem. - A Eur. J.* **24**, 17429–17433 (2018).
51. Xu, H. *et al.* Solving a new R2lox protein structure by microcrystal electron diffraction. *Sci. Adv.* **5**, eaax4621 (2019).
52. Liu, Y. *et al.* Weaving of organic threads into a crystalline covalent organic framework. *Science.* **351**, 365–369 (2016).
53. Zhang, Y.-B. *et al.* Single-Crystal Structure of a Covalent Organic Framework. *J. Am. Chem. Soc.* **135**, 16336–16339 (2013).
54. Ma, T. *et al.* Observation of Interpenetration Isomerism in Covalent Organic Frameworks. *J. Am. Chem. Soc.* **140**, 6763–6766 (2018).
55. Stef Smeets; Bin Wang; Magdalena O. Cichocka; Jonas Ångström; Wei Wan. Instamatic. (2018).
56. Kabsch, W. XDS. *Acta Crystallogr. Sect. D Biol. Crystallogr.* **66**, 125–132 (2010).
57. Sheldrick, G. M. A short history of SHELX. *Acta Crystallogr. Sect. A Found. Crystallogr.* **64**, 112–122 (2008).
58. Lind, C. Two Decades of Negative Thermal Expansion Research: Where do we stand? *Materials (Basel).* **5**, 1125–1154 (2012).
59. Takenaka, K. Negative thermal expansion materials: Technological key for control of thermal

expansion. *Sci. Technol. Adv. Mater.* **13**, (2012).

60. Schneemann, A. *et al.* Flexible metal–organic frameworks. *Chem. Soc. Rev.* **43**, 6062–6096 (2014).
61. Mason, J. A. *et al.* Methane storage in flexible metal–organic frameworks with intrinsic thermal management. *Nature* **527**, 357–361 (2015).
62. Coudert, F.-X. Responsive Metal–Organic Frameworks and Framework Materials: Under Pressure, Taking the Heat, in the Spotlight, with Friends. *Chem. Mater.* **27**, 1905–1916 (2015).
63. Kim, J. Y. *et al.* Selective Hydrogen Isotope Separation via Breathing Transition in MIL-53(Al). *J. Am. Chem. Soc.* **139**, 17743–17746 (2017).
64. Thallapally, P. K. *et al.* Gas-induced transformation and expansion of a non-porous organic solid. *Nat. Mater.* **7**, 146–150 (2008).
65. Wang, Z. *et al.* Soft Porous Crystal Based upon Organic Cages That Exhibit Guest-Induced Breathing and Selective Gas Separation. *J. Am. Chem. Soc.* **141**, 9408–9414 (2019).
66. Zhu, A.-X. *et al.* Coordination Network That Reversibly Switches between Two Nonporous Polymorphs and a High Surface Area Porous Phase. *J. Am. Chem. Soc.* **140**, 15572–15576 (2018).
67. Taylor, M. K. *et al.* Near-Perfect CO2/CH4 Selectivity Achieved through Reversible Guest Templating in the Flexible Metal–Organic Framework Co(bdp). *J. Am. Chem. Soc.* **140**, 10324–10331 (2018).
68. Krause, S. *et al.* A pressure-amplifying framework material with negative gas adsorption transitions. *Nature* **532**, 348 (2016).
69. Krause, S. *et al.* Towards general network architecture design criteria for negative gas adsorption transitions in ultraporous frameworks. *Nat. Commun.* **10**, 3632 (2019).

Chapter 5
Materials and Methods

1. Materials

All solvents were obtained from Sigma-Aldrich, Fisher, Alfa Aesar, and Jilin Province Yanshen Technology Co., Ltd. All chemicals and solvents were used as received. Anhydrous solvents were purchased from Sigma-Aldrich or Acros Organics and used without further purification. All gases for sorption analysis were supplied by BOC at a purity of ≥99.999%.

2. General Methods

2.1 Robot Configuration

A Chemspeed SWING POWDERDOSE robotic platform equipped with both solid and liquid dispensing tools (Figure 5.1) was used for HT crystallisation procedure. Liquid handling was carried out via a four-needle overhead dispensing tool powered by 4 syringe pumps (syringe volumes: 1, 10 or 25 ml). After each dispense, the syringe was washed with ethanol and dried before the next solvent was dispensed. HT Crystallisations were carried out in standard 8 ml glass vials, held in removable racks (80 vials in a 16×5 array). The dispensing was carried at RT in a closed hood system.

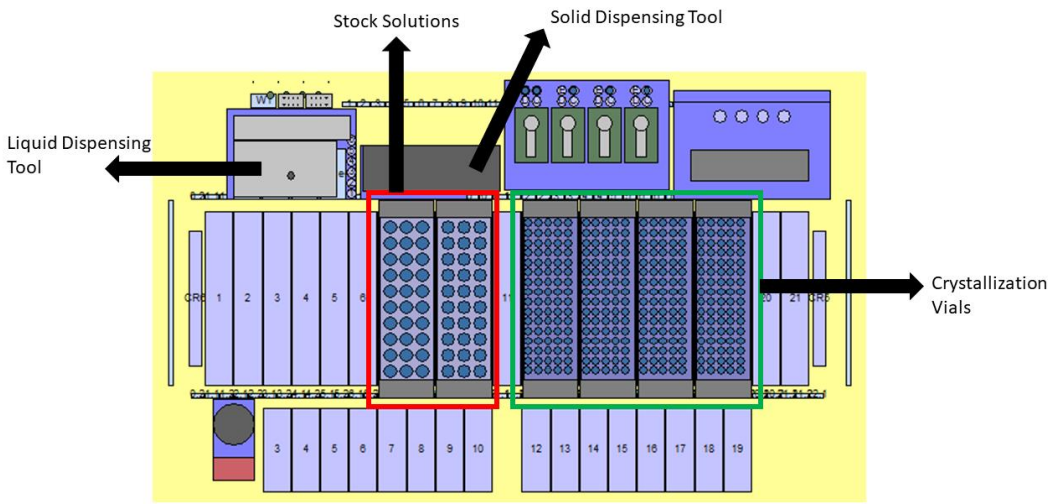

Figure 5.1. Chemspeed SWING POWDERDOSE robotic platform setup for HT crystallisation experiment.

2.2 Powder X-ray Diffraction (PXRD)

PXRD patterns were collected in transmission mode on samples held on thin Mylar film in aluminium well plates on a Panalytical Empyrean diffractometer, equipped with a high throughput screening XYZ stage, X-ray focusing mirror, and PIXcel detector, using Cu-Kα (λ = 1.541 Å) radiation. Unless stated, PXRD patterns were recorded at room temperature. Diffraction patterns were measured over the 2θ range 2−40°, in 0.013° steps, for 30 minutes. For variable temperature *in-situ* experiments, and for indexing, samples were loaded into borosilicate glass capillaries which were spun during data collections to improve powder averaging. PXRD data for these samples were recorded in transmission mode on a Panalytical Empyrean diffractometer, equipped with a sample spinner, X-ray focusing mirror, and PIXcel detector, using Cu-Kα (λ = 1.541 Å) radiation. For the variable temperature experiments, sample temperatures were controlled using an Oxford Cryosystems 700 series cryostream. High-resolution synchrotron PXRD dataset were collected using the I11 beamline at Diamond Light Source (λ = 0.825186 Å), which is equipped with a Mythen II position-sensitive detector. Sample recorded at Diamond Light Source were loaded in a borosilicate glass capillary that was spun to improve powder averaging during data acquisition and the sample was heated using an Oxford Hot-Air-Blower. PXRD patterns were indexed by Pawley fitting methods in TOPAS-Academic.[1]

2.3 Single Crystal X-ray Diffraction (SCXRD)

SC-XRD data sets were measured on a Rigaku MicroMax-007 HF rotating anode diffractometer (Mo-Kα radiation, λ = 0.71073 Å, Kappa 4-circle goniometer, Rigaku Saturn724+ detector); or at beamline I19, Diamond Light Source, Didcot, UK using silicon double crystal monochromated synchrotron radiation (λ = 0.6889 Å, Pilatus 2M detector). Rigaku frames were converted to Bruker compatible frames using the programme ECLIPSE[2]. Absorption corrections, using the multi-scan method, were performed with the program SADABS[3,4]. For synchrotron X-ray data, collected at

Diamond Light Source (λ = 0.6889Å) data reduction and absorption corrections were performed with xia2.[5] Structures were solved with SHELXT,[6] or by direct methods using SHELXS,[7] and refined by full-matrix least-squares on $|F|^2$ by SHELXL[89], interfaced through the programme OLEX2.[10] Attempts were always made to locate H atom positions for all the carboxylic acid OH groups, however, due to disorder this was not always possible. When this was not possible, OH groups were refined using the riding model. All other H-atoms were fixed in geometrically estimated positions and refined using the riding model. For some of the crystal structures, and where stated in the text, it was not possible to resolve solvent molecules in the large lattice voids. To avoid using always solvent masks during the refinements of these crystal structures, particularly where twinning was encountered, the disordered solvent was modelled as partially occupied O atoms, without riding H-atoms. Supplementary CIF files that include structure factors and responses to checkCIF alerts are available free of charge from the Cambridge Crystallographic Data Centre (CCDC) via www.ccdc.cam.ac.uk/data_request/cif. CIFs that have not been uploaded to the CCDC are included as Supporting Information with this thesis in this chapter.

2.4 3-D Electron Diffraction

Crystals were cooled to approximately 97 K using a Gatan 914 Cryo-Transfer holder. Three-dimensional electron diffraction data collection was conducted on a JEOL JEM-2100 LaB_6 transmission electron microscope, equipped with an Amsterdam Scientific Instruments Timepix hybrid pixel detector. Data were collected through the help of Instamatic[11] while continuously tilting the specimen and the acquired frames were processed using XDS[12]. Reflection conditions were checked using the RED software package[13]. The structure was solved using SHELXT,[14] where all the non-hydrogen atoms could be located in the initial structure solution. Hydrogen atoms were placed by means of a riding model.

2.5 Nuclear magnetic resonance (NMR)

NMR spectra were recorded on a Bruker 400 NMR spectrometer at 400 MHz (^{1}H) and 100 MHz (^{13}C) and referenced against the residual ^{1}H or ^{13}C signal of the solvent.

2.6 Thermogravimetric analysis (TGA)

Thermogravimetric analysis was carried out using a TA Q5000IR analyser with an automated vertical overhead thermobalance. Samples were heated at a rate of 10 °C/min under a dry N_2 atmosphere.

2.7 Differential Scanning Calorimetry (DSC)

DSC is commonly used to determine the change in temperature of a sample when undergoing a phase transition to determining whether a process is endo- or exothermic. This is particularly useful when studying crystalline materials, which can exhibit polymorphism, allowing us to determine the temperature at which a transformation occurs. DSC measurements were conducted on a TA Q2000 (instrument with a Refrigerated Cooling System 90 and an autosampler) at 10 °C/min under an N_2 atmosphere.

2.8 Scanning electron microscopy (SEM)

Imaging crystal morphologies was undertaken using a Hitachi S-4800 cold Field Emission Scanning Electron Microscope (FE-SEM). Samples were prepared by depositing dry crystals on 15 mm Hitachi M4 aluminium stubs using an adhesive high purity carbon tab before coating with a 2 nm layer of cadmium using an Emitech K550X automated sputter coater. Imaging was conducted at a working distance of 8 mm and a working voltage of 3 kV using a mix of upper and lower secondary electron detectors.

2.9 Gas Sorption Analysis

Surface areas were measured by nitrogen sorption at 77.3 K. Powder samples were

degassed on the analysis port under vacuum. Isotherm measurements were performed using a Micromeritics 2420 surface characterisation analyser, equipped with a Cold-Edge technologies liquid helium cryostat chiller unit for temperature control. Saturated CH_4 sorption was measured at 115 K using Micromeritics 3flex volumetric adsorption analyser.

2.10 Brunauer-Emmett-Teller (BET) Measurement

BET theory explains the adsorption of gas onto a surface.[15,16] The volume of gas (usually nitrogen) adsorbed to the surface of the particles is measured at the boiling point of nitrogen (77 K). The nitrogen gas is below the critical temperature at this temperature and the gas condenses on the surface of the particles. It is assumed that the gas condenses onto the surface in multilayers and the amount of adsorbed gas is correlated to the total surface area of the particles including pores at the surface. There are four main steps in the BET measurement:

1. Degas. The degas is done with a vacuum system at elevated temperature which depends on the stability of the samples. The samples need to be reweighed to take into account the mass loss.

2. Adsorption. This step gives an adsorption isotherm over a selected range of P/P0. P0 is the saturation pressure of adsorbate at the temperature of adsorption. The pressure continues to fall until the adsorbate and the adsorptive are in equilibrium during the adsorption of the gas on to the samples. The amount of adsorbate is the difference between the amount of gas admitted and the amount of remaining gas.

3. Desorption. A reverse of the adsorption step give a the desorption isotherm.

4. Dead-volume measurement. The dead volume in the sample cell must be calibrated before and after each measurement. To do that, helium gas is used for a blank run, because helium does not adsorb onto the sample.

3. References

1. TOPAS-Academic v. 5. Coelho Software, *Brisbane, Australia*, (2012).
2. Parsons, S. ECLIPSE. *The University of Edinburgh, Edinburgh, UK*, (2004).
3. Sheldrick, G. M. SADABS. *University of Göttingen, Germany*, (2008).
4. Krause, L., Herbst-Irmer, R., Sheldrick, G. M. & Stalke, D. Comparison of silver and molybdenum microfocus X-ray sources for single-crystal structure determination. *J. Appl. Crystallogr.* **48**, 3–10 (2015).
5. Winter, G. *et al.* DIALS: Implementation and evaluation of a new integration package. *Acta Crystallogr. Sect. D Struct. Biol.* **74**, 85–97 (2018).
6. Sheldrick, G. M. SHELXT - Integrated space-group and crystal-structure determination. *Acta Crystallogr. Sect. A Found. Crystallogr.* **71**, 3–8 (2015).
7. Sheldrick, G. M. A short history of SHELX. *Acta Crystallogr. Sect. A Found. Crystallogr.* **64**, 112–122 (2008).
8. Grimme, S., Ehrlich, S. & Goerigk, L. Effect of the damping function in dispersion corrected density functional theory. *J. Comput. Chem.* **32**, 1456–1465 (2011).
9. Sheldrick, G. M. Crystal structure refinement with SHELXL. *Acta Crystallogr. Sect. C Struct. Chem.* **71**, 3–8 (2015).
10. Dolomanov, O. V., Bourhis, L. J., Gildea, R. J., Howard, J. A. K. & Puschmann, H. OLEX2: A complete structure solution, refinement and analysis program. *J. Appl. Crystallogr.* **42**, 339–341 (2009).
11. S. Smeets, B. Wang, M. O. Cichocka, J. Ångström, W. W. Instamatic. (2018).
12. Kabsch, W. XDS. *Acta Crystallogr. Sect. D Biol. Crystallogr.* **66**, 125–132 (2010).
13. Wan, W., Sun, J., Su, J., Hovmöller, S. & Zou, X. Three-dimensional rotation electron diffraction: software RED for automated data collection and data processing. *J. Appl. Crystallogr.* **46**, 1863–1873 (2013).
14. Sheldrick, G. M. SHELXT – Integrated space-group and crystal-structure determination. *Acta Crystallogr. Sect. A Found. Adv.* **71**, 3–8 (2015).
15. Sinha, P. *et al.* Surface Area Determination of Porous Materials Using the Brunauer-Emmett-Teller (BET) Method: Limitations and Improvements. *J. Phys. Chem. C* **123**, 20195–20209 (2019).
16. Naderi, M. Surface Area: Brunauer-Emmett-Teller (BET). *Prog. Filtr. Sep.* 585–608 (2015).

Chapter 6
Conclusions and Future Work

1. Conclusions

In this thesis, several HOFs structures were constructed using molecules with carboxylic acid groups and their discovery was accelerated using different techniques. The structures and properties were also investigated using a combination of diffraction techniques, gas sorption analysis, thermal analysis, and calorimetry. It was also demonstrated that CSP structures can be discovered in the laboratory using a HT crystallisation method that was used to rapidly screen hundreds of different crystallisation conditions. For **TMA** and **ADTA** the HT screen was performed after CSP calculations indicated promising unknown porous crystal structures were waiting to be found experimentally.

The hybrid computational and experimental approach allowed new solvated porous structures for **TMA** to be discovered. In addition, hydrogen bond networks of **ADTA** that featured lower degrees of interpenetration than the previously reported 5-fold interpenetrated were discovered. The desolvated porous polymorph of **TMA**, δ-**TMA**, had a SA_{BET} = 910 m^2/g and was found by solvent exchanging one of the crystallised structures (**TMA**_2-33) with *n*-pentane before activating its pores. The thermal stability of δ-**TMA** phase was also explored, and its crystal structure was an excellent match to a low-energy predicted structure on its CSP energy landscape. The experimental 3-, 4-, 5-fold interpenetrated structures of **ADTA** also matched well with the predicted structures. More generally, the combination of CSP with HT crystallisation screening has the potential to aid the discovery of other porous molecular solids.

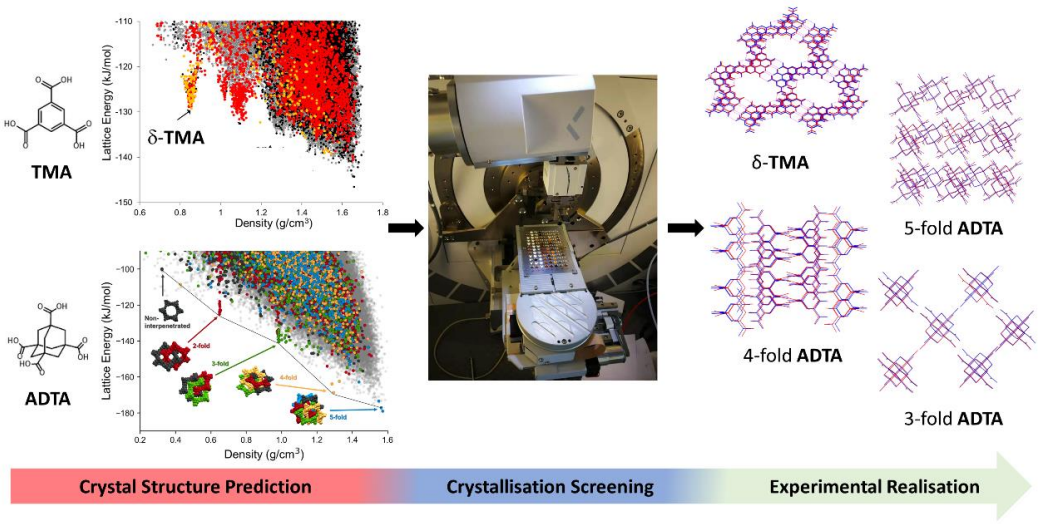

Figure 6.1. The diagram of the discovery of new structures of **TMA** and **ADTA**.

Inspired by the results with **TMA** and **ADTA**, five more carboxylic acid molecules with 3-fold symmetry and feature more conjugated cores compared to **TMA** (**M1**-**M5**) were investigated and crystallised from different conditions. Their single crystal structures were explored. THF was found to form a hydrogen bond with carboxylic acid in **M1** to generate a solvated structure, **M1-1**. By contrast, a mesoporous HOF was constructed with **M2** after crystallisation from dioxane/mesitylene. 3-D ED was used to determine the desolvated structure. **M2-2** is a rare example in mesoporous HOF and was formed by the carboxylic acid groups interaction to form $R_2^2(8)$ motifs. However, it wasn't possible to obtain an ideal high BET surface area for **M2-2** due to the unknown quantity of non-crystalline particles. A structural transformation was found to occur during the activation of **M3-1** and this led to the formation of a desolvated structure, **M3-2**, with smaller pores. Although **M4**, was crystallised from the same condition as **M2-1**, I was found that 1,4-dioxane hydrogen bonded with two of the carboxylic acid groups in **M4**, which prevented the formation of a comparable $R_2^2(8)$ hydrogen bonded network. The more conjugated molecule, **M5**, was found to form a large pore structure (**M5-1**) with water incorporated in the pores. As well and the trigonal molecules **M1**-**M5**, three molecules with four carboxylic acid analogues (**M6**-**M8**) were also explored. Porous clathrate structures of **M7** and **M8** were obtained from the evacuation of **M7-1** and **M8-1** with *n*-pentane solvent exchange and

the desolvated structures were determined with SCXRD.

ABTPA-2, which contains anthracene units that can adapt conformation, is a dynamic 2-D HOF material. A combination of the hydrogen-bonded network and anthracene cores were found to stabilise its porous crystal packings. **ABTPA-2** was also found to be dynamic and could respond to external stimuli, such as guest absorption and changes in sample temperature. The **ABTPA** HOF was found to change its conformation during crystal activation, which led to a structural change and the HOF underwent a highly unusual structural expansion in the process. The molecular structure of a HOF adapts during activation to initiate a structural expansion. Chemical analogs of **ABTPA** might also be promising HOF precursors and may exhibit similar behavior as HOF materials. Importantly, the expandable behavior can be explained by computational calculations used in the study. This was achieved by calculating the effect of crystal packing on conformational strain in predicted HOF structure. In the future, identifying structural pairs on the crystal structure landscape that represent routes for the relaxation of high intramolecular strain via a structural transformation to a less strained structure may provide a route to predict such behaviour.

For the first time, 3-D ED was used to determine the structure of a porous HOF structure. More broadly, the successful discovery of expandable **ABTPA-2** proved that 3-D ED is an accurate method to determine the structure of porous organic molecular solids rapidly. Especially, 3-D ED is an ideal supplement of SCXRD, which is essential when the crystals are too small. In the future, 3-D ED will become an important new tool for crystalline materials discovery.

2. Future work

2.1 The design and crystallisation of high conjugated carboxylic acid molecules

In chapter 4, the conjugated **ABTPA-2** structure had a high BET surface and good stability. Based on the **ABTPA** molecule, two similar molecules with different anthracene and pyrene core were designed (Figure 6.2). Since 1,3,6,8-tetra(4′-carboxyphenyl)pyrene (**TBAP**) and 4,4',4''-(1,3,3a1,4,6,7,9-heptaazaphenalene-2,5,8-triyl) tribenzoic acid (**M5**) were reported as organic photocatalysts for water splitting[1,2], the molecules shown in Figure 6.2 may also be promising photocatalytic candidates due to the presence of the π-conjugated systems. The anthracene and pyrene may influence the photocatalytic performance between these two molecules.

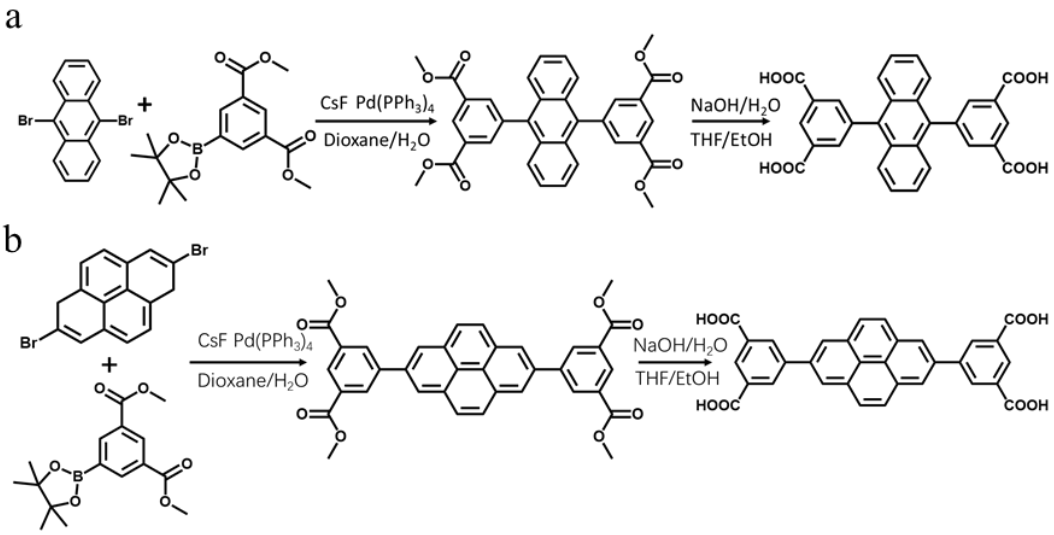

Figure 6.2. The synthetic method of high conjugated molecules.

2.2 The design and crystallisation of low symmetric carboxylic acid molecules

HOFs constructed with the low symmetric molecules are rare[3]. Here, two molecules in Figure 6.3 were designed. The low symmetry of the precursors may increase the possibility of forming structures from different crystallisation conditions. Also, the

extended and high conjugated system may increase the porosity and stability of HOF materials.

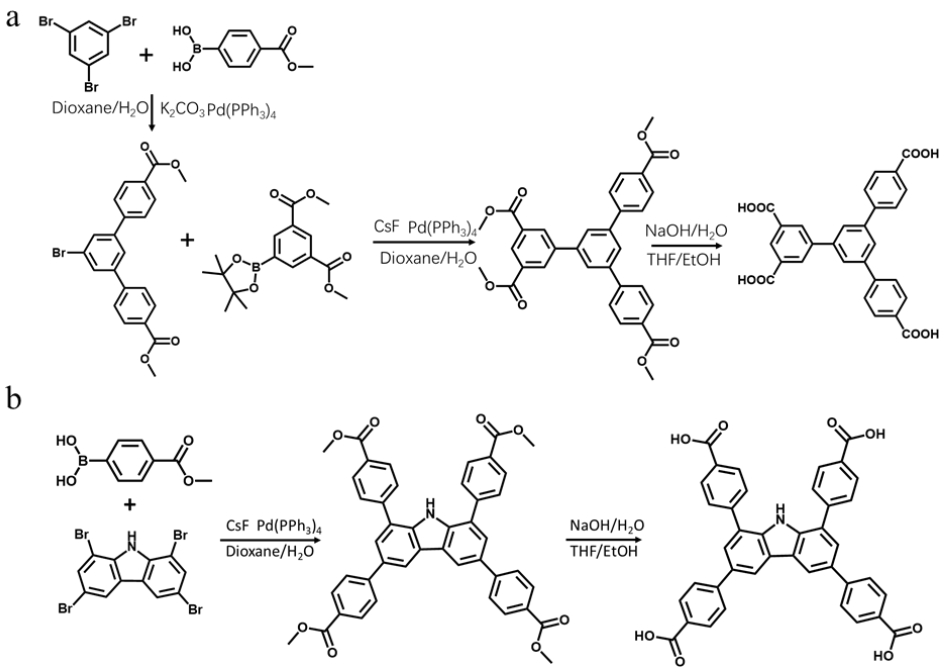

Figure 6.3. The synthetic method of high conjugated low symmetric molecules.

2.3 Combine high throughput crystallisation and serial electron diffraction to accelerate the discovery porous molecular solid

In chapter 2, a high throughput crystallisation workflow was developed, and phase identification was screened by PXRD. The serial electron diffraction (serial ED) is also an efficient method to promptly determine crystal structures, and some zeolites have recently been explored by the serial ED.[4] The combination of HT crystallisation screening and serial ED may further accelerate the discovery of molecular solids. Here, some different kinds of molecules (molecules with carboxylic acid groups[5], urea groups[6], and the covalent cage 1 (CC1)[7,8], Figure 6.4) could be good candidates for this study to determine the feasibility.

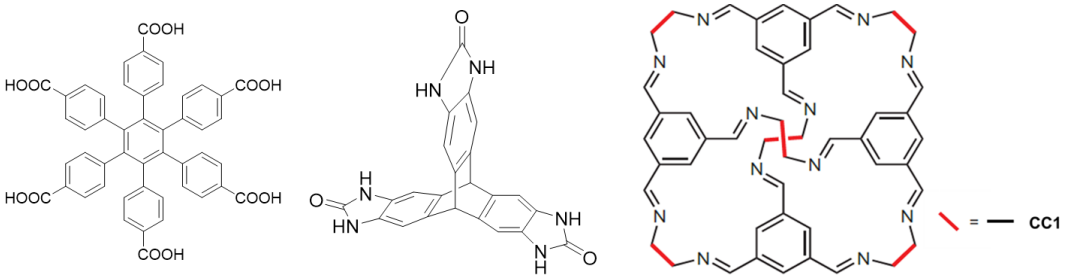

Figure 6.4. Different candidates (small molecules, porous organic cage) could be explored in a larger serial ED study.

3. References

1. Li, T. *et al.* Integrating active C3N4moieties in hydrogen-bonded organic frameworks for efficient photocatalysis. *J. Mater. Chem. A* **9**, 4687–4691 (2021).
2. Aitchison, C. M. *et al.* Photocatalytic proton reduction by a computationally identified, molecular hydrogen-bonded framework. *J. Mater. Chem. A* **8**, 7158–7170 (2020).
3. Wang, B. *et al.* Microporous Hydrogen-Bonded Organic Framework for Highly Efficient Turn-Up Fluorescent Sensing of Aniline. *J. Am. Chem. Soc.* **142**, 12478–12485 (2020).
4. Wang, B., Zou, X. & Smeets, S. Automated serial rotation electron diffraction combined with cluster analysis: An efficient multi-crystal workflow for structure determination. *IUCrJ* **6**, 854–867 (2019).
5. Kobayashi, K., Shirasaka, T., Horn, E. & Furukawa, N. Two-dimensional hexagonal hydrogen-bonded network with triangle-like large cavities: Hexakis(4-carboxyphenyl)benzene. *Tetrahedron Lett.* **41**, 89–93 (2000).
6. Pulido, A. *et al.* Functional materials discovery using energy-structure-function maps. *Nature* **543**, 657–664 (2017).
7. Jones, J. T. A. *et al.* On-Off Porosity Switching in a Molecular Organic Solid. *Angew. Chemie* **123**, 775–779 (2011).
8. Jelfs, K. E. *et al.* Conformer interconversion in a switchable porous organic cage. *Phys. Chem. Chem. Phys.* **13**, 20081–20085 (2011).